Autonomous Hybrid Powered Long Ranged Airship for Surveillance and Guidance

Steven Recoskie

Thesis submitted to the
Faculty of Graduate and Postdoctoral Studies
in partial fulfillment of the requirements
for the Doctorate in Philosophy in Mechanical Engineering

Ottawa-Carleton Institute for Mechanical and Aerospace Engineering
University of Ottawa

Acknowledgments

I would like to offer my utmost gratitude to my supervisor, Dr. Eric Lanteigne, for his guidance, support, enthusiasm, and endless patience throughout the course of this project. I take great pleasure to acknowledge the contribution of my co-supervisor, Dr. Wail Gueaieb, for all of his time and valuable input. I am deeply sorry to mention the death of my previous supervisor, Prof. Dr. Atef Fahim, who had an enormous impact on the original conception and direction of this research as well as shaping my own engineering career. For their help and advice designing several aspects of the dirigible prototype, I would like to recognize John Perrins, Léo Denner, Michael Burns, Stanley Weedmark and James McDermott. For their financial support, I would like to thank the National Sciences and Engineering Research Council of Canada (NSERC) and the Canada Foundation for Innovation (CFI). Finally, thank you to my family and friends for their loving support through my seemingly endless academic pursuits.

Abstract

With devastating natural disasters on the rise, technological improvements are needed in the field of search and rescue (SAR). Unmanned aerial vehicles (UAVs) would be ideal for the search function such that manned vehicles can be prioritized to distributing first-aid and ultimately saving lives. One of the major reasons that UAVs are under utilized in SAR is that they lack a long flight endurance which compromises their effectiveness. Dirigibles are well suited for SAR missions since they can hover and maintain lift without consuming energy and can be easily deflated for packaging and transportation. This research focuses on extending flight endurance of small-scale airship UAVs through improvements to the infrastructure design and flight trajectory planning.

In the first area, airship design methodologies are reviewed leading to the development and experimental testing two hybrid fuel-electric power plants. The prevailing hybrid power plant design consists of a 4-stroke 14cc gasoline engine in-line with a brushless DC motor/generator and variable pitch propeller. The results show that this design can produce enough mechanical and electrical power to support 72 hours of flight compared to 1-4 hours typical of purely electric designs. A power plant configuration comparison method was also developed to compare its performance and endurance to other power plant configurations that could be used in dirigible UAVs. Overall, the proposed hybrid power plant has a 600% increase in energy density over that of a purely electric configuration.

In the second area, a comprehensive multi-objective cost function is developed using spatially variable wind vector fields generated from computational fluid dynamic analysis on digital elevations maps. The cost function is optimized for time, energy and collision avoidance using a wavefront expansion approach to produce feasible trajectories that obey the differential constraints of the airship platform. The simulated trajectories including 1) variable vehicle velocity, 2) variable wind vector field (WVF) data, and 3) high grid resolutions were found to consume 50% less energy on average compared to planned trajectories not considering one of these three characteristics.

In its entirety, this research addresses current UAV flight endurance limitations and provides a novel UAV solution to SAR surveillance.

Preface

This thesis has been prepared in "Thesis by article" format described in the 2013 general regulations for a doctoral thesis, University of Ottawa, Faculty of Graduate Postdoctoral Studies.

"The minimum requirements for this thesis format are three articles for a doctorate. If the research embodied in the articles required approval of an ethics board or was part of a collaboration, this must be spelled out in a preface or statement. In this preface, the student must indicate the following: a) what ethics approvals, if any, were required and when those approvals were secured; b) what are the contributions of collaborators and/or co-authors, distinguish the student's own contributions from all other contributions. The thesis by article must have: a) a general introduction, which outlines the thesis topic, and how the articles that comprise the main body of the text will address the topic. b) a general discussion and conclusion, which integrates the material addressed in the various articles and provides a global summary and analysis. The student must get permission to use copyrighted material from any co-authors (if they hold copyright) as well as from publishers."

No ethics approvals were required for this research. The contributions of co-authors are listed on the following page. Copyright to republish the material from all manuscripts was obtained from Dr. Wail Gueaieb and Dr. Eric Lanteigne. Copyright has been obtained from the publisher of each respective journal for the final submission to the department.

Contributions of Co-authors

The manuscript-based format was used for Chapters 2, 3, 4 and 5 of this thesis. The chapters are not direct duplicates of the existing work. Several author original content additions and some formatting changes were made to promote clarity and coherence of the presented subject matter.

Chapter 2: Alcohol based hybrid UAV power plant The chapter is based on two manuscripts that were based on the same power plant configuration. The author presented the implementation of Chapter 2 to the International Conference on Unmanned Aircraft Systems, 2012, Philadelphia, US, in a full paper entitled "Dirigible UAV power plant design". A special edition, extended manuscript was published in the Journal of Intelligent and Robotic Systems, 69:69-81, 2013 entitled "Experimental testing of a hybrid power plant for a dirigible UAV" containing additional testing and results. This work was performed under the supervision of professors Dr. Atef Fahim, Dr. Wail Gueaieb and Dr. Eric Lanteigne who are the co-authors on both manuscripts. The author conducted the experiments, performed the analytics and prepared the Chapter. The professors acted in a supervisory role, aided in the conception of the design, and provided editing and technical support. The published manuscripts are included in Appendices A.1 and A.2, respectively.

Chapter 3: Gasoline based hybrid UAV power plant The chapter is based on a manuscript that was published to IEEE/ASME Transactions on Mechatronics, 19:606-614, 2014, entitled "Hybrid power plant design for a long range dirigible UAV". This work was performed under the supervision of professors Dr. Atef Fahim, Dr. Wail Gueaieb and Dr. Eric Lanteigne who are the co-authors of the manuscript. The author conducted the experiments, performed the analytics and prepared the Chapter. Dr. Atef Fahim contributed to the original conception of the research while Dr. Wail Gueaieb and Dr. Eric Lanteigne acted in a supervisory role, aided in the conception of the design, and provided editing and technical support. The published manuscript is included in Appendix A.3.

Chapter 4: Trajectory planning The chapter is currently under final revision and will be submitted to the AIAA Journal of Guidance, Control, and Dynamics. This work was performed under the supervision of professors Dr. Wail Gueaieb and Dr. Eric Lanteigne who are the co-authors of the manuscript. The author formulated the theoretical approach, performed the simulations and prepared the Chapter. The professors acted in a supervisory role, aided in the conception of the theoretical approach, and provided editing and technical support.

Chapter 5: Dynamic modelling and flight control The chapter is based on a manuscript in progress that will be submitted to an academic journal. The work was performed under the supervision of professors Dr. Wail Gueaieb and Dr. Eric Lanteigne who will be the co-authors of the potential manuscript. The author formulated the theoretical approach, performed the simulations and prepared the Chapter. The professors acted in a supervisory role, aided in the conception of the theoretical approach, and provided editing and technical support.

Table of Contents

List of Figures

List of Tables

Glossary

CFD Computational fluid dynamics

CLF Control Lypanov Function

CM Centre of mass

CV Centre of volume

DEM Digital elevation map

ETA Estimated time of arrival

HTA Heavier than air (aircraft)

LTA Lighter than air (aircraft)

MSZ Minimum separation zone

PWM Pulse width modulation

SOC State of charge

UAV Unmanned aerial vehicle

WVF Wind vector field

1. Introduction

1.1. Search and Rescue

There has been a rising trend in the occurrence of natural disasters which have more than doubled worldwide in the past two decades [1]. In the wake of the 2004 Asian earthquake and tsunami, it became clear that navigating disaster areas can sometimes prove impractical, if not impossible, and that technological improvements in the field of Search and Rescue (SAR) were needed to support rescuers, efficiently distribute first-aid, and ultimately save lives. Current SAR technologies consist of a combination of manned vehicles such as helicopters for both the search and rescue functions. National and international SAR organizations are currently looking for new search and rescue initiatives and have setup research funds and competitions to promote development [2, 3]. With limited manned SAR assets, first responders are increasingly eyeing unmanned vehicles as cost-effective alternatives or complements to manned operations. In May 2013, the first account of a civilian unmanned aerial vehicle (UAV) saving a person's life was reported following a car accident in rural Saskatchewan. Several weeks later, the Association for Unmanned Vehicle Systems International issued a statement predicting that disaster response would account for 10% of the future drone industry [4]. Unmanned aerial vehicles would be ideal for the search function such that manned vehicles can be prioritized to helping victims.

1.2. Current Solutions

In the SAR field, the collection of alternatives is broad ranging from satellites to search dogs. However, existing solutions consist mostly of manned crafts in disaster situations and volunteer search parties and sweeps in missing persons cases. Manned crafts, which are already firmly implanted in the industry, are typically costly to buy, operate and maintain. For example, a helicopter costs $1,600 per hour and a coast guard patrol boat costs $1,147 per hour [5]. When a C-130 cargo plane is needed, the cost soars to $7,600 per hour [5]. Furthermore, manned vehicles, as well as volunteer search parties, are prone to fatigue and panic which can bias their report of a situation. Volunteer search parties, although they

have no upfront purchase cost, still need to be lodged, fed, trained and equipped, which can add up to a significant expense. Satellite imagery and closed-circuit television (CCTV) cameras also figure amongst the alternate solutions. Satellite imagery's cost is prohibitive at $3,600 per scene and can only take pictures at specific times when the satellite is over the desired region [6]. CCTV cameras are a very inexpensive way to survey a situation, but they rely heavily on existing infrastructure that may or may not be damaged. Their lack of mobility is also a major limitation.

1.3. UAV Dirigibles

The use of UAVs for search and rescue is not a new idea, yet, UAVs are currently under utilized because they lack effectiveness. Current SAR UAVs are either small, battery powered propulsion systems which have very limited endurance or are very large military UAVs that are expensive to operate and cannot adequately survey disaster areas. Dirigibles are well suited for use as reconnaissances platform to aid rescue crews after disasters since they can maintain lift without consuming energy, take off and land vertically, and hover in place to monitor developments on the ground [7–11]. Figure 1.1 shows how current fixed wing, rotary wing and airship UAVs compare on the basis of endurance and payload. These data were collected and combined from multiple sources such as the US Department of Defense [12–15]. UAVs that do not travel, such as aerostats, and upper atmosphere UAVs were excluded. Data were also excluded if inconsistent between publications or when only a range was provided. Based on the shaded area in Figure 1.1, it can be seen that all small UAVs (indicated by payloads under 1 kg) have a flight endurance of four hours or less. A low flight endurance can severely limit a UAVs effectiveness in search and rescue operations. It should be noted that payload is only an indicator of vehicle size as some solar powered, upper atmosphere, fixed wing aircraft plotted are very large despite their small payload and impractical for SAR support.

Following several correspondences with various SAR organizations such as the Red Cross and the RCMP, a list of UAV performance criteria goals for search and rescue operations was defined and given in Table 1.1. A performance metric can also be used to compare the entire spectrum of UAVs [12]. Figure 1.2 combines three essential performance characteristics; maximum range, maximum endurance and payload versus unit cost for a baseline of existing technologies[1]. Other char-

[1]The maximum range and maximum endurance are mutually exclusive properties. Unit cost was the only information that was published in verifiable database sources and does not include maintenance, operating or total cost.

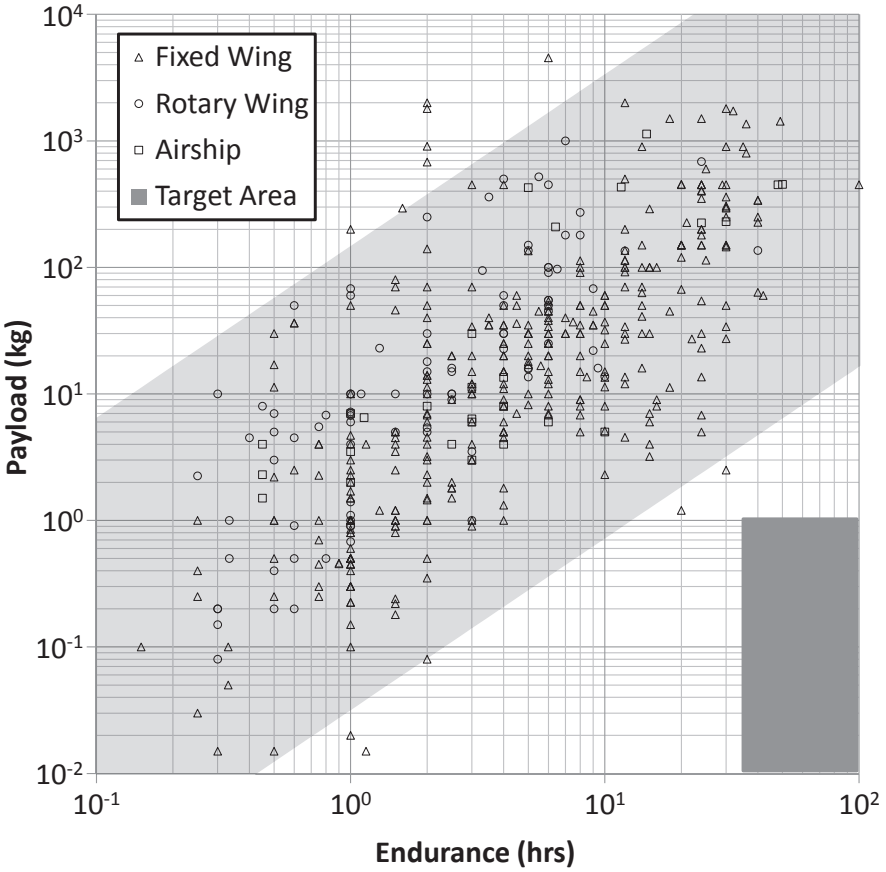

Figure 1.1.: UAV payload capacity versus endurance. Data was collected from both military and research agencies from several countries [12–16].

Table 1.1.: List of UAV performance goals

Property	Desired Value
Flight Endurance	$\geq$24 hours
Total Unit Construction Cost	$\leq$\$5,000 CAD
Flight Range	$\geq$10 km
Top Speed	$\geq$10 m/s
Payload excluding fuel	$\geq$1 kg
Cruise Altitude	200 m
Max Altitude	1,000 m
Packaged Volume	$\leq$250 L

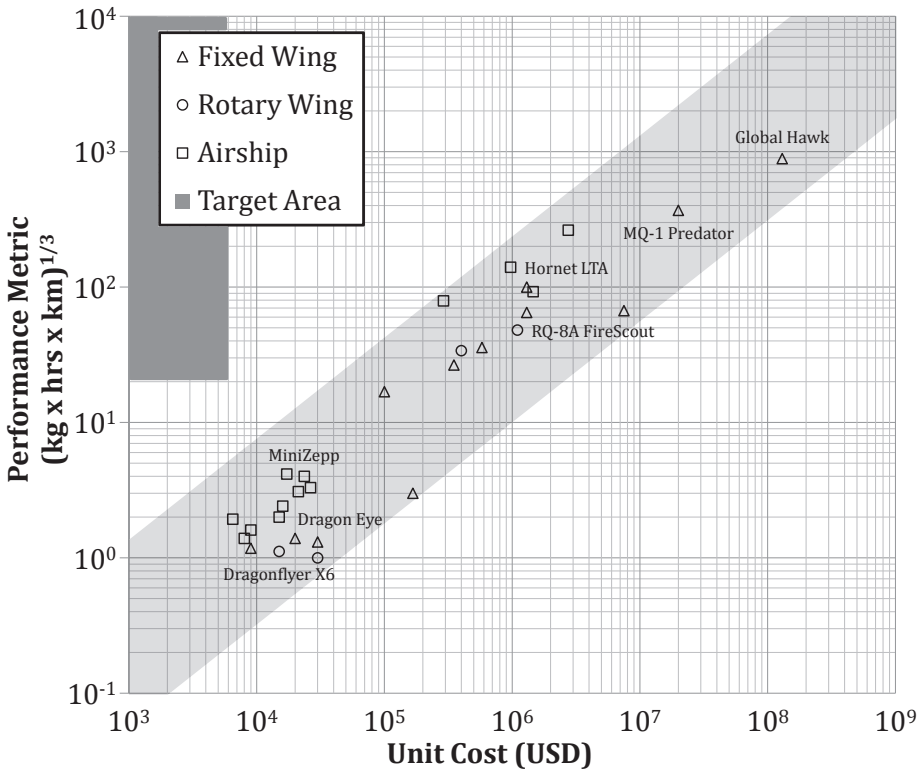

Figure 1.2.: UAV performance metric (payload x endurance x range) versus unit cost [12–16]

acteristics could also be added, such as deployment time, however this information is rarely published. The performance metric is defined as the cubed root of the product of range, endurance and payload. For this comparison, equal weights were given for each characteristic since they are related through other factors such as fuel capacity and travel speed, however, they could also be adjusted based on their importance for application specific requirements. The target areas shown in Figures 1.1 and 1.2 represent favorable surveillance characteristics for SAR UAVs and lie outside the area of existing UAV technologies. Based on these findings, it is clear that a robust UAV system is needed to meet the operational requirement of long endurance while maintaining a low unit cost.

1.4. Research Motivation and Contribution Areas

The objective of this research is to design, develop and evaluate a low cost, long endurance, autonomous UAV dirigible capable of providing crisis management solutions and search and rescue support. The goal is not to replace existing technologies, such as helicopters, but rather complement their abilities and ultimately allow for efficient distribution of resources. Much research has been devoted to

UAV airship design methodology over the past decade [17–19] but none were found with focus on long endurance. To achieve a long endurance, the research that follows focuses on both increasing energy conversion efficiency and reducing energy consumption.

Due to the unique advantages, requirements and limitations inherent of a dirigible UAV, several adaptations are required to existing conventional fixed-wing and rotary-wing research and technology. Although these adaptations are frequently challenging, they offer interesting research opportunities.

Major areas where significant potential improvements to these criteria were made are:

1. UAV hybrid power plant design
2. Multi-objective trajectory planning
3. Dynamic modelling and flight control

1.5. Thesis Outline

The following sections are divided into chapters based on the major areas defined in the previous section.

Chapters 2 and 3 present the design and experimental testing of two different novel hybrid power plant configurations (alcohol and gasoline engines, respectively). Each of these configurations are compared on the basis of power and energy density as a viable alternative to conventional pure electric and pure fossil fuel configurations. Several considerations were made to facilitate UAV integration such as autonomous start-up/shutdown and the identification of key operating points.

Chapter 4 presents a wavefront expansion type, multi-objective trajectory planner incorporating variable wind vector fields generated from computational fluid dynamic analysis on randomly generated digital elevation maps. Near optimal and feasible trajectories are generated at real-time speeds and simulated in large, realistic, and 3D environments. Four cases are developed to compare the impact of vehicle velocity, variable WVF data, and grid resolution on energy consumption and path feasibility.

Chapter 5 presents the airship dynamic model and two automatic flight controllers. Several additions are made to the conventional airship dynamic model including low speed rotational damping terms, mass compensation, parametric and modelling uncertainty, air ballasts, and tail thruster actuators. A backstepping based control law is developed and compared to conventional PID control for

trajectory following on the basis of control effort and tracking error for each of the cases in the previous chapter.

Chapter 6 concludes with a global summary of the contributions and significance of the research performed and then outlines a number of potential future directions for this research.

2. Alcohol Based Hybrid UAV Power Plant

The required propulsive power range of lighter than air (LTA) aircraft is much wider than that of heavier than air (HTA) aircraft since LTA aircraft do not require propulsive power for lift. The range of power requirements for rotary wing, fixed wing and LTA are presented in Figure 2.1. This presents a problem when selecting a suitable prime mover. Electrical power requirements for LTA aircraft can be over 65% of the total power and average cruise speeds compared to 15% for HTA aircraft [19]. Purely electric propulsion designs have significantly shorter flight endurance due to the lower energy density of electric power storage coupled with high electrical power requirements. Purely piston powered propulsion designs suffer from significant increases in specific fuel consumption at low engine power (during idling) and have a narrow peak efficiency range which makes varying the load on the engine undesirable. Furthermore, electrical energy storage is still required for avionics, therefore neither fuel or electric energy can be fully consumed during flight; the first depleted will limit flight endurance. The generally accepted ideal solution is to drive electric generators from piston-powered engines [17, 19–22]. This solution takes advantage of the high energy density of fossil fuels and wide peak efficiency operating range of electric motors.

2.1. Literature Review

Existing research into hybrid power plants for UAVs is limited, especially for dirigible-type UAVs. Glasscock *et al.* developed a hybrid alcohol-electric power

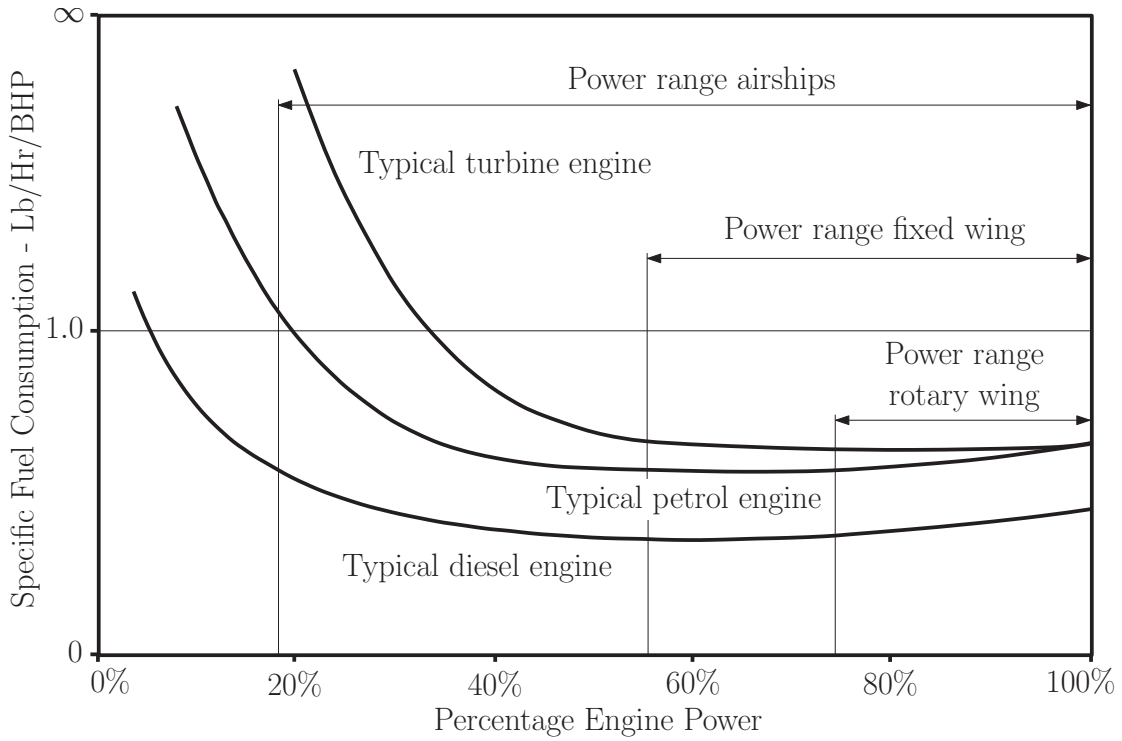

Figure 2.1.: Specific fuel consumption for different aircraft types. Adapted from [16, 19, 23]

plant for a fixed wing UAV [22]. The authors built a prototype with a model engine coupled in parallel with an electric generator and propeller through a gearbox shown in Figure 2.2. The prototype test results show that the UAV has the potential to increase performance (56% improvement to climb rate) and efficiency (13% improvement to endurance) compared to a solely internal combustion engine powered UAV. Gaide *et al.* simulated and tested a similar hybrid alcohol-electric power plant configuration for a fixed wing UAV [21]. The authors predicted a 60-70% increase in fuel efficiency over a traditional gas powered UAV of the same size. Experimental testing was limited to only testing the electric motor efficiency. Hiserote simulated several hybrid-electric propulsion system configurations for small fixed wing UAVs using Matlab [24]. He performed a comparison study of three power plant designs and three battery discharge strategies using weight fractions during three different mission objectives. An example of the parallel configuration is shown in Figure 2.3. He determined that the centerline-thrust design, a series hybrid with two dedicated electric motors, had a superior survivability and fuel efficiency. He also discussed both the advantages and limitations of using commercially available off the shelf (COTS) components.

Research into energy efficient and long endurance airship UAVs are largely unexplored to date and existing literature focuses on large, high altitude airship platforms used for communication and surveillance. Yu *et al.* presented a config-

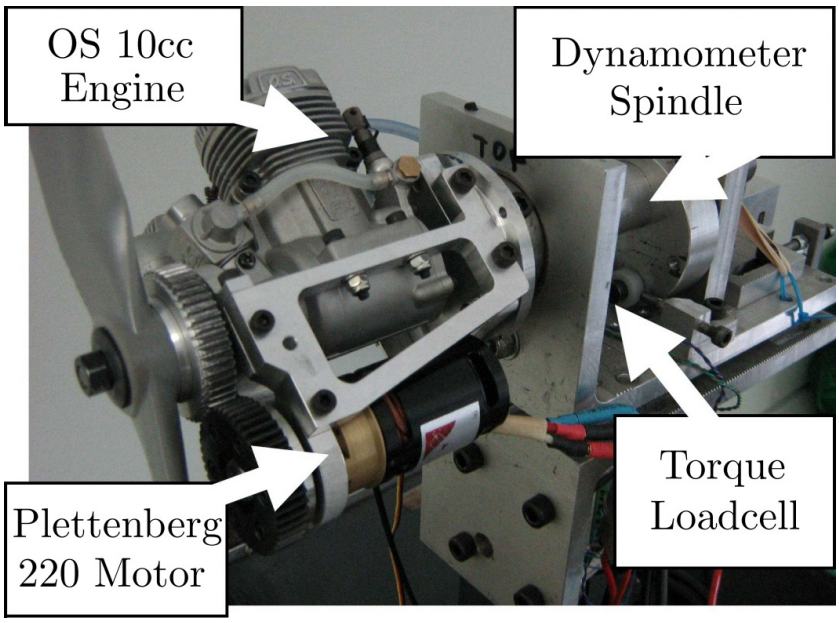

Figure 2.2.: Alcohol based hybrid power plant built by Glasscock *et al.* [22].

Figure 2.3.: Parallel hybrid propulsion system for a fixed-wing aircraft [24, 25]

uration analysis for high altitude and long endurance airships [26]. The authors proposed methods and trends of sizing sub systems based on geographical, atmospheric and operating conditions. The energy balance analysis relies on the use of photovoltaic solar cells and very large envelope surface area and volume (>200,000 m^3). Kotulla *et al.* presented the power management and control system for a multi-body high altitude airship [27]. The authors used Matlab to simulate a power management controller that manages a gas turbine, propulsion system and lithium battery State of Charge (SOC) over a 24h flight schedule. The proposed airship flies at an altitude of 20km and has an estimated volume of at least 28,000 m^3 based on the power rating. Lubkowski *et al.* investigated the regenerative power source options for a long duration loitering high altitude airship [28]. Based on the results, either luminescent solar concentrators or thin film photovoltaics were recommended for the baseline platform considered. The high altitude airship platform has a volume of 160,000 m^3 and flies at an altitude of 20km.

This chapter presents the design and testing for a novel hybrid power plant design for a UAV dirigible. First, power requirements and design considerations are discussed. Then an overview of the power plant design is presented, followed by the methodology and results of the experimental testing. The overall UAV design is then compared to existing UAVs on the basis of cost, payload, range and endurance.

2.2. Hybrid Power Plant Design

The proposed hybrid power plant consists of an engine, a brushless DC generator, and a propeller connected inline as shown in Figure 2.4. This configuration provides the most flexible operating conditions as both fuel and electrical energy can be depleted simultaneously (maximizing flight endurance). The engine can be shut down during periods when propulsion or electrical generation is not required and the generator can be run in reverse to start the engine when required. This eliminates the need for a separate starter motor. Starting and stopping the engine as required keeps the engine under constant load and maximum efficiency, and maintains the batteries in the their useful operating range. When the power plant is connected to the UAV, the engine is turned on according to the current flight conditions. These conditions include: distance remaining to target, UAV operating speed, opposing wind and the SOC of the battery. The proposed design can be adjusted for the following three scenarios:

1. Maximum engine efficiency - Minimizing engine fuel consumption and maxi-

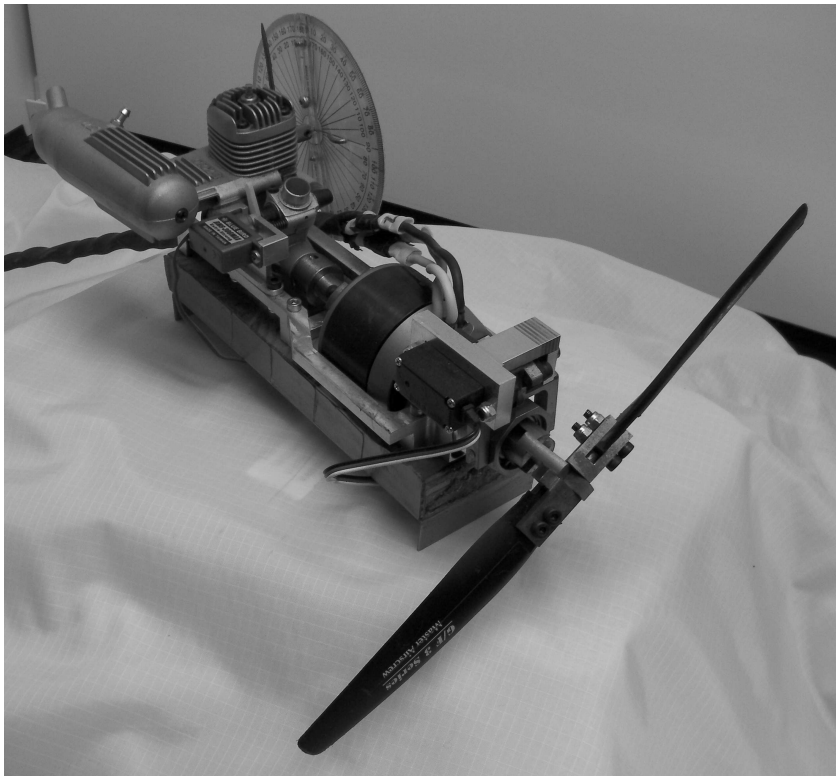

Figure 2.4.: Experimental hybrid power plant [23, 29]

mizing flight duration are paramount in this operating mode. The loading of the engine is held in its maximum efficiency zone by balancing the mechanical propulsion and electrical generation based on the current flight conditions, trip characteristics and SOC of the battery.

2. Maximum propulsion - This mode is used when propulsion is required but not electrical generation such as when the batteries are charged but the LTA needs to move to a position quickly. During this time, the batteries cells can be electrically disconnected and the propeller pitch can be adjusted to maximum thrust based on current airspeed.

3. Maximum electrical generation - This mode is used when electrical generation is required but not propulsion such as when the batteries need to recharge and the LTA is hovering in one place. During this time, the propeller pitch is adjusted to a feathered position and additional battery cells are electrically connected.

Properly matching the engine and generator speed ranges is essential to minimizing the specific fuel consumption of the engine. Maximum propeller efficiency can be achieved by implementing a variable pitch propeller.

2.2.1. Design considerations

The maximum in-flight fuel usage for LTA aircraft is restricted by the maximum takeoff weight and the minimum landing weight [19]. To extend the inflight fuel usage, it is assumed that air will be gradually collected to balance fuel depletion. For the purposes of this design, the maximum in-flight fuel usage will be limited to 3kg of fuel. If severe overpressure is detected, helium can be vented to prevent damage to the helium bladder. This method is ideal because it provides a means for altitude control and can regulate the dirigible's internal pressure to safe levels.

Another design consideration is the battery charging rate. The generally accepted charging rate of most lithium ion rechargeable batteries is no more than 1C (1 multiplied by the rated battery capacity). Ideally, the battery capacity should be minimized to reduce the weight of the power plant. Since the battery capacity is limited by the magnitude of power it can accept and the duration it is rated to accept it, the battery was chosen based on the maximum electrical generation of the selected engine-generator combination. Recently, new generation lithium polymer batteries have been released that offer twelve times the capacity charging rate. This significantly lowers the battery capacity limitation and thus reduces the size and weight of the battery.

2.2.2. Sizing

The initial sizing of the components was determined using the methodology proposed by Pant [18]. The iterative loop begins by estimating the helium volume storage of the airship, also known as the envelope. The envelope, air ballast and tail fin geometry, and the static lift were then calculated based on the volume estimate and the optimal aspect ratio. The optimal aspect ratio of airship length over diameter was selected to be 3.3 based on the minimum sum of form and skin drag on the streamlined National Physics Laboratory low drag airship body shape. The weights of the envelope, gondola, fins, and all sub-systems were estimated using preselected materials or weight factors modelled on existing LTAs [18, 19]. The work envelope is iterated until the difference of lift to weight converges to a satisfactory value [18]. Drag, total propulsion power, electric capacity and fuel weight were estimated based on the desired operating performance.

For the proposed UAV dirigible, the work envelope was iterated until a payload mass of 1 kg was achieved to allow for additional accessories or modifications. Given a net lift of 118N, the total installed propulsive power, electric capacity and fuel mass were estimated at 720W, 75Wh and 3kg, respectively.

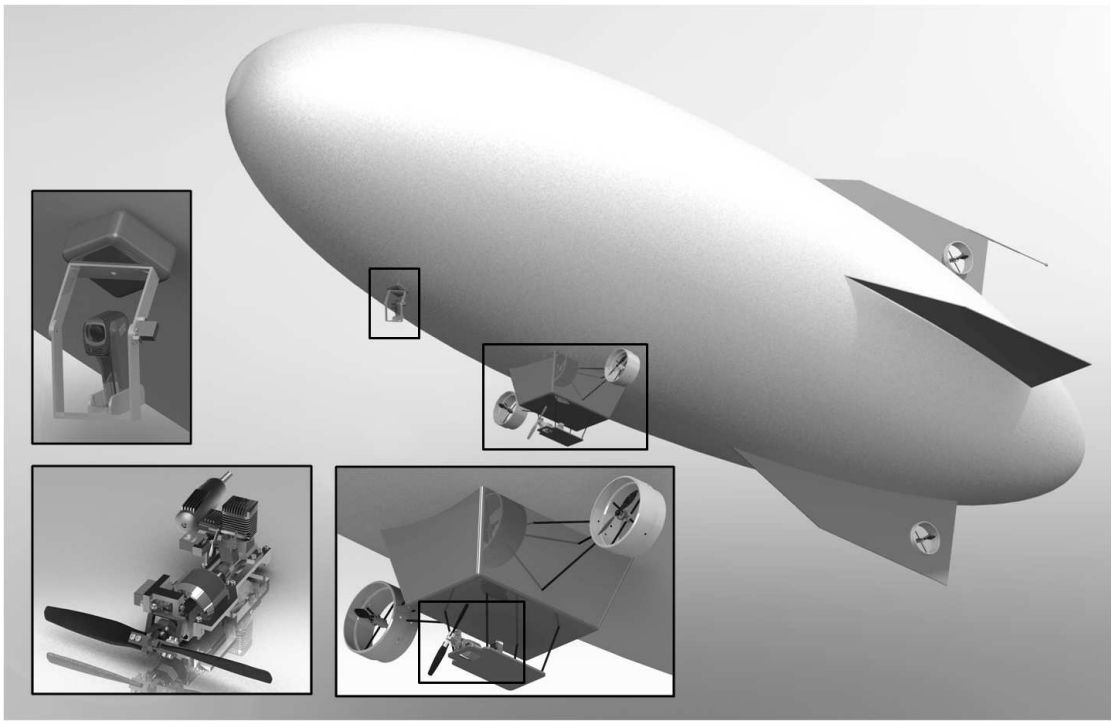

Figure 2.5.: Dirigible design (middle), camera, GPS and inertial navigation system (left), hybrid power plant (lower left), and auxiliary electric propulsion (below) [23, 29]

2.3. Hybrid Power Plant Design Overview

2.3.1. Hybrid power plant configuration

Three configurations that are common among hybrid electric road vehicles are series, parallel, and power split (a combination of series and parallel). The ideal configuration for a dirigible UAV will minimize the number of components (i.e. weight) and will minimize energy conversions and transformations (i.e. losses). A series configuration requires two energy conversion processes that reduces efficiency and prevents the engine from contributing to the total available propulsion power. A parallel configuration would require a controllable clutch mechanism to decouple the electric motor from the engine to prevent it from back driving.

The configuration chosen for this power plant is a power split configuration (full hybrid) with separately actuated propulsion which can be seen in Figure 2.5. It was determined that the weight of a controllable clutch mechanism was greater than adding two independent brushless DC propulsion systems to the vehicle, and these devices also contribute to the total available propulsion power. The hybrid power plant is in a parallel configuration while the additional electrically driven propellers act as the series portion. Two other benefits are the reduced dependence on a single propulsion system and increased operational flexibility.

2.3.2. Engine

Three options for the prime mover include petrol engines, diesel engines, and gas turbines. Gas turbines were omitted based on the relative scale of the UAV being designed (under 2 hp). The selection of the engine was based on the specific fuel consumption and weight per unit power. For petrol engines these values are 0.46 lb/(HP-hr) and 0.85 kg/HP while for diesel engines these values are 0.37 lb/(HP-hr) and 1.025 kg/HP [19]. Diesel engines are more efficient per HP and have improved reliability over spark ignition engines. Model (Glow-plug) engines operate similar to a diesel engine except for the fact that they have a heat filament to aid in combustion and that they use alcohol fuels rather than diesel fuel. A model engine was selected for this design for its high power to weight ratio and availability in the required horsepower range.

These engines come in two or four stroke cycles. Two stroke engines have a higher power to weight ratio, a lower cost per HP, and a simple construction with fewer moving parts. Four stroke engines have a higher fuel efficiency per HP, a longer engine life, a large range of peak engine performance, and tend to run quieter and cleaner. If the peak engine efficiency is matched with the generator output, and controlled in an on and off manner, then having a narrow peak efficiency range is sufficient. Therefore, a two stroke OS 25LA model engine was chosen for its high power to weight ratio.

2.3.3. Propulsion

The primary propulsion system consists of a variable pitch propeller connected to the model engine. The variable pitch propeller allows for the three different design scenarios proposed previously. The propeller pitch can be set to the feathered position to charge the battery pack without moving the aircraft. It can also be used to control the engine load for maximum engine efficiency, shown in Figure 2.6, when both generating electrical power and propelling. Alternatively, the propeller pitch can be optimized to maximize propulsion efficiency for a given engine speed when not generating electrical power.

In addition to the primary propulsion system, four additional brushless DC motors, connected to fixed pitch propellers, are used for low speed cruising when the engine is turned off, and for directional control while the UAV is hovering. This configuration provides greater maneuverability and eliminates the need for operating the engine at low RPMs. The UAV's electric propulsion is shown in Figure 2.5.

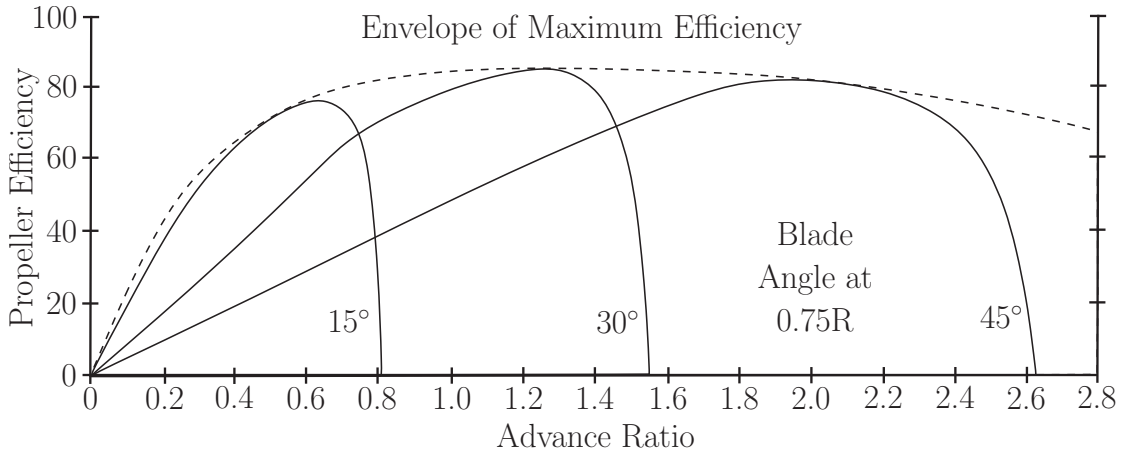

Figure 2.6.: Propeller efficiency versus advance ratio for various propeller pitches [23, 29, 30]

2.3.4. Starter / Generator

The motor constant of a DC motor is determined from the number of turns and size of the coil. It can be shown that the rated power of the motor is inversely proportional to the motor constant. The motor constant dictates the ratio of rotational speed to voltage and current to torque. The most important consideration when using a motor as both a starter and generator is the selection of the motor constant since the optimal values for these two functions are contradictory. As a generator, the motor constant needs to be sufficiently large such that voltage is generated at a higher potential than the batteries. Most small electronic devices operate at 12V or lower and small model engines run at very high speeds (typically in excess of 10kRPM). As a starter, the motor constant needs to be sufficiently small such that the starting torque can overcome inertia and friction in the engine[1]. The torque required to induce a single turn in the engine was experimentally determined to be approximately 0.7 Nm using a pulley and incremental weights.

A common solution is to add a transmission stage or separate motors for each function, however this adds weight, complexity and non negligible frictional losses. The solution was to use a large electrical motor (with a lower motor constant) and to down convert the output voltage to a useable range when generating electricity using a high efficiency switching buck converter.

The options for electric motors include induction, brushed DC, or brushless DC (a type of 3-phase synchronous motor). Brushless DC motors generate 3-phase AC when driven, therefore they require filtering and rectification. Brushless DC motors also need a specialized electronic speed controller. However, they benefit

[1]Particularly when the engine is starting cold, there is an interference fit between the piston head and the cylinder. As the engine heats up during combustion this tolerance increases allowing it to move more freely. This ensures a proper sealing during combustion.

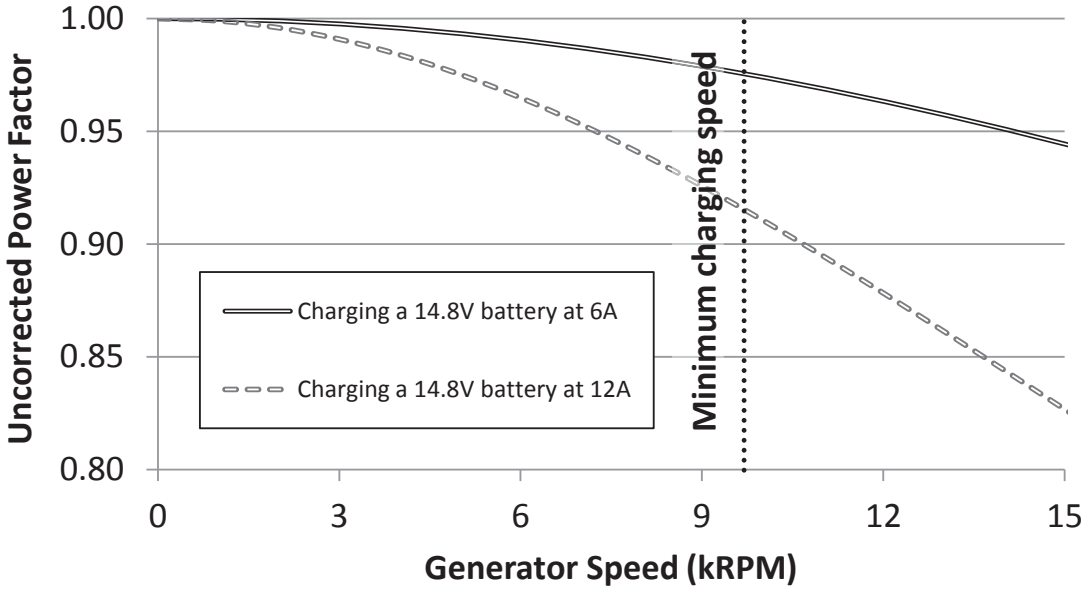

Figure 2.7.: Uncorrected power factor [23, 29]

from higher efficiency and a high power to weight ratio over conventional brushed DC motors. They have excellent heat dissipation, low noise, low maintenance, and great longevity and reliability because there are no brushes to replace [31]. An AXI 4120 brushless DC motor was selected since high efficiency power electronic circuits for motor control, filtering, rectification and DC/DC conversion have advanced to a point where they can be easily and inexpensively assembled in a small form factor using open source designs.

The main disadvantage of a brushless DC generator is that conventional rectification methods cannot achieve the maximum power possible because of a distorted or unsuitable current waveform [32]. A method is proposed by Lee [32] to maximize the power density of a brushless DC generator by actively switching rectifier diodes with PWM signals. Although this method of rectification provides higher efficiencies and the same power stage used for driving the motor could be theoretically used in reverse, its control is complex and requires a high-speed digital signal processor to detect the back EMF and current waveforms. Incorporating a 20 million instruction per second digital signal processor on-board for the sole purpose of rectification is unfeasible therefore a full bridge passive diode rectifier was selected for its low cost, simple construction and lack of complex control.

Another concern regarding power generation is the power factor. Unlike most power generation applications, the brushless DC generator will experience low resistance ($10^0\Omega$) and large operating speeds ($10^3 \frac{rad}{s}$) leading to high inductance. During high operating speeds, the power factor will begin to drift away from unity as the voltage becomes out of phase with the current. This is shown in Figure 2.7. The power factor can be corrected by adding a capacitor in parallel to the

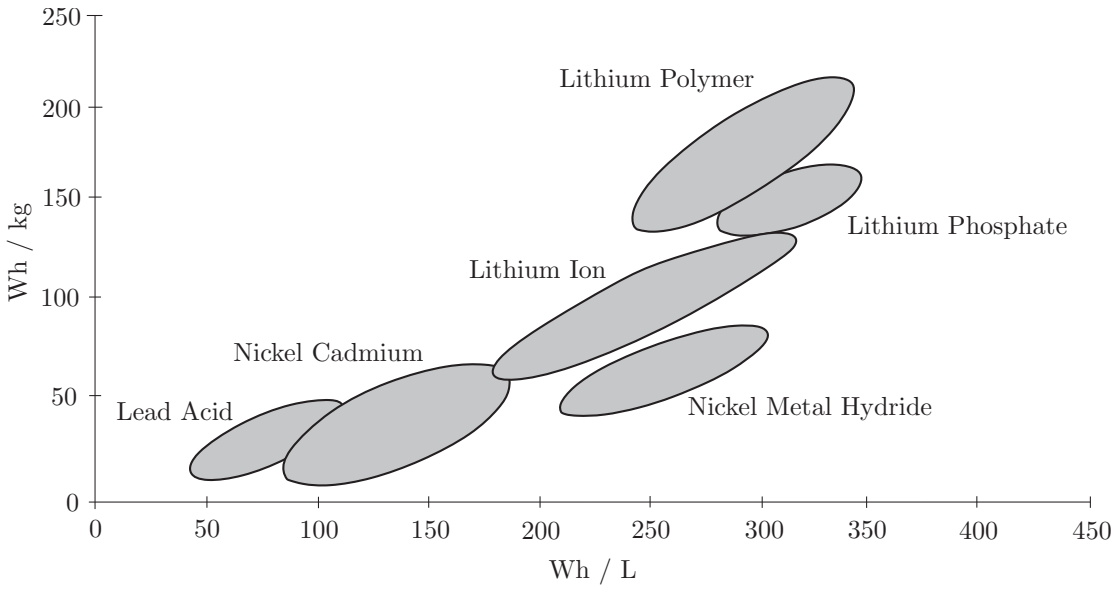

Figure 2.8.: Energy densities of various battery types [16, 23, 29, 33]

resistive load of each phase of the generator. This type of power factor correction is only optimal (close to unity) for one operating speed therefore the power factor will decrease as the generator speed moves away from the corrected speed. Since the engine's peak efficiency occurs over a narrow speed range and the engine operation would be relatively constant at the optimal speed, the passive power factor correction was selected. The results of experimental testing on the power generator were used to determine the optimal engine/generator speed and select the power correction factor. Three capacitors of 45.5 μF were used to correct the power factor at 9,300 RPM.

DC/DC conversion is also required in two separate cases on board the dirigible. First to regulate the output voltage of the generator to the working range of the battery charger (16.8V) and second to regulate the battery voltage down to 12V, 5V, and 3.7V sources used by the auxiliary components such as the on-board computer, electric propulsion motors and servo motors. A high efficiency step down (buck) controller circuit was selected for this purpose.

2.3.5. Energy storage

A comparison of different battery chemistries on the basis of energy mass density and energy volume density (Watt-hours/Liter) is shown in Figure 2.8. Lithium (ion) polymer batteries are a new type of lithium ion that were selected for their higher energy densities as shown in Figure 2.8. They have no memory effect, a good life cycle, high energy efficiency [34]. The most important attributes of this battery are its fast charge and discharge rates. This is vital to hybrid designs as one of the power limitations of hybrid power plants is the maximum charging

current the battery bank can safely accept.

Lithium polymer batteries are not tolerant to over charging or over discharging which both lead to overheating and battery damage so they require an added protection circuit to prevent these conditions [34]. Maximum heat generation in a properly ventilated battery occurs during the final stages of charging (trickle charging) and during discharging, especially as the SOC is low. Charging a lithium ion battery to 100% SOC, or discharging to 0% SOC will degrade its long term capacity [35]. The operational SOC range of a lithium ion battery is usually limited to a smaller range, such as 30% to 70%. This reduces the useful battery capacity to only 40% of the fully specified capacity [35]. Hybrid systems have the advantage of maintaining the battery in its useful range by charging more frequently.

Maintaining the battery within this useful battery capacity offers many advantages both for the battery and for the efficiency of the system. As with all batteries, their life is extended by avoiding the damaging and inefficient periods of overheating. In combination with a hybrid system, keeping the battery within its useful range increases the effective energy density of the system when combined with fuel. Avoiding low power input trickle charge when the battery is near full SOC ensures that the loading on the engine is more stable and the engine is only used in its peak efficiency range. Avoiding near empty SOC prevents battery voltage fluctuations and voltage cutoff during discharging.

There are two branches to the battery management system: the first is the electronic speed controller which controls engine start up and the second is the rectification, filtering, power conversion and charging circuitry which controls power generation. An image of these components is shown in Figure 2.9. The engine start up controller determines the optimal conditions to start the engine based on the flight conditions and the SOC of the battery. Once it is determined that usable electrical power can be collected from the generator, the series of rectifier, DC/DC converter and battery charger are connected through the relay to accept the charge. The battery banks can be switched on or off by means of a solid state relay. Voltage, current and temperature are monitored for cell protection and safety. The charge controller only uses the constant current charging mode to provide maximum power to the batteries while the engine is on and generation is needed.

2.4. Methodology

The experimental platform shown in Figure 2.4 consists of a glow engine, a brushless DC generator, and a controllable pitch propeller connected in series. The

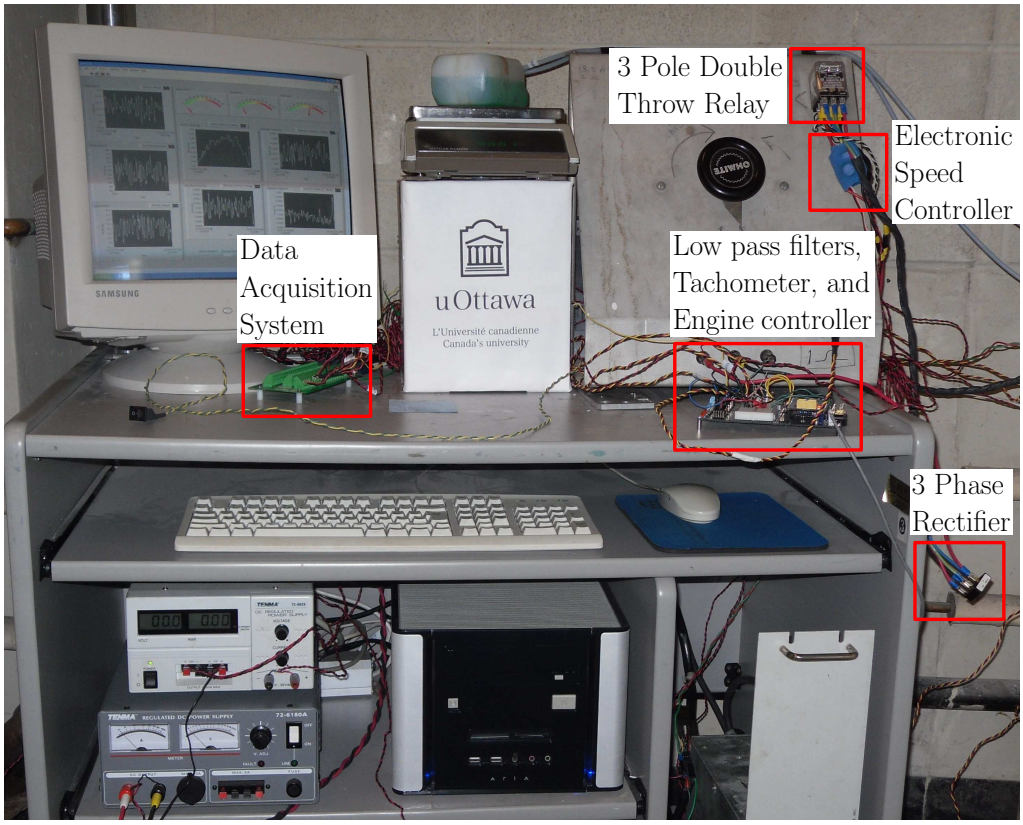

Figure 2.9.: Battery management system components

plant frame is fixed to a pressurized air bed that provides a virtually frictionless contact to the test bench. The static thrust of the propeller is measured by a cable connected to a digital scale. Fuel flow is measured by taking mass readings every 10ms.

The glow plug and electronic speed controller are connected to a double throw power relay that switches between the electronic speed controller (starter mode) and the 3-phase rectifier (generator mode). If the rotational speed of the brushless DC motor (measured by the frequency to voltage converter) is below 3000RPM, the relay is switched to the starter motor and the glow plug is powered. When generating, the electrical load of the battery and charger is simulated using a rheostat (variable resistance) set to the equivalent resistance of the charger and battery in series. The free stream air velocity is the velocity of the air entering the propeller. Tests were performed at five different free stream velocity speeds produced by an electric blower to simulate the effect of the dirigible traveling at those speeds.

The power plant's useful power output, energy consumption and overall efficiency were determined by varying the engine throttle, fuel mixture richness, propeller pitch, electrical load resistance, free stream velocity, and the nitromethane content in the fuel. Table 2.1 contains a list of all these control variables and their

Table 2.1.: List of controlled variables and their operating ranges

Parameter	Minimum	Maximum	Increment
Engine Throttle	50% (half)	100% (full)	12.5%
Needle Value	360 (lean)	720 (rich)	30
Propeller Pitch	15°	45°	15°
Electrical Resistance	1.4Ω	5.6Ω	1.4Ω
Free Stream Air Velocity	0 m/s	20 m/s	4 m/s
Nitromethane Content	5%	15%	5%

ranges.

2.5. Results and Discussion

The recorded data points were segmented into groups according to engine speed, and averaged to produce the operating envelope shown in Figure 2.10. Data points below the engine's start-up speed (3000 RPM) were omitted. The useful total power P_U was calculated based on the sum of propulsion power P_P and electrical power P_G such that,

$$P_U = P_P + P_G \tag{2.1}$$

where,

$$P_P = F_T \times \nu_f \tag{2.2}$$

$$P_G = V_g \times I_g \tag{2.3}$$

where P_U, P_P, andP_G are in [W], F_T is the propeller thrust in [N], ν_f is the free stream velocity in [m/s], V_g is the generation voltage in [V], and I_g is the generation current in [A].

Data points in the 98^{th} percentile were considered to represent the useful power operating envelope. All other data points below the envelope were omitted for clarity. Trend lines are polynomial fit using a least squares approach. Overall system efficiency, η_O, was calculated as the ratio of useful power over the input power, P_I [W]

$$\eta_O = \frac{P_U}{P_I} \tag{2.4}$$

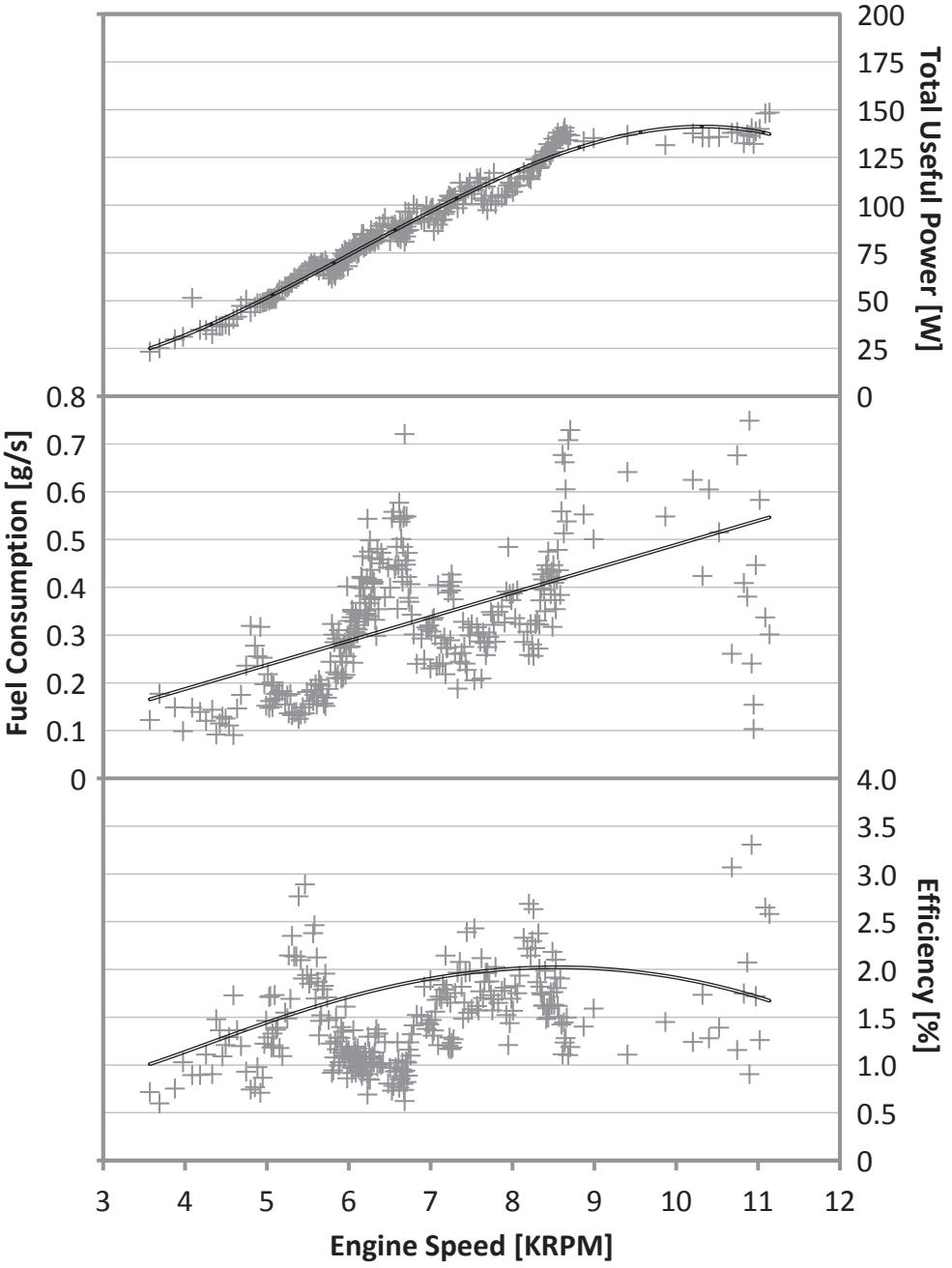

Figure 2.10.: Engine operating envelope for the OS 25LA two stroke glow engine [23, 29]

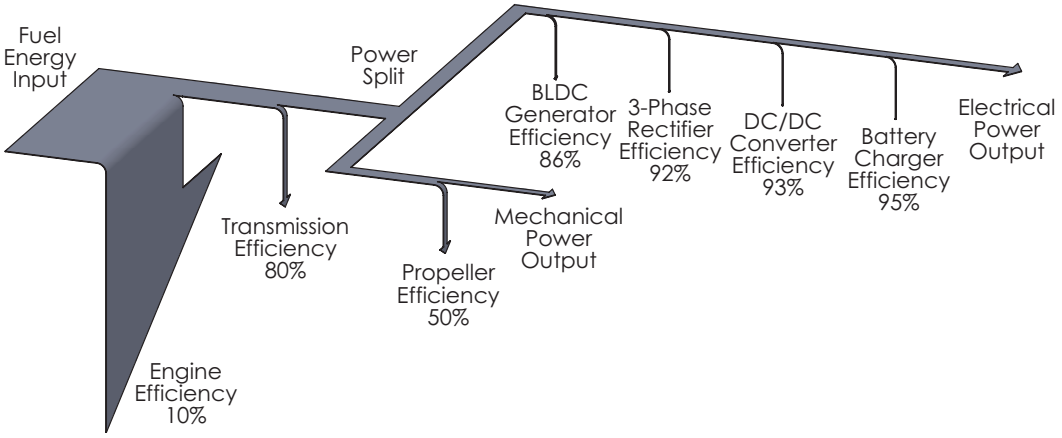

Figure 2.11.: Summary of hybrid power plant losses [23, 29]

The input power is defined by,

$$P_I = \dot{m}_f \times \rho_f \tag{2.5}$$

where $\dot{m}_F$ is the mass flow rate of fuel [g/s] and ρ_f is the fuel's energy density [J/g].

Based on the operating envelope, the engine was unable to reach it's optimal operating speed of 15000 RPM specified by the manufacturer due to the increase in torque caused by the friction in the bearings, and the added inertia of generator and other rotating components. The useful power begins to plateau after 9000 RPM and the maximum useful output power achieved was 148.4W. In comparison, the engine's rated output given in the manual is 447.6W (7.4% engine efficiency at 0.4g/s fuel consumption of 15% nitromethane glow fuel). This difference can be attributed to the loses due to propeller and generator efficiencies (maximum of 50% and 85% respectively) and friction torque in the bearings (the transmission efficiency is variable with engine speed but is roughly estimated to be 80%). A summary of these losses is shown in Figure 2.11. The engine's fuel consumption was much higher than expected at upwards of 0.4g/s at maximum efficiency which tended to lower overall efficiencies.

Two separate methods were used to calculate propeller efficiency. The first approach uses the classical definition for efficiency given by the ratio of useful propulsion power out over power absorbed,

$$\eta_{P1} = \frac{P_P}{P_A} = \frac{F_T \times \nu_f}{\omega_e \times T_P} \tag{2.6}$$

where P_P is the useful propulsion power [W], P_A is the power absorbed [W], ω_e is

the engine speed [rad/s], and T_P is the engine torque absorbed [Nm].

The propeller torque cannot be measured directly as it is a function of the engine torque, generator torque and frictional losses. Therefore, the propeller torque was estimated based on engine speed and propeller pitch using the following set of equations which were produced using propeller tables presented by Lesley [36],

$$C_T = 1.83 \times 10^9 * \theta^2 + 1.04 \times 10^8 * \theta + 1.70 \times 10^8 \tag{2.7}$$

$$T_P = C_T \times \omega_e^2 \tag{2.8}$$

where θ is the propeller pitch in inches measured at 3/4 propeller radius from the axis of rotation.

The second method used to calculate propeller efficiency is based on disk actuator theory [37],

$$\eta_{P2} = \frac{1}{1 + \frac{\nu_f - \nu_w}{\nu_f}} \tag{2.9}$$

where ν_w is the velocity of the air in the wake of the propeller [m/s].

Both methods produced efficiencies within 10% of each other however only the first method is presented in Figure 2.12 since it was considered to have lower cumulative uncertainty.

The propeller's efficiency for three pitch settings are plotted against the advance ratio in Figure 2.12. The advance ratio J is the ratio between the distance a propeller moves forward through the fluid during one revolution over the product of engine speed and propeller diameter,

$$J = \frac{\nu_f}{n_e \times d_p} \tag{2.10}$$

where n_e is the engine speed [rev/s], and d_p is the diameter of the propeller [m]. Error bars in the figure represent the combined measurement uncertainty of the individual sensor uncertainties.

Due to the size of the airship, flight speeds above $10\frac{m}{s}$ are unfeasible based on the total available propulsion power on-board. Therefore advance ratios above 0.3 are unfeasible. Propeller efficiency values correspond well with theoretical values presented by McCormick [30] shown in Figure 2.6. Based on the results of these tests, propeller pitch would remain between 0 and 15 degrees to maximize the propeller efficiency for all foreseeable flight conditions.

The maximum generator power is shown in Figure 2.13. The electrical resistance represents the electrical load applied from the electrical propulsion motors, servos,

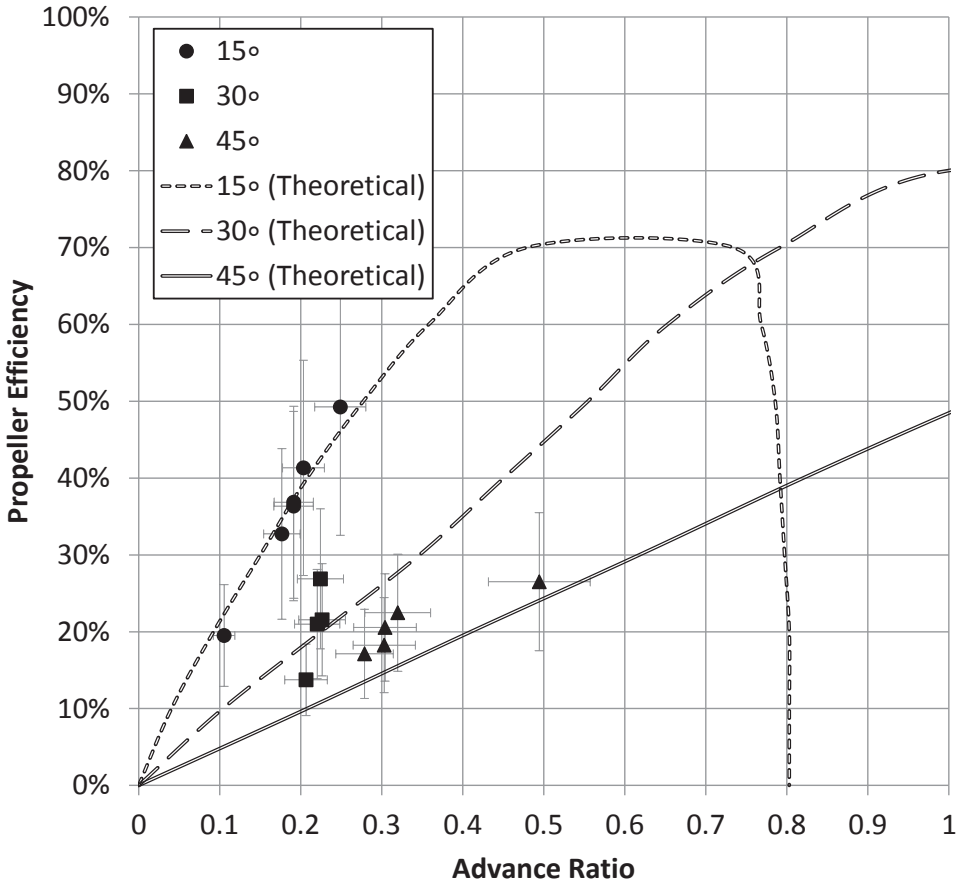

Figure 2.12.: Propeller efficiency at 3Ω resistance [23, 29]

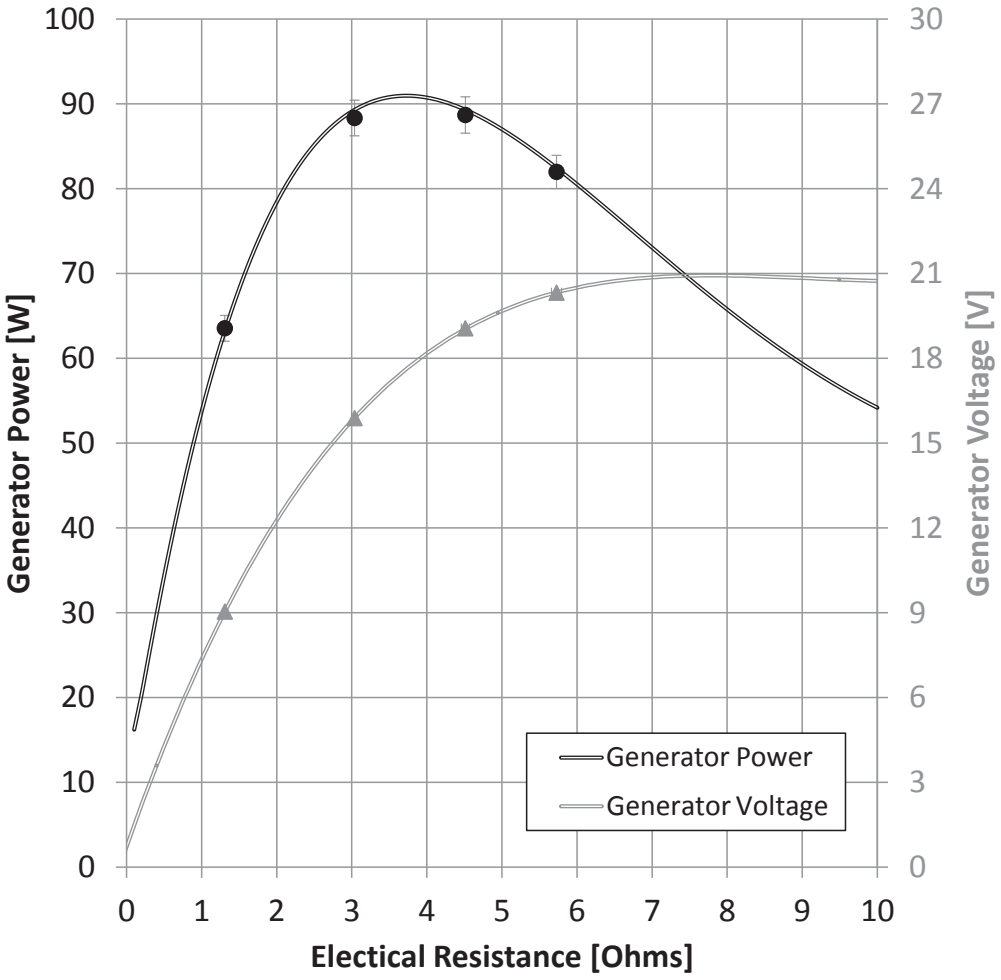

Figure 2.13.: Generator power at 15°propeller pitch [23, 29]

and other on board electronics. Only electrical power produced with voltages above 14.8V can be used due to the battery voltage therefore, resistances below 3Ω are not useful. Maximum electrical generation is achieved between 3Ω and 4.5Ω of 90W. Above 4.5Ω, power begins to drop as the engine is no longer able to increase it's speed to increase the voltage and the current reduces following Ohm's law.

The effect of nitromethane content on the operating envelope of the system is illustrated in Figure 2.14 . The useful power generated for all fuel types were within 20% at any given engine speed. However, the range of operating speeds significantly decreased with the decrease in nitromethane content. Fuel consumption was reduced with the use of the 10% fuel and increased with use of the 5%, compared to the 15%. This in turn resulted in higher efficiencies at the median nitromethane content of 10%. The increase in efficiency for the 10% fuel may be explained by the change in ignition timing caused by the change in fuel as glow engines are dependent on the catalytic reaction of the fuel for combustion. It is worth noting that the engine was much more difficult to start and tune with decreasing nitromethane content, and the engine struggled to reach a steady state for the majority of tests.

The average current draw required by the brushless DC motor to start the engine was measured to be 35.7A (with a peak of 49.6A) at 14.8V which translates into 538.4W. However, the average time before the engine began driving the brushless DC motor was 0.28 sec leading to an energy draw of the battery of 41.9mWh. The servos used to vary the engine throttle and pitch angle drew 1.08W and 2.00W and were typically used only at start-up for less than 5 seconds (1.5mWh and 2.8mWh, respectively). The glow plug drew a constant 7.58W over 5 seconds resulting in a drain of 10.5mWh. The microcontroller used to generate the PWM signals is run continuously, but enters a power save mode when not receiving an input. Thus reducing its active consumption from 20mW to 1.2mW and can be neglected. The total energy required to start the engine once is 56.7mWh or about 0.06% of the battery's capacity.

The current design can run the glow engine for 2.08 hours on 3 kg of fuel at the maximum efficiency point. Given the 88.8Wh battery capacity on-board plus 90W regeneration and assuming an average of 50W power draw from electric propulsion and electronics results in an overall flight endurance of 5.52 hours. With 60W mechanical propulsion during engine on time and assuming 30W electric propulsion on average the maximum range of the airship (with zero net wind) is 123km.

The method used previously to compare different battery chemistries in Figure 2.8 (also known as a Ragone plot) can be extended to compare different power

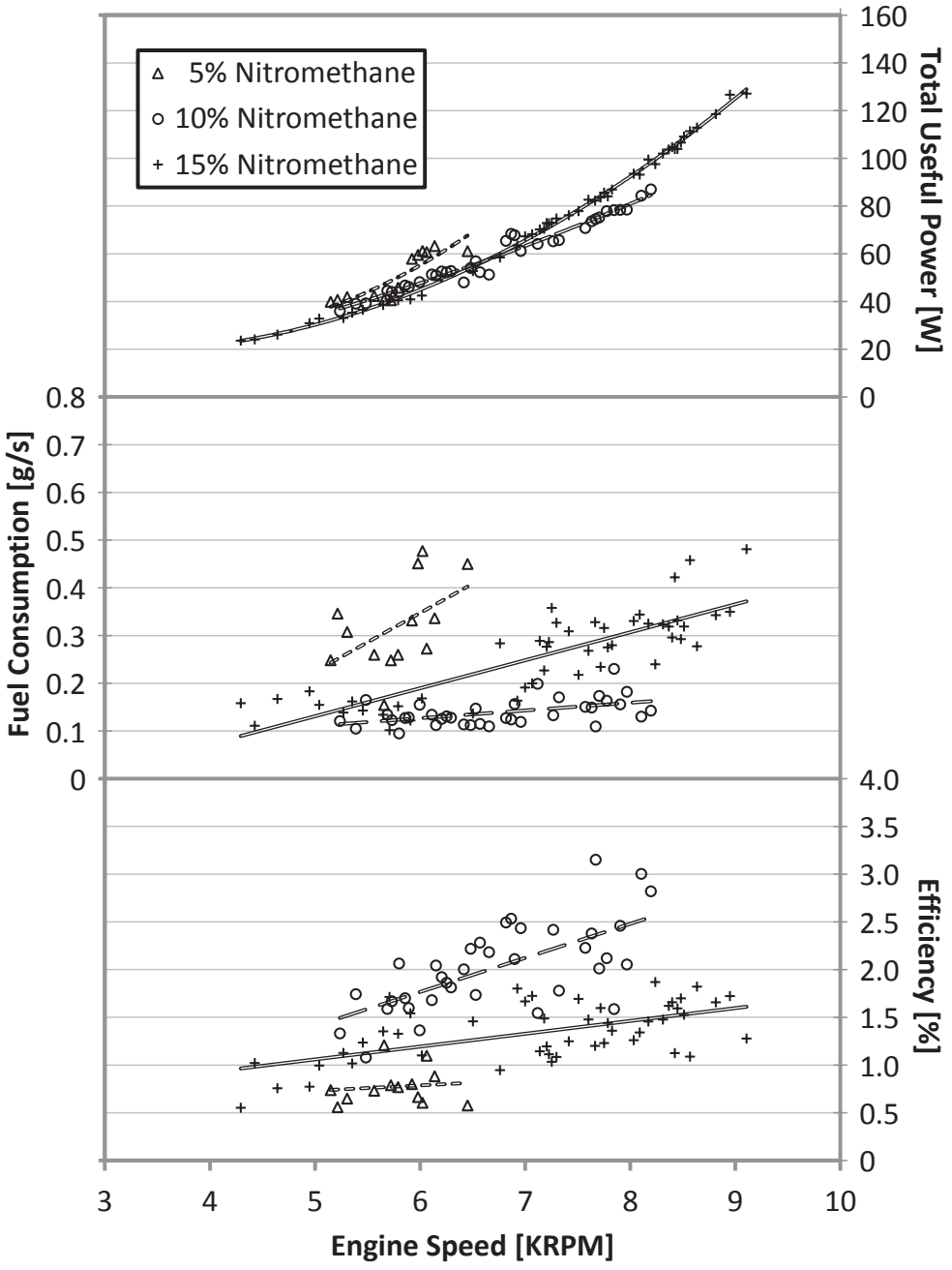

Figure 2.14.: Engine operating envelope for various nitromethane content fuels [29]

plant configurations. The power and energy density of the glow engine hybrid system at the optimal operating point can be calculated for a given amount of fuel. The power density, δ_P, is found by,

$$\delta_P = \frac{P_U}{\sum m_f + \sum m_v} \tag{2.11}$$

and energy density, δ_E, is found by,

$$\delta_E = \frac{P_U \times t_r}{\sum m_f + \sum m_v} \tag{2.12}$$

where t_r is the operating time in [h], $\sum m_f$ is the sum of fixed or dead masses such as the engine, motor and frame, and $\sum m_v$ is the sum of variable masses such as fuel in [kg] of batteries or a combination of both. These two equations form the operational limits of each system which are represented by lines shown in Figure 2.15. The horizontal asymptote is the maximum power density (performance) and is governed by the maximum output power of the power plant considered divided by the power plant's fixed mass. If the variable mass is infinitesimally small, maximum power density is achieved. The vertical asymptote is the maximum energy density (endurance) and is governed by the energy density of the fuel source. Increasing on-board fuel or battery mass will increase energy density to approach the fuel or battery energy density selected. However, this will also decrease power density as energy storage does not contribute to power output. Trend lines to his affect are included in Figure 3.8.

A circular point is plotted on Figure 2.15 for the current system supplied with 3 kg of fuel. Given the electric motor and propeller efficiency, and the same lithium polymer battery of the current system, similar points can be constructed for a fully electric system and a gasoline hybrid system. Figure 2.15 indicates a 30% improvement in energy density can be achieved with the current system over that of a fully electric system with 3 kg of dedicated batteries.

Energy density is paramount over power density for long duration missions as the mass of the fuel becomes larger than the mass of the power plant. Considering this, further improvement is possible if a 4-stroke gasoline engine is used in the place of the 2-stroke glow engine. Gasoline was calculated to have a 154% increase in energy density over glow fuel with 15% nitromethane and requires less oil in the mixture (which does not contribute towards useful work). A spark ignition would also provide practical benefits of reliable start up and ignition timing compared to a glow plug. Although 4-stroke engines generally weigh more than 2-stroke engines at the same power, they have significantly lower fuel consumption rates which becomes paramount when carrying over 1 kg of fuel. This can be seen in Figure 2.15. For lower variable masses (i.e. fuel) glow fuel hybrid systems would

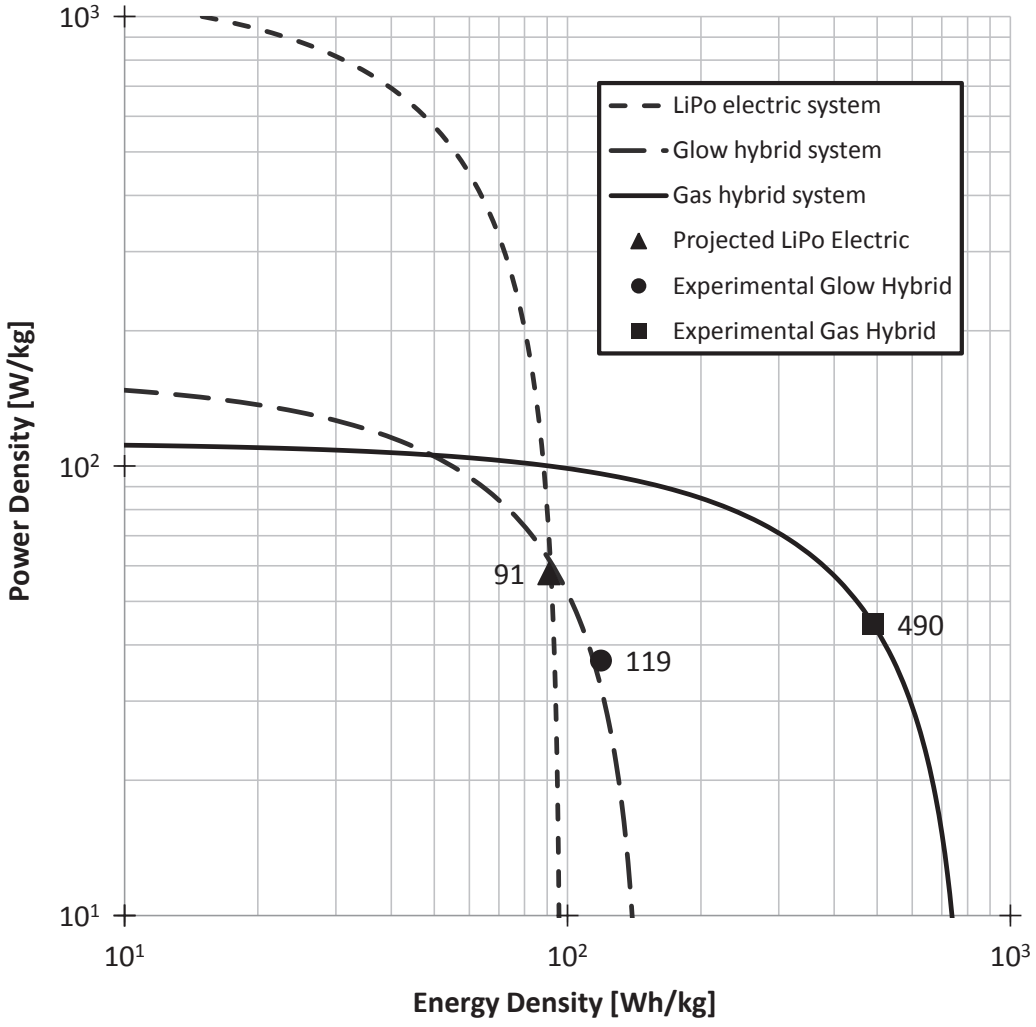

Figure 2.15.: Power density versus energy density for electric, glow hybrid and gas hybrid systems [23, 29]

exhibit a higher power density compared to gasoline hybrid engines.

The conservatively estimated overall cost for fabricating a single UAV is $5,000 CAD. The low material and manufacturing cost was achieved from using or modifying commercially available, off-the-shelf components. The performance metric presented in Figure 1.2 is given by,

$$C_P = \sqrt[3]{M_P \times D \times t_o} \tag{2.13}$$

where C_P $\left[kg^{\frac{1}{3}}km^{\frac{1}{3}}h^{\frac{1}{3}}\right]$ is the performance metric, M_P is the payload mass in [kg] , D is the UAV's range in [km] and t_o is the maximum operating time or endurance in [h] . Given the estimated payload of 1kg (excluding fuel) and the maximum endurance and maximum range previously calculated (5.52h and 123km respectively), the performance metric for this UAV design is 8.8. The average UAV cost metric at the same price point is 1.9 as shown in Figure 1.2. This represents a 363% increase compared to existing designs.

2.6. Chapter Summary

The energy density of the purposed hybrid power plant design was proven to be higher than an equivalent purely electric system through experimental testing, despite sub-par engine performance. Further increases are expected if a 4-stroke gasoline engine is implemented in a similar configuration. Future plans involve testing the aforementioned air ballasting system, implementing a new power plant design focused around a 4-stroke gas engine, and performing full scale tests of the completed UAV system. An estimated additional 154% increase could be expected for a similar design with implementation of a 4-stroke gasoline engine instead of the 2-stroke glow engine.

3. Gasoline Based Hybrid UAV Power Plant

Although the alcohol hybrid power plant proved to have significant advantages over purely electric systems, the low efficiency of the glow engine was a point of contention during the peer review process. Striving for a more efficient and reliable power plant solution, additional research was conducted with an alternate power plant design focused around a 4-stroke gasoline engine. This chapter presents the design of a gasoline-electric hybrid power plant for UAV dirigibles and outlines the performance of the experimental system. Tests were performed to determine the power plant's power output, energy consumption and overall efficiency with respect to changing the engine throttle, the fuel mixture richness, the propeller pitch, the electrical load resistance, and the freesteam velocity. Using these results, a UAV dirigible design equipped with this power plant is then compared to existing UAVs on the basis of cost, payload, range and endurance.

3.1. Changes to the Hybrid Power Plant Design

Based on the previous research with a 2-stroke OS 25LA model engine [23, 29], it was determined in section 2.5 that energy density is more important than power density when selecting a prime mover for maximizing flight endurance. Gasoline engines generally have lower power densities than glow engines but also have lower fuel consumption rates which becomes necessary when carrying over 1 kg of fuel for the same power. Gasoline has a 154% predicted increase in energy density over 15% nitromethane glow fuel and requires less oil in the mixture (which does not

contribute towards useful work). A spark ignition also provides reliable start up and ignition timing compared to glow plugs.

The experimental system presented in this chapter uses a Saito 4-stroke gasoline engine. This engine has a significantly higher fuel efficiency per HP, a larger range of peak engine performance, and a quieter and cleaner operation compared to the OS 25LA [29]. It also includes a closed loop spark plug controller with hall effect sensor feedback for optimal ignition timing.

Fundamentally, the configuration remained unchanged, consisting of an engine, brushless DC generator, and propeller connected inline. However, changing the prime mover in the power plant required several other modifications as the size and power output of the plant had doubled from 0.6 Hp to 1.2 Hp. A new structural frame was designed around the higher loadings. An improved pitch control mechanism was devised to solve set point stabilization problems inherent in the original design. A control servo was attached to the needle valve for precise fuel rate adjustments and to allow full autonomy. A block diagram of the power plant and UAV components is shown in Figure 3.1.

3.2. Methodology

The hybrid power plant prototype is shown in Figure 3.2. The power plant frame is fixed to a pressurized air bed that provides a virtually frictionless contact to the test bench. The thrust of the propeller is measured by a cable operated lever arm connected to a digital scale.

Fuel flow is measured by taking mass readings every 10s. The spark plug controller and electronic speed controller are connected to a double throw power relay that switches between the electronic speed controller (starter mode) and the 3-phase rectifier (generator mode). If the rotational speed of the brushless DC motor (measured by the frequency to voltage converter) is below 1000RPM, the relay is switched to starter motor and the spark plug controller is powered. When generating, the electrical load of the battery and charger is simulated using a rheostat set to the appropriate resistance. A freestream air flow is induced by the use of variable speed axial blower to simulate the movement of the UAV.

The power plant was run for a minimum of 60 seconds at each setting to allow the system to reach steady state. The experimental data was collected using LabView 8.2 with a NI PCI 6229 DAQ. Each input channel was sampled at a rate of 25 kHz. The measurement uncertainty contribution of the data acquisition card for each channel was negligible ($\pm 57\mu$V) for the full scale range of $\pm$100mV. The measurement uncertainty in each scale was $\pm$0.5g and $\pm$0.1g for the thrust and fuel scales, respectively. Two-pole digital low pass filters were applied to the

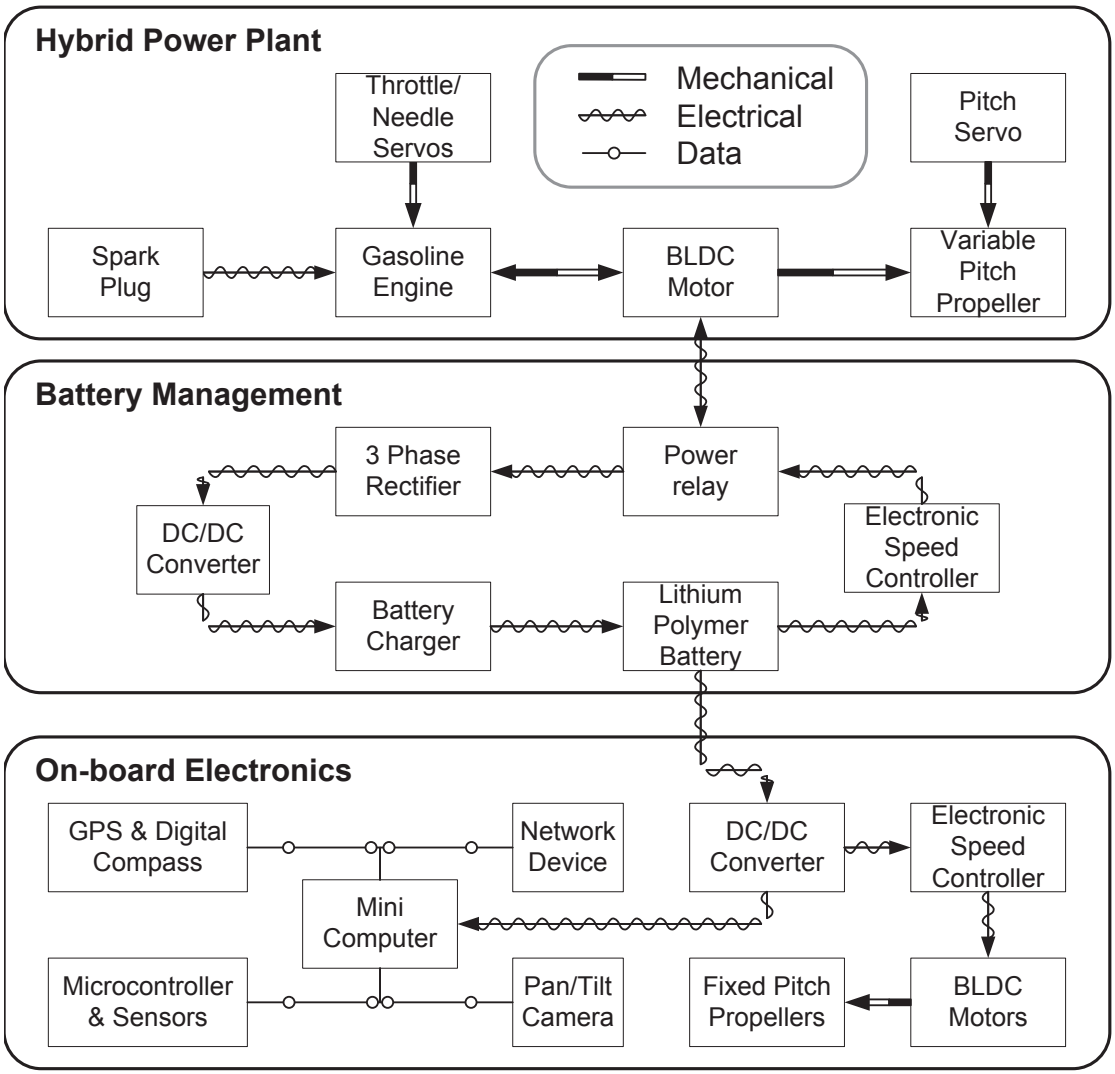

Figure 3.1.: Dirigible UAV component layout and power flow diagram [16]

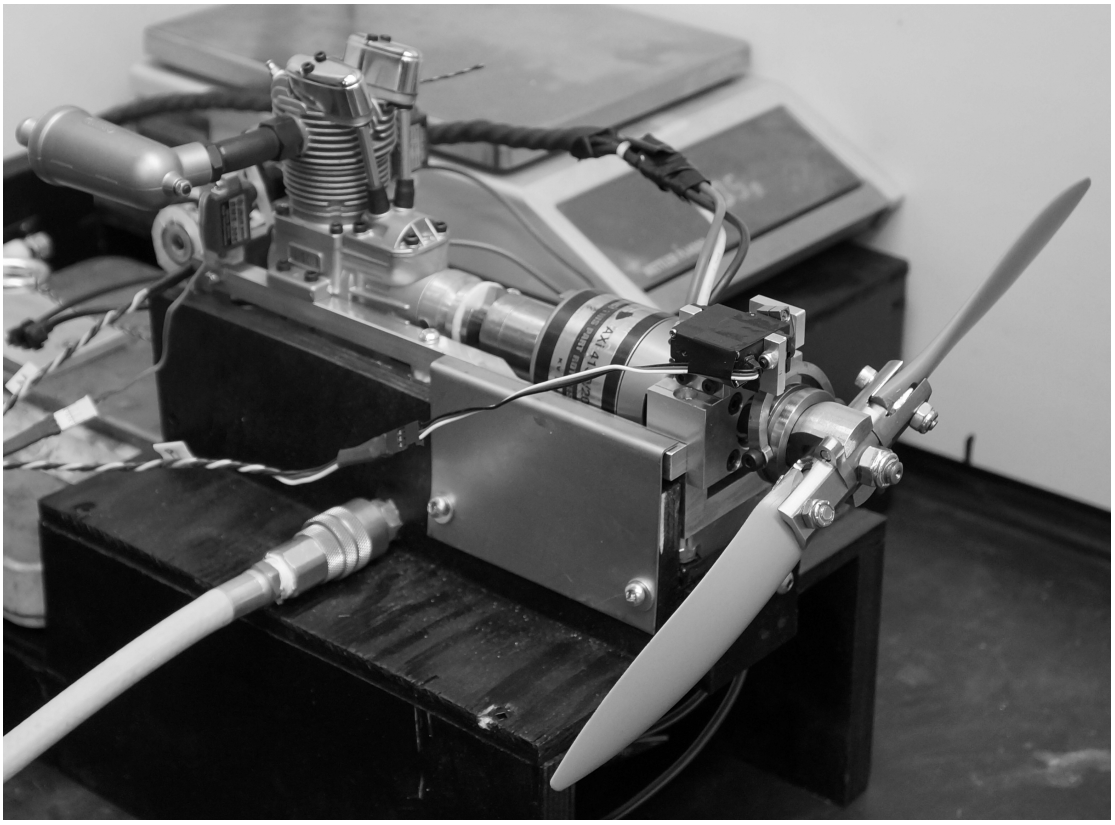

Figure 3.2.: Experimental hybrid power plant [16]

data recovered by both mass scale readings to eliminate noise caused by mechanical vibrations of the engine. The current drawn from the spark plug controller and electronic speed controller from their respective batteries was converted to a small proportional voltage using 4Ω current sense resistor circuits which have measurement uncertainties of ±1%. Four pulse width modulated control signals were generated by the DAQ that control the brushless DC motor starting speed, throttle position, needle valve position and propeller pitch position. The air speed in both the wake of the propeller and the free stream air produced from a variable speed axial blower were measured by taking their respective air pressures with respect to a static pressure measurement which each have a measurement uncertainties of $\pm 0.25 \frac{m}{s}$. The pressure sensors used to measure air speed have 1/10th the uncertainty of the ones used in previous work, which are shown to be one of the largest source of error [29]. The data collected was output into a raw text file for manual post processing. An overview of the test apparatus can be seen in Figure 3.3.

Tests were performed to determine the power plant's useful power output, energy consumption and overall efficiency with respect to changing engine throttle, fuel mixture richness, and the electrical load resistance for three propeller diameters. The pitch was set to a constant 15° and the free stream air velocity was set to 4.4

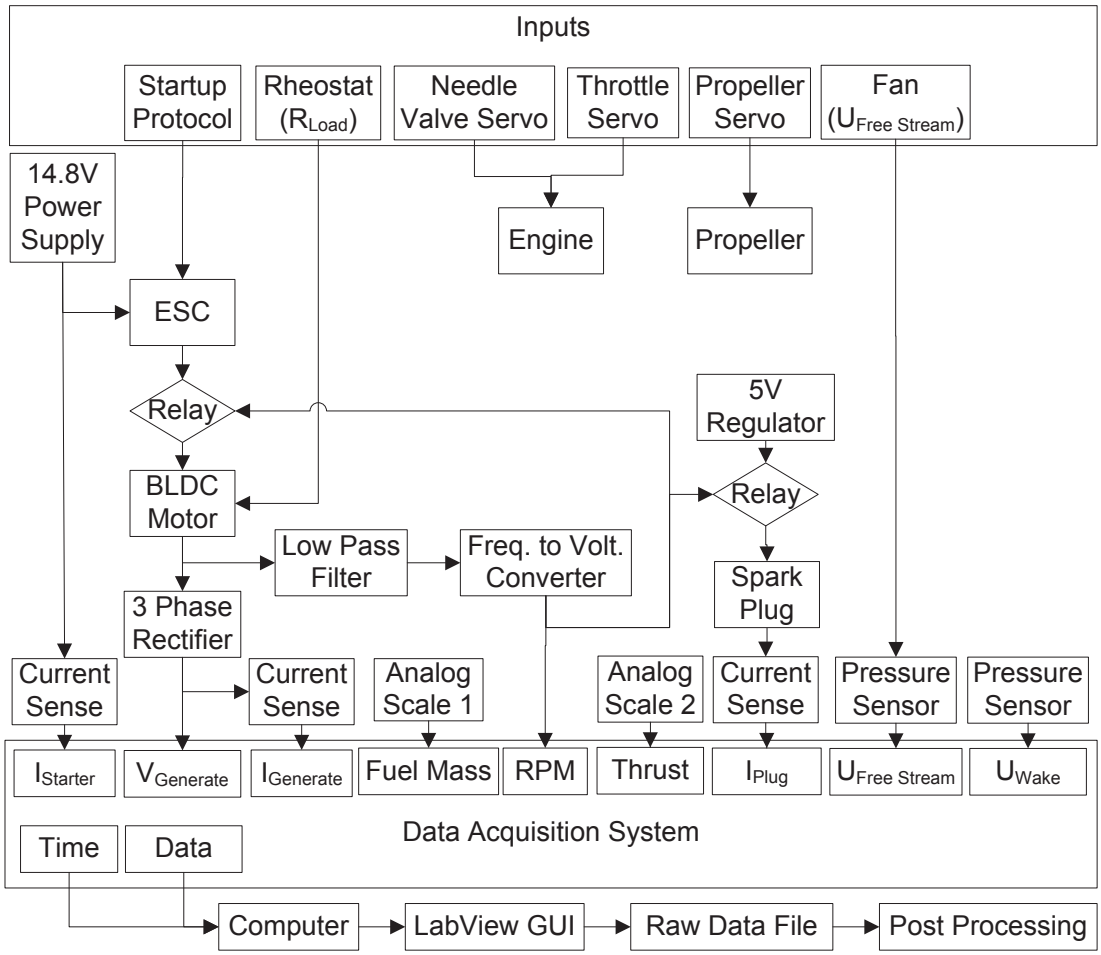

Figure 3.3.: Overview of testing apparatus configuration [16]

Table 3.1.: List of controlled variables and their operating ranges

Parameter	Minimum	Maximum	Increment
Engine throttle	40%	100% (full)	10%
Needle value	530° (lean)	550° (rich)	5
Electrical resistance	2.8Ω	8.8Ω	Variable

m/s. The angle of 15° was chosen based on previous findings of ideal efficiency [29]. Table 3.1 contains a list of controlled variables and their ranges, and the increment at which samples were collected.

3.3. Results

The recorded data points were segmented into groups according to engine speed, and averaged to produce the operating envelope shown in Figure 3.4. Data points below the engine's start-up speed were omitted. The total useful power was calculated based on the sum of propulsion and electrical power such that,

$$P_U = P_P + P_G = F_T \times \nu_f + V_g \times I_g \tag{3.1}$$

where P_U [W] is the total useful power produced, P_P [W] is the propulsion power, P_G [W] is the generation power, F_T [N] is the propeller thrust, ν_f [m/s] is the free stream velocity, V_g [V] is the generation voltage, and I_g [A] is the generation current.

Data points in the 98^{th} percentile were considered to represent the useful power operating envelope. Overall system efficiency, η_O, was calculated as the ratio of useful power over input power, P_I [W]

$$\eta_O = \frac{P_U}{P_I} = \frac{F_T \times \nu_f + V_g \times I_g}{\dot{m}_f \times \rho_f} \tag{3.2}$$

where $\dot{m}_f$ [g/s] is the mass flow rate of fuel and ρ_f [J/g] is the fuel's lower heating value.

As seen with the previous glow engine [29], the useful power begins to plateau while nearing the engine's maximum speed (9000 RPM) and the maximum useful output power achieved was 250W. In comparison, the engine's rated output given in the manual is 895.2W at 9200 RPM with a fuel consumption of 0.096g/s (22% engine efficiency). This difference can be attributed to the losses due to propeller and generator efficiencies (maximum of 50% and 86% respectively) and the friction torque in the bearings (the transmission efficiency is variable with engine speed but is roughly estimated to be 80%). A summary of these losses can be seen in Figure 3.5. The engine's fuel consumption was much higher than anticipated at

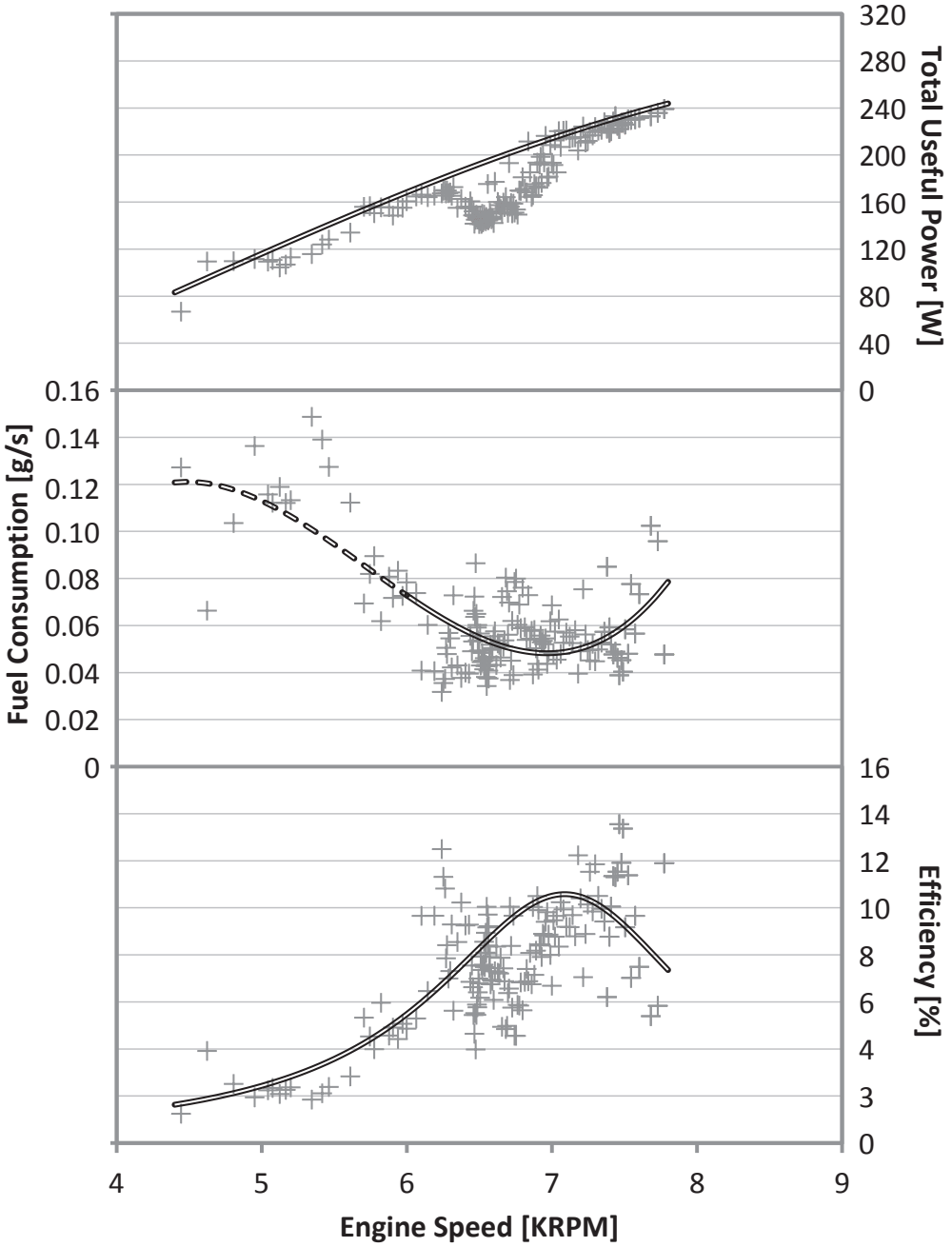

Figure 3.4.: Engine operating envelope for the hybrid power plant with 11" APC propeller [16]

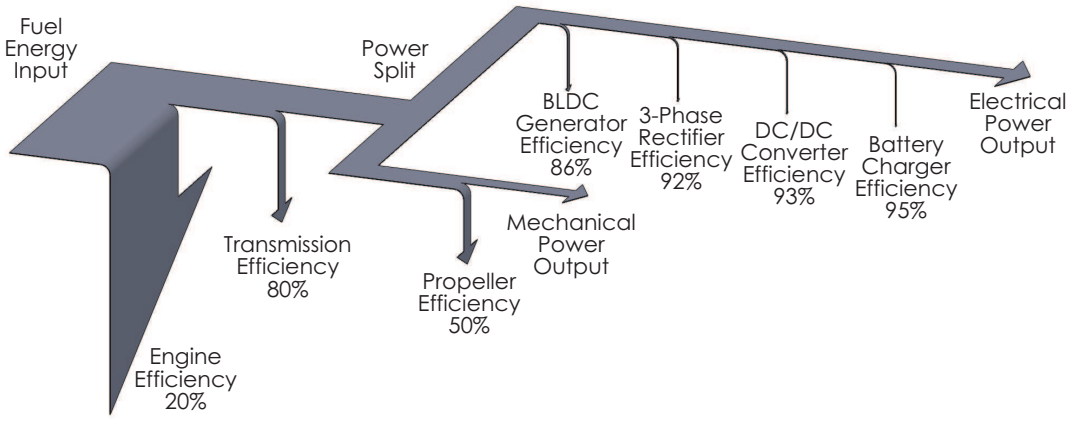

Figure 3.5.: Summary of hybrid power plant losses [16]

engine speeds below 6000 RPM (idling speeds). For these speeds, it's suspected that the ideal needle value setting was not found and the engine would not run consistently without stalling. Therefore, the portion of the fuel consumption trend below 6000 RPM is represented with a dashed line.

Commercially available APC propellers of 11", 12" and 14" diameters were modified, mounted and tested at 15° degrees pitch. Each propeller was machined using a computer aided mill and then balanced in the propeller shaft to an accuracy of within 1 gmm[1]. The rated propeller for the selected engine is 14", however, due to the additional load of the generator the engine would not start using the 14" propeller. The propeller's power and efficiency versus advance ratio are illustrated in Figure 3.6. The advance ratio is the ratio of the free stream fluid speed over the rate a propeller moves forward through the fluid and is defined as,

$$J = \frac{\nu_f}{n_e \times d_p} \tag{3.3}$$

where n_e [rev/s] is the engine speed, and d_p [m] is the diameter of the propeller.

The maximum propeller power for 11" and 12" propellers is shown in Figure 3.6 to be 60W and 65W, respectively. Propeller efficiency values for the 11" propeller correspond well with theoretical values presented by McCormick [30] and with the previously tested results [29]. Efficiency of the 12" propeller were slightly lower than expected as both curves should have the same trend if their pitch are exactly the same. The drop is likely explained by either non-identical pitch or slight increase in unbalance compared to the 11" propeller. Since there is an angle of twist to each propeller and due to limits in machining tolerances the exact

[1] 1gmm was the limiting precision of the balancing equipment available

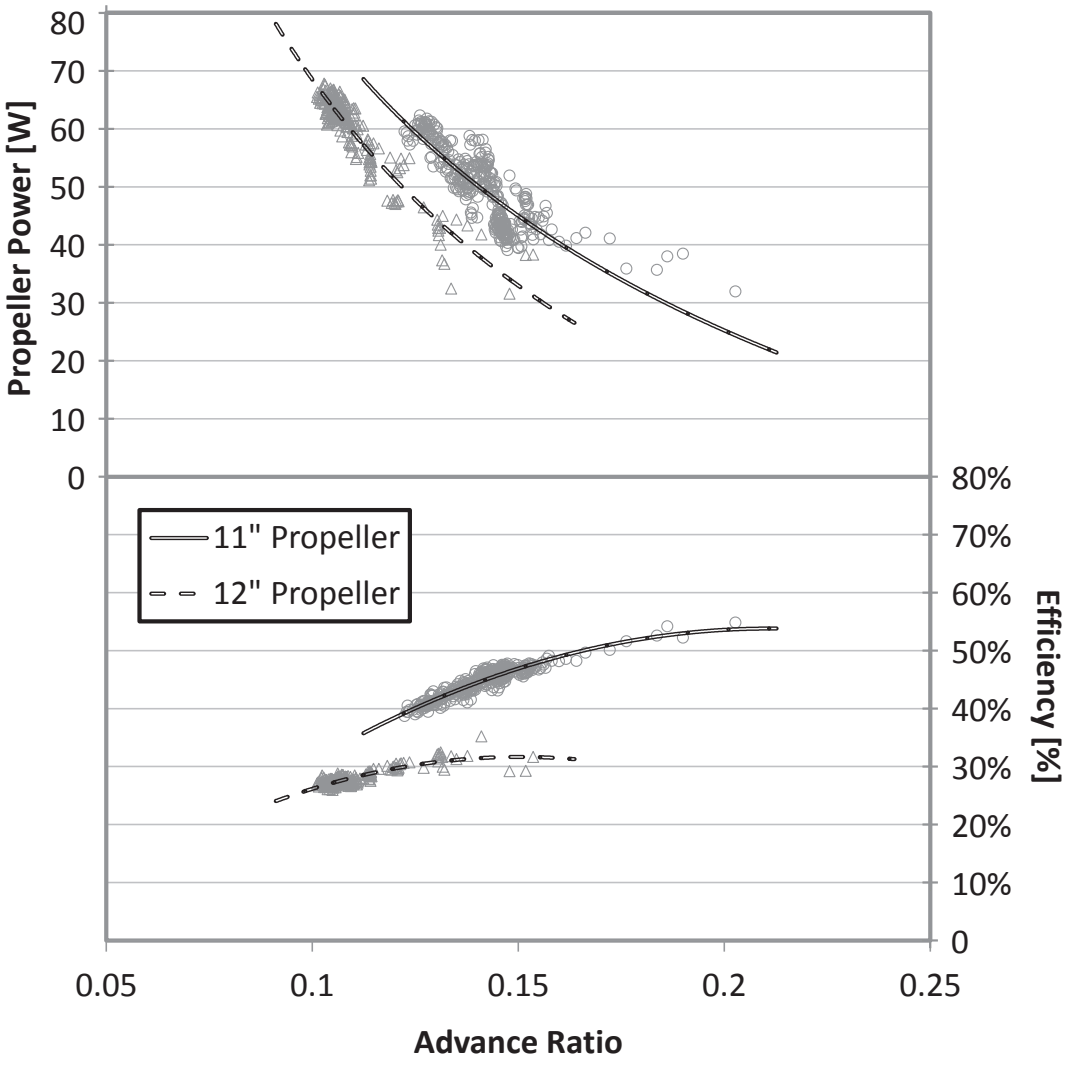

Figure 3.6.: Propeller efficiency for various propeller diameters at 3Ω resistance and 15°pitch [16]

pitch of each propeller when placed in the holder may differ slightly. Also, the importance of propeller balance should not be understated. It was noticed that a static unbalance of as little as 40gmm would violently shake the propeller blades from their holders.

The method used to calculate propeller efficiency is based on disk actuator theory [37],

$$\eta_{P2} = \frac{1}{1 + \frac{\nu_f - \nu_w}{\nu_f}} \tag{3.4}$$

where ν_w [m/s] is the velocity of the air in the wake of the propeller.

This method was chosen over the method previously used [29], since it does not require propeller torque estimation and has lower uncertainty with the implementation of more accurate pressure sensors. Due to the size of the airship, flight speeds above $10\frac{m}{s}$ are unfeasible based on the total available propulsion power on-board. Therefore advance ratios above 0.3 are unfeasible. Based on Figure 3.6, the results prove the previous claim [29] that slower rotating, smaller diameter propellers would result in higher advance ratios and therefore higher efficiency potential. Although propeller efficiency increases under these conditions, the propulsive power and therefore the productive work done decreases. A compromise between points of efficiency and performance must be chosen based on flight conditions and operational objectives.

The maximum generator power is shown in Figure 3.7 . The electrical resistance represents the electrical load applied from the electrical propulsion motors, servos, and other on board electronics. Only electrical power produced with voltages above 14.8V can be used due to the battery voltage therefore, resistances below 2.5Ω are not useful. A maximum electrical generation of 180W is achieved between 5Ω and 6Ω. Above 6Ω, power begins to drop as the engine is no longer able to increase it's speed to increase voltage further and the current reduces following ohm's law.

The torque required to induce a single turn in the engine was experimentally determined to be approximately 1.25 Nm for the gasoline engine compared to 0.7 Nm for the previous glow engine. The average current draw required by the brushless DC motor to start the engine was measured to be 13.5A at 14.8V which translates into 199.8W. However, the average time before the engine began driving the brushless DC was 0.67 sec leading to an energy draw of the battery of 37.2mWh. The servos used to vary the engine throttle, needle valve and pitch angle drew 1.08W, 1.08W and 2.00W and were only powered between changes. The spark plug controller drew a constant 3W continuously while the engine was running. The total energy required to start the engine once is 40.2mWh or about 0.06% of

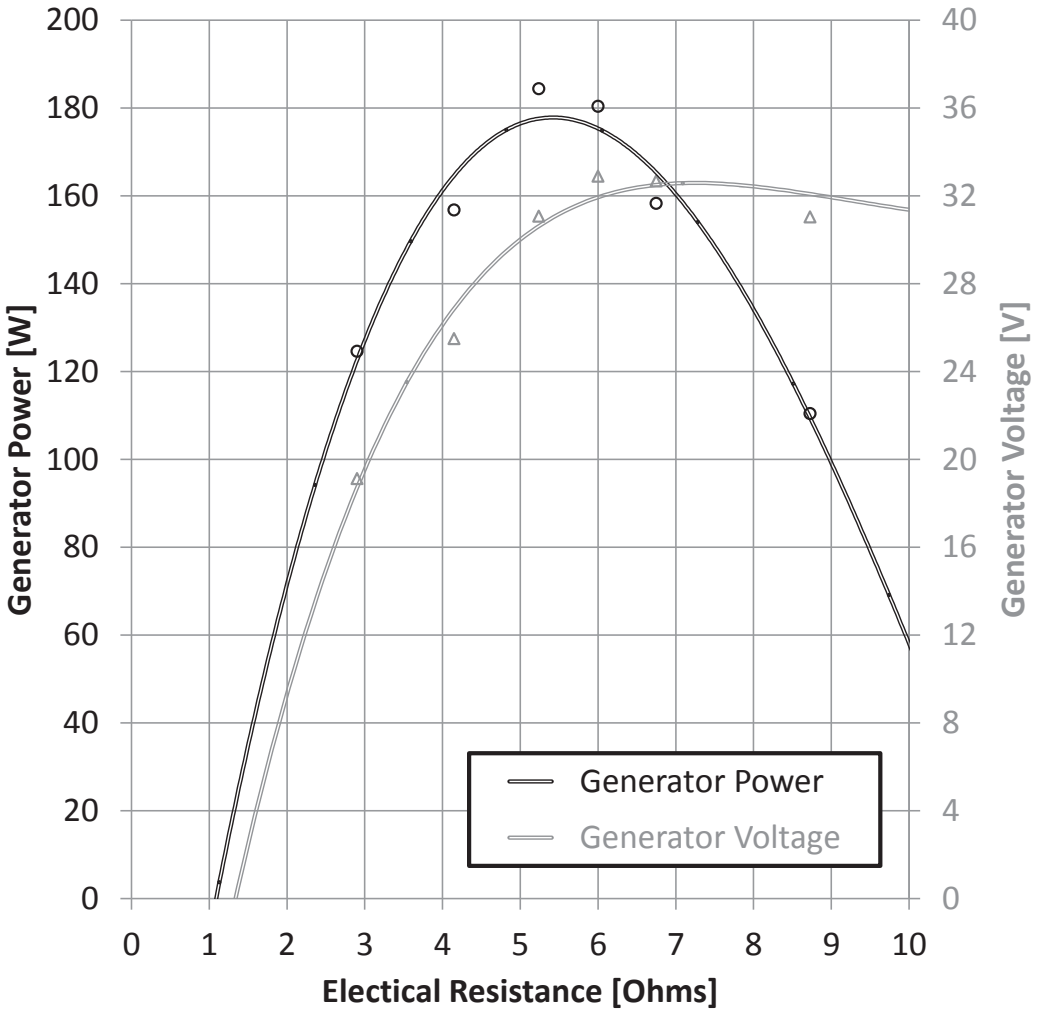

Figure 3.7.: Generator power with 11" APC propeller at 15°pitch [16]

the battery's capacity.

3.4. Discussion

The current design can run the gasoline engine for 17.7 hours on 3 kg of fuel at the maximum efficiency point. Given the 75Wh battery capacity on-board plus 170W regeneration while the engine is running, and assuming an average of 50W power draw from electric propulsion and electronics combined, this results in an additional 61.7 hours of flight on electric power. This totals a flight endurance of 79.4 hours (over 3 days). With 55W mechanical propulsion during engine "on" time and assuming 30W electric propulsion consumption on average, the maximum range potential of the airship (with zero net wind) is 1494 km. It should be noted that the term zero net wind does not refer to the absence wind, only that it is equal in magnitude and direction for both departure and return trips. Assuming a one-way flight with a constant head wind of 3m/s (10.8 km/h), this reduces the range to 637 km.

The new power plant can now be added to configuration comparison from Figure 2.15. As previously stated, the electrical power requirements for LTA aircraft can be up to 65% the total required power. To provide a fair comparison when introducing purely mechanical configurations, the percentage breakdown of mechanical and electrical useful power components must be specified as both electric and hybrid options can produce both types of power while pure piston engines cannot. The power split for Figure 3.8 is shown for a 50% mechanical 50% electrical power split, however, it could be easily modified for other percentages. Therefore, fossil fuel only systems must carry batteries to support the electrical demand which subtracts from the total weight of fuel. The power split only significantly effects the curves of the purely mechanical configurations as both the hybrid and electrical options can provide virtually any power split with little change in performance. If the power split is 90% mechanical or more of the total power, both the power density and energy density of glow and gas only systems surpasses their hybrid counterparts. This indicates the cross over point when selecting between purely mechanical or hybrid configurations. In addition to the power split, the range of power required as illustrated in Figure 2.1 is not captured in these two metrics as the efficiency of electrically driven motors is much more constant than the specific fuel consumption of piston engines [38]. Piston engines would need to include variable speed transmissions to have the same operational flexibility. However, to include the impact of this flexibility into the metrics would require selecting specific flight operating conditions which would diminish the applicability and significance of this comparison.

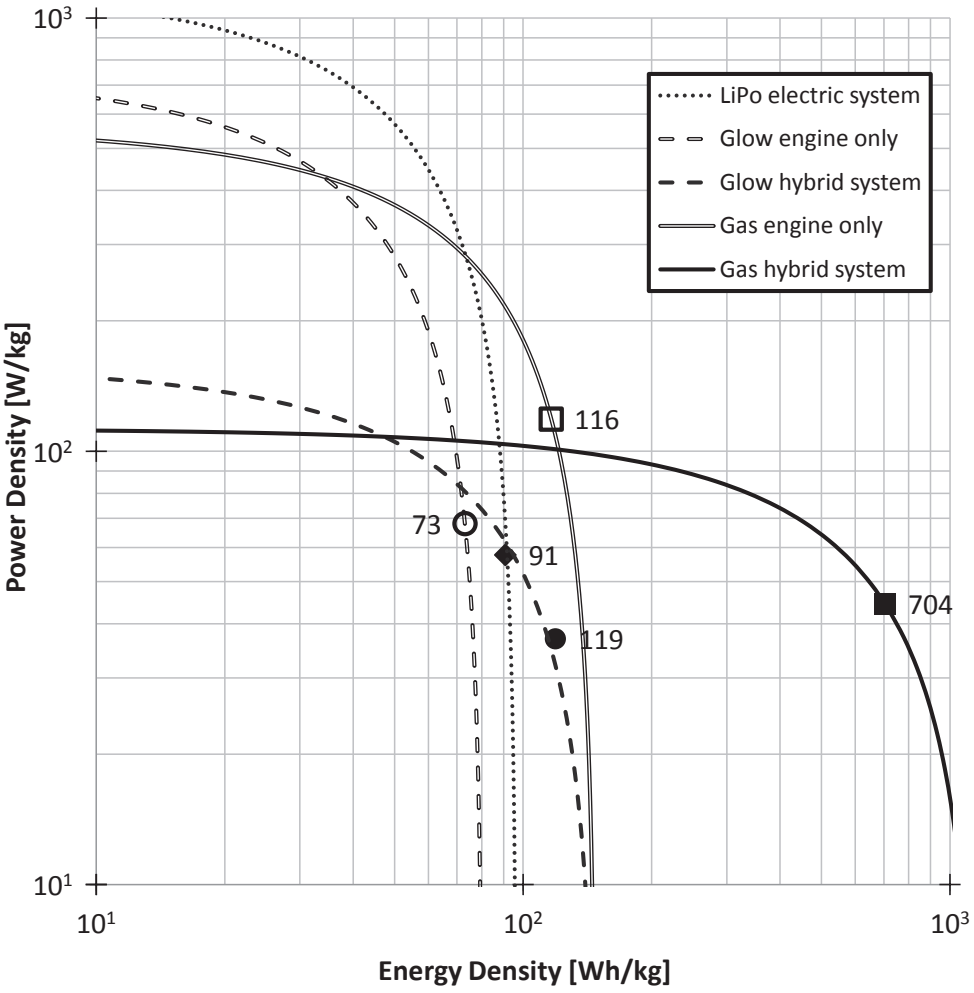

Figure 3.8.: Power density versus energy density for electric, glow hybrid and gas hybrid systems

The solid square point is plotted on Figure 3.8 for the current system with 3kg of fuel and one battery. Given the same propeller efficiency, a similar point can be constructed for a fully electric system with 3kg of the lithium polymer batteries and for the fossil fuel only systems with 3kg of fuel. Each point is labeled with its energy density value. Figure 3.8 indicates a 674% improvement in energy density with 3 kg worth of fuel plus battery over that of a fully electric system with 3 kg of batteries. The actual energy density of this system has shown to be higher than the original estimate from Figure 2.15 since the Saito engine not only used a higher energy dense fuel but also had a lower fuel consumption rate.

The conservatively estimated overall cost for fabricating a single UAV unit considering the new power plant is $6,000. Given the estimated payload of 1kg (excluding fuel) and the maximum endurance and maximum range previously cal-

culated (79.4h and 1495km respectively), the performance metric from equation (2.13) for this UAV design is 49.1. Considering the UAVs at the same price point in Figure 1.2, the average UAV has a performance metric of 1.9. This represents a 25 fold increase in operational performance compared to existing designs at the same unit cost. The performance, cost and endurance goals set by the target areas of Figures 1.1 and 1.2 have been achieved.

Now that the performance evaluation of the gas-electric hybrid power plant is complete, future work is required to apply power management algorithms for the different loading conditions. Many supervisory controllers previously developed for hybrid electric road vehicles could also be applied to a dirigible UAV power plant. One such option is the fuzzy logic controller for hybrid electric vehicles presented by Baumann *et al.* [38]. The major difference is that the load schedule (or "driving" schedule) is not standardized and is dependent on the planned flight trajectory which is not bound by roads. The possibility of combining the power management algorithm into the trajectory planning controller used for the UAV will be explored which will provide a manageable compromise between best performance and minimal energy consumption.

3.5. Chapter Summary

An in-line gas-electric hybrid power plant was designed, developed and evaluated as a low cost solution for a long range dirigible UAV. Tests were performed to study the effects of engine settings, propeller diameter, and electrical load on overall performance and to determine the optimal operating points. The power plant is then compared to other power plant configurations that could be used for a dirigible UAV. The energy density of the proposed hybrid power plant design was proven to be higher than equivalent purely electric, purely fossil fuel or the previously developed glow hybrid systems through experimental testing. Future work will involve implementing advanced power management algorithms, and performing full scale tests of the completed UAV system.

4. Multi-objective Trajectory Planning

Optimal path planning of unmanned vehicles is the process of generating an offline or online path to achieve a goal state at a minimum cost. For the case of aerial vehicles, the vehicle operates in large scale, three dimensional, time-varying environments and is subject to multiple flight constraints for which there is no exact analytical solution [39]. Since path planning algorithms are developed with simplifications and approximations to fit the particular characteristics of a path planning problem, the selection of the path planning algorithm depends on a well-characterized problem definition and on the computational power available. Many algorithms capable of solving planning problems are frequently too computationally expensive to implement in real-time, or if they are, they are not proven to be complete, sound or optimal [39, 40]. In addition, the steps and considerations for the implementation into a physical system are commonly overlooked [39].

4.1. Literature Review

Goerzen *et al.* developed a comprehensive literature summary of path planning algorithms that are categorized into ones with and without differential constraints [39]. Differential constraints refer to limitations such as velocity and acceleration limits, non-holonomic motion, and other higher-order dynamic constraints. The inclusion of these are important to promote more realistic and feasible paths [41]. The task of path planning can be categorized into five distinct stages: sensor model, terrain representation, roadmap generation, graph search, and trajectory generation [39]. The idealized sensor model detects and maps all critical points in the environment such as obstacles, and the initial position and goal position. Many path planner algorithms assume obstacles are known *a priori*, however, effectively identifying and mapping objects using machine vision, sonar, or other means in real-time is a difficult task for small-scale unmanned aerial vehicles (UAVs) [42]. The terrain representation stage divides the map into a finite search space and segments passable and impassable regions. A major challenge to robotic navigation in large unstructured environments is map representation [43]. One common method

to reduce the computational requirement of path planning is using multiple resolutions during terrain representation. Three approaches used in path planning are obstacle-based decomposition [44], wavelet decomposition [45], and action space (lattice) decomposition [46]. Roadmap generation is the process of producing a graph which is then searched for feasible paths or the optimal path (depending on the search approach), between the start and end configurations. The optimality of the path is a subjective based on multiple mission objectives such as time, energy and risk. Applying a scalar-valued preference (or weighting) function to relate each objective into a global cost function is a common approach in multi-objective optimization problems [47, 48]. Finally, trajectory generation can perform path smoothing and speed control assuming a velocity varying trajectory.

On completion of these five stages, re-planning is required since flight and environmental conditions vary with time. There are three different conditions that can trigger re-planning: (i) events: re-planned on the occurrence of new obstacles or map update; (ii) scheduled: re-planned automatically after a set amount of time elapsed or distance traveled; and (iii) errors: re-planned when the error between the UAV's internal and sensor representations exceeds a certain threshold [49].

Wind is a major concern for UAVs and commonly delays or cancels flights. Including this atmospheric disturbance in the path planning objectives is essential for small UAVs with limited propulsion power, as wind can severely increase the flight time of potential paths [50]. In some cases, the strength of the local wind is larger than the vehicle's velocity creating impassible zones (obstacles), which many planners do not account for [51]. When a wind vector field (WVF) is included, it is usually considered as a disturbance whose influence is suppressed by the vehicle's autopilot [52]. However, the wind vector field has the potential to be used as a source for powering the UAV to further reduce energy consumption and travel time [52, 53]. This has been especially important in the path planning of static soaring UAVs that use the vertical component of wind for lift or dynamic soaring UAVs that exploit the vertical gradients in the horizontal wind [54–58]. Two other sources of wind energy that can be exploited are horizontal shear layers and horizontal gusts [53, 59]. For example, unperturbed wind velocity creates a boundary layer with the earth's surface as shown in Figure 4.1, which is caused by the surface roughness of the terrain. During path planning, it is more energy efficient to fly at lower altitudes when traveling into a head wind and higher altitudes when traveling with the wind. The challenge in harnessing wind's energy potential for energy efficient path planning is the high variability and uncertainty of the wind magnitude and direction [55].

Potential field methods are uniquely suited to this path planning problem since much of the data available (such as digital elevation maps (DEMs) and WVFs) are

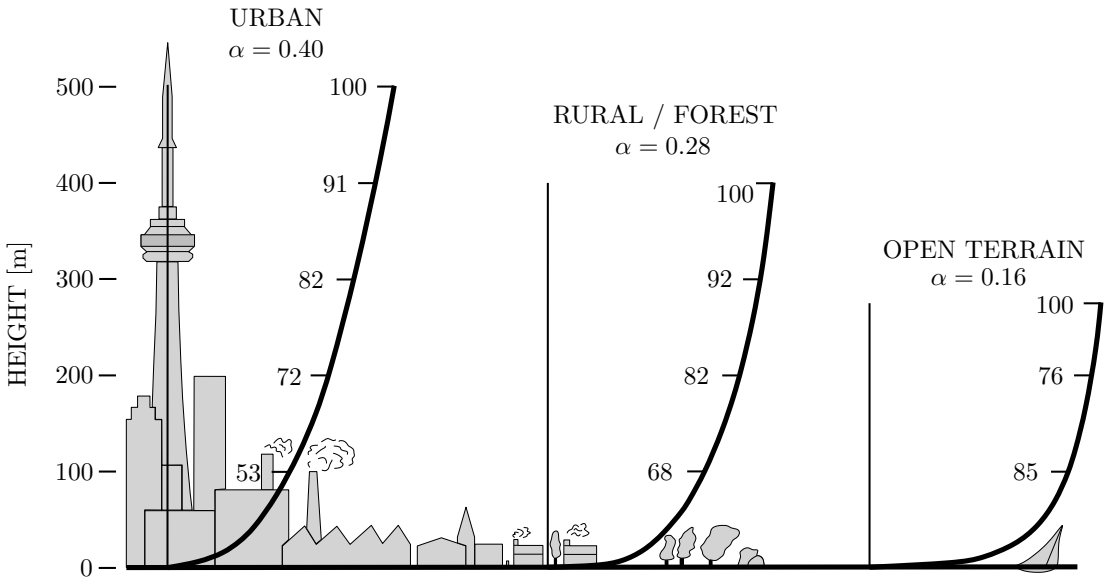

Figure 4.1.: Percent gradient wind, surface roughness α and boundary layer height for different situations. Adapted from Plate [60].

available in a discrete matrix form. The grid being searched is non-deterministic because of dynamic environment changes and the dependance on the UAV's approach direction between nodes. The wavefront expansion approach propagates the costs for the grid and does not rely on the field strengths being known *a priori*. A navigation policy can be applied to restrict grid connectivity during propagation based on dynamic constraints such as turning rate, pitching rate, velocity, and acceleration bounds. This policy promotes more realistic and feasible paths and has the added benefit of reducing the search space.

Soulignac presented a wavefront expansion type path planner for small UAVs that provides a feasible and minimum-time optimal path in the presence of strong current fields [51]. Unfortunately, the research is performed in 2D and does not include other objectives such as fuel or risk. Besada-Portas *et al.* presented an evolutionary algorithm based on-line planner for multiple UAVs in 3D that includes optimization of multiple mission objectives such as path length, fuel and several flight risks but has no mention of wind [61]. McManus developed a wavefront expansion type planner with multiple objectives (distance traveled, time taken, fuel consumed) for a UAV in 3D [62]. In the work, wind is added as a disturbance only and does not apply dynamic constraints to potential paths. Al-Sabban *et al.* presents a Markov Decision Process based fixed-wing UAV path planner that exploits wind energy to minimize energy consumption in an uncertain and time-varying wind field [53]. The simulation results showed almost 30% energy savings compared to a straight line path but was only conducted for one variable field sample. Also, the study was conducted in 2D with a constant ve-

hicle speed relative to the wind. Perhaps the most relevant work in this field is by Wu *et al.* who present an on-line, multi-objective, wavefront expansion based mission planner for fixed-wing UAVs in 3D that includes time, fuel, and several risk objectives in the presence of planar wind fields from weather forecasts [50]. However, their path planner uses a nodal resolution of 1 nautical mile with interpolated 10 nautical mile resolution wind fields to generate long range paths which cannot account for local terrain features.

Although there are many different path planning algorithms, many path planners (and path followers) found in the literature are based on uniform WVFs [63–66] (if they consider wind at all) or constant vehicle velocities (i.e. path planning) [51, 53, 61, 67, 68]. The few planners that account for variable wind conditions simplify the environment to two dimensions by assuming a fixed cruise altitude [51, 67, 68] or assume that the WVF is horizontally planar [50, 69, 70] with coarse resolution discretization of the flight space (>1 km). Coarse resolutions can oversimplify wind, obstacle and path data which can create issues for limited power, small scale airships.

The goal of this study is to develop a trajectory planner for a lighter-than-air UAV that, (i) provides minimal energy consumption flight trajectories, (ii) that are realistic and feasible in large, high resolution, 3D environments (iii) and are computed faster than they are predicted to be flown. The optimal flight trajectory is defined to be the one that reaches the goal position within the desired time while consuming the minimum amount of energy and avoiding obstacles at a sufficiently safe distance. The importance of each of these criteria should also be scalable based on the specific mission objectives. The trajectory planner is considered to operate in real-time if the trajectories are computed faster than the UAV traverses them.

In this chapter, a cost wavefront expansion type trajectory planner is developed that generates feasible, realistic and optimal trajectories in variable 3D wind fields. Trajectories are generated in real-time and simulated in large, highly realistic, 3D environments. A multi-objective cost function is presented using variable WVFs generated from computational fluid dynamic (CFD) analysis on digital elevations maps. The cost function includes the differential constraints of the physical dirigible platform and is optimized for time, energy and collision avoidance.

The chapter is organized as follows; first, a background on wind modelling and current wind usage is presented. Then the trajectory planning method is outlined followed by the development of the cost function. The trajectory planner is then simulated in a set of randomly generated 3D environments and effectiveness is evaluated based on several performance metrics.

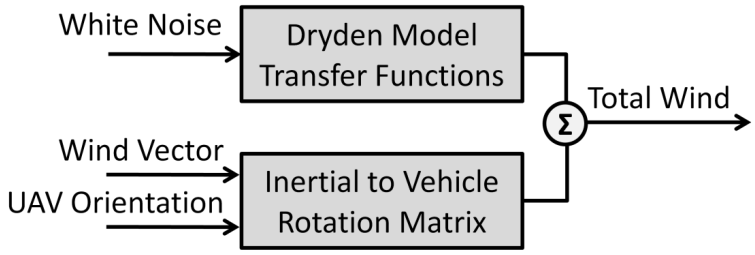

Figure 4.2.: Total wind modelled as the sum of bulk and gust components. Adapted from Beard [72].

4.2. Wind Vector Fields

Wind can be modelled as the vectored sum of two components, a stochastic (gust) component and a steady ambient component [71]. The gust component can be modelled using the Dryden model (a suitable approximation of the experimentally validated von Karman model), and is expressed in the vehicle body frame [72]. The Dryden model consists of passing white noise through the Dryden filter to produce the gust component as shown in Figure 4.2. The filter use generalized parameters based on flight conditions such as altitude and severity of turbulence which are defined in MIL-F-8785C [73]. This component is unpredictable, random, and cannot be used for planning.

The steady ambient wind is typically expressed in the earth inertial reference frame and can be modelled based on weather information for a given area. A constant and uniform steady wind vector field is typically employed since it is assumed that there is no prior knowledge of it [74]. However, wind vector fields are now available in 6 hour increments for multiple areas across North America [75] and will likely become more accurate, timely and wide spread as weather sensing technology advances. Figure 4.3 shows a typical wind vector field provided by the National Weather Service in the US. This weather information is expected to replace the uniform bulk wind model and be added to the gust model to give a better approximation for the optimal flight trajectory. Unfortunately, the finest resolution wind models generated from a national weather service found in literature was 10 nautical miles [50, 51, 55].

As an alternative to the publicly available weather information, CFD software is capable of estimating the spatially variable WVF over a DEM given sparse known wind stations. WindStation is one such software [76]. CFD software is especially useful where online weather information for an area is not available or periods when communication with the UAV is lost. It can also provide finer resolution fields capable of capturing local weather patterns such as wind currents around buildings [77]. Turbulence caused by wind flow around buildings has been

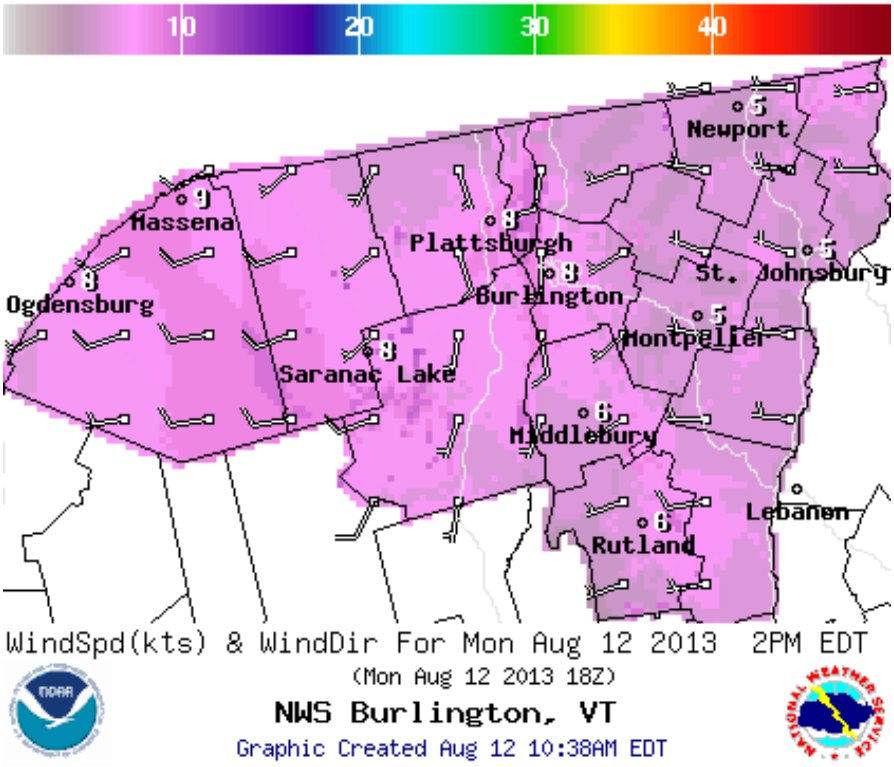

Figure 4.3.: A typical 2D wind vector field [75]

shown to cause a UAV to fail by following a previously successful trajectory when the UAV's dynamic model is introduced [78]. However, the low pressure zones created farther downstream from buildings where turbulence intensity is low have the potential to shield the UAV's trajectory from undesirable winds vectors. One current challenge is computing CFD wind data on three dimensional environments in real-time [77]. This may be the reason that there is limited literature on path planning in temporal flow fields [40].

4.3. Cost Wavefront Expansion Approach

Please note, the nomenclature for this chapter can be found in Appendix B.

The cost wavefront expansion approach starts from the UAV's current position and expands anisotropically outward toward the goal position, minimizing a cost function. The cost function is the sum of all trajectory objectives multiplied by the mission weights. The mission weights are dependent on the priority of mission's objectives and selected by the user *a priori*. The cost function is then searched using a multi-resolution, grid-sampled Dijkstra algorithm. This approach produces a trajectory that is complete and resolution optimal [39]. The cost function between any two nodes n and n' is given by

$$\mathbb{C}(n, n') = W_t \cdot \mathbb{C}_t(n, n') + W_e \cdot \mathbb{C}_e(n, n') + W_a \cdot \mathbb{C}_a(n, n') \tag{4.1}$$

$$W_t + W_e + W_a = 1 \tag{4.2}$$

where $\mathbb{C}$ are costs, W are operator weights and the subscripts t, e and a denote the time, energy, and avoidance objectives, respectively. Each objective's cost function, $\mathbb{C}_t$,$\mathbb{C}_e$, and $\mathbb{C}_a$, is mapped onto a common scale of zero to one and the weights are user-selectable such that constraint (4.2) is satisfied. In this way, the user can easily differentiate the priority of each objective with respect to the same common scale. The weights can be easily divided into linguistic priority variables (such as "low" or "high" priority) that can simplify operator training and integration.

The selection of resolution and scope are critical since the Dijkstra search algorithm is only resolution optimal and has a proven time complexity of $O(N \log N)$, where N is the number of nodes in the grid [39]. If the resolution is selected to be too large, the trajectory solution will generalize obstacles to be larger and over simplify wind vectors. If the resolution is selected to be too small for a large scope, the trajectory will not be generated in real-time. One approach to reduce computational time is to apply sub-optimality bounds through the inclusion of an inflated heuristic (a multiplier >1 that penalizes new path branches) [79]. It can be shown that the confidence of environmental information, such as wind, decreases as the distance away from the vehicle increases [80]. The optimal trajectory segments close to the goal node may change due to variations in temporal environmental information (such as wind vectors and the flight patterns of other aircraft). Thus, the value of determining the optimal trajectory segments near the goal node is diminished. Two types of methods can be imposed to mitigate this uncertainty. The first is the use of a multi-resolution grid, employing a fine resolution in the immediate vicinity of the UAV and a coarse resolution approaching the goal node. This approach is similar to the action space map decomposition approach outlined in [46]. Since both fine and coarse resolutions follow the same procedure, this chapter focuses on the short-range, fine resolution grid. Using this method, the sub-optimality condition can be effectively controlled by adapting the spatial range and gradient of resolution changes to maximize optimality within the computational constraints. The second method, which could also be applied during the implementation stage, is temporal replanning to keep information up-to-date similar to the three replanning triggers outlined in [49].

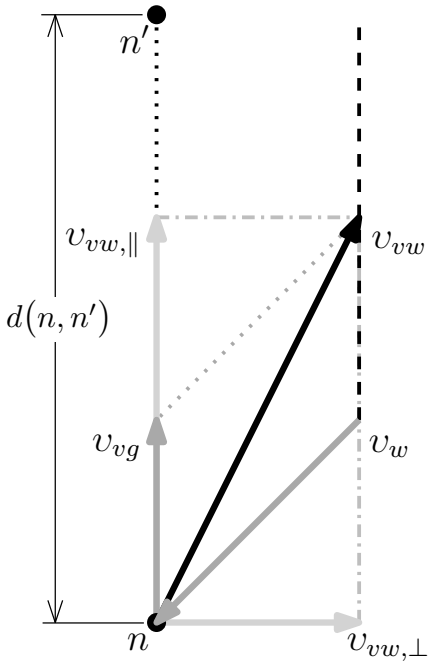

Figure 4.4.: Vector sum of wind, relative and ground velocities

4.4. Trajectory Objectives

The three objectives in (4.1) need to be simultaneously optimized for any given UAV mission. The trajectory objectives are suited to the limitations and availability of the physical model's on-board equipment where applicable. This is a desirable trait for a smooth transition to physical implementation of the planner.

Wind is added to each node according to the sum of WVF and gusts but assumed to be constant in between nodes (using the wind vector from the next node, n'). If the vehicle is to arrive at the next node, the vehicle's ground velocity, v_{vg}, must be parallel to the unit vector direction to that node, $\vec{v}_{vg}$. Thus, the perpendicular components of the wind, $v_{w,\perp}$, and the vehicle velocity relative to the wind, $v_{vw,\perp}$, must be equal and opposite. The parallel component of the vehicle's relative velocity, $v_{vw,\parallel}$, can then be optimized for the time and energy objectives depending on the current flight conditions. The velocity vector sum of these components is shown in Figure 4.4.

4.4.1. Arrival time

The time to traverse the cell can be approximated by,

$$t(n,n') \approx \begin{cases} \frac{o \cdot d(n,n')}{|v_{vg}|} = \frac{o \cdot d(n,n')}{\left|v_{vw,\parallel} + v_{w,\parallel}\right|}, & v_{vg} \cdot \vec{v}_{vg} > 0 \\ \infty, & v_{vg} \cdot \vec{v}_{vg} \leq 0 \end{cases} \tag{4.3}$$

where o is the orientation ratio (described in section 4.4.2) and d is the distance between nodes. This equation extends equation (2) from Wu *et al.* [50] by considering that the distances and vectors are three dimensional, and the time estimate approaches infinity when the wind magnitude along the vehicle trajectory equals the vehicle's cruise velocity. The equation adjusts for non-linear linear flight trajectory between nodes using the orientation ratio. It is assumed that for equilibrium, $v_{vw,\perp} = -v_{w,\perp}$, and the vehicle will achieve an angle of sideslip (crab angle) to offset lateral winds. This is an important distinction as although lateral winds reduce the vehicle's available goal oriented velocity, only the parallel component will reduce the traversal time. It is also important to note that the true traversal time depends on other factors such as vehicle stabilization effort and trajectory tracking error which require a complete dynamic model flight simulation for a more accurate approximation.

Although time between nodes can be minimized directly, it does not provide the operator any feedback on the complete path travel time before selecting a weight, which makes weight selection difficult. In real world applications, the desired travel time between any two grid nodes is time-dependent [81, 82]. In other words, the arrival time cost is a function of the progress of the aircraft has made towards arriving to the goal node. Therefore, it is appropriate to non-dimensionalize time by a user selectable time goal and the distance remaining to the final goal node. This also has the advantage of extending the arrival time factor to the time-dependent case where the remaining cost is dependent on the total cost so far (i.e. how on schedule the UAV is to meet a given ETA). Cumulative time can be non-dimensionalized by considering the user selectable arrival time to the goal node, t_g,

$$\mathbb{C}_t\left(n, n'\right) = \begin{cases} \left(\frac{t_{sum}(n)}{2t_g}\right) - \left(\frac{d_g - d_r(n')}{2d_g}\right) + \frac{1}{2}, & t_{sum} < t_g \\ 1, & t_{sum} \geq t_g \end{cases} \tag{4.4}$$

where d_g is the initial Euclidean distance from start to the goal node, d_r is the remaining Euclidean distance from the current node to the goal node, and t_{sum} is the total time spent from the start node to node n. When $\mathbb{C}_t$ is less than one half, the UAV is ahead of schedule, and when it is greater than one half the UAV is behind schedule. Equation (4.4) enables the trajectory planner to adapt to unforeseen environments. Since lighter-than-air vehicles do not need a forward velocity to maintain lift, the velocity of the UAV can be modified along the length of the path to successfully arrive at the goal node by the user set time. Under this assumption, the optimal vehicle speed for time at each node can be defined as,

$$v_{ot}(n') = \begin{cases} \left(\frac{d_r(n')}{t_g - t_{sum}(n)} - v_{w,\parallel} \cdot \vec{v}_{vg} \right), & t_{sum} < t_g \\ v_{v,\max}, & t_{sum} \geq t_g \end{cases} \tag{4.5}$$

If the current travel time has already exceeded the time goal, the vehicle speed for time is set to maximum vehicle velocity, $v_{v,\max}$, for the remaining duration of the flight. Changing the weight for arrival time, W_t, affects the choice of the path but also changes the vehicle's velocity which is further explained in section 4.4.2.

4.4.2. Energy consumption

For the simplest case, where input power is constant, the lowest energy path will be the path with the shortest arrival time. However, with the introduction of a set time goal and 3D wind vector fields, there is the potential of a velocity varying path (i.e. trajectory) that consumes less energy. Energy consumption estimates are dependent on multiple factors and are highly platform specific. Airships, like most UAVs, are under-actuated, non-holonomic vehicles which require additional energy to change orientation. Some fuel/energy consumption estimates include a limited number of flight parameters [61, 64], which can over simplify the energy consumption model. Rotational changes require energy and cannot be considered negligible for local or short range path planning and some maneuvers can even cause unstable behavior which can become costly to correct and re-establish course. A recent study by Al-Sabban *et al.* suggests that these changes as well as incorporating a six DOF model will affect path planning performance [53]. The model developed here attempts to include the differential constraints inherent to airships and other non-holonomic UAVs.

The theoretical energy required to change orientation as defined by an applied moment times an angle is negligible compared to that of forward motion for all but highly dynamic maneuvering of agile UAVs. However, due to the minimum turning radius of the vehicle, it must travel a longer path than the equivalent straight line path between two points. This increase in time directly leads to an increase in energy consumed which can not always be ignored. The additional time to travel between two points depends on two factors: the ratio of the minimum turning radius over the distance between nodes, $r_{min}/d(n, n')$, and the magnitude of the orientation change, ψ. Figure 4.5 shows an example of an idealized kinematic reorientation that takes into account the minimum turning radius. The true distance, $d'(n, n')$, is the arc length of the two tangent arcs; the first tangent to $v_{vg}(n)$ with radius r_{min} and the second is tangent to both the first arc and $v_{vg}(n')$. The orientation ratio, o, mentioned in Equation (4.3) is the ratio of the true distance over the idealized straight line distance, $d'(n, n')/d(n, n')$. Table 4.1

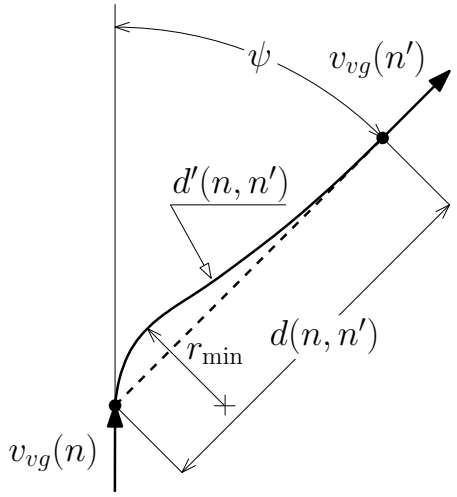

Figure 4.5.: Idealized reorientation between two nodes

Table 4.1.: Percent increase of path length versus orientation change and turning radius ratio

ψ (deg)	$r_{min}/d\,(n,n')$				
	0.01	0.05	0.1	0.2	0.3
30	0.02%	0.12%	0.25%	0.53%	0.83%
45	0.08%	0.41%	0.84%	1.83%	3.00%
60	0.18%	0.95%	1.99%	4.43%	7.45%
90	0.58%	3.03%	6.45%	14.71%	25.40%

shows examples of the impact of re-orientating the vehicle under different minimum turning radii. The minimum turning radius at cruise speed for the simulated lighter-than-air UAV platform is 10m. Considering a resolution between nodes of 50m, the increase in energy to reorient the vehicle is not negligible.

Conventional airship design have aerodynamic surfaces (tail rudders) instead of thrusters for directional control [19]. Rudders have the advantage of lower power consumptions over longer duration maneuvers but suffer from sluggish response time and ineffectiveness during low speed flight. These disadvantages are considered to be unacceptable traits for a small-scale lighter-than-air UAV. The platform being considered has a fixed pair of forward facing electric thrusters complimented by a hybrid gas-electric power plant and uses two tail mounted thrusters for directional control and roll stability [16, 29]. Small-scale airships typically use thrust vectoring or dynamic lift using aerodynamic surfaces for altitude control, which provide a fast control response but at a higher energy cost. The platform being considered also exploits the use of air ballasts (ballonets) for altitude control and pitch stability. These actuators use an electric air pump to change ballast volume. The ballonets also provide two essential alternate functions of pressure regulation to ensure structural integrity and weight ballasting to compensate for consumed

fuel of the power plant.

Considering this platform, the energy consumed to traverse between nodes is approximated by,

$$\mathbb{C}_e\left(n, n'\right) = \frac{\left(P_T + P_L + P_c\right) \cdot t\left(n, n'\right)}{E_c} \tag{4.6}$$

where P_T is the power required to propel the vehicle at the desired ground speed along the horizontal path, P_L is the power required to change altitude, P_c is the constant electrical power required to maintain on-board electronics and E_c is a constant energy used to normalize the cost. Substituting the definitions of mechanical power for propeller and pump actuators into equation (4.6) gives,

$$\mathbb{C}_e\left(n, n'\right) = \left(\frac{F_T}{\eta_T}\left|\upsilon_{vw}\right| + \frac{Q \triangle \rho\left(n, n'\right)}{\eta_{pump}} + P_c\right) \cdot \frac{t\left(n, n'\right)}{E_c} \tag{4.7}$$

where F_T is the force required from the UAV's actuators, Q is the air flow rate through the air ballast pump, and $\triangle \rho\left(n, n'\right)$ is the change in atmospheric pressure between nodes. The propeller forces applied by the UAV actuators, including the electric motors and the hybrid power plant, are non-linear functions of input electrical power. A propeller's efficiency, η_T, is dependent on the propeller advance ratio, which is the ratio of the vehicle's relative velocity, υ_{vw} over the product of the propeller's diameter and rotational speed. Based on a third order least squares fit of propeller efficiency curves from Figure 2.12 for a 12 inch propeller with 15° pitch spinning at 9000 RPM,

$$\eta_T \approx -2.59 \cdot 10^{-5} \upsilon_{vw}^3 + 2.07 \cdot 10^{-4} \upsilon_{vw}^2 + 4.15 \cdot 10^{-2} \upsilon_{vw} \tag{4.8}$$

when $0 < \upsilon_{vw} < 36 \frac{m}{s}$. Lastly, P_c is the constant electrical power requirement to maintain on-board electronics which can be up to 65% for dirigibles [19]. The inclusion of P_c is important for a dirigible as it prevents unrealistic loitering in drift fields when a loose time goal is set. The wind vector field is a crucial addition to the energy consumption model as longitudinal winds will effect the arrival time in (4.3) and compounds the effect of applied lateral winds in (4.7). For a force equilibrium,

$$F_T = F_d = \frac{1}{2} C_d \delta_{air} A \left|\upsilon_{vw}\right|^2 \tag{4.9}$$

The product of the axial drag coefficient and reference area, $C_d A$, in (4.9) can be estimated in a few methods. Using the empirical method proposed by Hoerner [83], the value for this platform is 0.229. Using the procedure outlined by Jones [84], the value is 0.147. Furthermore, the value is not constant for all flight conditions, and increases with both the angle of attack and the angle sideslip. Therefore,

for the airship to hold a constant crab angle into the wind is not trivial in the perspective of energy consumption. The value predicted by Jones was used as it was developed explicitly for airships [84].

The air ballast flow rate, Q, is assumed to be ballast volume change, $\triangle V_b$, required to remain neutrally buoyant with a change in altitude divided by the travel time,

$$Q = \frac{\triangle V_b\left(n, n'\right)}{t\left(n, n'\right)} = \frac{\triangle \delta_{air}\left(n, n'\right) V_v}{\delta_{air}\left(n\right) t\left(n, n'\right)} \tag{4.10}$$

where V_v is the envelope volume of vehicle. Substituting equations (4.3), (4.9) and (4.10) into equation (4.7) yields the complete energy objective function,

$$\begin{aligned} \mathbb{C}_e\left(n, n'\right) = & \left(\frac{C_d \delta_{air} A}{2\eta_T}\left|\upsilon_{vw}\right|^3 + P_c\right) \cdot \frac{o \cdot d(n,n')}{E_c\left|\upsilon_{vw,\parallel} + \upsilon_{w,\parallel}\right|} \\ & + \frac{\triangle \delta_{air}(n,n') V_v \triangle \rho(n,n')}{E_c \delta_{air}(n) \eta_{pump}} \end{aligned} \tag{4.11}$$

Equation (4.11) is a non-linear function with respect to $\upsilon_{vw,\parallel}$ which makes solving for the vehicle velocity for minimum energy, υ_{oe}, difficult. It can be solved using non-linear optimization or numerical methods but this was found to be too computationally expensive for the inner loop of the online planner. For these simulations, υ_{oe}, was solved directly assuming that η_T is constant and,

$$\upsilon_{vw}^3 \approx \upsilon_{vw,\parallel}^3 + \upsilon_{vw,\perp}^3 \tag{4.12}$$

The normalizing energy constant, E_c, is selected to be the energy consumed traversing the longest vector between nodes at $\upsilon_{vw} = \upsilon_{v,\max}$ with zero net wind (calculated to be 1.50Wh for the given platform).

Although the trajectory planner finds the optimal path based on the energy and time priorities, the vehicle's velocity along the path also has a significant impact. When time and energy priorities have conflicting vehicle speeds, a weighted sum of both optimal speeds is used to select the speed according to,

$$\upsilon_{vw,\parallel}\left(n'\right) = \begin{cases} \frac{W_t}{W_t + W_e} \cdot \upsilon_{ot}\left(n'\right) + \frac{W_e}{W_t + W_e} \cdot \upsilon_{oe}\left(n'\right), & \upsilon_{oe} < \upsilon_{ot} \\ \upsilon_{oe}, & \upsilon_{oe} \geq \upsilon_{ot} \end{cases} \tag{4.13}$$

while satisfying the vehicle's velocity limits of $0 < \upsilon_{vw}\left(n'\right) < \upsilon_{v,\max}$. If the vehicle speed for minimum energy is faster than the one for arriving on time, the vehicle speed for minimum energy is used.

4.4.3. Collision avoidance

In this model, collision avoidance refers to all types of collision risks including the terrain, restricted airspace regions, altitude limits and both static and dynamic obstacles. All types of risks are considered to have a finite minimum separation zone (MSZ) distance that forms around the centroid of obstacles. Each risk has a different MSZ distance is based on aircraft visual flight regulations or risk minimization. The collision avoidance objective cost is a repulsive field designed to strengthen exponentially as the vehicle approaches any MSZ limit. It is normalized from zero to one for normal flight conditions while operating outside any MSZ. The path planning approach presented here deals with collision avoidance from static and slow moving dynamic objects. The total collision avoidance factor at each node, $\mathbb{C}_a(n)$, is taken to be the maximum of three components such that,

$$\mathbb{C}_a(n) = \max\left(C_{a1}(n), C_{a2}(n), C_{a3}(n)\right) \tag{4.14}$$

The terrain component, $\mathbb{C}_{a1}$, that is adopted is,

$$\mathbb{C}_{a1}(n) = \begin{cases} \left(\frac{MSZ_l}{d_{vl,z}}\right), & z_v > z_l \\ \infty, & z_v \leq z_l \end{cases} \tag{4.15}$$

while for the pressure altitude ceiling component, $\mathbb{C}_{a2}$, is taken as,

$$\mathbb{C}_{a2}(n) = \begin{cases} \left(\frac{MSZ_m}{d_{vm,z}}\right), & z_v < z_m \\ \infty, & z_v \geq z_m \end{cases} \tag{4.16}$$

For buildings and all other static obstacles the function component, $\mathbb{C}_{a3}$, is defined as,

$$\mathbb{C}_{a3}(n) = \begin{cases} \max\left(\frac{MSZ_o}{d_{vo,z}}, \frac{MSZ_o}{|d_{vo,x}\,,\, d_{vo,y}|}\right), & (d_{vo,x}\,,\, d_{vo,y}\,,\, d_{vo,z}) > 0 \\ \frac{MSZ_o}{|d_{vo,x}\,,\, d_{vo,y}|}, & (d_{vo,x}\,,\, d_{vo,y}) > 0 \;\&\; d_{vo,z} \to 0 \\ \frac{MSZ_o}{d_{vo,z}}, & (d_{vo,x} \mid d_{vo,y}) \to 0 \;\&\; d_{vo,z} > 0 \\ \infty, & (d_{vo,x}\,,\, d_{vo,y}\,,\, d_{vo,z}) \to 0 \end{cases} \tag{4.17}$$

where MSZ_j are the predefined minimum separation zone distances, $d_{i,j}$ are distances between the vehicle v, and the terrain l, altitude ceiling m, and blocks of buildings o, along the x,y,z axis in Cartesian coordinates. The avoidance term $\mathbb{C}_{a3}$ is shown graphically in Figure 4.6.

Additional C_a terms similar to equation (4.17) can be added to include no-fly zones and dynamic aerial obstacles. The planner's ability to avoid dynamic

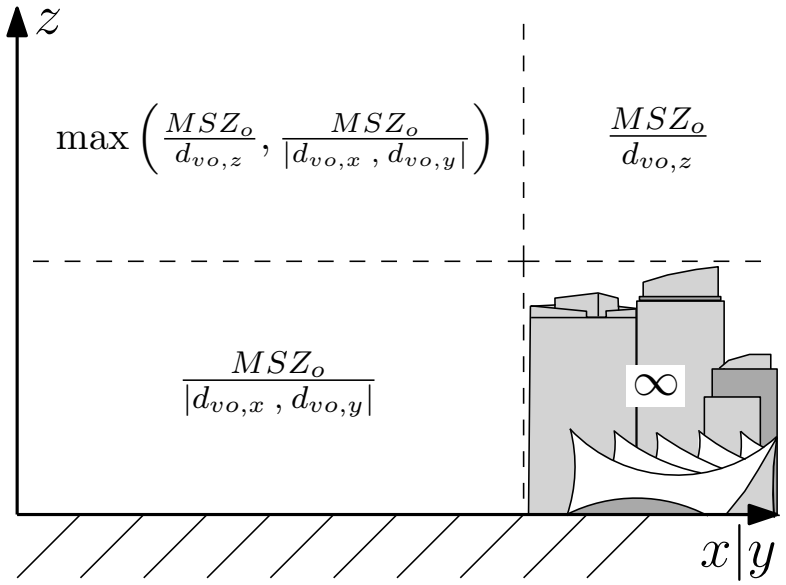

Figure 4.6.: Definition of term $\mathbb{C}_{a3}$ in relation to buildings

obstacles depends on the object's speed relative to the UAV, the frequency, range and uncertainty of the available on-board sensor information and the frequency of the re-planning process. A method to model the MSZ for dynamic obstacles that could be applied to this planner is presented by Wu et al [50].

4.5. Trajectory Planning

Once a multi-objective cost function field is formulated, the desired trajectory through the field is determined through 3D grid search techniques. A nodal list is generated based on an rectangular grid representation of 2000m×2000m×1000m with a nodal resolution of 50m×50m×10m. This resolution was chosen because it is roughly the same as 0.75 arc-sec digital elevation maps that are publicly available from GeoBase. To reduce the computational time, the connections between nodes are generated on the fly using the vector neighbor operator assigned in Figure 4.7 similar to the vector neighbors described in [50, 85]. The black arrow in Figure 4.7 represents the UAVs direction while the gray lines represent possible UAV directions (assuming that the nodes exist and are not outside the search environment). Redundant connections are eliminated (for example, [2, 2, 2] is excluded because it is a multiple of [1, 1, 1]). Furthermore, connections that create an angle greater than the critical turning or pitching angles of the UAV are also omitted.

The field strengths for obstacles are computed using (4.15) to (4.17). The field strengths for time and energy consumption are computed on demand as they depend on the nodal approach direction, wind conditions and other flight

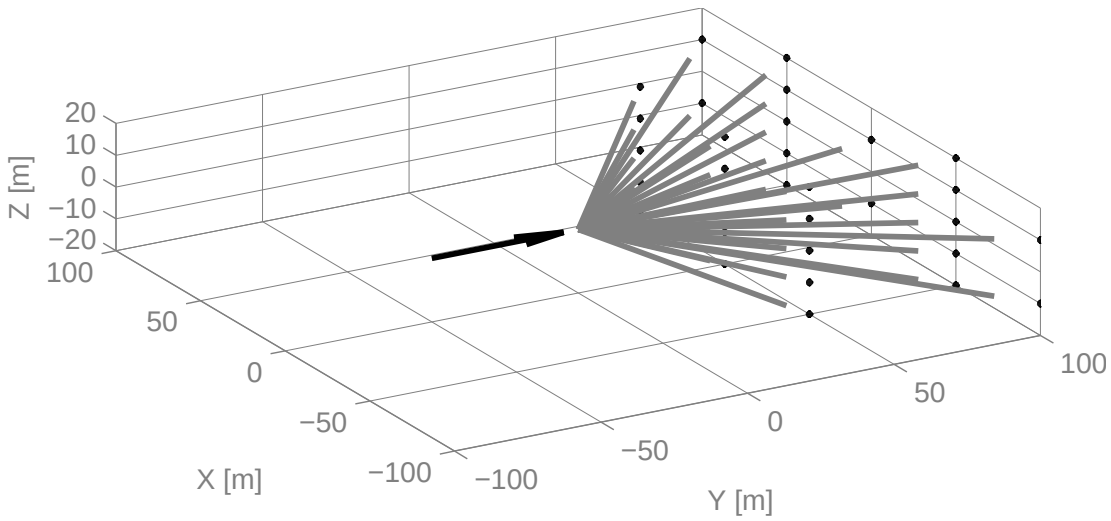

Figure 4.7.: Vector neighbor operator

characteristics. The multi-objective cost function is minimized using the Dijkstra algorithm [86] and the computational time, total trip time, energy consumption and the distance to the closest obstacle along the path are recorded. This process is repeated for all the samples for each scenario. A summary of the method is shown in Figure 4.8. To implement the multi-resolution trajectory planner in practice, the procedure steps in gray are removed and step 2 would be replaced by sensory inputs and real-time WVF generation. WVF data can be recomputed frequently to capture field changes over time and should be supplemented by publicly available weather forecasts for added confidence.

4.6. Case Definitions

As mentioned in section 4.1, many planners found in literature consider only uniform WVFs or assume constant vehicle velocity paths (path planning instead of trajectory planning). It is proposed that if the trajectory planner is equipped with the variable WVF data, it will be capable of making better decisions leading to more realistic and improved results. The energy consumption model presented in (4.11) is a third order function of the vehicle velocity relative to the wind, so it is reasonable to assume that the optimal velocity will vary with wind speed. Additionally, planners found in literature that do include variable WVFs were found to have a coarse nodal resolution (>1 km) due to the sparsely spaced WVF information provided from national weather services. However, the low resolution of a planner can oversimplify weather information between nodes reducing the planning problem to the shortest straight line path in a uniform wind field case. The following four test cases are identified to illustrate the importance of having

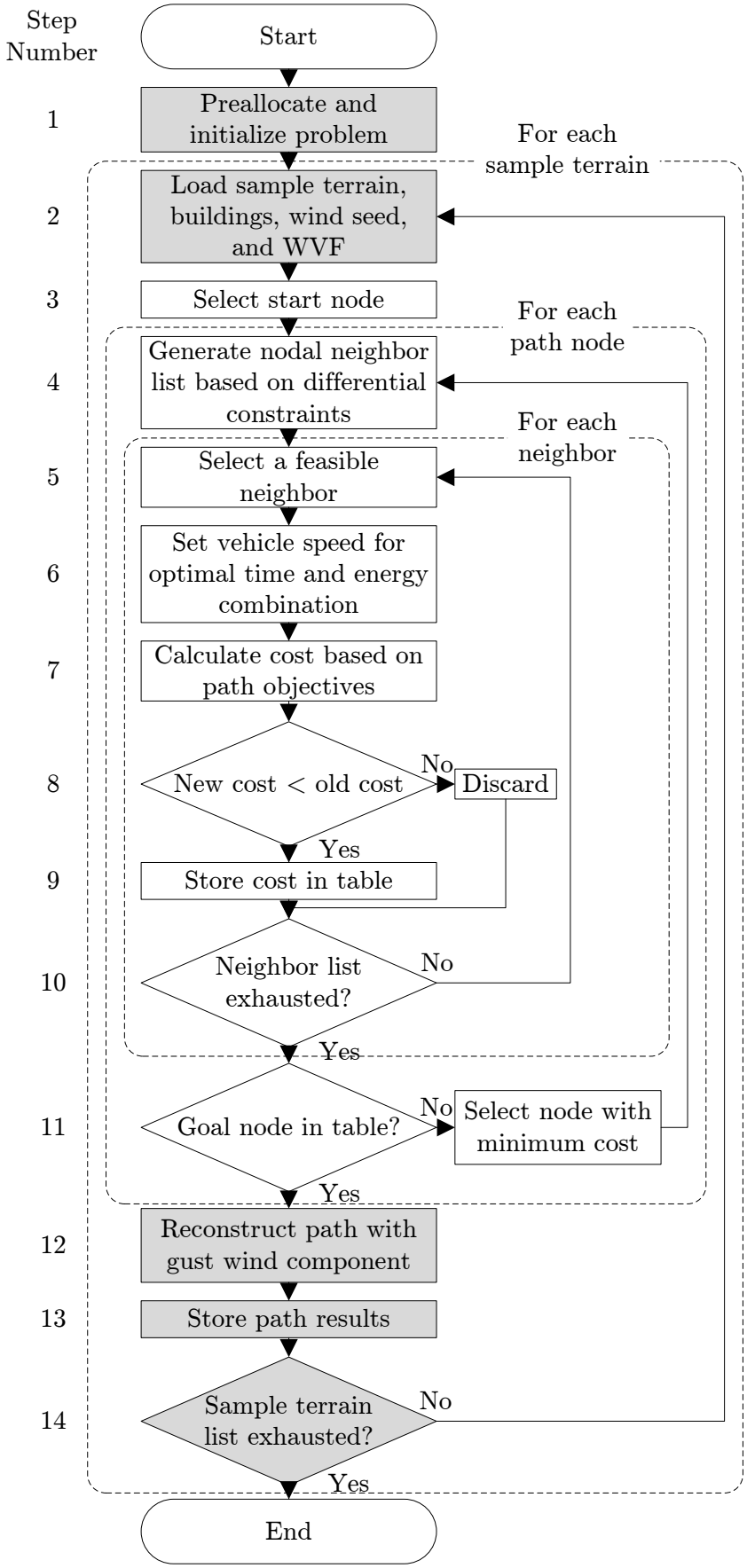

Figure 4.8.: Simulation flow chart

a fine nodal resolution, and including both variable WVFs and variable vehicle velocities into the planning process.

Case 1: Low spacial resolution This case represents the situation where there is no planning between start and end nodes, or the planner has a coarse geographical resolution (2km x 2km x 1km instead of 50m x 50m x 50m). The cost function (4.1) is modified to $\mathbb{C}(n, n') = d_r(n') + W_a \cdot \mathbb{C}_a(n, n')$. The planner constructs the shortest straight line trajectory between start and end nodes while still obeying vehicle constraints and avoiding known obstacles. The vehicle will however be equipped with the knowledge of the variable WVF and adjust velocity along the straight line path as normal.

Case 2: Constant velocity The planner will plan a path instead of a trajectory. The optimal velocity equation (4.13) is ignored and the vehicle velocity is held at a constant value throughout the planning process. The velocity value is equal to the distance between the start and goal nodes divided by the goal time. The vehicle will be equipped with the knowledge of the variable WVF and adjust the path according to the cost function as normal.

Case 3: Uniform WVF The planner is unaware of the WVF during the planning process and instead plans based on a constant and uniform WVF. The magnitude and direction of the uniform WVF is determined by the seed value of the variable WVF generation (i.e. average bulk flow direction and magnitude at all nodes). The vehicle will adjust both the vehicle velocity and path as originally intended.

Case 4: Purposed complete planner The full trajectory planner is applied as outlined in section 4.4. The planner is aware of the WVF during the planning process and optimizes both the vehicle velocity and path.

4.7. Results

The relative performance of the complete multi-objective trajectory planner proposed was studied through the comparison to each other planning case. Each of the four test cases were simulated in the same one hundred flight test environments. The DEM (terrain) for the test environments was generated based on statistical data from the real DEM of Vancouver, BC, Canada which is publicly available on GeoBase [87]. City blocks of buildings were then randomly added to the terrain and their placement was dependent on the grade of the topography. Producing geometrically accurate representations of a real world location was chosen over

Table 4.2.: Seed values for terrain generation

Parameter	Value
Mean altitude	600 m
Altitude standard deviation	600 m
Water table altitude	0 m
Mean grade	18.4 %
Max grade	306 %
Average number of blocks	20
Min block height	15 m
Max block height	200 m
Block length	100 m

Table 4.3.: WindStation 4.0.1 field generation input parameters

Parameter	Value
Surface roughness	2 m
Turbulence Model	k-epsilon
Max residual	1×10^{-5}

using samples from DEMs directly for this simulation since it reduced the memory required to store many different locations and provided infinite geographic combinations for probabilistic sampling. The terrains were randomly populated according to the seed variables typical of Vancouver which can be found in Table 4.2.

For each terrain, a 3D WVF was generated using the CFD software WindStation. The WVF was computed based on one wind vector seed and populates the entire control volume based on the interaction with terrain and building topography. The wind seed direction was a uniformly random integer between 0° and 359°. The wind seed magnitudes were produced based on the approximation that wind magnitude follows a Weilbull probability density function [88] with a shape value of 2 and a scale of $\mu_w/0.89$, where the mean wind velocity μ_w, for Vancouver is 3.61 m/s (averaged annually) [89]. The WVF resolution was set equal to the terrain's nodal resolution of 50m to negate any computational time required for interpolation between nodes. Pertinent software parameters that were selected for the WVF generation are listed in Table 4.3.

A trajectory was considered to have converged to a feasible solution if the planner finds an obstacle-free path that connects the start and end nodes and that satisfies the condition, $t < \infty$. If the trajectory selected had a magnitude of wind ($\left|v_{w,\perp} + v_{w,\parallel}\right|$) that is higher than the vehicle velocity along its length, then that trajectory is considered to have failed. If the planner cannot find a solution, such as when strong opposing wind vectors form a planar barrier that cannot be over-

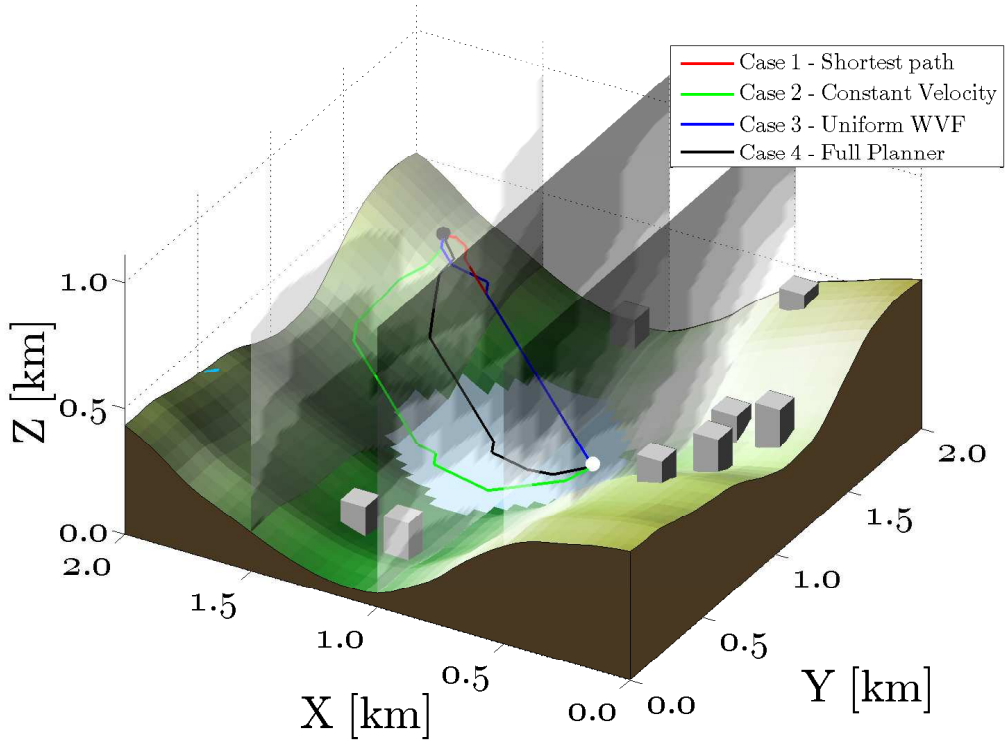

Figure 4.9.: Typical planned trajectory in a simulated city landscape showing WVF magnitude cross sections. Please refer to the full color PDF.

taken, then those solutions also do not converge. Trajectories were planned on a node to node basis (online planning) using the WVF data generated, however, it is not realistic to assume that this data is perfect. Therefore, stochastic (gust) wind was added to the steady field that the trajectory planner did not account for. The gust wind component was applied through the Dryden filter. If the total wind exceeded the vehicle velocity after planning the trajectory, the trajectory also did not converged to a feasible solution. Trajectories that do not meet the time goal are still considered to converge to a feasible solution but perform poorly due to their undesirably late arrival.

The three weights defined in the cost function (4.1) were all selected to be equal to $\frac{1}{3}$. The goal time t_g, is set to 300s and the maximum vehicle velocity is set to $12\frac{m}{s}$. Separate trajectories were produced for each case scenario and for each flight environment. Four performance criteria that were distinguished are the convergence rate, the average computational time, the average flight time, and the average energy consumption. Important note: only the results from the test environments that all four cases had produced a feasible trajectory for were considered for the averages (44/100). Figure 4.9 shows a typical environment with the planned trajectory for each case and cross sections of the variable WVF. Wind

Table 4.4.: Performance comparison between trajectories planned for the four test cases

Case	Convergence (%)	Avg. computation time (s)	Avg. flight time (s)	Avg. energy consumption (Wh)
1	57	15.2	388.9	181.7
4	94	41.7	206.9	43.9
Change	+64.9%	+173.9%	-46.8%	-75.8%

(a) Impact of nodal resolution

Case	Convergence (%)	Avg. computation time (s)	Avg. flight time (s)	Avg. energy consumption (Wh)
2	74	43.6	325.2	94.0
4	94	41.7	206.9	43.9
Change	+27.0%	-4.2%	-36.4%	-53.3%

(b) Impact of path planning versus trajectory planning

Case	Convergence (%)	Avg. computation time (s)	Avg. flight time (s)	Avg. energy consumption (Wh)
3	83	44.4	185.2	114.8
4	94	41.7	206.9	43.9
Change	+13.3%	-6.0%	+11.7%	-61.8%

(c) Impact of fixed versus variable WVF

seed direction in the example is approximately along the vector [-0.707, 0.707, 0] with a magnitude of 3.25m/s. A comparison of the summarized results from the 100 trials is shown in Table 4.4.

4.8. Discussion

There are several meaningful conclusions that can be drawn from the differential results of the cases described in section 4.5.

Comparison #1: Impact of nodal resolution

The first comparison shown in Table 4.5a, illustrates the impact of using a low resolution grid (2km x 2km x 1km) versus high resolution (50m x 50m x 10m) grid for trajectory planning. The high resolution trajectory planner converged to a

valid solution 94/100 times while the low resolution version only converged 57/100 times. The convergence rate for the shortest straight line case is understandably low since the vehicle has limited on-board power and the number of passable nodes are limited. Clearly, linearly interpolating coarse grid data can create potential issues for flight paths for small UAVs. Furthermore, the energy computation for the low resolution case for the trajectories that did converge was over 4 times higher than the high resolution version. Since the shortest straight line trajectory is used between the start and end nodes, the path planner cannot adapt or optimize its trajectory for local wind fields and thus must waste energy to overcome them. There is a significant decrease in computational time for the shortest straight line case which is caused by many of the potential trajectory options being naturally eliminated when optimizing for the shortest distance instead of minimum time and/or energy. However, the computational time for both cases is still only a fraction of the predicted flight time. It should also be emphasized that refining the grid resolution for any trajectory planner is not a trivial operation. Many search algorithms are too computationally expensive at such high resolutions. Also, some model assumptions such as negligible reorientation between nodes, begin to lose validity.

Comparison #2: Impact of path planning versus trajectory planning

The second comparison shown in Table 4.5b, illustrates the impact of using a constant vehicle velocity versus a planned variable velocity. The paths generated by ignoring the optimization of velocity were generally spatially similar to the complete trajectory planner. The constant velocity planner converged 20 less times due to the inability to overcome stronger lateral and head winds. Excluding velocity in the path planning process also excludes the option of planning the time the UAV will be in a given wind field. To fully optimize energy consumption, it is desirable to remain in tail winds for a longer period of time (by reducing airspeed) and passing through strong lateral and head winds quickly. A case study was conducted to highlight the function selecting vehicle velocity to minimize the energy consumption defined in equation 4.11. Consider the vehicle flying horizontally over a straight line distance of 100m, with varying amounts of parallel and perpendicular wind components, $-10\frac{m}{s} \leq v_{vw,||} \leq 5\frac{m}{s}$ and $v_{vw,\perp} = \ 0, \ \ 3, \ \ 6\frac{m}{s}$, respectively. If these wind components are known, the vehicle velocity, v_v, can be chosen to minimize energy which is shown by the white line on each surface in Figure 4.10. Clearly, since the line in each graph is not linear, the desired vehicle velocity for minimal energy consumption is not constant and should be included in

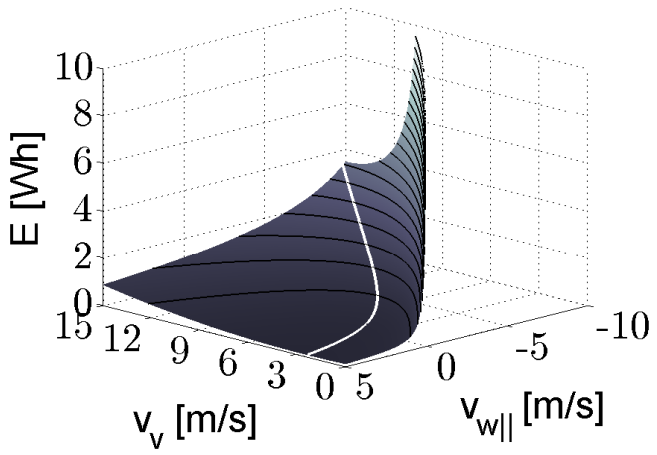

(a) $v_{vw,\perp} = 0\frac{m}{s}$

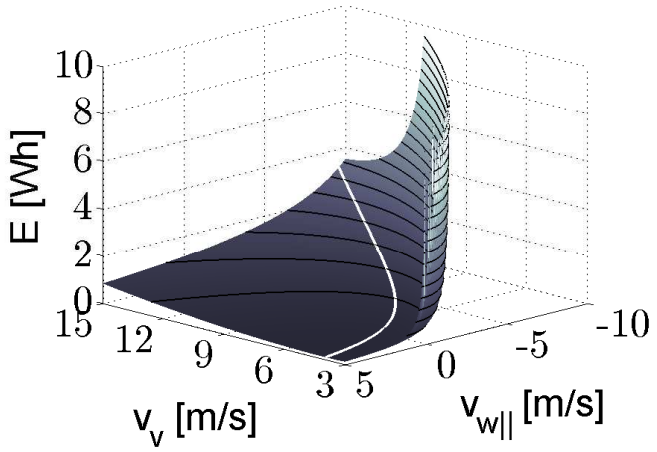

(b) $v_{vw,\perp} = 3\frac{m}{s}$

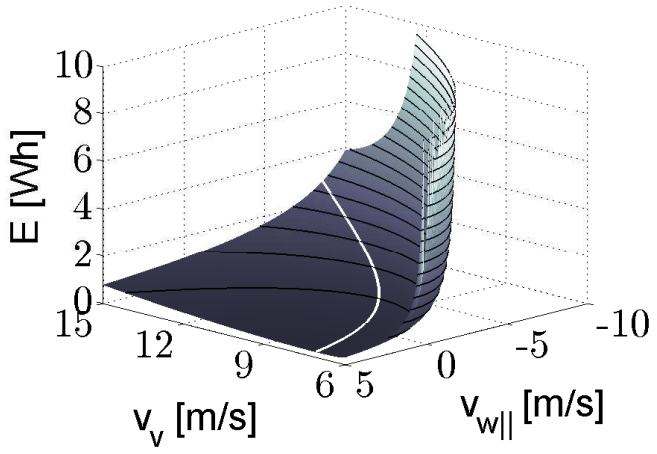

(c) $v_{vw,\perp} = 6\frac{m}{s}$

Figure 4.10.: Energy map for various lateral wind speeds

the planning process. Also notice that the optimal vehicle velocity never reaches $0\frac{m}{s}$ even in the presence of a pure tail wind because there is a non-negligible constant energy being consumed by the on-board electronics (camera, computer, telemetry, etc.).

Comparison #3: Impact of fixed versus variable WVF

The third comparison shown in Table 4.5c, illustrates the impact of the planner incorporating a fixed WVF or a spatially variable WVF into the planning process. The trajectories generated from the fixed WVF case were similar to the low resolution case, and they tended to take the shortest straight line to the goal node. Since the WVF was assumed to be uniform, the UAV would climb into higher magnitude wind speeds with considerable cost to energy consumption (2.6 times increase). The uniform WVF case converged less often due to the lack of awareness and planning for stronger head winds. When the trajectories did converge, they tended to be slightly faster (21.7s) than the complete planner version. However, noting the standard deviation in flight times for cases 3 and 4 to be 135s and 74s, respectively, the fixed WVF case arrives less predictably.

Additional comments

In addition to the comparisons between each case and the complete planner, several other general comments that can be made about the design of the trajectory planner. The energy consumed by trajectories generated by the complete trajectory planner using a variable trajectory and variable WVF data (case 4) was found to be at least 50% lower on average than any other case over all scenarios simulated. Figure 4.11 shows the average energy consumed for each case with a 95% confidence interval. The improvement in performance between the purposed planner and the other cases considering only 2 of the 3 key factors is greater than the error in performance caused by the random gust wind component. Therefore, the inclusion of all three key factors to UAV trajectory planning can be considered a significant improvement.

Furthermore, the proposed trajectory planner has a consistently higher convergence rate than any other case considering only 2 of the 3 key factors. The limited flight speed for small scale UAVs ($12\frac{m}{s}$ for this airship prototype) impose severe path restrictions and even impassible regions in upper altitude flight where wind magnitudes can be higher. The inability to adapt the path or vehicle velocity to avoid these conditions has been shown to reduce the feasibility of the trajectories that are produced.

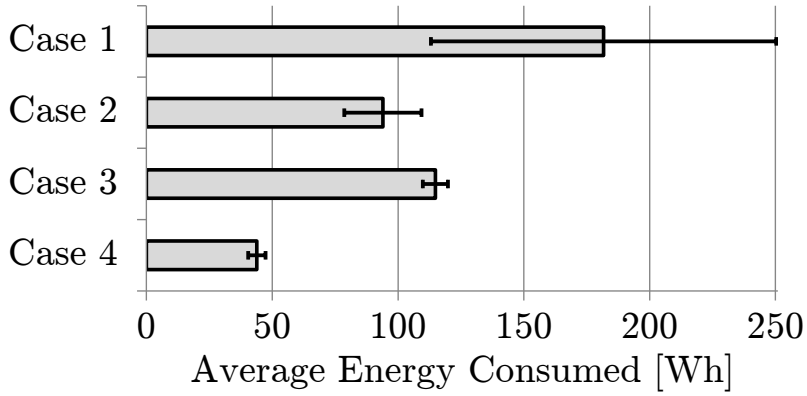

Figure 4.11.: Comparison of the average energy consumed per trial for each test case

The maximum computational time for the complete planner was 78 seconds. It is worth noting that the WVFs were loaded from a calculated *a priori* database in this work, so to include variable WVFs data using CFD computations in the physical UAV, there would be an increase in computational time. However, it was observed that the WVFs for these trials were calculated in 60 seconds, on average, and never more than 90 seconds using WindStation version 4.0.1[1]. The resulting total computational time to calculate the CFD WVF plus the trajectory over the 2km x 2km x 1km control volume would still be only a fraction of the predicted flight time to traverse the trajectory. Since the trajectories can be planned faster than they can be followed, it is reasonable to assume this trajectory planner could be used online. Depending on the desired resolution and on-board processing capabilities, it is foreseeable to include variable WVF generation into the replanning process thus incorporating time-varying flow fields. CFD generated WVF data could also be fused with national weather service predictions (when available) for added certainty.

The UAV attempts to arrive to the goal node before the goal time by adjusting both the path in (4.4) and adjusting the vehicle speed in (4.5). This redundancy leads to a conservative trajectory planning approach. Based on the one-to-one weight ratio of time and energy, the trajectory planner's ability to arrive at the goal node on time for cases 1 through 4 was 53.2%, 53.2%, 87.2%, and 91.5%, respectively. In addition, Case 4 arrived 32.5% earlier than expected, on average. If the weight for time is reduced, the arrival time will follow the goal time more closely. The average additional time due to reorientation of the UAV was roughly 1.5% per trial for all scenarios that converged. Therefore, the idealized

[1]The simulation was performed in Matlab R2010B using an Intel Core 2 Duo 2.80 GHz CPU with 4 GB of RAM.

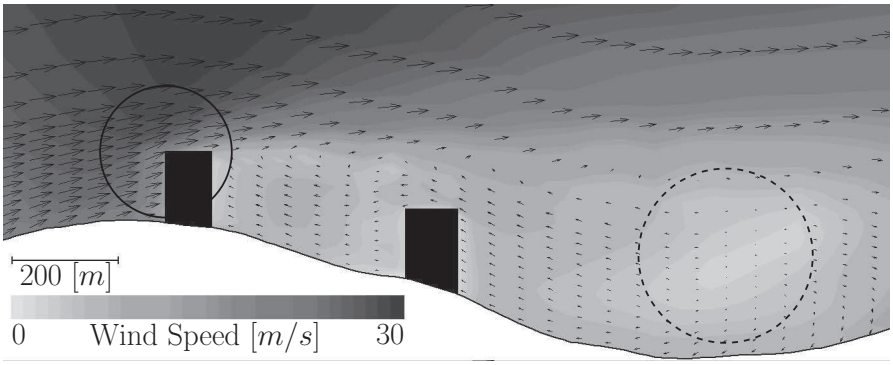

(a) Wind speed plot

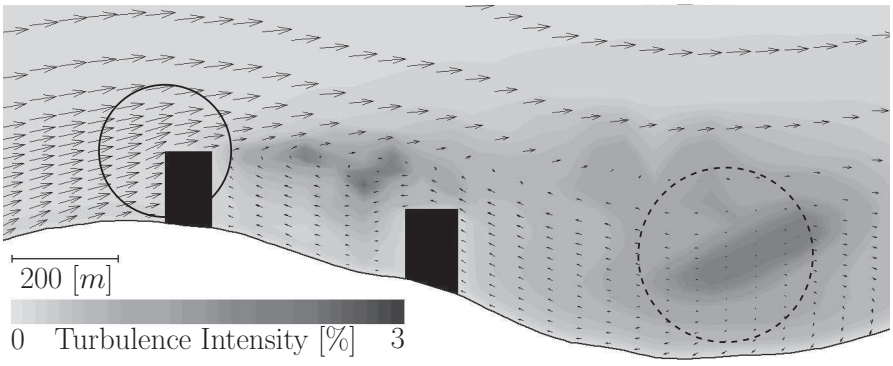

(b) Turbulence intensity plot

Figure 4.12.: Wind speed and turbulence intensity around mountain ridge and city blocks

reorientation of Figure 4.5 is relevant to this UAV platform.

The trajectory planner uses wind speed and direction to optimize the vehicle velocity and path. As an example, this means penalizing the area circled in a solid line and rewarding to the area circled in a dashed line in Figure 4.12a. Turbulence flows persist long into the wake of the disturbance and, although the intensity is a low percentage, it may have a detrimental effect on the flight performance. The software generated WVFs also produces the turbulence intensity fields, shown in Figure 4.12b, which could readily be incorporated into the objectives in the cost function. However, experimental flight data is required to fully realize the impact of turbulence intensity on flight performance and to properly utilize the turbulence data for trajectory planning.

Although this trajectory planner is developed based on an airship UAV, it could be extended to cover a variety of different platforms by redeveloping the energy consumption model from Section 4.4.2 and modifying the differential constraints in Section 4.5.

4.9. Chapter Summary

In this chapter, a wavefront expansion trajectory planner is proposed for a dirigible UAV incorporating a novel multi-objective function to be applied in large, highly realistic, 3D environments with variable WVFs. The proposed trajectory planner is simulated over a variety of flight conditions and multiple test environments. Recommendations are made to implement the trajectory planner on the physical platform. The inclusion of CFD generated, three dimensional, variable WVF data yielded significant improvements in trajectory feasibility and minimum energy consumption when compared to using uniform WVF information.

Although (4.11) encompasses many of the factors contributing to the energy consumption, it is still not complete. The aerodynamic drag on the vehicle is not constant for all flight conditions. Also, various degrees of stabilization are often required to maintain a UAV on a given trajectory which are not accounted for in this equation. Errors due to this stabilization effort will increase when trajectory aggressiveness increases (i.e. small t_g). Applying a trajectory following controller with the complete non-linear dynamic model will help validate the realism of the generated trajectories and will provide a more accurate prediction of the travel time and energy consumed.

5. Dynamic Modelling and Flight Control

This chapter details the development and simulation of the airship dynamics and trajectory following control. The unmanned airship mechanistic non-linear dynamic model is derived use the Newton-Euler method to evaluate two different types of trajectory following controllers. The control effort and tracking error results from the controllers are then used to validate both the feasibility and fuel economy of the trajectories generated by the planning algorithm described in Chapter 4. This work is also a necessary step towards realizing the autonomous hybrid airship platform since each controller is platform specific.

The chapter is organized as follows; first a literature review on airship dynamic models and trajectory tracking controllers is presented in section 5.1. Then, the development of the dynamic model is presented with relevant changes to the conventional model in section 5.2 and the control theory for both PID and backstepping control are developed with considerations made for actuator saturation and error coupling in section 5.3. Finally, the controllers are simulated and the results are discussed in section 5.6.

5.1. Literature Review

The literature review for this chapter is divided into two parts: Airship dynamic models and autonomous low-level flight control strategies.

5.1.1. Airship dynamic models

Gomes presented the first known non-linear dynamic model for an airship derived based on a Newton-Euler approach which has become an essential starting point for other future research [90]. A common practice is to decouple this model into longitudinal and lateral motion and linearize it about a trimmed flight condition. An analysis of the small perturbations of these equations of motions was constructed by Cook [91] and was used to determine the six visible stability modes common of modern airship flight [19, 92]. Based on step inputs of each control

action, the magnitude of the responses were small and the settling time was in the order of a minute. The sluggish response suggests the control actions are underpowered [19]. However, the airship is quite stable in both longitudinal and lateral directions due to its natural pendulum stabilizing moments and large virtual mass and inertia. Although the linearized model can predict how the airship will behave in steady state conditions at trimmed flight velocities it is not valid for all flight regimes. Therefore, only the complete non-linear equations of motion will be considered here.

As an alternative to the Newton-Euler approach, some literature also derives the system dynamics based on a Euler-Lagrangian approach [93–95]. This approach is based on combining kinetic and potential energy terms into the equation of conservation of momentum. However, both approaches consist of summing the forces applied to the vehicle.

There is a significant amount of literature that investigate modelling assumptions and present improvements to address shortcomings. One of these shortcomings is the requirement of experimental wind tunnel testing for each airship type to determine aerodynamic coefficients which can be lengthy and expensive. There has been several attempts to overcome this issue. Separate works from Mueller *et al.* and Ashraf *et al.* presented alternative methods to system identification using geometric data that can be used to model all airship types and sizes [96,97]. Yongmei *et al.* avoided the need for experimental wind tunnel tests by applying an adaptive control law to correct for any discrepancies in airship parameter values [98].

Mass compensation is frequently neglected in small-scale airships, however, the required mass of fuel for long endurance flights is a large fraction of the airship's overall mass (up to 25% for the airship prototype). Waishel *et al.* have simulated that time-varying mass can have a significant impact on system behaviour and control requirements and that a constant mass assumption is insufficient without mass compensation system [99].

In Gomes' model, air ballasts (also referred to as ballonets) are assumed to be set for the desired altitude and held constant [90]. In reality, ballonets can vary the mass of the airship and their motion relative to the hull, known as sloshing, can contribute to the airship dynamics [100,101]. Cai *et al.* presented a dynamic model for ballonets derived by Newton-Euler laws and Kirchhoff's equations [101]. The model also considers coupling between the ballasts and the airship body. However, steps to implement the model into a controller are not considered. Wu *et al.* presented an LQR linear feedback controller to propel a high altitude airship through buoyancy forces alone [102]. The unconventional model uses two ballonets and control is performed through a moving internal ballast (no thrusters).

Another consideration that has been studied but is not included here is the concept of structural flexibility. As an airship's hull is considered to be non-rigid, it will deform due to aerodynamic forces which will affect the dynamics. Bessert *et al.* presented a method to compensate lift coefficients for different types of common deformations [103]. Lateral bending forces caused by the vertical tail fins were observed to be the main source of deformation. Bennaceur *et al.* presented a model that allows for aeroelastic deformations that is based on the Euler-Lagrange approach [104]. The work also computed the differences in the added (virtual) mass terms for rigid-body and flexible airships. The authors concluded that the impact of flexibility in the dynamic model should not be neglected.

Along the same lines, the computation of the virtual mass and inertia has been approached from different directions. When any object accelerates through a fluid, the displaced fluid adds to the object's effective mass and inertia. These virtual mass and inertia terms are typically neglected for heavier than air aircraft. However, for a neutrally buoyant airship, virtual mass and inertia terms can be as large as the airship's own mass and inertia [105]. In Gomes' model, these terms are scaled based on empirical wind tunnel data [90]. Atkinson *et al.* presented an alternative to attaching virtual mass and inertia terms by allowing additional degrees of freedom to the displaced air through added acceleration coefficients [106]. Wang *et al.* presented a numerical method to calculate them based on CFD analysis which is compared to the theoretical Hess-Smith panel method [107].

Li *et al.* presented a detailed and comprehensive literature review of these considerations including experimental studies, analytical models and computational fluid dynamics (CFD) methods [100].

5.1.2. Trajectory tracking controllers

The basic definition of autonomy is to have the ability to self govern. In UAVs and other robotic devices, autonomy can be subdivided into levels from zero (remote control) to ten (full autonomy) based on mission complexity, environmental difficulty and robot human interaction [108]. More generally, autonomy can be categorized into three levels: organization, coordination and execution [109]. The organization level involves swarm coordination and high level learning capabilities, and is outside the scope of this research. The coordination level, as described in the previous chapter, provides the UAV with the ability to combine sensor inputs for improved accuracy, plan and re-plan trajectories in 3D and has some ability to deal with uncertainties that arise. The execution level provides a UAV with the minimum requirements to manipulate all of its actuators and follow a given trajectory within an acceptable error. The execution level (also known as autopilots) is a

heavily researched field in UAVs including airships. There exist numerous control methods that have been applied to the airship trajectory tracking problem such as PID [96, 110–112], gain scheduling [94, 113, 114], dynamic inversion [115, 116], backstepping [117–124], model predictive [125], sliding mode [126, 127] and reinforcement learning control [128]. Both Liu *et al.* and Potdaar *et al.* presented detailed summaries and explanations of the low level control methods used for autonomous airships [129, 130]. Assuming that the trajectories generated by the planner are both feasible and near optimal, higher levels of advanced control (such as adaptive or reinforcement learning control methods) may not be necessary for trajectory tracking and are not investigated here. Two methods that are commonly chosen for trajectory tracking are PID and backstepping.

PID is the traditional control strategy which can be easily implemented and is considered here as a minimum standard. Since it is a linear and symmetric feedback system, it is expected to have difficulty with the highly non-linear dynamic system. Mueller *et al.* presented a set of separate PID controllers to independently stabilize each trajectory tracking error of an airship [96]. The controllers were simulated with various step inputs and shown to be stable for a range of vehicle speeds in a wind free environment. Elfes *et al.* presented experimental PI execution level controls for altitude, pitch and yaw of an airship used for planetary exploration [111]. The tracking performance was satisfactory, however, the authors admit that the control type was chosen because of it's quick implementation to gain autonomous field test experience and that more robust and precise controllers were being investigated.

Backstepping, on the other hand, uses Control Lypanov Functions (CLF) which are based on the dynamic model inversion and has been proven to offer robustness in the presence of parametric uncertainties [120]. Backstepping has also been proven to solve under actuated systems and can provide asymptotically stable solution to airship path tracking [118, 119, 123, 131].

Hygounenc *et al.* presented backstepping-based subcontrollers for each airship flight regime (takeoff, trimmed flight, landing) [121]. The model relies on the decoupling of longitudinal and lateral motion and is linearized during trimmed flight conditions. Simulations show the airship transition between flight regimes in a wind free environment.

Kahale *et al.* presented a Lyapunov function based controller for path tracking of an airship in the presence of unknown wind gusts [117]. Although the performance results prove to be stable, it is only kinematically modelled and is missing several physical constraints such as actuator saturation.

A recent paper presented by Liesk *et al.* uses a combined backstepping/Lyapunov method to control a fin-less airship and is validated with experimental testing [122].

Separate controllers were developed for three of the vehicle's degrees of freedom. Unfortunately, the control law is developed for a unconventional actuator orientation (4 vertical thrusters) and is not easily comparable to conventional airships.

The closest related work is by Azinheira *et al.*, who presented a backstepping controller for realistic path tracking of an underactuated airship [123]. The controller tracks trajectories in 3D and accounts for wind (constant and gust), actuator saturation and underactuation constraints. The trajectories included portions of several flight regimes such as hovering, ascent and trimmed flight. However, their airship model consists of conventional airship actuators (thrust vectoring and aerodynamic control surfaces) with no mass compensation or quantitative assessment of energy consumption needed for long endurance.

5.2. Airship Dynamic Model Development

In order to apply trajectory tracking control strategies, a complete dynamic mechanistic model of the airship is needed based on the physical characteristics of the prototype platform as well as empirical coefficients derived from similar airship designs. The model presented by Gomes is still commonly used today. Not found in the work of Gomes is the concept of modeling and parametric uncertainty which are important to ensure controller robustness considering some aspects of the model are scaled from empirical relationships. The second modification to the Gomes model is the adaptation to the input state matrix and control vectors to suit the unique configuration of the UAV prototype. This section also develops modifications to include rotational aerodynamic dampening to further improve the reliability and theoretical accuracy of the model at low flight speeds.

The model's reference system is shown in Figure 5.1 and its equation of motion is defined as,

$$\mathbf{M}\ddot{\mathbf{x}}_\mathbf{v} + \mathbf{D}(\dot{\mathbf{x}}_\mathbf{v}) = \mathbf{A}(\dot{\mathbf{x}}_\mathbf{v}) + \mathbf{G}(\mathbf{T}) + \mathbf{E} + \mathbf{U} \tag{5.1}$$

Where,

- **M** is the 6x6 mass matrix
- **D** is the 6x1 dynamics vector
- **A** is the 6x1 aerodynamic vector
- **G** is the 6x1 gravitational and buoyancy vector
- **E** is the 6x1 model uncertainty vector

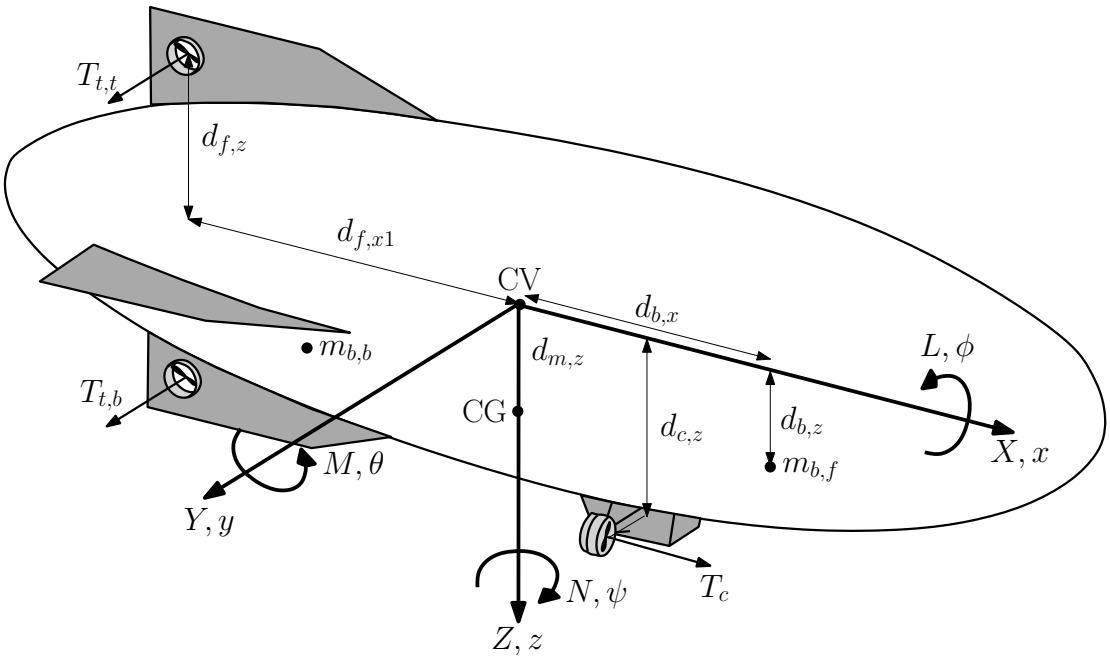

Figure 5.1.: Body axis convention. Adapted from [90]

- $\mathbf{U}$ is the 6x1 input force vector
- $\mathbf{x_v}$ is the 6x1 state vector
- $\mathbf{R_1}$ is the 3x3 rotation matrix

The vehicle has 6 DOF, three linear and three angular, which are defined in the vehicle (body) frame. The state convention is written as

Positions: $\mathbf{x} = \begin{bmatrix} x & y & z & \phi & \theta & \psi \end{bmatrix}^T$, where x, y, and z are Cartesian coordinates and ϕ, θ, and ψ are Euler angles corresponding to roll, pitch and yaw, respectively.

Velocities: $\dot{\mathbf{x}} = \begin{bmatrix} \nu & | & \omega \end{bmatrix}^T = \begin{bmatrix} \dot{x} & \dot{y} & \dot{z} & \dot{\phi} & \dot{\theta} & \dot{\psi} \end{bmatrix}^T$, where the components of $\dot{\mathbf{x}}$ are the rates of change of the previous vector.

Reference frames: Both the position and the velocity vectors can be defined in either the earth or vehicle reference frames which have the subscripts g and v, respectively. In some instances, the repetitive vehicle frame subscripts have been removed for clarity.

Forces and moments: $\mathbf{F} = \begin{bmatrix} X & Y & Z & L & M & N \end{bmatrix}^T$, where X, Y, and Z are forces along x, y, and z and L, M, and N are roll, pitch and yaw moments, respectively.

The complete nomenclature for the remainder of this chapter can be found in Appendix C.

5.2.1. Inertia matrix

After applying simplifications due to vehicle symmetry, the mass matrix is given by,

$$\mathbf{M} = \begin{bmatrix} \mathbf{M_a} & -m\mathbf{d_{CG}^T} \\ m\mathbf{d_{CG}} & \mathbf{J_a} \end{bmatrix} = \begin{bmatrix} m_x & 0 & 0 & 0 & md_{m,z} & 0 \\ 0 & m_y & 0 & -md_{m,z} & 0 & md_{m,x} \\ 0 & 0 & m_z & 0 & -md_{m,x} & 0 \\ 0 & -md_{m,z} & 0 & J_x & 0 & -J_{xz} \\ md_{m,z} & 0 & -md_{m,x} & 0 & J_y & 0 \\ 0 & md_{m,x} & 0 & -J_{xz} & 0 & J_z \end{bmatrix} \tag{5.2}$$

where $\mathbf{d_{CG}}$, is a skew symmetric matrix containing distances between the CV and CM,

$$\mathbf{d_{CG}} = \begin{bmatrix} 0 & -d_{m,z} & 0 \\ d_{m,z} & 0 & -d_{m,x} \\ 0 & d_{m,x} & 0 \end{bmatrix} \tag{5.3}$$

and $\mathbf{M_a}$ and $\mathbf{J_a}$ are the added mass and added inertia matrices with terms,

$$m_x = (1 + k_1)\, m \tag{5.4}$$

$$m_y = m_z = (1 + k_2)\, m \tag{5.5}$$

$$J_x = I_x\,(1 + \sigma_1) \tag{5.6}$$

$$J_y = I_y\,(1 + k')\,(1 + \sigma_1) \tag{5.7}$$

$$J_z = I_z\,(1 + k')\,(1 + \sigma_1) \tag{5.8}$$

$$J_{xz} = I_{xz}\,(1 + \sigma_1) \tag{5.9}$$

The masses and inertias in the mass matrix are found based on the dimensions of the airship in the computer-aided drafting program SolidWorks, while virtual masses terms k_1, k_2, and k' above are approximated using the works of Lamb [105] and Munk [132]. The moments of inertia and product of inertia are known to have considerable error [98]. The uniformly distributed random percentage, σ_1, was added to model this parametric uncertainty which has a bilateral symmetry threshold of 30%. All other terms, such as off diagonal virtual terms, are typically assumed to be negligible and have been removed for clarity. Table 5.1 shows a summary of the physical characteristics of the airship platform.

Table 5.1.: Airship prototype characteristics

Symbol	Description	Value	Units
m	Airship mass	14.68	kg
V	Airship volume	12	m^3
$l_{v,z}$	Airship diameter	1.868	m
$l_{v,x}$	Airship length	6.541	m
$d_{m,z}$	Distance between CM and CV along Z	0.540	m
$d_{m,x}$	Distance between CM and CV along X	0	m
$d_{b,z}$	Distance between the ballonets and CV along Z	2.000	m
$d_{b,x}$	Distance between the ballonets and CV along X	0.500	m
I_x	Moment of inertia about OX	9.65	m^2kg
I_y	Moment of inertia about OY	142.76	m^2kg
I_z	Moment of inertia about OZ	147.59	m^2kg
I_{xz}	Product of inertia about OY	-3.94	m^2kg
k_1	Lamb's inertia ratio along OX	0.1069	-
k_2	Lamb's inertia ratio along OY or OZ	0.8239	-
k'	Lamb's inertia ratio about OY or OZ	0.5155	-

5.2.2. Dynamics vector

The vehicle dynamics vector is given by,

$$\mathbf{D} = \begin{bmatrix} D_X & D_Y & D_Z & D_L & D_M & D_N \end{bmatrix}^T = \begin{bmatrix} \omega \times \mathbf{M_a}\nu - m\omega \times (\omega \times \mathbf{r_{CG}}) \\ (\omega \times \mathbf{J_a}\omega) + m\mathbf{r_{CG}} \times (\omega \times \nu) \end{bmatrix} \tag{5.10}$$

where the axis convention is defined in Figure 5.1. The forces and moments in equation (5.10) are derived based on Newton's laws for rigid body motion about the CV in the body frame. These equations consist of both centrifugal ($\omega \times \mathbf{M_a}\nu_{\mathbf{CG}}$) and Coriolis ($\omega \times \mathbf{J_a}\omega$) components which are a function of the linear and angular velocities of the vehicle, $\nu = \begin{bmatrix} \dot{x} & \dot{y} & \dot{z} \end{bmatrix}^T$ and $\omega = \begin{bmatrix} \dot{\phi} & \dot{\theta} & \dot{\psi} \end{bmatrix}^T$, respectively. Since the centre of rotation is considered to be offset from the centre of mass, the velocity used for these components be modified according to $\nu = \nu_{\mathbf{CG}} + \omega \times \mathbf{r_{CG}}$ where $\mathbf{r_{CG}} = \begin{bmatrix} d_{m,x} & 0 & d_{m,z} \end{bmatrix}^T$. Written in component form, the dynamics vector becomes,

$$D_X = m_z\dot{z}\dot{\theta} - m_y\dot{\psi}\dot{y} + m\left(d_{m,x}\left[\dot{\theta}^2 + \dot{\psi}^2\right] - d_{m,z}\dot{\psi}\dot{\phi}\right) \tag{5.11}$$

$$D_Y = m_x\dot{x}\dot{\psi} - m_z\dot{\phi}\dot{z} - m\left(d_{m,x}\dot{\phi}\dot{\theta} + d_{m,z}\dot{\psi}\dot{\theta}\right) \tag{5.12}$$

$$D_Z = m_y\dot{y}\dot{\phi} - m_x\dot{\theta}\dot{x} + m\left(d_{m,z}\left[\dot{\theta}^2 + \dot{\phi}^2\right] - d_{m,x}\dot{\psi}\dot{\phi}\right) \tag{5.13}$$

$$D_L = (J_z - J_y)\,\dot{\psi}\dot{\theta} - J_{xz}\dot{\phi}\dot{\theta} + md_{m,z}\left(\dot{\phi}\dot{z} - \dot{x}\dot{\psi}\right) \tag{5.14}$$

$$D_M = (J_x - J_z)\,\dot{\phi}\dot{\psi} + J_{xz}\left(\dot{\phi}^2 - \dot{\psi}^2\right) + m\left(d_{m,z}\left[\dot{z}\dot{\theta} - \dot{\psi}\dot{y}\right] + d_{m,x}\left[\dot{\theta}\dot{x} - \dot{y}\dot{\phi}\right]\right) \tag{5.15}$$

$$D_N = (J_y - J_x)\,\dot{\theta}\dot{\phi} + J_{xz}\dot{\theta}\dot{\psi} + md_{m,x}\left(\dot{x}\dot{\psi} - \dot{\phi}\dot{z}\right) \tag{5.16}$$

5.2.3. Aerodynamics vector

The aerodynamics vector acts to dampen linear and rotational rates of change in the vehicle. The coefficients within the aerodynamic terms are determined through wind tunnel testing that result in figures of non-dimensional and steady-state, lift, drag, and rotational stability derivative coefficients. As mentioned previously, one of the shortcomings of the model is the requirement of experimental wind tunnel testing for each airship type which can be lengthy and expensive. The vector presented here is an adaptation of the work of Mueller *et al.* who presented an alternative method to system identification using airship geometry [96].

One interesting note is that many non-linear equations of motion presented in literature use aerodynamic models that are linear combination of terms containing angle of attack α, angle of sideslip, β, and control surface deflections (if applicable), all of which are multiplied by the square of the trimmed vehicle velocity, v_o [19, 84, 90, 96, 97]. This assumes that rotational rates only effect the aerodynamic forces indirectly through induced angles of attack or sideslip. These models can be adequate for medium to high speed flight with light (or no) disturbances. A major flaw with this approach is that aerodynamic dampening is reduced asymptotically with relative vehicle speed. Gomes was one of the first to present rotational pitch and yaw damping terms to the model [90]. Unfortunately, the terms are also a product of the forward airspeed and have no effect at hover. The work also ignores roll dampening. Ashraf *et al.* presented a model with rotational dampening terms but incorrectly formulated the moments by multiplying by the dynamic pressure twice resulting in them being overly conservative [97]. The model also neglects hulls effects which are on the same order of magnitude as the fins.

This research incorporates the aerodynamic model derived based on the work of both Jones and Mueller [84, 96] with additional rotational dampening added. The aerodynamic vector is given by,

$$\mathbf{A} = \begin{bmatrix} A_X & A_Y & A_Z & A_L & A_M & A_N \end{bmatrix}^T \tag{5.17}$$

where the axis convention is defined in Figure 5.1. Each term is defined as,

$$A_X = \hat{P}\left[C_{X1}\cos^2\alpha\cos^2\beta + C_{X2}\sin(2\alpha)\sin\left(\frac{\alpha}{2}\right)\right] \tag{5.18}$$

$$A_Y = \hat{P}\left[C_{Y1}\cos\left(\frac{\beta}{2}\right)\cos(2\beta) + C_{Y2}\sin(2\beta) + C_{Y3}\sin\beta\sin|\beta|\right] \tag{5.19}$$

$$A_Z = \hat{P}\left[C_{Z1}\cos\left(\frac{\alpha}{2}\right)\cos(2\alpha) + C_{Z2}\sin(2\alpha) + C_{Z3}\sin\alpha\sin|\alpha|\right] \tag{5.20}$$

$$A_L = \hat{P}\Big[C_{L1}\sin\beta\sin|\beta|\Big] + \frac{1}{2}\rho_a C_{L2}\dot{\phi}\left|\dot{\phi}\right| \tag{5.21}$$

$$A_M = \hat{P}\left[C_{M1}\cos\left(\frac{\alpha}{2}\right)\sin(2\alpha) + C_{M2}\sin(2\alpha) + C_{M3}\sin\alpha\sin|\alpha|\right] + \frac{1}{2}\rho_a C_{M4}\dot{\theta}\left|\dot{\theta}\right| \tag{5.22}$$

$$A_N = \hat{P}\left[C_{N1}\cos\left(\frac{\beta}{2}\right)\sin(2\beta) + C_{N2}\sin(2\beta) + C_{N3}\sin\beta\sin|\beta|\right] + \frac{1}{2}\rho_a C_{N4}\dot{\psi}\left|\dot{\psi}\right| \tag{5.23}$$

where the steady state dynamic pressure is defined as $\hat{P} = \frac{1}{2}\rho_a \upsilon_0^2$ and the angles of attack and side slip relative to the air are defined as $\alpha = \arctan\left(\frac{\dot{z}}{\dot{x}}\right)$ and$\beta = \arcsin\left(\frac{\dot{y}}{\sqrt{\dot{x}^2+\dot{y}^2+\dot{z}^2}}\right)$, respectively. The factors relating aerodynamic forces due to control surface deflections are removed from the conventional model.

The last term on each aerodynamic moment are the added rotational dampening that are proportional to the angular rates squared. The magnitude of these three terms is driven from the dynamic pressure which negligible at trim flight speeds but become the primary aerodynamic dampening moments at low speed flight nearing hover. The coefficients of drag are,

$$C_{X1} = -\left[C_{Dho}S_h + C_{Dfo}S_f + C_{Dgo}S_g\right] \tag{5.24}$$

$$C_{X2} = C_{Y1} = C_{Z1} = (k_2 - k_1)\,\eta_k I_1 S_h \tag{5.25}$$

$$C_{Y2} = C_{Z2} = -\frac{1}{2}\left(\frac{\delta C_L}{\delta\alpha}\right)_f S_f \eta_f \tag{5.26}$$

$$C_{Y3} = -\left[C_{Dch}J_1 S_h + C_{Dcf}S_f + C_{Dcg}S_g\right] \tag{5.27}$$

$$C_{Z3} = -\left[C_{Dch}J_1 S_h + C_{Dcf}S_f\right] \tag{5.28}$$

$$C_{L1} = C_{Dcg} S_g d_{c,z} \tag{5.29}$$

$$C_{L2} = -2 C_{Dcf} S_f d_{f,z}^3 \tag{5.30}$$

$$C_{M1} = -C_{N1} = -\left(k_2 - k_1\right) \eta_k I_3 S_h l_{v,x} \tag{5.31}$$

$$C_{M2} = -C_{N2} = -\frac{1}{2} \left(\frac{\delta C_L}{\delta \alpha} \right)_f S_f \eta_f d_{f,x1} \tag{5.32}$$

$$C_{M3} = -C_{N3} = -\left[C_{Dch} J_2 S_h l_{v,x} + C_{Dcf} S_f d_{f,x2} \right] \tag{5.33}$$

$$C_{M4} = C_{N4} = -\left[C_{Dcf} S_f d_{f,x2}^3 + \frac{l_{v,z} l_{v,x}^4}{240} \right] \tag{5.34}$$

Much of the notation for this set of equations is only used locally so it is not included in the nomenclature found in the appendix. Please refer to Table 5.2 for variable definitions.

The coefficients C_{L2}, C_{M4}, and C_{N4} are new additions to the conventional airship model that are derived based on conventional external incompressible viscous flow theory [37]. An example of the derivation is provided here for the pitch direction (the fourth term of (5.22)). The aerodynamic (drag) moment due to a rotational rate about the z-axis is defined as the integral over the length of the airship of the linear drag force of both the fins and hull.

$$A_{M4} = -\int_{-l_{v,x}/2}^{l_{v,x}/2} \left[F_{D,f} + F_{D,h} \right] d\tau \tag{5.35}$$

The effects of the gondola are ignored here since the gondola has a low projected area. The familiar equation for linear drag force can be inserted for both fins and hull. The equivalent linear velocity at any one point along the length of the airship is assumed to be equal to the rotational rate times the distance between that point and the CV.

$$A_{M4} = -2 \int_0^{l_{v,x}/2} \left[\frac{1}{2} C_{Dcf} S_f \rho_a \left(\tau \dot{\theta} \right)^2 + \frac{1}{2} C_{Dh} S_h \rho_a \left(\tau \dot{\theta} \right)^2 \right] d\tau \tag{5.36}$$

Rotation is assumed to be about the CV of the envelope and the length of the airship in front and behind the CV is assumed to be equal to $\frac{l_{v,x}}{2}$. Factoring out the dynamic pressure exposes the equivalent coefficient of drag for the drag moment,

$$A_{M4} = \frac{1}{2} \rho_a \dot{\theta} \left| \dot{\theta} \right| \left[-2 \int_0^{l_{v,x}/2} \left(C_{Dcf} S_f \tau^2 + C_{Dh} S_h \tau^2 \right) d\tau \right] \tag{5.37}$$

The two terms within the integral correspond to the drag moment caused by the fins and hull, respectively. Since the fins only exist in a short segment of the

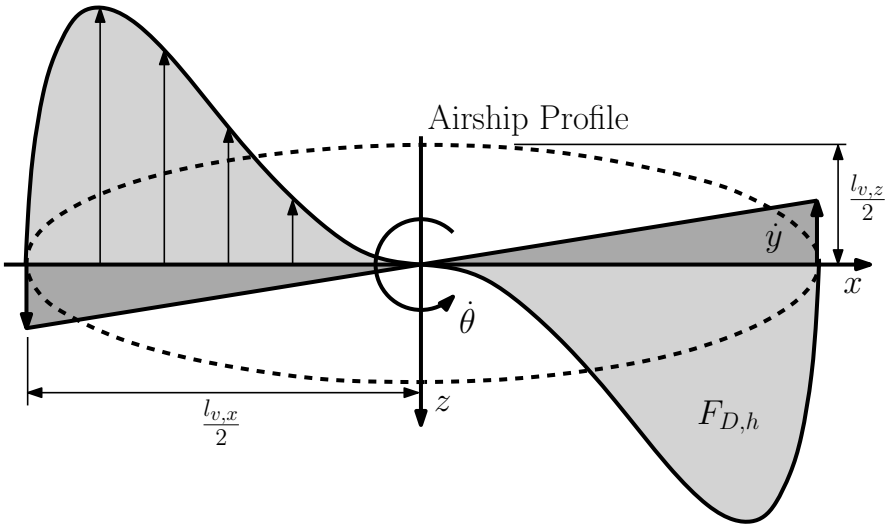

Figure 5.2.: Aerodynamic drag force profile on the bare airship hull, $F_{D,h}$, produced from a pitch rate, $\dot{\theta}$

airship length, the integral of force over the length can be approximated by a point force at the aerodynamic centre of the fins, $d_{f,x2}$. The coefficient of drag for cross-flow over the fins, C_{Dcf}, is already known.

The drag moment on the hull is more difficult to evaluate since the projected half hull area, S_h, is a function of airship length according to the,

$$S_h = 2\int \sqrt{\frac{l_{v,z}^2}{4} - \left(\frac{l_{v,z}^2\tau^2}{l_{v,x}^2}\right)}d\tau \tag{5.38}$$

The coefficient of drag for the hull, C_{Dh}, is a function of the length τ since the hull diameter and equivalent linear velocity varies with the distance from the centre of rotation. The coefficient of drag is difficult to estimate since there are components of flow around the hull and flow slipping along the hull, however, it can be related to the Reynolds number of the flow. Ignoring the regions within 5% of the CV and the end of the airship, the Reynolds number for the flow around the hull normalized by rotational rate varies from 1×10^4 to $1.1 \times 10^5[\frac{Re}{rad/s}]$. Assuming rotational rates are always below 3 rad/s, the coefficient of drag for flow around a smooth cylinder is approximately $C_D = 1$ for the entire range of Reynolds numbers [37]. The shape of the bare hull drag force, $F_{D,h}$, along the airship length, $l_{v,x}$, is shown in Figure 5.2.

Therefore the moment drag coefficient, C_{M4}, can be simplified to:

$$C_{M4} = -C_{Dcf}S_f d_{f,x2}^3 - 2\int_0^{l_{v,x}/2} S_h\tau^2 d\tau = -\left[C_{Dcf}S_f d_{f,x2}^3 + \frac{l_{v,z}l_{v,x}^4}{240}\right] \tag{5.39}$$

Table 5.2.: Parameters used to calculate aerodynamic forces

Symbol	Description	Value	Units
$l_{v,z}$	Airship diameter	1.868	m
$l_{v,x}$	Airship length	6.541	m
C_{Dho}	Hull zero-incidence drag coefficient [83]	0.024	-
C_{Dfo}	Fin zero-incidence drag coefficient [83]	0.006	-
C_{Dgo}	Gondola zero-incidence drag coefficient [96]	0.01	-
C_{Dch}	Hull cross-flow drag coefficient [83]	0.32	-
C_{Dcf}	Fin cross-flow drag coefficient [133]	2.0	-
C_{Dcg}	Gondola cross-flow drag coefficient [96]	1.0	-
$\left(\frac{\delta C_L}{\delta \alpha}\right)_f$	Derivative of fin lift-coefficient [133]	5.687	-
S_h	Hull reference area, $V^{2/3}$	5.241	m^2
S_f	Fin reference area [19]	2.160	m^2
S_g	Gondola reference area [19]	0.067	m^2
$d_{f,x1}$	Distance between CV to GC of fins along X	2.352	m
$d_{f,x2}$	Distance between CV to AC of fins along X	2.368	m
$d_{f,z}$	Distance between CV to AC of fins along Z	0.915	m
$d_{c,z}$	Distance between CV to AC of gondola along Z	0.915	m
η_f	Fin efficiency factor [84]	0.20	-
η_h	Hull efficiency factor [84]	1.50	-
I_1	Hull integrals [96]	0.350	-
I_3		-0.124	-
J_1		1.202	-
J_2		-0.158	-

C_{N4}, is considered to be the same since the airship has the same profiles in pitch and yaw with the exception of the gondola. The derivation of C_{L2} includes only the components due to form drag on the fins and is multiplied by 2 since all 4 fins are in effect. Only the drag on the fins is assumed to impact the coefficient for roll (i.e. negligible hull skin drag).

All other variables and coefficients are summarized in Table 5.2 and include references to where they can be determined for any airship platform using a combination of semiemperical models and geometric functions.

5.2.4. Gravitational and buoyancy vector

The gravitational and buoyancy vector accounts for gravitational and buoyancy forces applied to the vehicle. Since these forces align with the axes of the earth

reference frame, they must be premultiplied by a rotation matrix to convert them to the body reference frame. Pendulum moments are produced by the CM being located below the CV. The centre of buoyancy is assumed to be the same as the CV. The fuel tank is assumed to be located closely to the CM such that fuel consumed does not affect the location of the CM, a_x and a_z.

$$\mathbf{G} = \begin{bmatrix} m\mathbf{g} \\ m\mathbf{d_{CG}}\mathbf{g} \end{bmatrix} - \begin{bmatrix} \rho_a V\mathbf{g} \\ \rho_a V\mathbf{d_{CV}}\mathbf{g} \end{bmatrix} \tag{5.40}$$

where $\mathbf{d_{CG}}$ is defined in equation (5.3), $\mathbf{d_{CV}} = 0_{3\times3}$ since the centre of buoyancy is assumed to be at CV, $\mathbf{g} = \begin{bmatrix} g_1 & g_2 & g_3 \end{bmatrix}^T = \mathbf{R_1}^T \begin{bmatrix} 0 & 0 & g \end{bmatrix}^T$ is the gravitational vector expressed in the body frame and a rotation matrix, $\mathbf{R_1}$ (also known as the 123 or roll-pitch-yaw Euler sequence),

$$\mathbf{R_1} = \begin{bmatrix} \cos\theta\cos\psi & \sin\phi\sin\theta\cos\psi - \cos\phi\sin\psi & \cos\phi\sin\theta\cos\psi + \sin\phi\sin\psi \\ \cos\theta\sin\psi & \sin\phi\sin\theta\sin\psi + \cos\phi\cos\psi & \cos\phi\sin\theta\sin\psi - \sin\phi\cos\psi \\ -\sin\theta & \sin\phi\cos\theta & \cos\phi\cos\theta \end{bmatrix} \tag{5.41}$$

Written in component form, the gravitational and buoyancy vector becomes,

$$G_X = (m - \rho_a V)\, g_1 \tag{5.42}$$
$$G_Y = (m - \rho_a V)\, g_2 \tag{5.43}$$
$$G_Z = (m - \rho_a V)\, g_3 \tag{5.44}$$
$$G_L = -m d_{mz} g_2 \tag{5.45}$$
$$G_M = m\,(d_{mz} g_1 - d_{mx} g_3) \tag{5.46}$$
$$G_N = m d_{mx} m g_2 \tag{5.47}$$

5.2.5. Uncertainty terms

In addition to the parameter uncertainty of the inertia terms, σ_1, previously mentioned in subsection 5.2.1, there is also uncertainty in the model formulation. This uncertainty arises from assumptions made about the vehicle aerodynamics and the actuator dynamics. For example, aerodynamic forces are assumed to be linear combinations of individual airship features and drag coefficients are assumed to be constant. Additionally, the model is derived based on unseperated, steady state flow which is not always true. These variations will result in an unknown, higher order aerodynamic model. Therefore, the uncertainty vector is modelled as,

$$\mathbf{E} = \sigma_2 \left(\mathbf{A} + \mathbf{U}\right)^T \tag{5.48}$$

where σ_2 is a 6x1 vector of uniformly distributed random percentages within the range of $\pm 10\%$. This range was chosen based on the variation between methods to determine empirically derived constants and is discussed in detail in Section 5.6.

5.2.6. Input force vector

The forces applied to the airship from the various actuators are contained in the input force vector which is the product of the control vector $\mathbf{u}$, and the input state matrix, $\mathbf{B}$, such that,

$$\mathbf{U} = \mathbf{B}\left(\mathbf{R_1}\right)\mathbf{u}$$

A common technique in control simulations is to assume that thrust forces can be applied directly. Unfortunately, the unmodelled dynamics of the electric motors and propellers can oversimplify and under estimate the real control effort required to apply such forces. In reality, thrust force depends heavily on the advance ratio of each propeller which changes based on the relative airspeed of the vehicle. The thrust generated by the propellers on the engine and all electric motors is modelled as,

$$T = \frac{P\eta}{\upsilon_r} \tag{5.49}$$

where P is the input power to the actuator, υ_r is the relative airspeed across the propeller, and η is the combined efficiency of the electric motor and propeller. The thrust produced from the hybrid power plant and the two forward facing electric thrusters are combined into one resultant thruster for simplicity.

The input vector is defined by the forward thruster cluster (u_1), the front and rear air ballasts (u_2 and u_3), and top and bottom tail thrusters (u_4 and u_5) into one 5 dimensional vector written as,

$$\mathbf{u} = \begin{bmatrix} u_1 & u_2 & u_3 & u_4 & u_5 \end{bmatrix}^T = \begin{bmatrix} P_c & V_{b,f} & V_{b,r} & P_{t,t} & P_{t,b} \end{bmatrix}^T \tag{5.50}$$

The input vector uses power (P) as the input for propulsion systems and volume of air (V) as the input for the air ballasts. The air ballasts were included here in the input vector instead of in the gravity vector to consolidate all the control inputs. The sum of all five actuator forces as they apply in the vehicle body frame is,

$$\mathbf{U} = \begin{bmatrix} T_c \\ 0 \\ 0 \\ 0 \\ d_{c,z}T_c \\ 0 \end{bmatrix} - \begin{bmatrix} \mathbf{g} \\ \mathbf{d_{CB}g} \end{bmatrix} \rho_a V_{b,f} - \begin{bmatrix} \mathbf{g} \\ \mathbf{d_{CB}g} \end{bmatrix} \rho_a V_{b,r} + \begin{bmatrix} 0 \\ T_{t,t} \\ 0 \\ d_{f,z}T_{t,t} \\ 0 \\ -d_{f,x}T_{t,t} \end{bmatrix} + \begin{bmatrix} 0 \\ T_{t,b} \\ 0 \\ -d_{f,z}T_{t,b} \\ 0 \\ -d_{f,x}T_{t,b} \end{bmatrix} \tag{5.51}$$

where $\mathbf{d_{CB}}$ is a skew symmetric matrix containing the distances between the CV of the airship and each ballonet defined as,

$$\mathbf{d_{CB}} = \begin{bmatrix} 0 & -d_{b,z} & 0 \\ d_{b,z} & 0 & -d_{b,x} \\ 0 & d_{b,x} & 0 \end{bmatrix}$$

Separating the (5.50) from (5.77), yields the input state matrix which describes how the input vector applies forces and moments on the vehicle,

$$\mathbf{B} = \begin{bmatrix} \frac{T_c}{P_c} & -\rho_a \mathbf{g_1} & -\rho_a \mathbf{g_1} & 0 & 0 \\ 0 & 0 & 0 & \frac{T_t}{P_t} & \frac{T_t}{P_t} \\ 0 & -\rho_a \mathbf{g_3} & -\rho_a \mathbf{g_3} & 0 & 0 \\ 0 & 0 & 0 & l_{fx}\frac{T_t}{P_t} & -l_{fx}\frac{T_t}{P_t} \\ l_{cz}\frac{T_c}{P_c} & -\rho_a(\mathbf{g_3}d_{b,x} - \mathbf{g_1}d_{b,z}) & -\rho_a(\mathbf{g_3}d_{b,x} + \mathbf{g_1}d_{b,z}) & 0 & 0 \\ 0 & 0 & 0 & -l_{fz}\frac{T_t}{P_t} & -l_{fz}\frac{T_t}{P_t} \end{bmatrix} \tag{5.52}$$

Based on experimental results in [29], $\frac{T_c}{P_c} = \frac{\eta_c}{\upsilon_{r,x}} = -2.59 \cdot 10^{-5}\upsilon_{r,x}^2 + 2.07 \cdot 10^{-4}\upsilon_{r,x} + 4.15 \cdot 10^{-2}$ [s/m] is defined for an 11 inch propeller at 15° pitch and 9000 RPM within the range $0 < \upsilon_{r,x} < 36\frac{m}{s}$ and $\frac{T_t}{P_t} = \frac{\eta_t}{\upsilon_{r,y}} = -2.37 \cdot 10^{-5}\upsilon_{r,y}^2 - 7.32 \cdot 10^{-4}\upsilon_{r,y} + 6.07 \cdot 10^{-2}$ [s/m] for a 7 inch propeller at 15° pitch and 12000 RPM within the range $0 < |\upsilon_{r,y}| < 28\frac{m}{s}$.

An energy consumption model can now be defined based on the commanded inputs. The air ballast pump power can be defined based on Bernoulli's equation as,

$$P_b = \frac{\left(\left|\triangle\hat{P}_a\right| + \hat{P}_o\right)|Q_b|}{10^3\eta_p}$$

where $\triangle\hat{P}_a$ is the differential air pressure for changes in altitude, $\hat{P}_o$ is the constant internal envelope overpressure required for rigidity, η_p is the air pump efficiency,

and $Q_{b,f}$ and $Q_{b,r}$ are the volume flow rates of air to the front and rear ballasts, respectively.

The partial energy consumed in Wh, over one time step, $\triangle t$, is,

$$\triangle E = \sum \begin{bmatrix} |P_c| & |P_{b,f}| & |P_{b,r}| & |P_{t,t}| & |P_{t,b}| \end{bmatrix}^T \triangle t/3600 \left[\frac{sec}{h}\right] \tag{5.53}$$

The total energy consumed is then,

$$E = \sum_{t=0}^{t_{end}} \triangle E \tag{5.54}$$

and will be used as a performance comparison metric between trajectories and controllers. As energy is consumed, mass on-board is lost from the conversion of liquid gasoline to exhaust gases. Although the hybrid power plant is currently used in an on-off fashion, mass change due to fuel consumption is assumed to be linear and defined by the empirical relationship,

$$\triangle m = -C \triangle E \tag{5.55}$$

where C is a constant. Using the results from the experimental testing of the hybrid power plant running at the most efficient operating point from Section 3.3, we can say that the ratio of the fuel consumed in one hour over the total useful power produced in one hour is,

$$C = \frac{0.05\frac{g}{sec} \cdot 3600\frac{sec}{1h} \cdot 1h}{220W \cdot 1h} = 0.82 \left[\frac{g}{Wh}\right] \tag{5.56}$$

5.2.7. Kinematics

The dynamic equations of motion in equation (5.1) dictate how the vehicle will accelerate based on the applied forces. Vehicle kinematics are applied in tandem to determine the vehicle's velocity and positional changes and how they translate to the earth reference frame.

Coordinates and trajectories in the earth reference frame can be determined from the equivalent states in body reference frame pre-multipled by the Jacobian matrix,

$$\dot{\mathbf{x}}_\mathbf{g} = \mathbf{J}\dot{\mathbf{x}}_\mathbf{v} + \upsilon_\mathbf{w} = \begin{bmatrix} \mathbf{R_1} & 0_{3\times3} \\ 0_{3\times3} & \mathbf{R_2} \end{bmatrix} \dot{\mathbf{x}}_\mathbf{v} + \upsilon_\mathbf{w} \tag{5.57}$$

where $\mathbf{R_1}$ is the rotation matrix described in equation (5.41), $\upsilon_\mathbf{w}$ is the total wind (steady + gusts) in a 6x1 vector defined in section 4.2 and,

$$\mathbf{R_2} = \begin{bmatrix} 1 & \sin\phi\tan\theta & \cos\phi\tan\theta \\ 0 & \cos\phi & -\sin\phi \\ 0 & \sin\phi\sec\theta & \cos\phi\sec\theta \end{bmatrix} \tag{5.58}$$

Since a direct solution is not feasible for the highly non-linear equations of motion, numerical methods are applied for an approximate solution. If we set a small time step, t_i, it can be assumed that acceleration is constant over that step and thus the vehicle's motion obeys the kinematic equations,

$$\dot{\mathbf{x}}_\mathbf{v}(t_n) = \dot{\mathbf{x}}_\mathbf{v}(t_{n-1}) + \ddot{\mathbf{x}}_\mathbf{v}(t_n)\, t_i \tag{5.59}$$

$$\mathbf{x_g}(t_n) = \mathbf{x_g}(t_{n-1}) + \dot{\mathbf{x}}_\mathbf{g}(t_n)\, t_i \tag{5.60}$$

Next, the acceleration, $\ddot{x}_v$, from (5.1) can be reevaluated for the new vehicle and environmental conditions and this process is continued iteratively. A time step of $t_i = 50ms$ was determined to be sufficiently small to not interfere with the natural frequencies of the model as observed during simulations. To improve the accuracy of motion, a 4th order Runge-Kutta approximation was applied to equations (5.59) and (5.60).

Implementation of the Runge-Kutta-Fehlberg 4/5 method should be considered to improve the computational efficiency for use in the physical system. It computes both the 4th order and 5th order solution at each step, and uses the error between the two approximations to automatically adapt the step size to within a desired threshold accuracy. The simulation time was in the order of seconds and therefore Runge-Kutta-Fehlberg 4/5 was not required here[1].

5.2.8. Summary of additions to conventional airship dynamic models

The following subsection outlines the notable extensions to existing airship dynamic models.

Airship actuator selection and modeling

The main design goal of this airship platform is to operate over long endurance as determined as this was to be a limiting factor for many small UAVs [16,29]. It was experimentally proven that a fixed pair of forward facing electric thrusters complimented by a hybrid gas-electric power plant can provide significant endurance

[1]Simulations were performed in Matlab R2010B using an Intel Core 2 Duo 2.80 GHz CPU with 4 GB of RAM

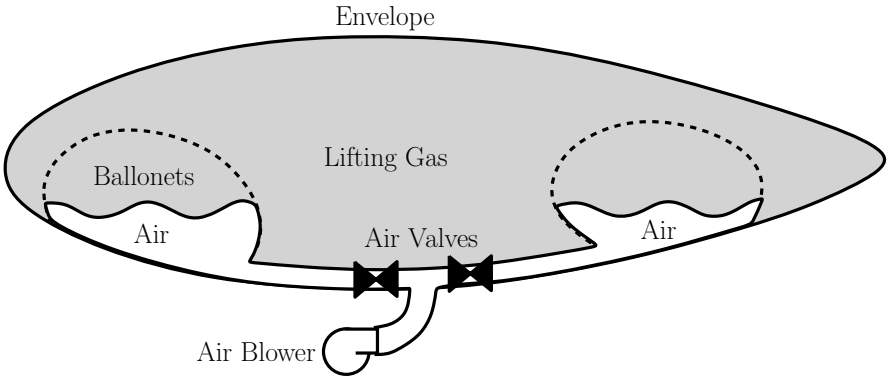

Figure 5.3.: Pressure control system for a non-rigid airship. Adapted from [19]

improvements over a purely electric system [16, 29]. The dynamic model combines all three thrust forces into one resultant for simplicity. Only the right mounted electric thruster is shown in Figure 5.1. Since this airship platform employs a gasoline engine, the airship mass will decrease by up to 25% during flight and this requires compensation.

Small scale airships typically use thrust vectoring or dynamic lift using aerodynamic surfaces for altitude control, which provide a fast control response but require continuous power to maintain an altitude. Thrust vectoring alone also increases the differential pressure between the lifting gas and the atmosphere at higher altitudes which can compromise the structural integrity of the envelope [19]. The solution to these drawbacks is the use of air ballasts (ballonets) for mass compensation, pressure equalization, altitude control and pitch stability. In a ballonet controlled airship, the structure and aerodynamic stiffness of the aircraft is maintained by a constant applied overpressure. By inflating the ballonets with air, the mass of the airship increases (for the same envelope volume) causing the airship to descend. Similarly, when the ballonets are emptied, the helium is allowed to expand, the mass decreases for the same buoyancy and the airship begins to rise. Conventional designs have two ballonets, one at the bow and one at the stern, to fine tune the centre of gravity and allow for pitch control, if required. The ballasts are inflated using an electric air pump and air volumes are controlled by a set of valves. Figure 5.3 shows a conventional ballonet system.

Although ballonets have been used in large-scale airships, the concept of downsizing them for altitude and pitch control is unique to this work. Also, two tail mounted thrusters were added to provide both directional control and optional roll stability. The combination of these two types of actuators eliminates the need for aerodynamic control surfaces (elevators and rudders) which are seen on conventional airships. Aerodynamic control surfaces have the advantage of lower power consumption for sustained control inputs but suffer from sluggish response

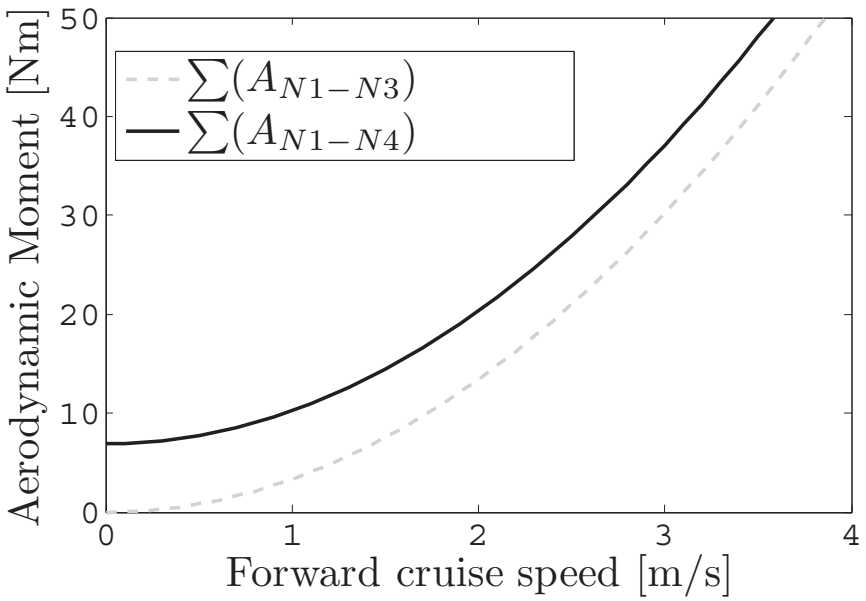

Figure 5.4.: Low speed aerodynamic dampening

time and ineffectiveness at low flight speeds [94, 134]. These disadvantages were considered to be unacceptable for a small scale and long endurance dirigible UAV that frequently experiences all flight regimes.

The arrangement of actuators used on the physical platform and the concept of variable vehicle mass is unconventional in previously derived airship dynamic models but has been incorporated in this work.

Added aerodynamic terms

One of the major drawbacks of conventional non-linear airship dynamic models is that they are not defined for all flight regimes; specifically low speed flight. The effects of aerodynamic terms typically exponentially diminish with the decreasing forward cruising speed of the airship. The original derivation is reasonable since the conventional airship configuration relies on aerodynamic control surfaces, which have diminishing effectiveness a low speeds as well. However, for small-scale airships that have limited cruise speeds that can be further reduced by the impact of wind disturbances, there is a necessity for the model to be well defined in both regimes.

Let's consider a simple case study to illustrate the impact of the added aerodynamic terms. Given a constant angle of side slip $\beta = +5°$ and an instantaneous turning rate of $\dot{\psi} = -0.15$ rad/s, the total aerodynamic moment, A_N, can be plotted as a function of forward cruising speed $\dot{x}$ with and without the contribution of A_{N4}. Figure 5.4 represents the sums of the aerodynamic moments applied to the vehicle if entering a turn at any cruise speed between 0 and 4m/s. For this

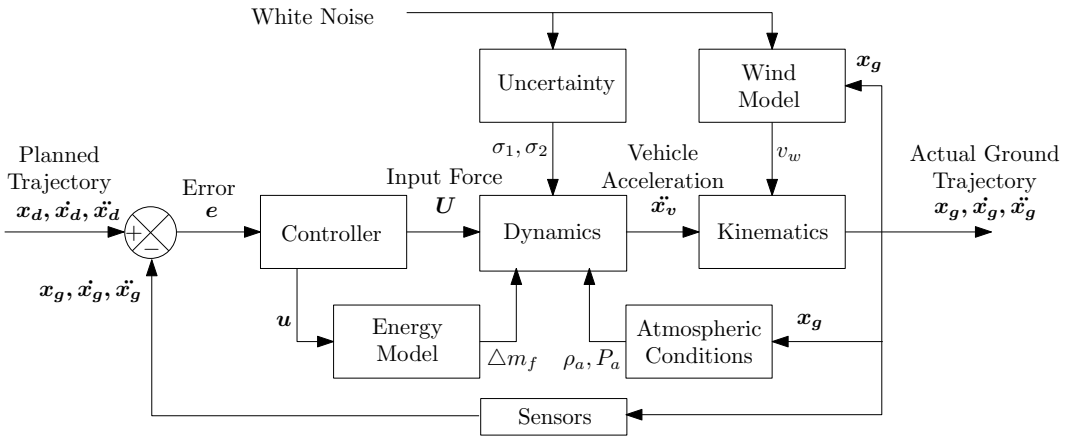

Figure 5.5.: Block diagram of control system

scenario, the aerodynamic dampening term A_{N4} contributes 100% to the total moment at a cruise of 0m/s, 50% at 1.43m/s, and 5% at 6.24m/s. Logically, if a turning moment is applied to the airship during hover, air resistance will resist the motion. At higher cruising speeds, the weather cock stability proved by the tail fins will dominate the restoring moment. Although these appear to be reasonable results, the validity of the aerodynamic terms require experimental testing which is recommended for future work.

Uncertainty terms

Regardless of the level of detail of the dynamic model, there will always be discrepancies with the physical model. To account for these discrepancies, parameter uncertainty terms were added to items that are the least known such as the vehicle's real and virtual inertia. Modelling uncertainty terms were also added to account for sensor noise, unaccounted dynamics and modelling assumptions such as rigid body motion. The inclusion of uncertainty will provide an unbiased and more realistic environment for observing controller performance.

5.3. Flight Control Law Development

The following section details the development of two types of flight controllers that were applied for trajectory following. A block diagram of the control system overview is shown in Figure 5.5. It is important to emphasize that the controllers themselves are used here as example solutions. They are not considered to be new control theory nor are they necessarily the optimal solution.

5.3.1. Simulated environment, constraints and tracking error

There are several commonalities identified between the controller designs which will be introduced here. First, the desired trajectory (both path and vehicle velocity) is produced from the trajectory planner and is considered to be already known [135]. The validation will be performed on a case-study basis using the worst-case energy consumption scenario predicted by the trajectory planner as the case environment (shown previously in Figure 4.9). The same variable WVF that was added for the trajectory planner is also applied in the simulated environment for both controllers. The wind consists of two parts, a steady component that was calculated based on CFD analysis and a gust component which is generated by a Dryden filter [135].

The second commonality are actuator saturation constraints, which are imposed based on the physical airship prototype as follows,

Resultant forward thrust power: $u_1 : 0 \leq P_f \leq 1540W$

Air ballast volume: $u_{2,3} : 0L \leq V_b \leq 1300L$[2]

Air ballast flow rate: $\dot{u}_{2,3} : -12\frac{L}{s} \leq Q_b \leq 12\frac{L}{s}$

Tail thrust power: $u_{4,5} : 0 \leq P_t \leq 340W$

Third, the definition of errors are defined as,

$$\mathbf{e} = \mathbf{x_d} - \mathbf{x_g} \tag{5.61}$$

$$\dot{\mathbf{e}} = \dot{\mathbf{x}}_\mathbf{d} - \dot{\mathbf{x}}_\mathbf{g} = \dot{\mathbf{x}}_\mathbf{d} - \mathbf{J}\dot{\mathbf{x}}_\mathbf{v} \tag{5.62}$$

$$\ddot{\mathbf{e}} = \ddot{\mathbf{x}}_\mathbf{d} - \ddot{\mathbf{x}}_\mathbf{g} = \ddot{\mathbf{x}}_\mathbf{d} - \mathbf{J}\ddot{\mathbf{x}}_\mathbf{v} - \dot{\mathbf{J}}\dot{\mathbf{x}}_\mathbf{v} \tag{5.63}$$

where $\dot{\mathbf{x}}_\mathbf{g}$ if the vehicle's velocity in the earth fixed frame, $\dot{\mathbf{x}}_\mathbf{v}$ is the vehicle's velocity in the vehicle frame, and the desired trajectory $\dot{\mathbf{x}}_\mathbf{d}$ is known to be,

$$\mathbf{x_d} = \begin{bmatrix} x_d \\ y_d \\ z_d \\ \phi_d \\ \theta_d + \alpha + K_z\theta_e \\ \psi_d + \beta + K_y\psi_e \end{bmatrix} \quad \dot{\mathbf{x}}_\mathbf{d} = \begin{bmatrix} \mathbf{T_r} & 0_{3\times3} \\ 0_{3\times3} & 0_{3\times3} \end{bmatrix} \begin{bmatrix} \upsilon_d \\ 0 \\ 0 \\ 0 \\ 0 \\ 0 \end{bmatrix} \quad \ddot{\mathbf{x}}_\mathbf{d} = \begin{bmatrix} 0 \\ 0 \\ 0 \\ 0 \\ 0 \\ 0 \end{bmatrix} \tag{5.64}$$

[2]The air ballasts start with 400L of air during take off

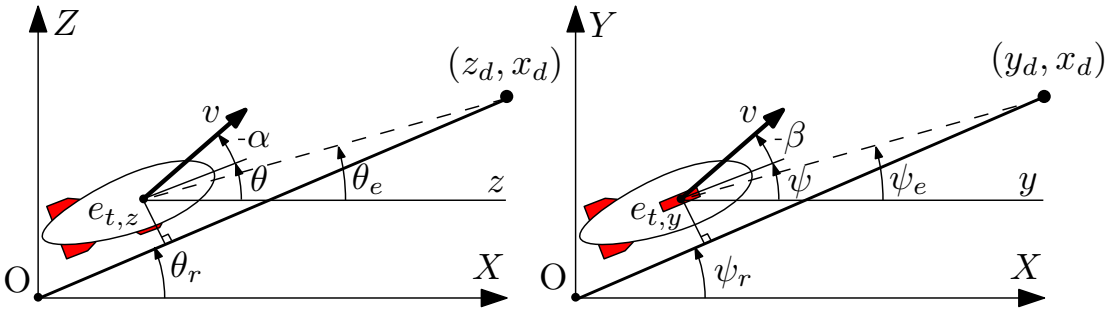

Figure 5.6.: Definition of pitch (left) and direction (right) angles for an example trajectory

where $\mathbf{I}_{3\times3}$ is an identity matrix, $\mathbf{T_r} = \mathbf{T}\left(\begin{bmatrix} 0 & \theta_r & \psi_r \end{bmatrix}^T\right)$ with θ_r and ψ_r being the pitch and direction angles between waypoints n and n' in the earth reference frame, and K_y and K_z are design weighing factors which are chosen to be equal to one. Since the airship is underpowered, if the errors are corrected independently it will likely result in actuator saturation [123]. The pitch, θ_e, and yaw, ψ_e, angles between the airship's current orientation and the vector of the euclidean distance to the desired position were added to both controllers similar to the method proposed by Azinheira [123] in order to reduce redundant correction. These two angles can be observed in Figure 5.6. Pitch angle θ_e, can be used to quickly adjust altitude in same way that yaw angle ψ_e, can be used to quickly adjust course direction. Utilizing these two factors should provide the following benefits over independent error correction:

- Faster response
- Smoother input requests
- Reduce actuator saturation time
- Reduce overall control effort and energy consumption

The desired roll and desired pitch angles are chosen here to be equal to zero ($\phi_d = \theta_d = 0$). This is intuitive as the vehicle's passive pendulum stability will naturally tend towards these values.

Furthermore, two additional trajectory tracking errors, e_{t1} and e_{t2}, are identified for a baseline of tracking performance used for comparison. These tracking errors are representative of the UAVs perpendicular deviation from the path which, if too large, could risk collision with static obstacles. The distance between the vehicle's CV and perpendicular to the desired trajectory in a vertical plane is defined as e_{t2}. The distance between the vehicle's CV and perpendicular to the desired trajectory in a horizontal plane is defined as e_{t1}. These two tracking errors are illustrated in Figure 5.6.

Finally, both controllers were implemented at a rate of 20Hz. This frequency is at least one decade higher than the fastest frequency observed from the open loop plant dynamics (0.6Hz for the roll pendulum mode).

5.4. PID Control

The first type of control implemented for trajectory tracking is PID. Control allocation is performed based on prior knowledge of the system's behavior. Five errors are identified for correction:

Ground velocity: $\dot{e}_1 = \upsilon_d - \dot{x}_g$

Altitude: $e_3 = z_d - z_g$

Roll: $e_4 = \phi_d - \phi$

Pitch: $e_5 = (\theta_d + \alpha + k_z\theta_e) - \theta$

Orientation (yaw): $e_6 = (\psi_d + \beta + k_y\psi_e) - \psi$

The first error is the difference in desired (υ_d) and actual ground velocity where the tracking point along the path changes at a rate equal to the desired ground velocity from the trajectory planner. This error can be corrected by the forward thrust cluster, u_1, directly. For the four last errors, pairs of actuators contribute to reduce the errors so it is useful to define intermediate control variables. The intermediate variable for each error is defined as,

$$\widetilde{u}_j = K_{pj}e_j + K_{ij}\int_0^t e_j(\tau)\,d\tau + K_{dj}\frac{d}{dt}e_j(t) \tag{5.65}$$

where the index j is from the errors listed above. Knowing the system configuration we can say that the vehicle orientation ($\widetilde{u}_6$) is regulated by the sum of tail thrusters ($u_4 + u_5$) while roll angle ($\widetilde{u}_4$) is controlled by the difference ($u_4 - u_5$) . Altitude ($\widetilde{u}_3$) is governed by the sum of ballonet volumes ($u_2 + u_3$) while the difference ($u_3 - u_2$) controls the pitch angle ($\widetilde{u}_5$). Rearranging for the actual control inputs yields,

$$\mathbf{u} = \begin{bmatrix} u_1 \\ u_2 \\ u_3 \\ u_4 \\ u_5 \end{bmatrix} = \begin{bmatrix} \widetilde{u}_1 \\ \widetilde{u}_3 - \widetilde{u}_5 \\ \widetilde{u}_3 + \widetilde{u}_5 \\ \widetilde{u}_6 + \widetilde{u}_4 \\ \widetilde{u}_6 - \widetilde{u}_4 \end{bmatrix} \tag{5.66}$$

Since the airship is under powered the gains in equation (5.65) must be chosen carefully not to constantly saturate the inputs and produce a bang-bang control solution.

5.5. Backstepping Control

Backstepping control uses a Control Lypanov Function (CLF) to stabilize virtual states of strict feedback dynamic systems [122]. Each state is stabilized separately until the final external control is determined. Since the position of the vehicle in equation (5.61) cannot be controlled directly through the vehicle's actuators, a virtual velocity is introduced to stabilize the position,

$$\mathbf{e_2} = \dot{\mathbf{e}}_\mathbf{1} + K_1 \mathbf{e_1} \tag{5.67}$$

$$\dot{\mathbf{e}}_\mathbf{2} = \ddot{\mathbf{e}}_\mathbf{1} + K_1 \dot{\mathbf{e}}_\mathbf{1} \tag{5.68}$$

where $\mathbf{e_1} = \mathbf{e}$ from (5.61), and K_1 is a positive definite design matrix. Let's consider the CLF for the first step to be,

$$W_1 = \frac{1}{2}\mathbf{e_1^T e_1} \tag{5.69}$$

then it's time derivative is,

$$\dot{W}_1 = \mathbf{e_1^T}\dot{\mathbf{e}}_\mathbf{1} = -\mathbf{e_1^T} K_1 \mathbf{e_1} + \mathbf{e_1^T e_2} \tag{5.70}$$

If $\mathbf{e_2}$ is minimized to zero in the next step, $\dot{W}_1$ will be negative definite and the position tracking error $\mathbf{e_1}$ will converge asymptotically to zero.

Now let's consider the CLF for the second step,

$$W_2 = \frac{1}{2}\mathbf{e_1^T e_1} + \frac{1}{2}\mathbf{e_2^T e_2} \tag{5.71}$$

then it's time derivative is,

$$\dot{W}_2 = \mathbf{e_1^T}\dot{\mathbf{e}}_\mathbf{1} + \mathbf{e_2^T}\dot{\mathbf{e}}_\mathbf{2} \tag{5.72}$$

If the virtual control action is chosen such that,

$$\dot{\mathbf{e}}_\mathbf{2} = -\mathbf{e_1} - K_2 \mathbf{e_2} \tag{5.73}$$

where K_2 is another positive definite design matrices, then the time derivative of the second CLF becomes,

$$\dot{W}_2 = \mathbf{e_1^T}\left(\mathbf{e_2} - K_1\mathbf{e_1}\right) - \mathbf{e_2^T}\left(\mathbf{e_1} + K_2\mathbf{e_2}\right)$$

$$\dot{W}_2 = -\mathbf{e_1^T}K_1\mathbf{e_1} - \mathbf{e_2^T}K_2\mathbf{e_2} \tag{5.74}$$

Using Barbalat's lemma, it can shown that,

1. W_2 is lower bounded since $\mathbf{e_1^2}, \mathbf{e_2^2} \geq 0$, then $W_2 \geq 0$
2. $\dot{W}_2$ is negative semi-definite since $\mathbf{e_1^2}, \mathbf{e_2^2} \geq 0$, and $K_1, K_2 > 0$, then $\dot{W}_2 \geq 0$
3. $\dot{W}_2$ is uniforming continuous in time: As a result of 2, W_2 is non-increasing and thus is bounded by $0 \leq W_2(t) \leq W_2(t_0)$. Therefore, $e_1(t)$ and $e_2(t)$ are also bounded according to (5.71) which ensures $\ddot{W}_2(t)$ is finite.

Thus, according to Lypanov control theorem, $W_2(t) \to 0$ as $t \to \infty$ and the system is globally asymptotically stable for constant desired $\mathbf{x_d}$ [136, 137]. Using the virtual control action defined in equation (5.73), the real control force can be found through algebraic manipulation. First, virtual states are removed by setting equation (5.73) equal to equation (5.68) and substituting in equations (5.67), such that,

$$\ddot{\mathbf{e}}_\mathbf{1} + K_1\dot{\mathbf{e}}_\mathbf{1} = -\mathbf{e_1} - K_2\left(\dot{\mathbf{e}}_\mathbf{1} + K_1\mathbf{e_1}\right) \tag{5.75}$$

Next, the acceleration, $\ddot{\mathbf{x}}$, which is related to the real control force through the equations of motion (5.1), can be found by substituting equation (5.63) into (5.75) and rearranging,

$$\begin{aligned}\ddot{\mathbf{x}} &= \mathbf{J^{-1}}\left[\left(1 + K_1K_2\right)\mathbf{e_1} + \left(K_1 + K_2\right)\dot{\mathbf{e}}_\mathbf{1} - \dot{\mathbf{J}}\dot{\mathbf{x}} - \ddot{\mathbf{x}}_\mathbf{d}\right] \\ &= \mathbf{M^{-1}}\left(-\mathbf{D}(\dot{\mathbf{x}}) + \mathbf{A}(\dot{\mathbf{x}}) + \mathbf{G}(\lambda) + \mathbf{B}(\lambda)\,\mathbf{u}\right)\end{aligned} \tag{5.76}$$

Since the uncertainty terms are unpredictable, they are removed from the desired control response. Finally, the desired control force, $\mathbf{U}$, can be found through

$$\mathbf{U} = \mathbf{B}(\lambda)\,\mathbf{u}$$

$$\mathbf{U} = \mathbf{M}\left(\mathbf{J^{-1}}\left[\left(1 + K_1K_2\right)\mathbf{e_1} + \left(K_1 + K_2\right)\dot{\mathbf{e}}_\mathbf{1} - \dot{\mathbf{J}}\dot{\mathbf{x}} - \ddot{\mathbf{x}}_\mathbf{d}\right]\right) \tag{5.77}$$

$$- \left(-\mathbf{D}(\dot{\mathbf{x}}) + \mathbf{A}(\dot{\mathbf{x}}) + \mathbf{G}(\lambda)\right) \tag{5.78}$$

where K_1 and K_2 are tunable diagonal positive-definite matrices.

Table 5.3.: Summary controller performances

Parameter	Case #1	Case #2	Case #3	Case #4
Travel time (s)	154.2	132.8	126.2	147.2
Travel distance (m)	2044	2066	1967.1	2005
Fuel consumed (g)	74.4	86.0	62.2	48.2
Average $e_{t,y}$ (m)	18.2	17.6	16.1	12.1
Maximum $e_{t,y}$ (m)	42.1	53.4	53.7	40
Average $e_{t,z}$ (m)	18.3	17.9	16.1	12.1
Maximum $e_{t,z}$ (m)	42.1	86.6	86.6	40

(a) PID controller performance

Parameter	Case #1	Case #2	Case #3	Case #4
Travel time (s)	169.5	189.0	158.0	161.5
Travel distance (m)	2177.7	2347.6	2060.1	2013.6
Fuel consumed (g)	86.0	114.5	86.9	68.4
Average e_{t1} (m)	12.5	11.7	9.0	5.5
Maximum e_{t1} (m)	43.9	45.6	45.6	25.5
Average e_{t2} (m)	12.6	11.8	9.1	5.6
Maximum e_{t2} (m)	75.9	79.6	61.7	48.0

(b) Backstepping controller performance

5.6. Results and Discussion

Figure 5.7 shows PID trajectory tracking for a trajectory which includes model and parametric uncertainty, and wind with gusts, for the same trajectory presented in Figure 4.9. A summary of the test results are presented in Table 5.3. Both the travel time and the travel distance generated by the controller simulations correspond well with the values predicted by the trajectory planner for this case study environment. The energy consumption, however, is at least 50% higher during trajectory following for both controllers in all cases. This increase can be attributed to the effects of introducing the full dynamic model and uncertainty. The stabilization of transient behaviors clearly plays a significant role in the required control effort, especially with frequent directional changes in strong winds. The concept of a longer flight path due to reorientation that is introduced in Figure 4.5 is evident in the Figure 5.7. Changes in orientation are not negligible for the airship considering the 50m path resolution. The trajectory generated by the planner was not smoothed before passing to the two trajectory followers so these changes in orientation contribute to the observed tracking error. The average tracking error of 12.1m for the full planner (case #4) is modest considering the length of the vehicle is 6.3m. All of the listed maximum directional and altitude tracking errors for the full planner are below the MSZ threshold of 50m set in

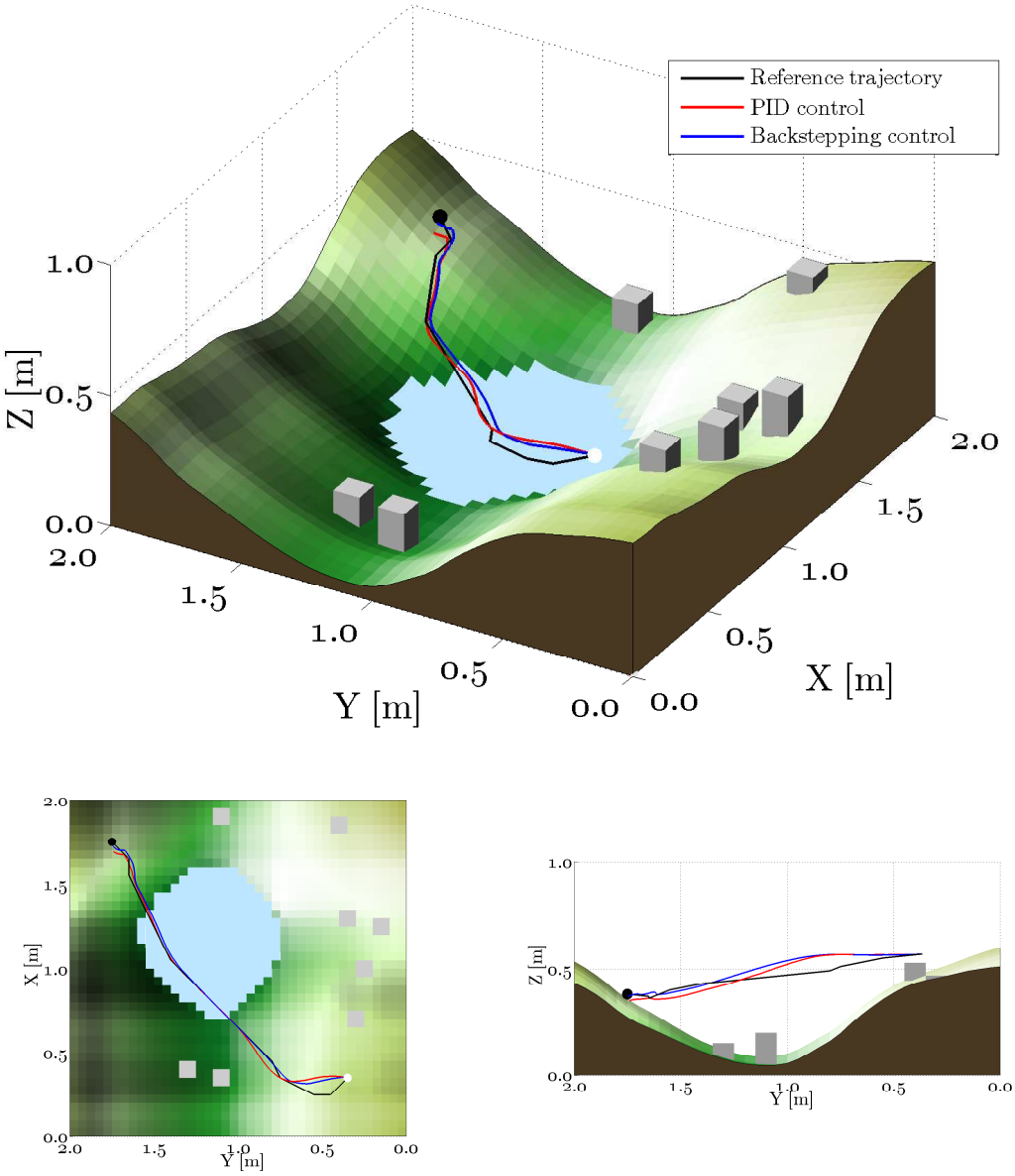

Figure 5.7.: An example of PID and backstepping trajectory tracking. Note: please refer to the full color PDF.

the trajectory planning process and thus, considered to be within an acceptable margin. If more or less obstacle separation is desired, the MSZ should be adjusted during the trajectory planning process to suit.

Backstepping was shown to have a 50% decrease in tracking error and a 40% increase in fuel consumption versus PID for the full planner trajectory in this case study. Observing (5.77) we can see that even in the case where errors are zero, input force is requested to offset dynamic, aerodynamic and gravitational forces. Although the inclusion of these non-linear model terms promotes increases in stability and tracking performance, it also tends to have larger fluctuating control requests leading to an increase fuel consumption. It should be noted that these results are subjective to the controller design parameters chosen.

The design parameters for both controllers in this case study were manually tuned to reduce both tracking error and energy consumption. Controller tuning can be a challenging process as mentioned by the work of Mountinho [94], due to non-linearities such as state coupling in the system. This is further complicated by the introduction of multiple tuning objectives in this work (tracking error and energy consumption). Ideally, the trajectory following controller would be capable of adaptive auto tuning based on the optimization of an objective function that would incorporate several mission goals. Nonlinear model predictive control is one such method that could be applied with this purpose and is an interesting avenue for future work.

The necessity to have active control authority over pitch and roll is questionable. Allowing only passive stabilization of pitch and roll by the vehicle's natural pendulum moments which appears to be sufficient to successfully track the trajectory. Although the tracking error was observed to be slightly greater in some cases, there was a 25% reduction in fuel consumption on average when compared to active stabilization. The magnitude of the static restoring moments diminish at low angles, and with consistent wind and uncertainty disturbances, the actuators are constantly providing control effort to correct them. Having command over pitch and yaw does have advantages in some foreseeable situations. For example, if pitch and yaw are held closer to zero, the vehicle's camera will require less gimbal stabilization to focus and track targets on the ground. However, a dead-band region should still be included to reduce unnecessary control effort.

The airship is underpowered, especially in the vertical direction. The air ballasts can be used for active altitude and pitch control over longer distances but have a sluggish response to aggressive maneuvers due to severe rate limitations. Incorporating the pitch coupling factor, θ_e, helps significantly to mitigate these drawbacks. The percentage of the time that the forward thrusters, air ballasts and tail thrusters are in saturation are given in Table 5.4.

Table 5.4.: Percentage of saturation time per actuator

Actuator	Time in Saturation
Forward thrusters	2.1%
Air ballast pumps	28.9%
Tail thrusters	0.1%

One noticeable attribute is the vehicle's ability to maneuver in a variety of severe flight conditions. Many airship controllers are developed for either tracking during trimmed flight or tracking a point during hover. However, since the model contains aerodynamic terms that do not depend on the relative airspeed and the vehicle has rotational control authority that does not depend on aerodynamic surfaces, the UAV can transition and perform well in both flight conditions. For example, when the same PID controller is set to track a stationary point for 10 minutes in the presence of a strong wind (7m/s) and uncertainty, it has an average tracking error of 15.5m with a maximum of 51.7m.

The inclusion of wind into the model is considered to be based on the kinematic vector addition with the vehicle velocity vector as is done in several other flight controllers [68, 117, 123]. The assumption of kinematic addition of wind is theoretically valid for steady state conditions but for variable wind with gusts, the transient behavior is over simplified, especially rotational disturbances which are ignored. In practice, wind speed does not effect vehicle ground speed directly. Wind causes drag forces and moments which induce linear and rotational vehicle velocities. Azinheria *et al.* present one possible method of including wind-induced forces and torques into the airship dynamics [93].The impact of these effects are assumed to absorbed by the model uncertainty but its magnitude is worth investigating in future research.

The magnitude and distribution of the uncertainties assumed in this study are difficult to validate. Virtual mass and inertia terms were developed from well known empirical models [105, 132] however their precision when scaled down to a $12m^3$ airship is debatable. Also, the dynamic model does not include effects such as structural flexibility or ballonet sloshing dynamics which introduce further non-linearities into the model. Although these effects could be modelled theoretically, their impact is highly subjective to the nature of the infrastructure assembly. Future work is recommended to quantify the uncertainties by comparing this theoretical model to an empirical model derived from experimental results.

5.7. Chapter Summary

Both controllers successfully track trajectories generated by the trajectory planner in the presence of both uncertainty and variable wind with unknown gusts. The results presented here indicate that the trajectories generated from the trajectory planner underestimate the energy consumption, but nevertheless, are feasible and realistic. The maximum tracking errors for both controllers was determined to be within the MSZs imposed by the trajectory planner, thus mitigating the risk of collisions with known objects. As predicted, the airship response is sluggish and underpowered, especially in the vertical direction. The air ballasts were proven to provide adequate long term altitude control and but are energy intensive for dynamic pitch stabilization. In general, allowing passive stabilization of roll and pitch through restorative pendulum moments reduces the required control effort leading to reduced energy consumption with minor increase in trajectory tracking error. Active roll and pitch correction is only recommended is special circumstances such as aiding camera gimbal stabilization.

6. Global Summary

6.1. Contributions

To summarize, the primary contributions of this thesis are as follow:

1. Two novel hybrid power plants were conceptualized, designed, manufactured and experimentally tested. These power plants are presented as viable alternatives to purely electric storage systems and the prevailing solution provides mechanical and electrical power for up to 72 hours of flight endurance compared to one to 4 hours for equivalent purely electric storage systems. Every effort was made to increase the operating efficiency of the power plant to maximize the potential of the fuel being spent. Incorporating a variable pitch propeller has proven to increase the operating flexibility and maximize propeller efficiency of the power plant. The key operating set points for various flight conditions were identified which are essential to the control and full-scale testing operation.

2. A wavefront expansion trajectory planner was developed for a dirigible UAV incorporating a novel multi-objective cost function applied to large, highly realistic, 3D environments with spatially variable WVFs generated from computational fluid dynamic (CFD) analysis on digital elevations maps. The cost function includes the differential constraints of the physical dirigible platform and is optimized for time, energy and collision avoidance to produce feasible, realistic and optimal trajectories. Trajectories were generated in real-time speeds and simulated over a variety of randomly generated test environments and flight conditions. The results of the simulation on a small-scale airship UAV showed that the inclusion of 1) variable vehicle velocity, 2) variable WVF data, and 3) high grid resolutions yields significant improvements in trajectory feasibility and energy economy when compared to simulations using only two of these three elements. Recommendations were made to implement the trajectory planner on the physical platform.

3. A complete dynamic mechanistic model of the UAV was developed that extends existing models by including low speed rotational damping, variable vehicle mass, parametric and modelling uncertainty, and air ballast

and tail thruster actuators. Two flight controllers were developed to track the trajectories generated from the previously developed trajectory planner. Considerations were made to prevent actuator saturation and address error coupling. The controllers were compared on the basis of control effort and tracking error. The trajectories generated by the planner were shown to underestimate energy consumption overall, however, they retain their relative performance compared to the other cases and can be feasibly followed.

In addition to the individual advancement of the literature that is presented in each manuscript topic area, the research project as a whole was advanced in other areas worth noting:

- The hybrid power plant has been attached to the gondola along with much of the electronics required to implement the designed trajectory planner and flight controller. Some of the electronics that were sourced and installed include a GPS unit, a three axis digital compass, a three axis pitot tube, Pico-ITX minicomputer, and forward and tail propellers driven by brushless DC motors. In keeping with the thesis goals, the use of commercially available components enable a low cost and modular design that can be adapted to other devices (e.g. infrared cameras, microphone and speakers) according to specific mission objectives.

- Custom electronics were developed for several applications such as power conversion, sensor feedback filtering, and power plant management (including autonomous engine start-up).

- In order to physically realize this solution, many innovations needed to be made to conventional, small-scale, airship infrastructure design to accommodate the large changes in mass due to fuel consumption. Ballonets used in large-scale airships were miniaturized, designed and constructed as an alternative altitude control system to thrust vectoring for small UAVs. An actuated helium pressure regulation valve was designed to ensure structural integrity. An air blower and air valving system was built to actuate the ballonets.

- Several innovations were made in material and component selection, assembly techniques and design integration to reduce weight and improve reliability of the envelope structure. For example, a dual layer envelope construction is used to separate the roles of helium barrier layer and load bearing, component mounting and environmental protection layer.

The platform's impressive performance characteristics, such as endurance, cannot be attributed to one element but is the sum of each part. The concert of innovations presented here have real potential as an effective and efficient platform to aid in search and rescue.

6.2. Future Directions

The research topics outlined below represent possible future directions that were outside the scope of the primary research objectives of this thesis. These areas were discovered through the author's own review of the current literature, peer review comments to submitted manuscripts, or recommendations of subject matter experts.

6.2.1. Advanced power management system

One area of future work is to apply intelligent power management algorithms for the different power plant loading conditions. The currently proposed flight controller tracks trajectories based on combined input from the gasoline-electric hybrid power plant and forward electric thrusters. The ideal combination of power inputted from these two independent sources depends the current state of the UAV (efficiency of each actuator, fuel remaining, battery SOC, tracking error, etc.) and should be optimized for the different scenarios outlined in section 2.2. Similarly, the power plant itself has several customizable set points. The current power plant controller is configured in an on-off operation when a command is sent from the UAV's on-board computer. Although the key operating set points were determined in this work, when to enact each set point also depends on the current state of the UAV.

Another important consideration is the requirements of the charge and discharge controller for the on-board battery. As mentioned previously in section 2.3.5, maintaining the battery within this useful battery capacity offers many advantages such as increased battery life and change/discharge efficiency. Maximizing power usage from the engine will lead to increased fuel efficiency but is limited by the charging rate of the battery system. The currently selected battery (Thunder Power 65C 5000mAh) has a proposed charging rate of 12C. Unfortunately, there are no commercially available battery chargers available that can charge at such rates and the side effects on the battery are unknown. The power management system should incorporate battery temperature and health in addition to the SOC.

Many supervisory controllers previously developed for hybrid electric road vehicles could be applied to the dirigible UAV power plant for this purpose. One

such option is the fuzzy logic controller for hybrid electric vehicles presented by Baumann et al [38]. The major difference is that the load schedule (or "driving" schedule) is not standardized and is dependent on the planned flight path which is not bound by roads. Using the trajectories generated by the trajectory planner as a guide, the optimal power plant operation could be determined through non-linear optimization techniques.

6.2.2. Air ballast testing and validation

The infrastructure of an airship is a well researched field with decades of literature published dating back to the late 19th century. Khoury and Gillett provide a comprehensive review of historical airship design practices, general principles and other considerations [19]. The most recent developments in airship technology are hull shape optimization [138, 139], unconventional shape designs [140], advances in materials including composite structures [141, 142], as well as some considerations of ballonet sloshing [142]. However, there is a very limited number of experimental and theoretical studies on ballonets that can be found to literature [100].

One future direction for this research is to investigate the use of an air ballast based altitude control system and compare its performance and energy consumption to conventional thrust vectoring for small UAVs. The purpose of this study would be to design a theoretical altitude control system that could later be applied in practice to a similar physical system. Typical methods of controlling airship altitude include using directional propellers (thrust vectoring), aerodynamic lift or ballonets. For most small airships, propellers can be a light weight solution for altitude control but require continuous power to maintain set positions and velocities. Aerodynamic lift requires relatively high speeds and complicates the option of hovering in one place. Ballonets on the other hand, take full advantage of the properties of helium and air to provide a low power solution to altitude control. In keeping with the research goal, reducing power consumption for altitude control will further extend flight endurance. The ballonets will also provide the alternate functions of pressure regulation to ensure reliability and weight ballasting to compensate for consumed fuel of the power plant.

Following the completion of the envelope assembly, the air ballasts should be experimentally tested. The results of the tests will provide the control responses used for the autopilot and trajectory planning controller designs. In addition, the air ballast power consumption data will be used to determine the efficiency and effectiveness of the air ballasts. This information can be used in a comparison study using thrust vectoring as a baseline (the conventional method of altitude control for small UAVs) to validate the use of air ballasts for small airship designs.

The comparison can be based on a performance metric that includes energy consumption, weight and performance indicators such as response time for various flight scenarios. The goal would be to determine if the benefit of increased in energy efficiency outweighs the increased weight penalty of adding an air ballast system. Also, if there is a benefit, to quantify the increase and the envelope size crossover point at which it becomes negligible.

6.2.3. Collision avoidance using a reactive replanning subroutine

All UAVs need to be certified by the air traffic control agency for use in restricted air space. Based on the use and dimensions of the prototype, it would need to be obtain a Special Flight Operation Certificate from Transport Canada [143]. Transport Canada states that the industry is not mature enough to merit a regulatory structure, and that each application is considered on a case-by-case basis [143]. The application requires the demonstration of the predictability and reliability of the UAV in the desired environment. When operating a UAV outside of visible range, there are additional requirements to prove satisfactory risk mitigation measures are in place. One of these measures is to have a "detect, sense and avoid" capability. The "avoid" aspect of this capability is handled by the path planner. Specifically, it is the ability to avoid collisions of static and dynamic obstacles.

Reactive re-planning algorithm must be able to execute and react quickly, especially for fast moving fixed wing UAVs. The algorithm typically re-plans only the most immediate segment of the path and needs to be able to re-plan at a higher frequency than the primary path planner. For this reason, it is usually implemented as a separate function that oversees flight operations and can interrupt the planned path when obstacles are detected. The UAV's ability to avoid dynamic obstacles depends on the object's speed relative to the UAV, the frequency, range and uncertainty of the available on-board sensor information and the frequency of the re-planning process. It's imperative that the MSZ from other aircraft is sufficiently large for UAVs with slow cruise velocities and reaction times, such as airships. The MSZ values should change based on the aircraft's probability density function of it's predicted linear trajectory [50]. If the path does not cross within 2σ of the aircraft's estimated position, the risk is deemed negligible. The standard deviation, σ, of the aircraft is modelled as a function of time and acceleration capability of the aircraft (if known) [144]. The MSZ for a moving object is increased based on a function of the object's relative speed and the uncertainty of it's trajectory.

One the largest hurdles of the sense and avoid problem is the detection of ob-

stacles. Many sensors such as RADAR or LADAR that are used in large scale UAVs are too large and heavy for micro UAVs [42]. Two sensors that have been used in collision avoidance are laser range finders and optic flow sensors. Griffiths et al presented an obstacle avoidance algorithm that relies on a laser range finder and optic flow sensors fixed to a small fixed wing UAV [42]. Using the laser range finder, they were able to implement an algorithm that avoids a single obstacle on the planned path. One of the limitations of the laser range finder used for the experiments was that it has a fixed forward direction (i.e. non-scanning) and therefore could not detect dynamic obstacle collisions. The optic flow sensors were positioned out the left and right wings with the intended use to allow the UAV to fly equidistant between walls (when walls are detected).

The use of vision based obstacle algorithms is well researched and still emerging field of study. Lorigo et al presented an visual-based obstacle avoidance system for a ground vehicle [145]. The system uses multiple independent visual processing modules that compare visual properties such as intensity gradients and color information to determine the perceived locations of obstacles. Olivares-Mendez et al developed see and avoid approach for a unmanned quad-rotor using fuzzy logic control to tune PID gains [146]. An on-board camera identifies a distinct and known static object and uses a fuzzy logic controller to ensure the object remains to the side edge of the video capture screen as the vehicle passes the obstacle. This method is limited to static obstacles know *a priori* and avoiding them at a fixed altitude. Zsedrovits et al investigate dynamic obstacle avoidance using a see-and-avoid algorithm to avoid air to air collisions of fixed wing aircraft [147]. The algorithm tracks and measures the distance and angle between the wing span of approaching fixed wing aircraft. The velocity vector is then calculated based on the rate of change of wing span and angle to be used to determine a safe path around the obstacle. This method was limited to fixed wing dynamic obstacles traveling on a straight flight course. Oliensis presents a critical review of several structure-from-motion algorithms as well as general experimental issues [148].

6.2.4. Full scale testing

Several sub-assembly tests were conducted that have not been mentioned previously. The two layer dirigible envelope consisting of a 2 mil Mylar helium barrier and a rip-stop nylon outer layer (used to protects the helium barrier and allows for the mounting of on-board components) was constructed. For ease of assembly and added reliability, a dual layer construction was used to separate the roles of helium barrier layer and load bearing and environmental protection layer. Commercially available materials such as polyester blown films and ripstop nylon were

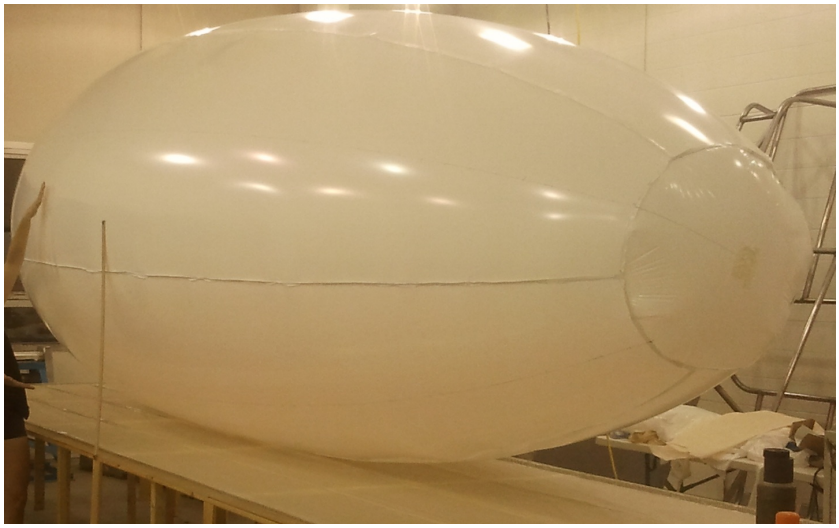

Figure 6.1.: Helium barrier

used for the envelope for availability and ease of assembly. The helium barrier was seamed by heat sealing when possible to reduce weight and adhesives otherwise. Figure 6.1 shows the helium barrier shape and construction. The helium envelope was pressure and leak tested by applying a soapy water solution and marking areas that bubble. Circular patches are cut and adhered to repair any damaged areas. . The load bearing layer was be machine sewn together with reinforced mounting supports for the fins and other mechanical devices. Two ballonets were constructed out of the same material used for the helium barrier. A high volume centrifugal blower was modified to be used for inflating and deflating the ballonets and a custom two-way valving system is purposed to direct the flow and hold air pressure in the ballonets. Helium is injected using a custom Schroeder valve fitted with a control servo for helium release during flight. The first complete assembly test was performed in a large, two story laboratory can be seen in Figure 6.2.

The next steps for the project is to perform full scale testing of the assembled dirigible UAV. Initial flight tests should be performed indoors to troubleshoot any potential problems with control or communication to the UAV. These tests will also be used as a baseline for the determining the control responses of each actuator to a step input used to perform system parameter identification. Parameter identification will be used to finely tune the reference model in the simulated trajectory planner and flight controller to mimic the physical prototype. Future tests should incorporate the trajectory planner and flight controller mentioned in Chapters 4 and 5, respectively. Ideally, the recommendations made previously in this section would also be implemented.

To facilitate full scale testing, a safety procedure has been outlined to mitigate any health risks during the initial flight test and included in Appendix D. Propul-

Figure 6.2.: Dirigible UAV fully assembled

sion, telemetry and power management systems have been fully instrumented into the gondola and onto the envelope. After some final modifications, the outdoor flight tests are proposed for Spring 2014, in a suitable flight space (at low altitude with a safety tether), to validate the design for real world surveillance operations.

References

[1] Internal Displacement Monitoring Centre, "Press Release - 42 million displaced by sudden natural disasters in 2010. http://www.internal-displacement.org/ [Online; Accessed June 2014]," 2011.

[2] Government of Canada, "National Search and Rescue Secretariat. http://www.nss.gc.ca [Online; Accessed June 2014]."

[3] Public Safety Canada, "Government of canada announces significant investment for emergency preparedness projects across canada, Government of Canada, Public Safety Canada. http://goo.gl/VqR6FA [Online; Accessed June 2014] Published in," 2011.

[4] H. Kelly, "Drones and the future of disaster response," May 2013.

[5] T. Sharples, "Get into Trouble Outdoors - Who Pays for the Rescue? http://www.time.com/time/nation/article/0,8599,1892621,00.html [Online; Accessed June 2014]," 2009.

[6] MacDonald, Dettwiler and Associates Ltd, "Geospatial services international - pricing information," Technical Report, MDA Corporation, 2012.

[7] J. Rao, Z. Gong, J. Luo, and S. Xie, "Unmanned airships for emergency management," in *Proceedings of the IEEE International Safety, Security and Rescue Robotics Workshop*, pp. 125–130, 2005.

[8] T. Fukao, A. Yuzuriha, T. Suzuki, T. Kanzawa, T. Oshibuchi, K. Osuka, T. Kohno, M. Okuyama, Y. Tomoi, and M. Nakadate, "Inverse optimal velocity field control of an outdoor blimp robot," in *Proceedings of the 17th IFAC World Congress*, pp. 4374–4379, 2008.

[9] H. Saiki, T. Fukao, T. Urakubo, and T. Kohno, "Hovering control of outdoor blimp robots based on path following," in *Proceedings of the IEEE International Conference on Control Applications*, pp. 2124–2129, 2010.

[10] R. Jia, M. T. Frye, and C. Qian, "Control of an airship using particle swarm optimization and neural network," in *Proceedings of the IEEE International Conference on Systems, Man and Cybernetics*, pp. 1809–1814, IEEE, 2009.

[11] P. Gonzalez, W. Burgard, R. Sanz, and J. Fernandez, "Developing a low-cost autonomous indoor blimp," *Journal of Physical Agents*, vol. 3, pp. 43–52, 2009.

[12] R. Valerdi, J. Merrill, and P. Maloney, "Cost metrics for unmanned aerial vehicles," *Proceedings in the AIAA 16th Lighter-Than-Air Systems Technology Conference and Balloon Systems Conference*, pp. 1–6, 2005.

[13] Reed Business Information Limited, "UAV Directory. http://goo.gl/BpIEH [Online; Accessed June 2014] Published in," 2010.

[14] US Department of Defense, "Unmanned aircraft systems roadmap 2005-2030," Technical Report, 2005.

[15] US Department of Defense, "2009 Worldwide UAV Roundup," Technical Report, 2009.

[16] S. Recoskie, A. Fahim, W. Gueaieb, and E. Lanteigne, "Hybrid power plant design for a long range dirigible UAV," *IEEE/ASME Transactions on Mechatronics*, vol. 19, pp. 606–614, 2013.

[17] A. Gawale and R. Pant, "Design studies of power plant system of non-rigid airships," Technical Report, Aerospace Engineering Department, Indian Institute of Technology, 2004.

[18] R. S. Pant, "A methodology for determination of baseline specifications of a non-rigid airship," *AIAA Journal*, vol. 6830, pp. 1–9, 2003.

[19] G. A. Khoury and J. D. Gillett, *Airship technology*. Cambridge university press London, 1999.

[20] P. Bogusz, M. Korkosz, and J. Prokop, "A study of design process of BLDC motor for aircraft hybrid drive," in *Proceedings of the IEEE International Symposium on Industrial Electronics*, pp. 508–513, 2011.

[21] D. Gaide, C. Humbargar, D. Larrabee, J. Marshman, E. Petersen, E. Serani, and E. Wormer, "Hybrid electric integrated optimized system; design of a hybrid propulsion system for aircraft," Technical Report, AIAA, 2011.

[22] R. R. Glassock, J. Y. Hung, L. F. Gonzalez, and R. A. Walker, "Multimodal hybrid powerplant for unmanned aerial systems (UAS) robotics," *Proceedings in the 24th Bristol International Unmanned Air Vehicle Systems Conference*, pp. 1–13, 2009.

[23] S. Recoskie, A. Fahim, W. Gueaieb, and E. Lanteigne, "Dirigible UAV power plant design," in *Proceedings of the International Conference on Unmanned Aircraft Systems*, pp. 1–9, 2012.

[24] R. M. Hiserote, "Analysis of hybrid-electric propulsion system designs for small unmanned aircraft systems," Master's thesis, Air Force Institute of Techology Wright-Patterson AFB, 2010.

[25] Paur, J. Wired Magazine, "Hybrid Power Comes to Aviation. http://goo.gl/EKF8fq [Online; Accessed June 2014]," 2009.

[26] D. Yu and X. Lv, "Configurations analysis for high-altitude/long-endurance airships," *Aircraft Engineering and Aerospace Technology*, vol. 82, pp. 48–59, 2010.

[27] M. Kotulla and S. Staudacher, "Power management and controls of a propulsion system for a lighter than air high altitude platform," in *Proceedings of the ASME Turbo Expo 2005: Power for Land, Sea, and Air*, vol. 1, pp. 601–607, 2012.

[28] S. Lubkowski, B. Jones, E. Rojas, and D. Morris, "Trade-off analysis of regenerative power source for long duration loitering airship," in *Proceedings of the IEEE Systems and Information Engineering Design Symposium*, pp. 25–30, 2010.

[29] S. Recoskie, A. Fahim, W. Gueaieb, and E. Lanteigne, "Experimental testing of a hybrid power plant for a dirigible UAV," *Journal of Intelligent and Robotic Systems*, vol. 69, pp. 69–81, 2013.

[30] B. W. McCormick, *Aerodynamics, aeronautics, and flight mechanics*. John Wiley and Sons, 1979.

[31] G. Rizzoni and T. T. Hartley, *Principles and applications of electrical engineering*. McGraw-Hill Higher Education, 2004.

[32] H. W. Lee, *Advanced control for power density maximization of the brushless DC generator*. PhD thesis, Texas A&M University, 2003.

[33] Woodbank Communications Ltd, "Battery and energy technologies http://www.mpoweruk.com/chemistries.htm/ [online; accessed june 2014] published in," 2010.

[34] M. Yoshio, R. J. Brodd, and A. Kozawa, *Lithium-ion batteries: science and technologies*. Springer Verlag, 2009.

[35] G. Zimmer, "Battery management design for high power lithium battery stacks," Technical Report, Linear Technology, 2009.

[36] E. P. Lesley, "Propeller tests to determine the effect of number of blades at two typical solidities," Technical Report, Stanford University, Daniel Guggenheim Aeronautical Laboratory, NACA Technical Note 698, 1939.

[37] R. W. Fox, A. T. McDonald, and P. J. Pritchard, *Introduction to fluid mechanics*, vol. 7. John Wiley & Sons New York, 1985.

[38] B. M. Baumann, G. Washington, B. C. Glenn, and G. Rizzoni, "Mechatronic design and control of hybrid electric vehicles," *IEEE/ASME Transactions on Mechatronics*, vol. 5, pp. 58–72, 2000.

[39] C. Goerzen, Z. Kong, and B. Mettler, "A survey of motion planning algorithms from the perspective of autonomous UAV guidance," *Journal of Intellegent Robotic Systems*, vol. 57, pp. 65–100, 2010.

[40] T. Lolla, M. P. Ueckermann, K. Yigit, P. J. H. Jr., and P. F. J. Lermusiaux, "Path planning in time dependent flow fields using level set methods," in *Proceedings of the IEEE International Conference on Robotics and Automation*, pp. 166–173, 2012.

[41] Z. Kong, V. Korukanti, and B. Mettler, "Mapping 3D guidance performance using approximate optimal cost-to-go function," in *Proceedings of the AIAA Navigation, Guidance and Control Conference*, pp. 1–21, 2009.

[42] S. Griffiths, J. Saunders, A. Curtis, T. McLain, and R. Beard, "Obstacle and terrain avoidance for miniature aerial vehicles," *IEEE Robotics and Automation Magazine*, vol. 3, pp. 34–43, 2006.

[43] J. Guivant, E. Nebot, J. Nieto, and F. Masson, "Navigation and mapping in large unstructured environments," *The International Journal of Robotic Research*, vol. 23, pp. 449–472, 2004.

[44] S. Kambhampati and L. S. Davis, "Multiresolution path planning for mobile robots," *IEEE Journal on Robotics and Automation*, vol. RA-2, pp. 135–145, 1986.

[45] D. K. Pai and L. M. Reissell, "Multiresolution rough terrain motion planning," *IEEE Transactions on Robotics and Automation*, vol. 14, pp. 19–33, 1998.

[46] M. Likhachev and D. Ferguson, "Planning long dynamically feasible maneuvers for autonomous vehicles," *The International Journal of Robotics Research*, vol. 28, pp. 933–945, 2009.

[47] Y. Sawaragi, H. Nakayama, and T. Tanino, *Theory of Multiobjective Optimization*. Academic Press, Inc., 1985.

[48] J. Guivant, E. Nebot, J. Nieto, and F. Masson, "Survey of multi-objective optimization methods for engineering," *Structural and multidisciplinary optimization*, vol. 26, pp. 369–395, 2004.

[49] C. Cocaud, "Autonomous tasks allocation and path generation of UAVs," Master's thesis, Ottawa-Carleton Institute for Mechanical and Aerospace Engineering, University of Ottawa, 2006.

[50] P. P. Y. Wu, D. Campbell, and T. Merz, "On-board multi-objective mission planning for unmanned aerial vehicles," in *Proceedings of the IEEE Aerospace conference*, pp. 1–10, 2009.

[51] M. Soulignac, "Feasible and optimal path planning in strong current fields," *IEEE Transactions on Robotics*, vol. 27, pp. 89–98, 2011.

[52] A. A. Masoud, "A harmonic potnetial field apparoach for planning motion of a UAV in a cluttered environment with a drift field," in *Proceedings of the IEEE Conference on Decision and Control*, pp. 7665–7671, 2011.

[53] W. H. Al-Sabban, L. F. Gonzalez, R. N. Smith, and G. F. Wyeth, "A wind-energy based path planning for electric unmanned aerial vehicles using markov decision processes," in *Proceedings of the IEEE International Conference on Robotics and Automation*, pp. 1–6, 2013.

[54] N. R. J. Lawrance and S. Sukkarieh, "A guidance and control strategy for dynamic soaring with a gliding UAV," in *Proceedings of the IEEE International Conference on Robotics and Automation*, pp. 3632–3637, 2009.

[55] J. Rubio and S. Kragelund, "The trans-pacific crossing: long range adaptive path planning for UAVs through variable wind fields," in *Proceedings of the 22nd Digital Avionics Systems Conference*, pp. 1–12, 2003.

[56] J. W. Langelaan, J. Spletzer, C. Montella, and J. Grenestedt, "Wind field estimation for autonomous dynamic soaring," in *Proceedings of the IEEE International Conference on Robotics and Automation*, pp. 16–22, 2012.

[57] A. Chakrabarty and J. Langelaan, "UAV flight path planning in time varying complex wind-fields," in *Proceedings of the American Control Conference*, pp. 2568–2574, 2013.

[58] A. Chakrabarty and J. W. Langelaan, "Energy Maps for Long Range Path Planning for Small and Micro UAVs," in *Proceedings of the Guidance, Navigation and Control Conference*, pp. 1–13, 2009.

[59] J. W. Langelaan, "Biologically inspired flight techniques for small and micro unmanned aerial vehicles," in *Proceedings of the Guidance, Navigation and Controls Conference*, pp. 1–13, 2008.

[60] P. C. Plate, *Aerodynamic Characteristics of Atmospheric Boundary Layers*. USAEC Critical Review Series, 1971.

[61] E. Besada-Portas, L. de la Torre, J. M. De La Cruz, and B. Andres-Toro, "Evolutionary trajectory planner for multiple UAVs in realistic scenarios," *IEEE Transactions on Robotics*, vol. 26, pp. 619–634, 2010.

[62] I. A. McManus, *A Multidisciplinary Approach to Highly Autonomous UAV Mission Planning and Piloting for Civilian Airspace*. PhD thesis, Queensland University of Technology, 2001.

[63] D. R. Nelson, D. B. Barber, T. W. McLain, and R. W. Beard, "Vector field path following for miniature air vehicles," *Proceedings of the IEEE Transactions on Robotics*, vol. 23, pp. 519–529, 2007.

[64] Z. Sjanic, "On-line mission planning based on model predictive control," Master's thesis, Division of Automatic Control, Department of Electrical Engineering, Linkoping University, 2001.

[65] L. Techy and C. A. Woolsey, "Minimum-time path planning for unmanned aerial vehicles in steady uniform winds," *Journal of Guidance Control and Dynamics*, vol. 32, pp. 1736–1746, 2009.

[66] A. A. Doshi, S. P. N. Singh, and A. J. Postula, "Towards reduced-order models for online motion planning and control of UAVs in the presence of wind," in *Australasian Conference on Robotics and Automation*, pp. 1–7, 2012.

[67] M. Soulignac, P. Taillibert, and M. Rueher, "Time-minimal path planning in dynamic current fields," in *Proceedings of the IEEE International Conference on Robotics and Automation*, pp. 2473–2479, 2009.

[68] C. Liu, O. McAreet, and W.-H. Chen, "Path following for small UAVs in the presence of wind disturbance," in *Proceedings of the UKACC International Conference on Control*, pp. 613–618, 2012.

[69] S. Lee and H. Bang, "Three-Dimensional Ascent Trajectory Optimization for Stratospheric Airship Platforms in the Jet Stream," *Journal of Guidance, Control, and Dynamics*, vol. 30, pp. 1341–1352, 2007.

[70] J. B. Mueller, Y. J. Zhao, and W. L. Garrad, "Optimal Ascent Trajectories for Stratospheric Airships Using Wind Energy," *Journal of Guidance, Control, and Dynamics*, vol. 32, pp. 1232–1245, 2009.

[71] R. F. Stengel, *Flight Dynamics*. Princeton University Press, 2004.

[72] R. W. Beard and T. McLain, *Small Unmanned Aircraft*. Princeton University Press, 2012.

[73] US Air Force, "Military specification: Flying qualities of piloted airplanes MIL-F-8785C," Technical Report, US Department of Defense, 1980.

[74] R. L. McNeely, R. V. Iyer, and P. R. Chandler, "Tour planning for an unmanned air vehicle under wind conditions," *Journal of Guidance, Control, and Dynamics*, vol. 30, pp. 1299–1306, 2007.

[75] National Oceanic and Atmospheric Administration, "National Weather Service http://graphical.weather.gov/sectors/ [Online; Accessed June 2014]."

[76] A. M. G. Lopes, "Windstation - a software for the simulation of atmospheric flows over complex topography," *Environmental Modelling & Software*, vol. 18, pp. 81–96, 2003.

[77] A. Harmat, I. Sharf, and M. Trentini, "A hybrid particle/grid wind model for realtime small UAV flight simulation," in *Proceedings of the International Conference on Intelligent Robots and Systems*, pp. 3780–3785, 2012.

[78] D. Galway, "Urban wind modeling with application to autonomous flight," Master's thesis, Department of Mechanical Engineering, Carleton University, 2009.

[79] D. Ferguson, M. Likhachev, and T. Stentz, "A guide to heuristic-based path planning," in *Proceedings of the International Workshop on Planning under Uncertainty for Autonomous Systems, International Conference on Automated Planning and Scheduling*, pp. 1–10, 2005.

[80] S. Behnke, "Local multiresolution path planning," in *Proceedings of the 7th RoboCup International Symposium*, pp. 332–343, 2003.

[81] U. Demiryurek, F. Banaei-Kashani, and C. Shahabi, "A case for time-dependent shortest path computation in spatial networks," in *Proceedings of the 18th SIGSPATIAL International Conference on Advances in Geographic Information Systems*, pp. 474–477, 2010.

[82] M. P. Wellman, M. Ford, and K. Larson, "Path Planning under Time-Dependent Uncertainty," in *Proceedings of the 11th Conference on Uncertainty in Artificial Intelligence*, pp. 532–539, 2013.

[83] S. F. Hoerner, *Fluid Dynamic Drag*. Hoerner Fluid Dynamics, 1965.

[84] S. P. Jones and J. D. DeLaurier, "Aerodynamic estimation techniques for aerostats and airships," in *Proceedings of the AIAA Lighter-than-Air Systems Conference*, pp. 120–126, 1981.

[85] J. W. Langelaan, "Tree-based trajectory planning to exploit atmospheric energy," in *Proceedings of the American Control Conference*, pp. 2328–2333, 2008.

[86] S. M. Lavalle, *Planning Algorithms*. Cambridge University Press, 2006.

[87] Canadian Council on Geomatics, "http://www.geobase.ca/ [online; accessed june 2014]."

[88] A. Garcia, J. L. Torres, E. Prieto, and A. De Francisco, "Fitting wind speed distributions: A case study," *Solar Energy*, vol. 62, pp. 139–144, 1998.

[89] Environment Canada, "Wind Speed over the Last Year (monthly data) for Vancouver. http://vancouver.weatherstats.ca/ [Online; Accessed June 2014]."

[90] S. B. V. Gomes, *An Investigation of the Flight Dynamics of Airships with Application to the YEZ-2A*. PhD thesis, Cranfield Institute of Technology, 1990.

[91] M. V. Cook, "The linearised small perturbation equations of motion for an airship," Technical Report, Cranfield Institute of Technology, 1990.

[92] S. B. V. Gomes and J. J. G. Ramos, "Airship dynamic modeling for autonomous operation," in *Proceedings of the International Conference on Robotics & Automation*, pp. 3462–3467, 1998.

[93] J. R. Azinheira, E. Carneiro de Paiva, and B. S. S., "Influence of Wind Speed on Airship Dynamics," *Journal of Guidance, Control, and Dynamics*, vol. 25, pp. 1116–1124, 2002.

[94] A. B. Moutinho, *Modeling and Nonlinear Control for Airship Autonomous Flight*. PhD thesis, Universidade Tecnica De Lisboa Instituto Superior Tecnico, 2007.

[95] P. G. Thomasso, "Equations of Motion of a Vehicle in a Moving Fluid," *Journal of Aircraft*, vol. 37, pp. 630–639, 2000.

[96] J. B. Mueller, M. A. Paluszek, and Y. Zhao, "Development of an aerodynamic model and control law design for a high altitude airship," in *Proceedings of the AIAA 3rd Unmanned Unlimited Technical Conference*, pp. 1–4, 2004.

[97] M. Z. Ashraf and M. A. Choudhry, "Dynamic modeling of the airship with MatLab using geometrical aerodynamic parameters," *Aerospace Science and Technology*, vol. 25, pp. 56–64, 2011.

[98] W. Yongmei and Z. Ming, "Trajectory tracking of a high altitude unmanned airship based on adaptive feedback linearization," in *Proceedings of the International Conference on Mechatronic Science, Electric Engineering and Computer*, pp. 2257–2261, 2011.

[99] J. Waishek, V. Kumar, and A. Dogan, "Investigation into the Time Varying Mass Effect on Airship Controller Performance," in *Proceedings of the AIAA Atmospheric Flight Mechanics Conference*, pp. 1–12, 2009.

[100] Y. Li, M. Nahon, and I. Sharf, "Airship dynamics modeling: A literature review," *Progress in Aerospace Sciences*, vol. 47, pp. 217–239, 2011.

[101] Z. Cai, W. Qu, and Y. Xi, "Dynamic modeling for airship equipped with ballonets and ballast," *Applied Mathematics and Mechanics*, vol. 26, pp. 1072–1082, 2005.

[102] X. Wu, C. Moog, and Y. Hu, "Modelling and linear control of a bouyancy-driven airship," in *Proceedings of the 7th Asian Control Conference*, pp. 75–80, 2009.

[103] N. Bessert and O. Frederich, "Nonlinear airship aeroelasticity," *Journal of Fluids and Structures*, vol. 21, pp. 731–742, 2005.

[104] S. Bennaceur and N. Azouz, "Contribution of the added masses in the dynamic modelling of flexible airships," *Nonlinear Dynamics*, vol. 67, pp. 215–226, 2012.

[105] H. Lamb, "The inertia coefficients of an ellipsoid moving in fluid," Technical Report, Aeronautical Research Committee, 1918.

[106] C. J. Atkinson and R. G. Urso, "Modeling of Apparent Mass Effects for the Real-Time Simulation of a Hybrid Airship," in *Proceedings of the AIAA Modeling and Simulation Technologies Conference and Exhibit*, pp. 1–12, 2006.

[107] X. Wang, Y. Ma, and S. X., "Modeling of stratosphere airship," in *Proceedings of the 3rd International Symposium on Systems and Control in Aeronautics and Astronautics*, pp. 738–743, 2010.

[108] H. Huang, K. Pavek, B. Novak, J. Albus, and E. Messina, "A Framework For Autonomy Levels For Unmanned Systems (ALFUS)," in *Proceedings of the AUVSI's Unmanned Systems North America*, pp. 1–9, 2005.

[109] H. Chen, X. Wang, and Y. Li, "A survey of autonomous control for UAV," in *Proceedings of the International Conference on Artificial Intelligence and Computational Intelligence*, pp. 267–271, 2009.

[110] E. Carneiro de Paiva, B. S. S., and M. Bergerman, "A Robust Pitch Attitude Controller for Aurora's Semi-Autonomous Robotic Airship," in *Proceedings of the 13th Lighter-Than-Air Systems Technology Conference*, vol. 25, pp. 141–148, 1999.

[111] A. Elfes, J. F. Montgomery, J. L. Hall, S. S. Joshi, J. Payne, and C. F. Bergh, "Autonomous flight control for a planetary exploration aerobot," in *Proceedings of the 8th International Symposium on Artifical Intelligence, Robotics and Automation in Space*, vol. 603, pp. 1–8, 2005.

[112] W. Adamski, P. Hennan, Y. Bestaoui, and K. Kozlowski, "Control of Airship in Case of Unpredictable Environment Conditions," in *Proceedings of the Conference on Control and Fault Tolerant Systems*, pp. 843–848, 2010.

[113] A. Moutinho and J. Azinheira, "A Gain-Scheduling Approach for Airship Path Tracking," *Informatics in Control Automation and Robotics*, vol. 15, pp. 263–275, 2008.

[114] J. Nakpiam, O. Daskiran, C. M. Elliott, and A. Dogan, "Airship Waypoint Navigation in the Presence of Wind," in *Proceedings of the AIAA Atmospheric Flight Mechanics Conference*, pp. 1–27, 2012.

[115] D. M. Acosta and S. S. Joshi, "Adaptive Nonlinear Dynamic Inversion Control of an Autonomous Airship for the Exploration of Titan," in *Proceedings*

of the AIAA Guidance, Navigation and Control Conference and Exhibit, pp. 1–13, 2007.

[116] A. Moutinho and J. Azinheira, "Path control of an autonomous airship using dynamic inversion," in *Proceedings of the 5th Symposium on Intelligent Autonomous Vehicles*, pp. 1–6, 2004.

[117] E. Kahale, P. C. Garcia, and Y. Bestaoui, "Autonomous path tracking of a kinematic airship in presence of unknown gust," *Journal of Intellegent Robotic Systems*, vol. 69, pp. 431–446, 2013.

[118] H. Bang, S. Lee, and H. Lee, "Nonlinear trajectory tracking using vectorial backstepping approach," in *Proceedings of the International Conference on Control, Automation and Systems*, pp. 169–174, 2008.

[119] L. Beji, A. Abichou, and Y. Bestaoui, "Stabilization of a nonlinear underactuated autonomous airship - a combined averaging and backstepping approach," in *Proceedings of the International Workshop on Robot Motion and Control*, pp. 223–229, 2002.

[120] F. Repoulias and E. Papadopoulos, "Robotic airship trajectory tracking control using a backstepping methodology," in *Proceedings of the IEEE International Conference on Robotics and Automation*, pp. 188–193, 2008.

[121] E. Hygounenc and P. Soueres, "Automatic airship control involving backstepping techniques," in *Proceedings of the IEEE International Conference on Systems, Man and Cybernetics*, vol. 6, pp. 1–6, 2010.

[122] T. Liesk, M. Nahon, and B. Boulet, "Design and experimental validation of a nonlinear low-level controller for an unmanned fin-less airship," *IEEE Trandsactions on Control System Technology*, vol. 21, pp. 1–9, 2013.

[123] J. R. Azinheira, A. Moutinho, and E. Carneiro de Paiva, "A backstepping controller for path-tracking of an underactuated autonomous airship," *International Journal of Robust and Nonlinear Control*, vol. 19, pp. 418–441, 2009.

[124] G. Murguia-Rendon, H. Rodriguez-Cortes, and M. Velasco-Villa, "Trajectory tracking control for the planar dynamics of a thrust vectored airship," in *Proceedings of the 52nd IEEE International Midwest Symposium on Circuits and Systems*, pp. 329–332, 2009.

[125] H. Fukushima, S. Ryosuke, and F. Matsuno, "Model predictive control of an autonomous blimp with input and output constraints," in *Proceedings of*

the IEEE Conference on Computer Aided Control System Design, pp. 2184–2189, 2006.

[126] Y. Yang, J. Wu, and Z. W., "Trajectory tracking for an autonomous airship using fuzzy adaptive sliding mode control," *Zhejian University Science C Computer and Electronicss*, vol. 13, pp. 534–543, 2012.

[127] F. P. Benjovengo, E. C. Piava, and S. S. Bueno, "Sliding Mode Control Approaches for an Autonomous Unmanned Airship," in *Proceedings of the 18th AIAA Lighter-Than-Air Systems Technology Conference*, pp. 1–12, 2009.

[128] J. Ko and D. J. Klien, "Gaussian Processes and Reinforcement Learning for Identification and Control of an Autonomous Blimp," in *Proceedings of the IEEE International Conference on Robotics and Automation*, pp. 1–6, 2007.

[129] Y. Liu, Z. Pan, D. Stirling, and F. Naghdy, "Control of autonomous airship," in *Proceedings of the International Conference on Robotics and Biomimetics*, vol. 9, pp. 2457–2462, 2009.

[130] T. S. Potdaar, A. Sinha, and R. S. Pant, "Controller Design for an Outdoor Autonomous Airship ," in *Proceedings of the AIAA Lighter-Than-Air Systems Technology Conference*, pp. 1–11, 2013.

[131] J. R. Azinheira and A. Mountinho, "Hover control of an uav with backstepping design including input saturation," *IEEE Transactions on Control Systems Technology*, vol. 16, pp. 517–526, 2008.

[132] M. M. Munk, "Aerodynamics of airships," *Aerodynamic Theory*, vol. 6, pp. 32–48, 1936.

[133] D. P. Raymer, *Aircraft Design: A Conceptual Approach.* AIAA Journal, 1989.

[134] Z. Zheng, W. Huo, and Z. Wu, "Autonomous airship path following control: Theory and experiments," *Control Engineering Practice*, vol. 21, pp. 769–788, 2013.

[135] S. Recoskie, W. Gueaieb, and E. Lanteigne, "Application of variable wind vector fields to a 3D multi-objective path planner for airship UAVs," *Submitted to IEEE Transactions on Robotics*, vol. PP, pp. 1–11, 2013.

[136] M. Kristic, I. Kanellakopoulos, and P. Kokotovic, *Nonlinear and Adaptive Control Design.* Wiley-Interscience, NY, 1995.

[137] H. K. Khalil, *Nonlinear Systems.* Prentice-Hall, NJ, 2002.

[138] T. S. Kanikdale, "Optimization of airship envelope shape using computational fluid dynamics," Master's thesis, Department of Aerospace Engineering, Indian Institute of Technology, Bombay, 2004.

[139] T. Lutz and S. Wagnery, "Drag reduction and shape optimization of airship bodies," Technical Report, Institute for Aerodynamics and Gas Dynamics, University of Stuttgart, Germany, 1998.

[140] L. Liao and I. Pasternak, "A review of airship structural research and development," *Progress in Aerospace Sciences*, vol. 45, pp. 83–96, 2009.

[141] W. Kang, Y. Suh, K. Woo, and I. Lee, "Mechanical property characterization of film fabric laminate for stratospheric airship envelope," *Composite Structures*, vol. 75, pp. 151–155, 2006.

[142] S. Maekawa, M. Nakadate, and A. Takegaki, "Structures of the low-altitude stationary flight test vehicle," *Journal of Aircraft*, vol. 2, pp. 662–666, 2007.

[143] Transport Canada, Government of Canada, "Unmanned air vehicle - Standards. http://goo.gl/nOkXGT [Online; Accessed June 2014]," 2010.

[144] D. Rathbun, S. Kragelund, and A. Pongpunwattana, "An evolution based path planning algorithm for autonomous motion of a uav through uncertain environments," in *Proceedings of the AIAA/IEEE Digital Avionics Systems Conference*, vol. 2, pp. 551–607, 2002.

[145] L. M. Lorigo, R. A. Brooks, and W. E. L. Grimsou, "Visually-guided obstacle avoidance in unstructured environments," in *Proceedings of the IEEE/RSJ International Conference on Intelligent Robots and Systems*, vol. 1, pp. 373–379, 1997.

[146] M. A. Olivares-Mendez, L. Mejias, P. Campoy, I. Mellado-Bataller, and I. Mondragon, "UAS See-and-Avoid using two different approaches of fuzzy control," in *Proceedings of the International Conference on Unmanned Aircraft Systems*, pp. 1–9, 2012.

[147] T. Zsedrovits, A. Zarandy, B. Vanek, T. Peni, J. Bokor, and T. Roska, "Estimation of relative direction angle of distant, approaching airplane in sense-and-avoid," *Journal of Intelligent and Robotic Systems*, vol. 69, pp. 407–415, 2013.

[148] J. Oliensis, "A critique of structure-from-motion algorithms," *Computer Vision and Image Understanding*, vol. 2, pp. 172–214, 2000.

A. Manuscripts

A.1. Dirigible UAV Power Plant Design

Presentation and full paper in the International Conference on Unmanned Aircraft Systems, 2012.

Dirigible UAV Power Plant Design

Steven Recoskie, Atef Fahim, Wail Gueaieb, Eric Lanteigne

***Abstract*—Dirigibles have the ability to take off and land vertically, hover and maintain lift without consuming energy and can be easily deflated for packaging and transportation. As such, dirigibles are well suited for surveillance and surveyance missions such as rescue and aid operations after disasters. This paper reviews hybrid dirigible UAV design considerations and presents a novel hybrid power plant design. The hybrid power plant design consists of a 2-stroke 4cc glow engine in-line with a brushless DC motor/generator and variable pitch propeller capable of producing a maximum power output of 148.4W.**

Introduction

Dirigibles have several advantages over fixed wing and rotary wing aircraft. They have the ability to maintain lift without consuming energy making them ideal for long range and long endurance missions. This ability also allows them to take off and land vertically without the need for a runway and hover in place to monitor developments on the ground. Dirigibles can be easily deflated for packaging and transportation and then inflated on site before operation. As such, dirigibles are well suited for use as reconnaissances platform to aid rescue crews after disasters [1]–[5].

An endurance and payload comparison between fixed wing, rotary wing and dirigible UAVs is shown in Figure 1. These data were collected and combined from multiple sources [6]–[9]. UAVs that do not travel, such as aerostats, and upper atmosphere UAVs were excluded. Data were also excluded if inconsistent between publications or when only a range was provided. Based on the data in Figure 1, it can be seen that the majority of UAVs with payloads under 1 kg have a flight endurance of 1 hour or less. Furthermore, UAVs that have large payload and endurance tend to have large unit cost. Cost metrics can be used to compare the performance of the entire spectrum of UAVs [6]. A cost metric consisting of the cubed root of the products of range, endurnace, and payload is applied for a baseline of existing techonologies. Based on the performance results shown in Figure 2, it is clear that a robust UAV system is needed to meet the operation requirements of both long endurance and long range while maintaining a low unit cost.

This paper presents the design and testing for a novel hybrid power plant design for a UAV dirigible. First, power requirements and design considerations are discussed. Then an overview of the power plant design followed by the methodology and results from the experimental testing. The UAV design is then compared to existing UAVs on the basis of cost, payload, range and endurance.

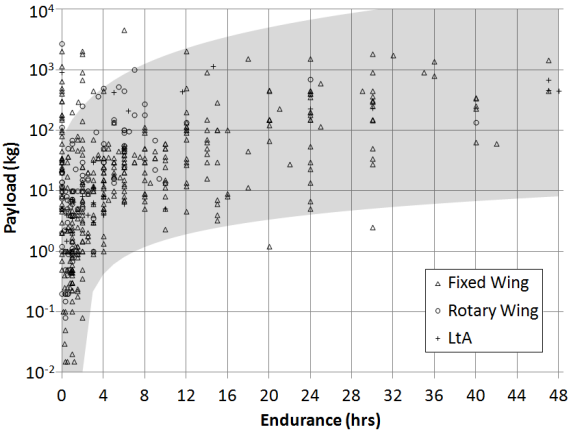

Figure 1: UAV Payload Capacity versus Endurance. Data was collected from both military and research agencies from several countries. These data were summarized from multiple sources [6]–[9].

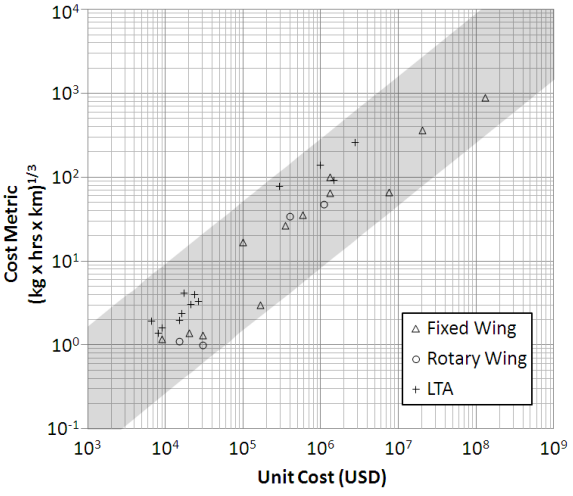

Figure 2: UAV Cost Metric (Payload x Endurance x Range) versus Unit Cost [6]–[9]

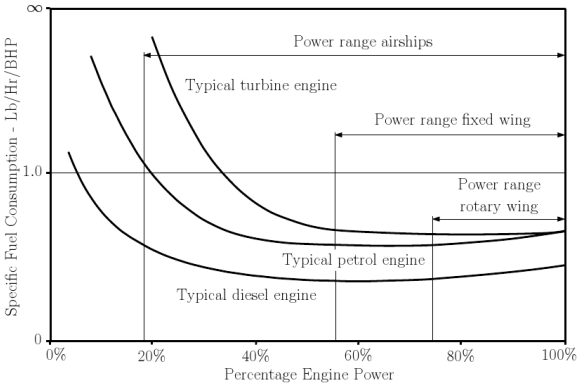

Figure 3: Specific Fuel Consumption for different aircraft types [10]

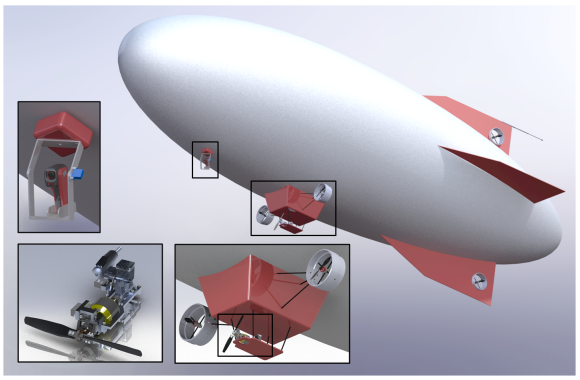

Figure 4: Dirigible design (middle), camera, GPS and inertial navigation system (left), hybrid power plant (lower left), and auxiliary electric propulsion (below)

Dirigible UAV Power Requirements

The propulsive power requirements of lighter than air (LTA) aircraft are far greater than of heavier than air (HTA) aircraft as LTA aircraft do not require propulsive power for lift. This presents a problem when selecting a suitable prime mover. Electrical power requirements for LTA aircraft can be over 65% total power and average cruise speeds compared to 15% for HTA aircraft [10]. Purely electric propulsion designs have significantly shorter flight endurance due to the lower energy density of electric power storage coupled with high electrical power requirements. Purely piston powered propulsion designs suffer from significant increases in specific fuel consumption at low engine power (during idling) and have a narrow peak efficiency range which makes varying the load on the engine undesirable. Furthermore, electrical energy storage is still required for avionics, therefore neither fuel or electric energy cannot be fully consumed during flight (the first depleted will limit flight endurance). The generally accepted ideal solution is to drive electric generators from piston powered propulsion engines [10], [11].

Hybrid Power Plant Design

The proposed hybrid power plant consists of an engine, a brushless DC generator and a propeller connected in series as shown in Figure 4. This configuration provides the most flexible operating conditions as both fuel and electrical energy can be depleted simultaneously (maximizing flight endurance). The engine can be shut down during periods when propulsion or electrical generation is not required and the generator can be run in reverse to start the engine when required, eliminating the need for a separate starter motor. Starting and stopping the engine as required keeps the engine under constant load and maximum efficiency, and maintains the batteries in the their useful operating range. Properly matching the engine and generator speed ranges can minimize specific fuel consumption of the engine. Maximum propeller efficiency can be achieved by implementing a variable pitch propeller. When the power plant is connected to the UAV, the engine is turned on according to the current flight conditions. The conditions can include distance remaining to target, UAV operating speed, opposing wind and the State of Charge (SOC) of the battery. This design can be adjusted for the following three scenarios:

1) Maximum engine efficiency - Minimizing engine fuel consumption and maximizing flight duration are paramount in this operating mode. The loading of the engine is held in its maximum efficiency zone by balancing the mechanical propulsion and electrical generation based on the current flight conditions, trip characteristics and SOC of the battery.
2) Maximum propulsion - This mode is used when propulsion is required but not electrical generation such as when the batteries are charged but the LTA needs to move to a position quickly. During this time, the batteries cells can be electrically disconnected and the propeller pitch can be adjusted to maximum thrust based on current airspeed.
3) Maximum electrical generation - This mode is used when electrical generation is required but not propulsion such as when the batteries need to recharge and the LTA is hovering in one place. During this time, the propeller pitch is adjusted to a feathered position and additional battery cells are electrically connected.

Design Considerations

The maximum in-flight fuel usage for LTA aircraft is restricted by the maximum takeoff weight and the minimum landing weight [10]. To extend the inflight fuel usage, it is assumed that air will be gradually collected to balance fuel depletion. For the purposes of this design, the maximum in-flight fuel usage will be limited to 3kg of fuel. If severe overpressure is detected, helium will be vented to prevent damage to the helium bladder. This method is ideal because it provides a means for altitude control and can regulate the dirigible's internal pressure to safe levels.

Another design consideration is the battery charging rate. The generally accepted charging rate of most lithium ion

rechargeable batteries is no more than one times the battery capacity. Hybrid designs benefit over purely electric designs in that most of the energy is stored in fuel which has a much higher energy density then a battery's energy density. Ideally, the battery capacity should be minimized to reduce the weight of the power plant. Since the battery capacity is limited by the magnitude of power it can accept and the duration it is rated to accept it, the battery was chosen based on the maximum electrical generation of the selected engine-generator combination. Recently, new generation lithium polymer batteries have been released that offer twelve times the capacity charging rate. This significantly lowers the battery capacity limitation and thus reduces the size and weight of the battery.

Sizing

The initial sizing of the components was determined using the methodology proposed by Pant [12]. The iterative loop begins by estimating the helium volume storage of the airship, also known as the envelope. The envelope, air ballast and tail fin geometry, and the static lift were then calculated based on the volume estimate and the optimal aspect ratio. The optimal aspect ratio of airship length over diameter was selected to be 3.3 based on the minimum sum of form and skin drag on the streamlined National Physics Laboratory low drag airship body shape. Drag, total propulsion power, electric capacity and fuel weight were estimated based on the desired operating performance. The weights of the envelope, gondola, fins, and all sub-systems were estimated using preselected materials or weight factors modeled on existing LTAs [10], [12]. The work envelope is iterated until the difference of lift to weight (payload) converges to a satisfactory value [12].

HYBRID POWER PLANT DESIGN OVERVIEW

Engine

Three options for the prime mover include petrol engines, diesel engines and gas turbines. Gas turbines can be omitted based on the relative scale of the UAV being designed (under 2 hp). Engine selection effects specific fuel consumption and weight per unit power. For petrol engines these values are 0.46 lb/(HP-hr) and 0.85 kg/HP while for diesel engines these values are 0.37 lb/(HP-hr) and 1.025 kg/HP [10]. Diesel engines are more efficient per HP and have improved reliability over spark ignition engines. Model (Glow-plug) Engines operate similar to a diesel engine except for the fact that they have a heat filament to aid in combustion and that they use alcohol fuels rather than diesel fuel. A table of fuel properties is presented in Table I. Model engines are best suited for this design and are readily available in the required horsepower range.

These engines come in two or four stroke cycles. Two stroke engines have a higher power to weight ratio, a lower cost per HP, and a simple construction with fewer moving parts. Four stroke engines have a higher fuel efficiency per HP, a longer engine life, a large range of peak engine performance, and tend to run quieter and cleaner. If the peak engine efficiency is matched with the generator output, and controlled in an on and off manner, then having a narrow peak efficiency range is sufficient. A two stroke OS 25LA model engine was chosen for its high power to weight ratio.

[1]The purpose of castor oil in 2-stroke glow fuel is for lubrication. During normal operating, oil is not considered to burn during combustion and as such does not contribute to the lower heating value value of the fuel mix.

Table I: Fuel properties

Fuel Type	Density $\left[\frac{kg}{L}\right]$	Lower heating value $\left[\frac{MJ}{kg}\right]$
Petrol	0.745	43
Diesel	0.832	45.4
Ethanol	0.789	31.1
Methanol	0.792	19.9
Nitromethane	1.137	11.3
Castor Oil	0.961	0[1]
15% Glow Fuel	0.874	15.0

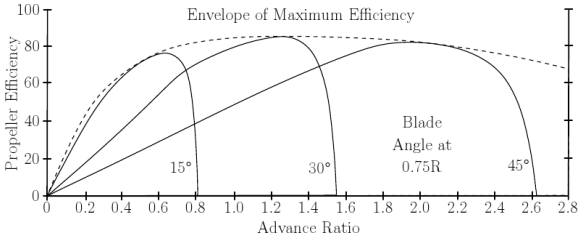

Figure 5: Propeller efficiency versus advance ratio for various propeller pitches [13]

Propulsion

The primary propulsion system consists of a variable pitch propeller connected to the model engine. The variable pitch propeller allows for the three different design scenarios proposed previously. The propeller pitch can be set to the feathered position to charge the battery pack without moving the aircraft. It can also be used to control the engine load for maximum engine efficiency when both generating electrical power and propelling. Alternatively, the propeller pitch can be optimized to maximize propulsion efficiency for a given engine speed when not generating electrical power.

In addition to the primary propulsion system, four additional brushless DC motors, connected to fixed pitch propellers, are used for low speed cruising when the engine is turned off, and for directional control while the UAV is hovering. The UAV's electric propulsion is shown in Figure 4.

Starter/ Generator

The motor constant of a DC motor is determined from the number of turns and size of the coil. It can be shown that the rated power of the motor is inversely proportional to the motor constant. The motor constant dictates the ratio of rotational speed to voltage and current to torque. The most important consideration when using a motor as both a starter and generator is the selection of motor constant because

the optimal values for these two functions are contradictory. As a generator, the motor constant needs to be sufficiently large such that voltage is generated at a higher potential than the batteries. Most small electronic devices operate at 12V or lower and small model engines run at very high speeds (typically in excess of 10kRPM). As a starter, the motor constant needs to be sufficiently small such that the starting torque can overcome inertia and friction in the engine[2]. The torque required to induce a single turn in the engine was experimentally determined to be approximately 0.7 Nm using a pulley and incremental weights.

A common solution is to add a transmission stage or separate motors for each function, however this adds weight, complexity and non negligible frictional losses. The solution was to use a large electrical motor (with a lower motor constant) and to down convert the output voltage to a useable range when generating using a high efficiency switching buck converter.

The options for electric motors include induction, brushed DC, or brushless DC (a type of 3-phase synchronous motor). Brushless DC motors generate 3-phase AC when driven, therefore they require filtering and rectification. Brushless DC motors also need a specialized electronic speed controller. However, they benefit from higher efficiency and a high power to weight ratio over conventional brushed DC motors. They have excellent heat dissipation, low noise, low maintenance, and great longevity and reliability because there are no brushes to replace [14]. An AXI 4120 brushless DC motor was selected since high efficiency power electronic circuits for motor control, filtering, rectification and DC/DC conversion have advanced to a point where they can be easily and inexpensively assembled in a small form factor using open source designs.

The main disadvantage of a brushless DC generator is that conventional rectification methods cannot achieve the maximum power possible because of a distorted or unsuitable current waveform [15]. A method is proposed by Lee [15] to maximize the power density of a brushless DC generator by actively switching rectifier diodes with PWM signals. Although this method of rectification provides higher efficiencies and the same power stage used for driving the motor could be theoretically used in reverse, its control is complex and requires a high-speed digital signal processor to detect the back EMF and current waveforms. Incorporating a 20 million instruction per second digital signal processor on-board for the sole purpose of rectification is unfeasible therefore a full bridge passive diode rectifier was selected for its low cost, simple construction and lack of complex control.

Another concern regarding power generation is the power factor. Unlike most power generation applications, the brushless DC generator will experience low resistance ($10^0\Omega$) and large operating speeds ($10^3 \frac{rad}{s}$) leading to high inductance.

[2]Particularly when the engine is starting cold, there is an interference fit between the piston head and the cylinder. As the engine heats up during combustion this tolerance increases allowing it to move more freely. This ensures a proper sealing during combustion.

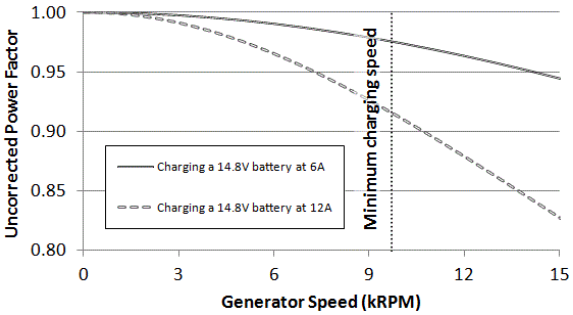

Figure 6: Uncorrected Power Factor

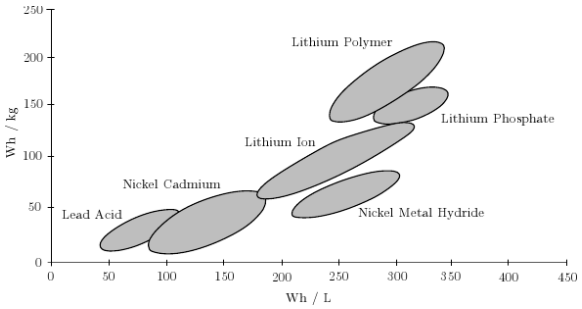

Figure 7: Energy densities of various battery compositions [16]

During high operating speeds, the power factor will begin to drift away from unity as the voltage and current become out of phase with each other as shown in Figure 6. The power factor can be corrected by adding a capacitor in parallel to the resistive load per phase of the generator. This type of power factor correction is only optimal (close to unity) for one operating speed therefore the power factor will decrease as the generator speed moves away from the corrected speed. Since the engine's peak efficiency occurs over a narrow speed range and the engine operation would be relatively constant at the optimal speed, passive power factor correction will be adequate. The results of experimental test on the power generator were used to determine the optimal engine/generator speed and select the power correction factor.

DC/DC conversion is also required in two separate cases on board the dirigible. First to regulate the output voltage of the generator to the working range of the battery charger (16.8V) and second to regulate the battery voltage down to 12V, 5V, and 3.7V sources used by the auxiliary components such as the on-board computer, electric propulsion motors and servo motors. A high efficiency step down (buck) controller circuit was selected for both situations.

Energy Storage

A comparison of different battery chemistries on the basis of energy mass density and energy volume density (Watt-hours/Liter) is shown in Figure 7. Lithium polymer batteries are the newest generation of lithium batteries offering the

highest energy density compared to other types. They have no memory effect, a good life cycle, high energy efficiency [17]. The most important attributes of this battery are its fast charge and discharge rates. This is vital to hybrid designs as one of the power limitations of hybrid power plants is the charging current provided by the generator. The maximum charging rate for lithium polymer batteries is limited to one times the capacity. The battery capacity must be chosen as a compromise been maximizing charging rate and minimizing weight.

Lithium polymer batteries are not tolerant to over charging or over discharging which both lead to thermal runaway so they require an added protection circuit to prevent these conditions [17]. Battery damage and thermal runaway are associated with overheating. Maximum heat generation in a properly ventilated battery occurs during the final stages of charging (trickle charging) and during discharging (increases as the SOC is reduced). Charging a Li-Ion battery to 100% SOC, or discharging to 0% SOC will degrade its long term capacity [18]. Li-Ion operation SOC is usually limited to a smaller range, such as 30% to 70%. This reduces the useful battery capacity to only 40% of the fully specified capacity [18]. Therefore, the practical energy density of the battery is reduced. Although the useful battery capacity is a limitation of purely electric systems, hybrid systems have the advantage of maintaining the battery in it's useful range by charging more frequently. This offers many advantages both for the battery and the efficiency of the system. As with all batteries, its life is extended by avoiding the damaging and inefficient periods of overheating shown in Figure 8. In combination with a hybrid system, keeping the battery within its useful range increases the effective energy density of the system when combined with fuel. Avoiding low power input trickle charge when the battery is near full SOC ensures that the loading on the engine is more stable and the engine is only used in its peak efficiency range. Avoiding near empty SOC prevents battery voltage fluctuations and voltage cutoff during discharging.

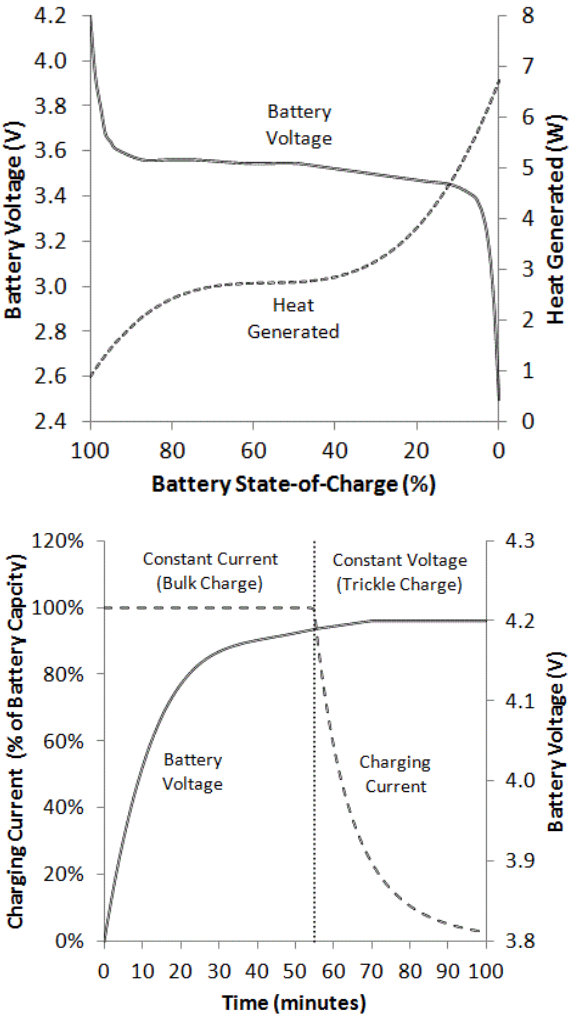

Figure 8: Typical Discharge (top) and Charge (bottom) Curves of a Lithium-Ion Battery [18]

Methodology

The hybrid power plant shown in Figure 9 consists of a glow engine, a brushless DC generator, a controllable pitch propeller. The plant frame is fixed to a pressurized air bed that provides a virtually frictionless contact to the test bench. The static thrust of the propeller is measured by a cable connected to a digital scale. Fuel flow is measured by taking mass readings every 10ms. The glow plug and electronic speed controller are connected to a double throw power relay that switches between the electronic speed controller (starter mode) and the 3-phase rectifier (generator mode). If the rotational speed of the brushless DC motor (measured by the frequency to voltage converter) is below 3000RPM, the relay is switched to starter motor and the glow plug is powered. When generating, the electrical load of the battery and charger is simulated using a rheostat (variable resistance) set to the equivalent resistance of the charger and battery in series. The free stream air velocity represents the velocity of the air entering the propeller. Tests were performed at five different free stream velocity speeds produced by an electric blower to simulate the effect of the dirigible traveling at those speeds.

Tests were performed to determine the power plant's useful power output, energy consumption and overall efficiency with respect to changing engine throttle, fuel mixture richness, propeller pitch, electrical load resistance, and free steam velocity. Table II contains a list of controlled variables and their ranges.

Results

The recorded data points were segmented into groups according to engine speed, and averaged to produce the operating envelope shown in Figure 10. Data points below the engine's start-up speed (3000 RPM) were omitted. Useful

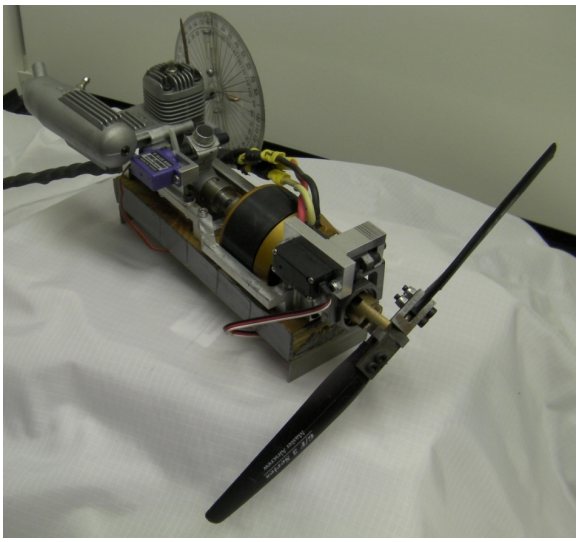

Figure 9: Experimental hybrid power plant

Table II: List of controlled variables and their operating ranges

Parameter	Minimum	Maximum	Increment
Engine Throttle	50% (half)	100% (full)	12.5%
Needle Value	360 (lean)	720 (rich)	30
Propeller Pitch	15°	45°	15°
Electrical Resistance	1.4	5.6	1.4
Free Stream Air Velocity	0 m/s	20 m/s	4 m/s

power was calculated based on the sum of propulsion and electrical power such that,

$$P_U = P_P + P_G$$

$$P_U = F_T \times \nu_f + V_g \times I_g$$

Where P_U is the total useful power produced [W], P_P is the propulsion power [W], P_G is the generation power [W], F_T is the propeller thrust [N], ν_f is the free stream velocity in [m/s], V_g is the generation voltage [V], and I_g is the generation current [A].

Data points in the 98^{th} percentile were considered to represent the useful power operating envelope. Overall system efficiency, η_O, was calculated as the ratio of useful power over input power, P_I [W]

$$\eta_O = \frac{P_U}{P_I}$$

The input power is defined by,

$$P_I = \dot{m}_F \times \rho_e$$

where $\dot{m}_F$ is the mass flow rate of fuel [g/s] and ρ_e is the fuels energy density [W/g].

Based on the operating envelope, the engine was unable to reach it's optimal operating speed of 15000 RPM specified by the manufacturer due to the increase in torque caused by friction bearings and the added inertia of generator and other rotating components. The useful power begins to plateau after 9000 RPM and the maximum useful output power achieved was 148.4W. In comparison, the engine's rated output given in the manual is 447.6W (7.4% engine efficiency at 0.4g/s fuel consumption of 15% nitromethane glow fuel). This difference can be attributed to the loses due to propeller and generator efficiencies (maximum of 50% and 85% respectively) and friction torque in bearings (the transmission efficiency is variable with engine speed but is roughly estimated to be 80%). A summary of these losses is shown in Figure 11. The engine's fuel consumption was much higher than expected at upwards of 0.4g/s at maximum efficiency which tended to lower overall efficiencies.

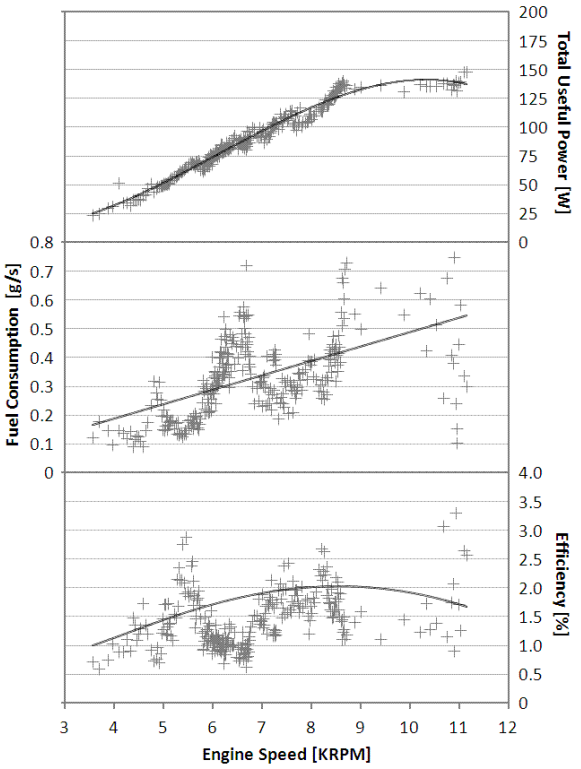

Figure 10: Engine operating envelope for the OS 25LA two stroke model aero engine

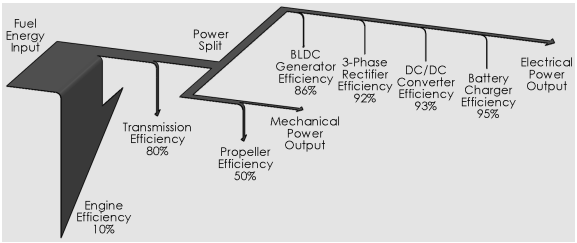

Figure 11: Summary of hybrid power plant losses

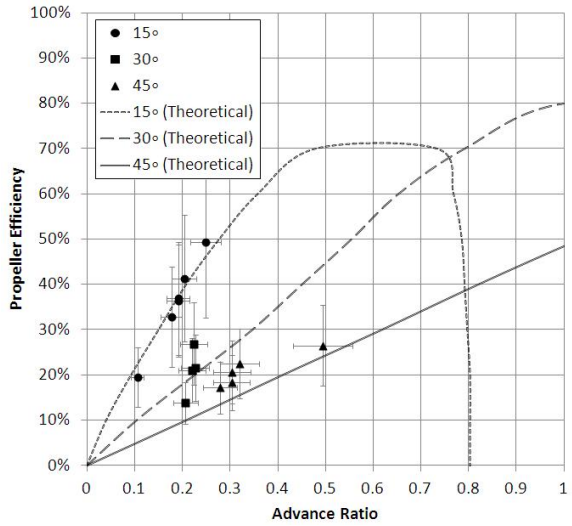

Figure 12: Propeller efficiency at 3Ω resistance

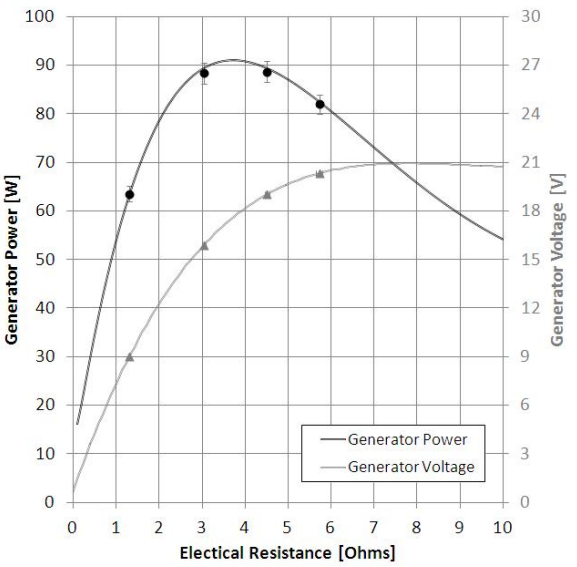

Figure 13: Generator power at 15°propeller pitch

The propeller's efficiency for three pitch settings versus advance ratio are illustrated in Figure 12. Propeller pitch was measured at 0.75R from the axis of rotation. The advance ratio is the ratio between the distance a propeller moves forward through the fluid during one revolution and is defined as,

$$J = \frac{\nu_f}{n_e \times d_p}$$

Where n_e is the engine speed [rev/s], and d_p is the diameter of the propeller [m].

Propeller efficiency values correspond well with theoretical values presented by McCormick [13] shown in Figure 5. Two separate methods were used to calculate propeller efficiency and compared. The first approach uses the classical definition for efficiency as the ratio of useful propulsion power out over power absorbed and was written as,

$$\eta_{P1} = \frac{P_P}{P_A} = \frac{F_T \times \nu_f}{\omega_e \times T_P}$$

Where P_P is the useful propulsion power [W], P_A is the power absorbed [W], ω_e is the engine speed [rad/s], and T_P is the engine torque absorbed [Nm].

The propeller torque cannot be measured directly as it is a function of the engine torque, generator torque and frictional losses. Therefore, the propeller torque was estimated based on engine speed and propeller pitch using the following set of equations which were produced using propeller tables presented by Lesley [19],

$$C_T = 1.83 \times 10^9 * \theta^2 + 1.04 \times 10^8 * \theta + 1.70 \times 10^8$$

$$T_P = C_T \times \omega_e^2$$

Where θ is the propeller pitch in inches.

The second method used to calculate propeller efficiency is based on disk actuator theory [20],

$$\eta_{P2} = \frac{1}{1 + \frac{\nu_f - \nu_w}{\nu_f}}$$

where ν_w is the velocity of the air in the wake of the propeller [m/s].

Both methods produced efficiencies within 10% however only the first method is presented in Figure 12 since it was considered to have lower cumulative error. Due to the size of the airship, flight speeds above $10\frac{m}{s}$ are unfeasible based on the total available propulsion power on-board. Therefore advance ratios above 0.3 are unfeasible. Based on Figure 12, propeller pitch will remain between 0 and 15 degrees to maximize the propeller efficiency for all foreseeable flight conditions.

The maximum generator power is shown in Figure 13. The electrical resistance represents the electrical load applied from the electrical propulsion motors, servos, and other on board electronics. Only electrical power produced with voltages above 14.8V can be used due to the battery voltage therefore, resistances below 3Ω are not useful. Maximum electrical generation is achieved between 3Ω and 4.5Ω of 90W. Above 4.5Ω, power begins to drop as the engine is no longer able to increase it's speed to increase the voltage and the current reduces following ohm's law.

The average current draw required by the brushless DC motor to start the engine was measured to be 35.7A (with a peak of 49.6A) at 14.8V which translates into 538.4W. However, the average time before the engine began driving the brushless DC motor was 0.28 sec leading to an energy draw of the battery of 41.9mWh. The servos used to vary the engine throttle and pitch angle drew 1.08W and 2.00W and were typically used only at start up for less than 5 seconds (1.5mWh and 2.8mWh, respectively). The glow

plug drew a constant 7.58W over 5 seconds resulting in a drain of 10.5mWh. The microcontroller used to generate the PWM signals is run continuously, but enters a power save mode when not receiving an input. Thus reducing its active consumption from 20mW to 1.2mW and can be neglected. The total energy required to start the engine once is 56.7mWh or about 0.06% of the battery's capacity.

The current design can run the glow engine for 2.08 hours on 3 kg of fuel at the maximum efficiency point. Given the 88.8Wh battery capacity on-board plus 90W regeneration and assuming an average of 50W power draw from electric propulsion and electronics results in an overall flight endurance of 5.52 hours. With 60W mechanical propulsion during engine on time and assuming 30W electric propulsion on average the maximum range of the airship (with zero net wind) is 123km.

The power and energy density of the glow engine hybrid system at the optimal operating point can be calculated for a given amount of fuel. The power density, δ_P, is found by,

$$\delta_P = \frac{P_U}{\sum m_f + \sum m_v}$$

and energy density, δ_E, is found by,

$$\delta_E = \frac{P_U \times t_r}{\sum m_f + \sum m_v}$$

Where t_r is the operating time, $\sum m_f$ is the sum of fixed or dead masses such as the engine, motor and frame, and $\sum m_v$ is the sum of variable masses such as fuel, the number or capacity of batteries or a combination of both. These two equations form the operational limits of each system which are represented by lines shown in Figure 14. The horizontal asymptote is the maximum power density and is governed by the maximum output power of the power plant considered. If the variable mass is infinitesimally small, maximum power density is achieved. The vertical asymptote is the maximum energy density and is governed by the energy density of the fuel source. If the power plant has an infinite supply of fuel or batteries, the maximum energy density is achieved, since the operating time depends on the about of fuel or the total capacity of batteries available.

A point is plotted on Figure 14 for the current system given 3 kg of fuel. Given the electric motor and propeller efficiency and lithium polymer batteries as the current system, similar points can be constructed for a fully electric system and a gasoline hybrid system. Figure 14 indicates a 31% improvement in energy density with 3 kg worth of fuel over that of a fully electric system with 3 kg of batteries. Energy density is paramount over power density for long duration missions as the mass of the fuel becomes larger than the mass of the power plant. Considering this, further improvement is possible if a 4-stroke gasoline engine is used in the place of the 2-stroke glow engine. Gasoline has a 154% increase in energy density over 15% glow fuel and requires less oil in the mixture (which does not contribute towards useful work). A spark ignition would also provide practical benefits of reliable start up and ignition timing compared

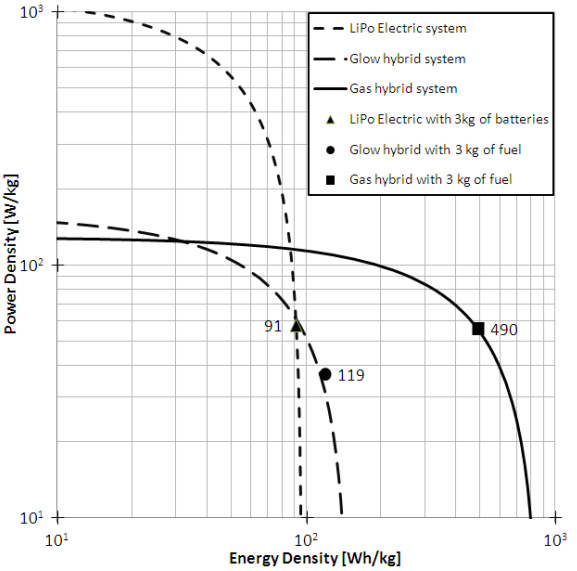

Figure 14: Power density versus energy density for electric, glow hybrid and gas hybrid systems

to a glow plug. Although 4-stroke engines generally weigh more than 2-stroke engines at the same power, they have significantly lower fuel consumption rates which becomes paramount when carrying over 1 kg of fuel.

The conservatively estimated overall cost for fabricating a single unit is $5,000. The cost metric as presented in Figure 2 for this UAV design is 8.8. The average UAV cost metric at the same price point is 1.9. This represents a 363% increase compared to existing designs.

Conclusion

The energy density of the purposed hybrid power plant design was proven to be higher than an equivalent purely electric system through experimental testing, despite subpar engine performance. Utilizing a 4-stroke gasoline based engine such as the Saito fg-14b, which has a manual rated power output of 895.2W and fuel consumption of 0.096g/s (22.8% engine efficiency using gasoline with 20:1 synthetic oil mix), would increase overall efficiency substantially. A further 154% increase is expected for a similar design with implementation of this engine instead of the 2-stroke glow engine.

References

[1] J. Rao, Z. Gong, J. Luo, and S. Xie, "Unmanned airships for emergency management," in *Safety, Security and Rescue Robotics, Workshop, 2005 IEEE International*, pp. 125–130, IEEE, 2005.

[2] T. Fukao, A. Yuzuriha, T. Suzuki, T. Kanzawa, T. Oshibuchi, K. Osuka, T. Kohno, M. Okuyama, Y. Tomoi, and M. Nakadate, "Inverse optimal velocity field control of an outdoor blimp robot," in *Proc. of the 17th IFAC World Congress*, pp. 4374–4379, 2008.

[3] H. Saiki, T. Fukao, T. Urakubo, and T. Kohno, "Hovering control of outdoor blimp robots based on path following," in *Control Applications (CCA), 2010 IEEE International Conference on*, pp. 2124–2129, IEEE.

[4] R. Jia, M. Frye, and C. Qian, "Control of an airship using particle swarm optimization and neural network," in *Systems, Man and Cybernetics, 2009. SMC 2009. IEEE International Conference on*, pp. 1809–1814, IEEE, 2009.
[5] P. González, W. Burgard, R. Sanz Domínguez, and J. López Fernández, "Developing a low-cost autonomous indoor blimp," *Journal of Physical Agents. Vol. 3, No. 1 (Jan. 2009). ISSN 1888-0258, pp. 43-52*.
[6] R. Valerdi, J. Merrill, and P. Maloney, "Cost metrics for unmanned aerial vehicles," in *AIAA 16th Lighter-Than-Air Systems Technology Conference and Balloon Systems Conference*.
[7] R. B. I. Limited, "Uav directory," 2010.
[8] D. Defense, "Unmanned aircraft systems roadmap 2005-2030," tech. rep., Tech. rep., August, 2005.
[9] D. Defense, "2009 worldwide uav roundup," tech. rep., Tech. rep., August, 2009.
[10] G. Khoury and J. Gillett, *Airship technology*. Cambridge university press London, 1999.
[11] A. Gawale and R. Pant, "Paper 2004-01-design studies of power plant system of non-rigid airships," *Aerospace Engineering Department, Indian Institute of Technology Bombay, Mumbai-400076*.
[12] R. Pant, "A methodology for determination of baseline specifications of a non-rigid airship," *AIAA Paper*, vol. 6830, 2003.
[13] B. McCormick, *Aerodynamics, aeronautics, and flight mechanics*. Wiley, 1979.
[14] G. Rizzoni and T. Hartley, *Principles and applications of electrical engineering*. McGraw-Hill Higher Education, 2004.
[15] H. Lee, *Advanced control for power density maximization of the brushless DC generator*. PhD thesis, Texas A&M University, 2003.
[16] W. C. Ltd, "Battery and energy technologies," 2010.
[17] M. Yoshio, R. Brodd, and A. Kozawa, *Lithium-ion batteries: science and technologies*. Springer Verlag, 2009.
[18] G. Zimmer, "Battery management design for high power lithium battery stacks," tech. rep., Linear Technology, 2009.
[19] P. Lesley, E, "Propeller tests to determine the effect of number of blades at two typical solidities," tech. rep., Stanford University, Daniel Guggenheim Aeronautical Laboratory, NACA Technical Note 698, 1939.
[20] R. Fox, A. McDonald, and P. Pritchard, *Introduction to fluid mechanics*, vol. 7. John Wiley & Sons New York, 1985.

A.2. Experimental Testing of a Hybrid Power Plant for a Dirigible UAV

J Intell Robot Syst (2013) 69:69–81
DOI 10.1007/s10846-012-9764-8

Experimental Testing of a Hybrid Power Plant for a Dirigible UAV

Steven Recoskie · Atef Fahim · Wail Gueaieb · Eric Lanteigne

Received: 29 June 2012 / Accepted: 31 July 2012 / Published online: 24 August 2012

Abstract Dirigibles have the ability to take off and land vertically, hover and maintain lift without consuming energy, and can be easily deflated for packaging and transportation. As such, dirigibles are well suited for surveillance and surveyance missions such as rescue and aid operations after disasters. This paper reviews hybrid dirigible UAV design considerations, then presents a novel hybrid power plant design. The hybrid power plant design consists of a 2-stroke 4cc glow engine in-line with a brushless DC motor/generator and variable pitch propeller. The experimental results have shown that the hybrid power plant is capable of producing a power output of 148.4 W.

Keywords Dirigible · Unmanned aerial vehicle · Hybrid power plant · Long endurance · Low cost · Variable pitch propeller · Energy efficient systems

S. Recoskie ( ) · A. Fahim · E. Lanteigne
Mechanical Engineering, University of Ottawa, Ottawa, Canada
e-mail:

W. Gueaieb
Electrical Engineering, University of Ottawa, Ottawa, Canada

1 Introduction

Dirigibles have several advantages over fixed wing and rotary wing aircraft. They have the ability to maintain lift without consuming energy making them ideal for long range and long endurance missions. This ability also allows them to take off and land vertically without the need for a runway and hover in place to monitor developments on the ground. Dirigibles can be easily deflated for packaging and transportation and then inflated on site before operation. As such, dirigibles are well suited for use as reconnaissances platform to aid rescue crews after disasters [1–5].

An endurance and payload comparison between fixed wing, rotary wing and dirigible UAVs is shown in Fig. 1. These data were collected and combined from multiple sources [6–9]. UAVs that do not travel, such as aerostats, and upper atmosphere UAVs were excluded. Data were also excluded if inconsistent between publications or when only a range was provided. Based on the shaded area in Fig. 1, it can be seen that the majority of UAVs with payloads under 1 kg have a flight endurance of 1 h or less. Furthermore, UAVs that have large payload and endurance tend to have large unit cost.

Cost metrics can also be used to compare the performance of the entire spectrum of UAVs [6]. A cost metric consisting of the cubic root of the products of range, endurance, and payload is

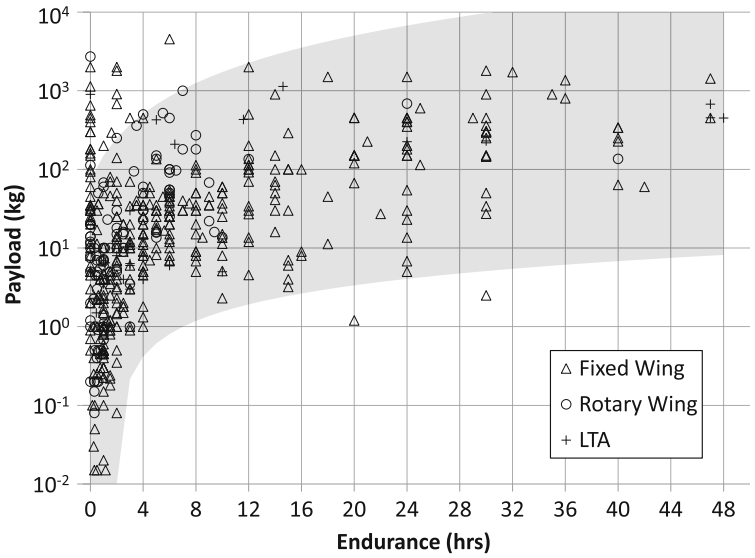

Fig. 1 UAV payload capacity versus endurance. Data was collected from both military and research agencies from several countries. These data were summarized from multiple sources [6–9]

applied for a baseline of existing technologies. Based on the performance band shown in Fig. 2, it is clear that a robust UAV system is needed to meet the operation requirements of both long endurance and long range while maintaining a low unit cost.

This paper presents the design and testing for a novel hybrid power plant design for a UAV dirigible. First, power requirements and design considerations are discussed. Then an overview of the power plant design is presented, followed by the methodology and results of the experimental testing. The UAV design is then compared to existing UAVs on the basis of cost, payload, range and endurance.

1.1 Dirigible UAV Power Requirements

The propulsive power range of lighter than air (LTA) aircraft are far greater than of heavier than air aircraft as shown in Fig. 3. This presents a problem when selecting a suitable prime mover. Electrical power requirements for LTA aircraft can be over 65 % total power [10]. Purely electric propulsion designs have significantly shorter flight endurance due to the lower energy density of electric power storage coupled with high

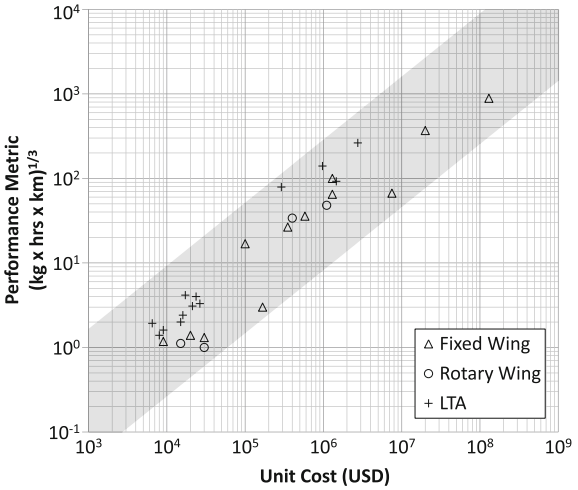

Fig. 2 UAV cost metric (payload × endurance × range) versus unit cost [6–9]

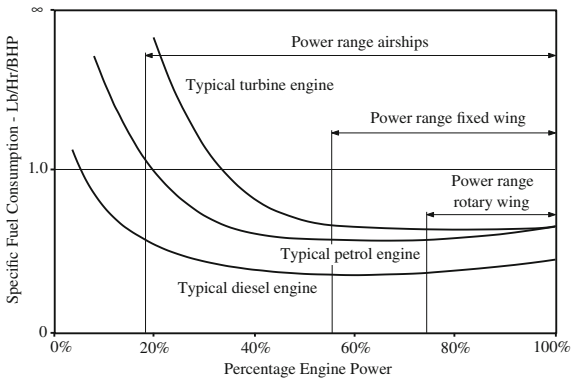

Fig. 3 Specific fuel consumption for different aircraft types [10]

electrical power requirements. Purely piston powered propulsion designs suffer from significant increases in specific fuel consumption at low engine power (during idling) and have a narrow peak efficiency range which makes varying the load on the engine undesirable. Furthermore, electrical energy storage is still required for avionics, therefore neither fuel or electric energy cannot be fully consumed during flight (the first depleted will limit flight endurance). The generally accepted ideal solution is to drive electric generators from piston powered propulsion engines [10, 11]. The proposed system extends the piston engine and electric motor combination by including a variable pitch propeller that acts as the primary mover. It will be shown that this allows for both fuel and electric energy to be completely consumed while eliminating the losses associated with running the engine at low engine power.

1.2 Hybrid Power Plant Design

The proposed hybrid power plant consists of an engine, a brushless DC generator, and a propeller connected in series as shown in Fig. 4. This configuration provides the most flexible operating conditions and the maximum flight endurance. The engine can be shut down during periods when propulsion or electrical generation is not required and the generator can be run in reverse to start the engine when required. This eliminates the need for a separate starter motor. Starting and stopping the engine as required keeps the engine under constant load and maximum efficiency, and maintains the batteries in the their useful operating range. When the power plant is connected to the UAV, the engine is turned on according to the current flight conditions. These conditions include: distance remaining to target, UAV operating speed, opposing wind, and the State of Charge (SOC) of the battery. The proposed design can be adjusted for the following three scenarios:

(1) Maximum engine efficiency—Minimizing engine fuel consumption and maximizing flight duration are paramount in this operating mode. The loading of the engine is held in its maximum efficiency zone by balancing the mechanical propulsion and electrical generation based on the current flight conditions, trip characteristics and SOC of the battery.
(2) Maximum propulsion—This mode is used when propulsion is required but not electrical generation such as when the batteries are charged but the LTA needs to move to a position quickly. During this time, the batteries cells can be electrically disconnected and the propeller pitch can be adjusted to maximum thrust based on current airspeed.
(3) Maximum electrical generation—This mode is used when electrical generation is required but not propulsion such as when the batteries need to recharge and the LTA is hovering

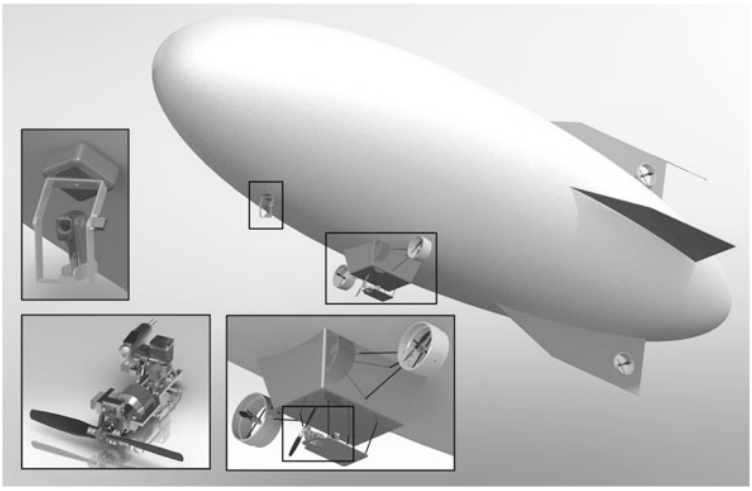

Fig. 4 Dirigible design (*middle*), camera, GPS and inertial navigation system (*left*), hybrid power plant (*lower left*), and auxiliary electric propulsion (*below*)

in one place. During this time, the propeller pitch is adjusted to a feathered position and additional battery cells are electrically connected.

Properly matching the engine and generator speed ranges is essential to minimizing the specific fuel consumption of the engine. Maximum propeller efficiency can be achieved by implementing a variable pitch propeller.

1.3 Design Considerations

The maximum in-flight fuel usage for LTA aircraft is restricted by the maximum takeoff weight and the minimum landing weight [10]. To extend the inflight fuel usage, it is assumed that air will be gradually collected to balance fuel depletion. For the purposes of this design, the maximum in-flight fuel usage will be limited to 3 kg of fuel. If severe overpressure is detected, helium will be vented to prevent damage to the helium bladder. This method is ideal because it provides a means for altitude control and can regulate the dirigible's internal pressure to safe levels.

Another design consideration is the battery charging rate. The generally accepted charging rate of most lithium ion rechargeable batteries is no more than one times the battery capacity. Ideally, the battery capacity should be minimized to reduce the weight of the power plant. Since the battery capacity is limited by the magnitude of power it can accept and the duration it is rated to accept it, the battery was chosen based on the maximum electrical generation of the selected engine-generator combination. Recently, new generation lithium polymer batteries have been released that offer twelve times the capacity charging rate. This significantly lowers the battery capacity limitation and thus reduces the size and weight of the battery pack.

1.4 Sizing

The initial sizing of the components was determined using the methodology proposed by Pant [12]. The iterative loop begins by estimating the helium volume storage of the airship, also known as the envelope. The envelope, air ballast and tail fin geometry, and the static lift were then calculated based on the volume estimate and the optimal aspect ratio. The optimal aspect ratio of airship length over diameter was selected to be 3.3 based on the minimum sum of form and skin drag on the streamlined National Physics Laboratory low drag airship body shape. The weights of the envelope, gondola, fins, and all sub-systems were estimated using preselected materials or weight factors modeled on existing LTAs [10, 12]. The work envelope is iterated until the difference of lift to weight (payload) converges to a satisfactory value [12]. Drag, total propulsion power, electric capacity and fuel weight were estimated based on the desired operating performance.

For the proposed UAV dirigible the weight of the work envelope was iterated until a payload of 1 kg was achieved to allow for additional accessories or modifications. Given a net lift of 12 kg, the total installed propulsive power, electric capacity and fuel weight were estimated at 720 W, 75 Wh and 3 kg, respectively.

2 Hybrid Power Plant Design Overview

2.1 Engine

Three options for the prime mover include petrol engines, diesel engines, and gas turbines. Gas turbines were omitted based on the relative scale of the UAV being designed (under 2 hp). The selection of the engine was based on the specific fuel consumption and weight per unit power. For petrol engines these values are 0.46 lb/(HP-hr) and 0.85 kg/HP while for diesel engines these values are 0.37 lb/(HP-hr) and 1.025 kg/HP [10]. Diesel engines are more efficient per HP and have improved reliability over spark ignition engines. Model (Glow-plug) Engines operate similar to a diesel engine except for the fact that they have a heat filament to aid in combustion and that they use alcohol fuels rather than diesel fuel. A model engine was selected for this design for its high power to weight ratio and availability in the required horsepower range.

These engines come in two or four stroke cycles. Two stroke engines have a higher power to

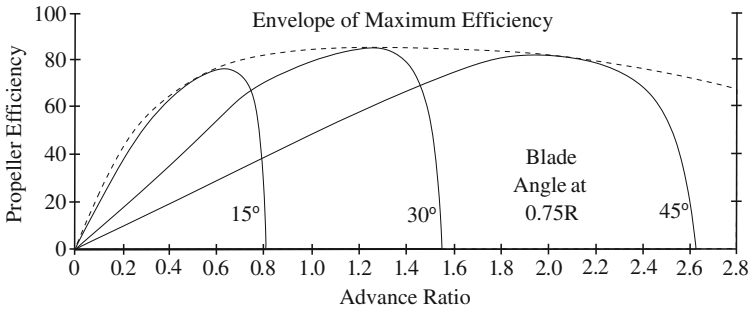

Fig. 5 Propeller efficiency versus advance ratio for various propeller pitches [13]

weight ratio, a lower cost per HP, and a simple construction with fewer moving parts. Four stroke engines have a higher fuel efficiency per HP, a longer engine life, a large range of peak engine performance, and tend to run quieter and cleaner. If the peak engine efficiency is matched with the generator output, and controlled in an on and off manner, then having a narrow peak efficiency range is sufficient. Therefore, a two stroke OS 25LA model engine was chosen for its high power to weight ratio.

2.2 Propulsion

The primary propulsion system consists of a variable pitch propeller connected to the model engine. The variable pitch propeller allows for the three different design scenarios proposed previously. The propeller pitch can be set to the feathered position to charge the battery pack without moving the aircraft. It can also be used to control the engine load for maximum engine efficiency when both generating electrical power and propelling. Alternatively, the propeller pitch can be optimized to maximize propulsion efficiency for a given engine speed when not generating electrical power (Fig. 5).

In addition to the primary propulsion system, four additional brushless DC motors, connected to fixed pitch propellers, are used for low speed cruising when the engine is turned off, and for directional control while the UAV is hovering. This configuration provides greater maneuverability and eliminates the need for operating the engine at low RPMs. The UAV's electric propulsion is shown in Fig. 4.

2.3 Starter/Generator

The motor constant of a DC motor is determined from the number of turns and size of the coil. It can be shown that the rated power of the motor is inversely proportional to the motor constant. The motor constant dictates the ratio of rotational speed to voltage and current to torque. The most important consideration when using a motor as both a starter and generator is the selection of motor constant since the optimal values for these two functions are contradictory. As a generator, the motor constant needs to be sufficiently large such that voltage is generated at a higher potential than the batteries. Most small electronic devices operate at 12 V or lower and small model engines run at very high speeds (typically in excess of 10 kRPM). As a starter, the motor constant needs to be sufficiently small such that the starting torque can overcome inertia and friction in the engine.[1] The torque required to induce a single turn in the engine was experimentally determined to be approximately 0.7 Nm using a pulley and incremental weights.

A common solution is to add a transmission stage or separate motors for each function, however this adds weight, complexity and non negligible frictional losses. The solution was to use a large electrical motor (with a lower motor constant) and to down convert the output voltage to a

[1]Particularly when the engine is starting cold, there is an interference fit between the piston head and the cylinder. As the engine heats up during combustion this tolerance increases allowing it to move more freely. This ensures a proper sealing during combustion.

useable range when generating electricity using a high efficiency switching buck converter.

The options for electric motors include induction, brushed DC, or brushless DC (a type of 3-phase synchronous motor). Brushless DC motors generate 3-phase AC when driven, therefore they require filtering and rectification. Brushless DC motors also need a specialized electronic speed controller. However, they benefit from higher efficiency and a high power to weight ratio over conventional brushed DC motors. They have excellent heat dissipation, low noise, low maintenance, and great longevity and reliability because there are no brushes to replace [14]. An AXI 4120 brushless DC motor was selected since high efficiency power electronic circuits for motor control, filtering, rectification and DC/DC conversion have advanced to a point where they can be easily and inexpensively assembled in a small form factor using open source designs.

The main disadvantage of a brushless DC generator is that conventional rectification methods cannot achieve the maximum power possible because of a distorted or unsuitable current waveform [15]. A method is proposed by Lee [15] to maximize the power density of a brushless DC generator by actively switching rectifier diodes with PWM signals. Although this method of rectification provides higher efficiencies and the same power stage used for driving the motor could be theoretically used in reverse, its control is complex and requires a high-speed digital signal processor to detect the back EMF and current waveforms. Incorporating a 20 million instruction per second digital signal processor on-board for the sole purpose of rectification is unfeasible therefore a full bridge passive diode rectifier was selected for its low cost, simple construction and lack of complex control.

Another concern regarding power generation is the power factor. Unlike most power generation applications, the brushless DC generator will experience low resistance ($10^0\Omega$) and large operating speeds ($10^3 \frac{\text{rad}}{\text{s}}$) leading to high inductance. During high operating speeds, the power factor will begin to drift away from unity as the voltage becomes out of phase with the current. This is shown in Fig. 6. The power factor can be corrected by adding a capacitor in parallel to the resistive load of each phase of the generator. This type of power factor correction is only optimal (close to unity) for one operating speed therefore the power factor will decrease as the generator speed moves away from the corrected speed. Since the engine's peak efficiency occurs over a narrow speed range and the engine operation would be relatively constant at the optimal speed, the passive power factor correction was selected. The results of experimental test on the power generator were used to determine the optimal engine/generator speed and select the power correction factor. Three capacitors of 45.5 μF were used to correct the power factor at 9,000 RPM.

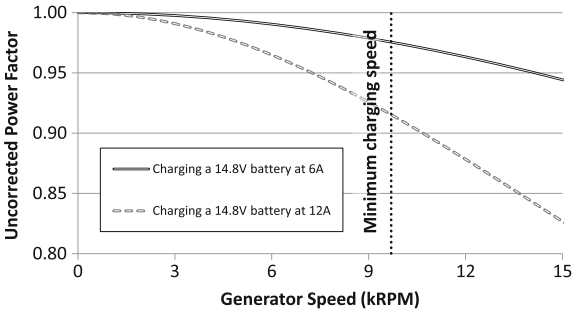

Fig. 6 Uncorrected power factor

DC/DC conversion is also required in two separate cases on board the dirigible. First to regulate the output voltage of the generator to the working range of the battery charger (16.8 V) and second to regulate the battery voltage down to 12 V, 5 V, and 3.7 V sources used by the auxiliary components such as the on-board computer, electric propulsion motors and servo motors. A high efficiency step down (buck) controller circuit was selected for this purpose.

2.4 Energy Storage

A comparison of different battery chemistries on the basis of energy mass density and energy volume density (Watt-hours/Liter) is shown in Fig. 7. Lithium polymer batteries are the newest generation of lithium batteries offering the highest energy density compared to other types. They have no memory effect, a good life cycle, high energy efficiency [17]. The most important attributes of this battery are its fast charge and discharge rates. This is vital to hybrid designs as one of

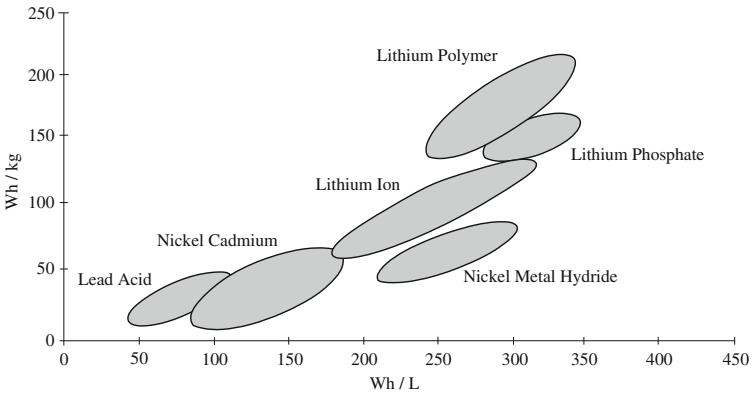

Fig. 7 Energy densities of various battery types [16]

the power limitations of hybrid power plants is the charging current provided by the generator. The maximum charging rate for lithium polymer batteries is limited to one times the capacity. The battery capacity must be chosen as a compromise been maximizing charging rate and minimizing weight.

Lithium polymer batteries are not tolerant to over charging or over discharging which both lead to thermal runaway. Therefore, they require an added protection circuit to prevent these conditions from occurring [17]. Battery damage and thermal runaway are associated with overheating which, in a properly ventilated battery, occurs during the final stages of charging (trickle charging) and during discharging (increases as the SOC is reduced) as shown in Fig. 8. Charging a Li-Ion battery to 100 % SOC, or discharging to 0 % SOC will degrade its long term capacity [18]. Li-Ion operation SOC is usually limited to a smaller range, such as 30 % to 70 %. This reduces the useful battery capacity to only 40 % of the fully specified capacity [18].

Although the useful battery capacity is a limitation of purely electric systems, hybrid systems have the advantage of maintaining the battery in it's useful range by charging more frequently. This offers many advantages both for the battery and the efficiency of the system. Avoiding low power input trickle charge when the battery is near full SOC ensures that the loading on the engine is more stable and the engine is only used in its peak efficiency range. Avoiding near empty SOC prevents battery voltage fluctuations and voltage cutoff during discharging.

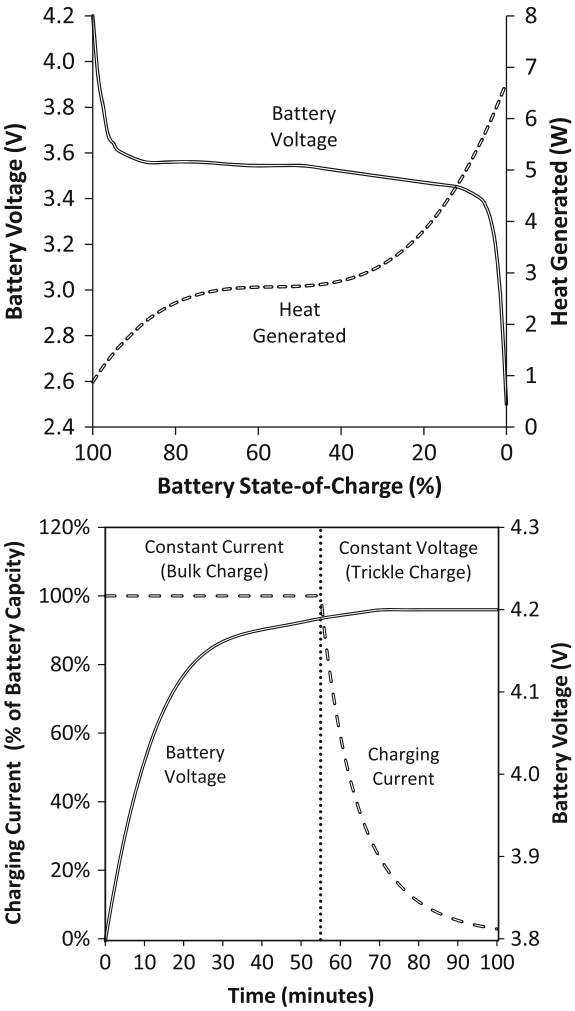

Fig. 8 Typical discharge (*top*) and charge (*bottom*) curves of a Lithium-Ion battery [18]

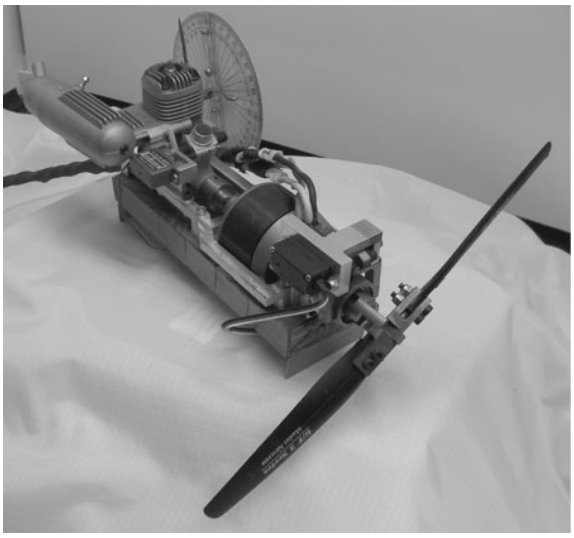

Fig. 9 Experimental hybrid power plant

3 Methodology

The experimental platform shown in Fig. 9 consists of a glow engine, a brushless DC generator, and a controllable pitch propeller connected in series. The plant frame is fixed to a pressurized air bed that provides a virtually frictionless contact to the test bench. The static thrust of the propeller is measured by a cable connected to a digital scale. Fuel flow is measured by taking mass readings every 10 ms. The glow plug and electronic speed controller are connected to a double throw power relay that switches between the electronic speed controller (starter mode) and the 3-phase rectifier (generator mode). If the rotational speed of the brushless DC motor (measured by the frequency to voltage converter) is below 3000 RPM, the relay is switched to starter motor and the glow plug is powered. When generating, the electrical load of the battery and charger is simulated using a rheostat (variable resistance) set to the equivalent resistance of the charger and battery in series. The free stream air velocity is the velocity of the air entering the propeller. Tests were performed at five different free stream velocity speeds produced by an electric blower to simulate the effect of the dirigible traveling at those speeds.

The power plant's useful power output, energy consumption and overall efficiency were determined by varying the engine throttle, fuel mixture richness, propeller pitch, electrical load resistance, free steam velocity, and the nitromethane content in the fuel. Table 1 contains a list of all these control variables and their ranges.

4 Results

The recorded data points were segmented into groups according to engine speed, and averaged to produce the operating envelope shown in Fig. 10. Data points below the engine's start-up speed (3000 RPM) were omitted. The useful total power P_U was calculated based on the sum of propulsion power P_P and electrical power P_G such that,

$$P_U = P_P + P_G$$

where,

$$P_P = F_T \times v_f$$

$$P_G = V_g \times I_g$$

where P is in [W], F_T is the propeller thrust in [N], v_f is the free stream velocity in [m/s], V_g is the generation voltage in [V], and I_g is the generation current in [A].

Data points in the 98th percentile were considered to represent the useful power operating

Table 1 List of controlled variables and their operating ranges

Parameter	Minimum	Maximum	Increment
Engine throttle	50 % (half)	100 % (full)	12.5 %
Needle value	360 (lean)	720 (rich)	30
Propeller pitch	15°	45°	15°
Electrical resistance	1.4	5.6	1.4
Free stream air velocity	0 m/s	20 m/s	4 m/s
Nitromethane content	5 %	15 %	5 %

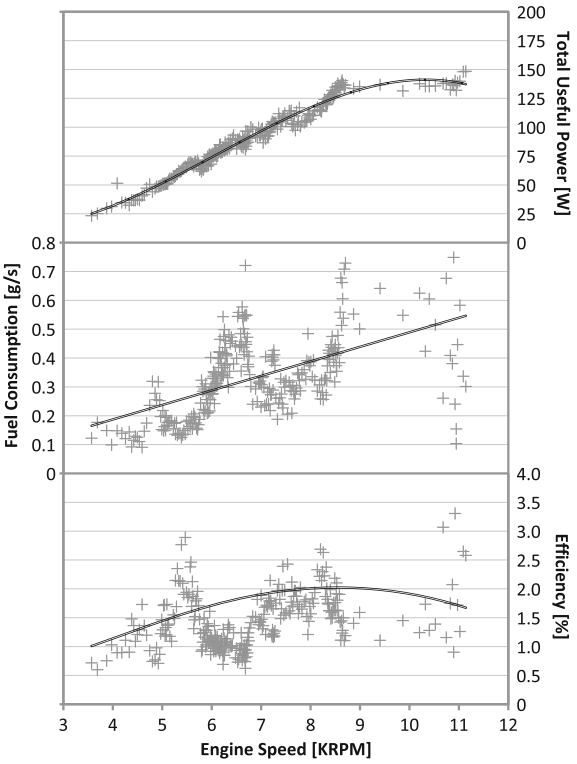

Fig. 10 Engine operating envelope for the OS 25LA two stroke model aero engine

envelope. Overall system efficiency, η_O, was calculated as the ratio of useful power over the input power, P_I [W]

$$\eta_O = \frac{P_U}{P_I}$$

The input power is defined by,

$$P_I = \dot{m}_F \times \rho_e$$

where $\dot{m}_F$ is the mass flow rate of fuel [g/s] and ρ_e is the fuels energy density [W/g].

Based on the operating envelope, the engine was unable to reach it's optimal operating speed of 15000 RPM specified by the manufacturer due to the increase in torque caused by the friction in the bearings, and and the added inertia of generator and other rotating components. The useful power begins to plateau after 9000 RPM and the maximum useful output power achieved was 148.4 W. In comparison, the engine's rated output given in the manual is 447.6 W (7.4 % engine efficiency at 0.4 g/s fuel consumption of 15 % nitromethane glow fuel). This difference can be attributed to the loses due to propeller and generator efficiencies (maximum of 50 % and 85 % respectively) and friction torque in the bearings (the transmission efficiency is variable with engine speed but is roughly estimated to be 80 %). A summary of these losses is shown in Fig. 11. The engine's fuel consumption was much higher than expected at upwards of 0.4 g/s at maximum efficiency which tended to lower overall efficiencies.

Two separate methods were used to calculate propeller efficiency. The first approach uses the classical definition for efficiency given by the ratio of useful propulsion power out over power absorbed,

$$\eta_{P1} = \frac{P_P}{P_A} = \frac{F_T \times v_f}{\omega_e \times T_P}$$

where P_P is the useful propulsion power [W], P_A is the power absorbed [W], ω_e is the engine speed [rad/s], and T_P is the engine torque absorbed [Nm]. Note that the propeller torque

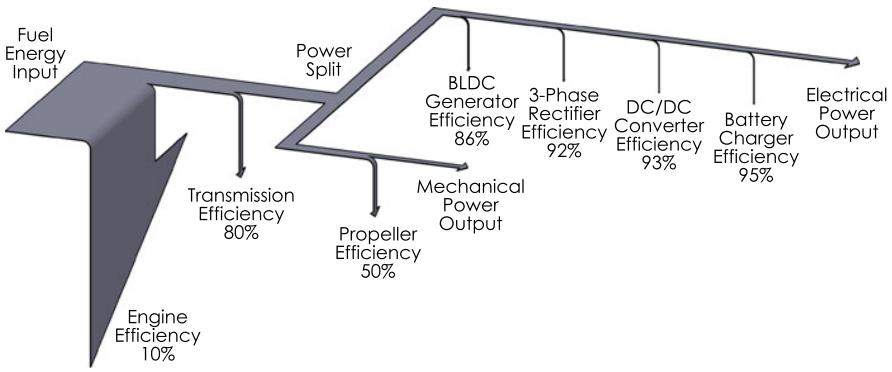

Fig. 11 Summary of hybrid power plant losses

cannot be measured directly as it is a function of the engine torque, generator torque and frictional losses. Therefore, the propeller torque was estimated based on engine speed and propeller pitch using the following set of equations which were produced using propeller tables presented by Lesley [19],

$$C_T = 1.83\times10^9 * \theta^2 + 1.04\times10^8 * \theta + 1.70\times10^8$$

$$T_P = C_T \times \omega_e^2$$

where θ is the propeller pitch in inches measured at 3/4 propeller radius from the axis of rotation.

The second method used to calculate propeller efficiency is based on disk actuator theory [20],

$$\eta_{P2} = \frac{1}{1 + \frac{v_f - v_w}{v_f}}$$

where v_w is the velocity of the air in the wake of the propeller [m/s].

The propeller's efficiency for three pitch settings are plotted against the advance ratio in Fig. 12. The advance ratio J is the ratio between the distance a propeller moves forward through the fluid during one revolution over the product of engine speed and propeller diameter,

$$J = \frac{v_f}{n_e \times d_p}$$

where n_e is the engine speed [rev/s], and d_p is the diameter of the propeller [m].

Both methods produced efficiencies within 10 % however only the first method is presented in Fig. 12 since it was considered to have lower cumulative error. Due to the size of the airship, flight speeds above $10\frac{m}{s}$ are unfeasible based on the total available propulsion power on-board. Therefore advance ratios above 0.3 are unfeasible. Propeller efficiency values correspond well with theoretical values presented by McCormick [13] shown in Fig. 5. Based on the results of these tests, the propeller pitch will remain between 0 and 15 degrees to maximize the propeller efficiency for all foreseeable flight conditions.

The maximum generator power is shown in Fig. 13. The electrical resistance represents the electrical load applied from the electrical propulsion motors, servos, and other on board electronics. Only electrical power produced with voltages above 14.8 V can be used due to the battery voltage therefore, resistances below 3Ω are not useful. Maximum electrical generation is achieved between 3Ω and 4.5Ω of 90 W. Above 4.5Ω, power begins to drop as the engine is no longer able to increase it's speed to increase the voltage and the current reduces following ohm's law.

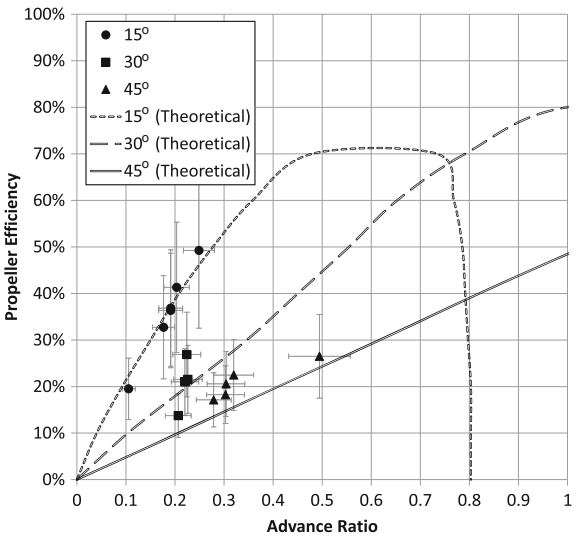

Fig. 12 Propeller efficiency at 3Ω resistance

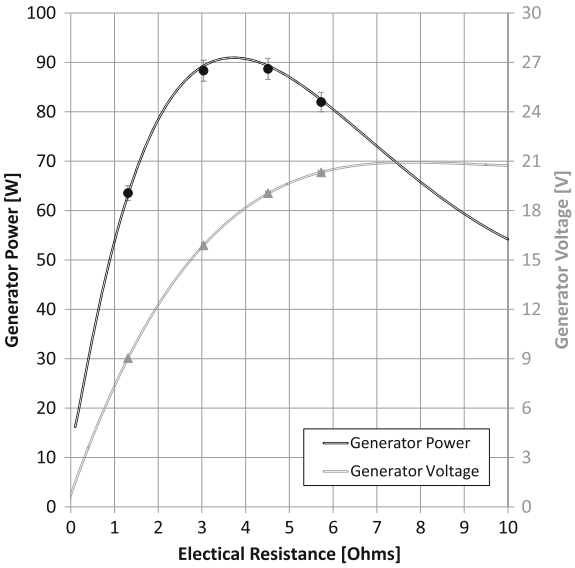

Fig. 13 Generator power at 15° propeller pitch

The effect of nitromethane content on the operating envelope of the system is illustrated in Fig. 14. The useful power generated for all fuel types were within 20 % at any given engine speed. However, the range of operating speeds significantly decreased with the decrease in nitromethane content. Fuel consumption was reduced with the use of the 10 % fuel and increased with use of the 5 %, compared to the 15 %. This in turn resulted in higher efficiencies at the median nitromethane content of 10 %. The increase in efficiency for the 10 % fuel may be explained by the change in ignition timing caused by the change in fuel as glow engines are dependent on the catalytic reaction of the fuel for combustion. It is worth noting that the engine was much more difficult to start and tune with decreasing nitromethane content, and the engine struggled to reach a steady state for the majority of tests.

The average current draw required by the brushless DC motor to start the engine was measured to be 35.7 A (with a peak of 49.6 A) at 14.8 V which translates into 538.4 W. However, the average time before the engine began driving the brushless DC motor was 0.28 s leading to an energy draw of the battery of 41.9 mWh. The servos used to vary the engine throttle and pitch angle drew 1.08 W and 2.00 W and were typically used only at start-up for less than 5 s (1.5 mWh and 2.8 mWh, respectively). The glow plug drew a constant 7.58 W over 5 s resulting in a drain of 10.5 mWh. The microcontroller used to generate the PWM signals is run continuously, but enters a power save mode when not receiving an input. Thus reducing its active consumption from 20 mW to 1.2 mW and can be neglected. The total energy required to start the engine once is 56.7 mWh or about 0.06 % of the battery's capacity.

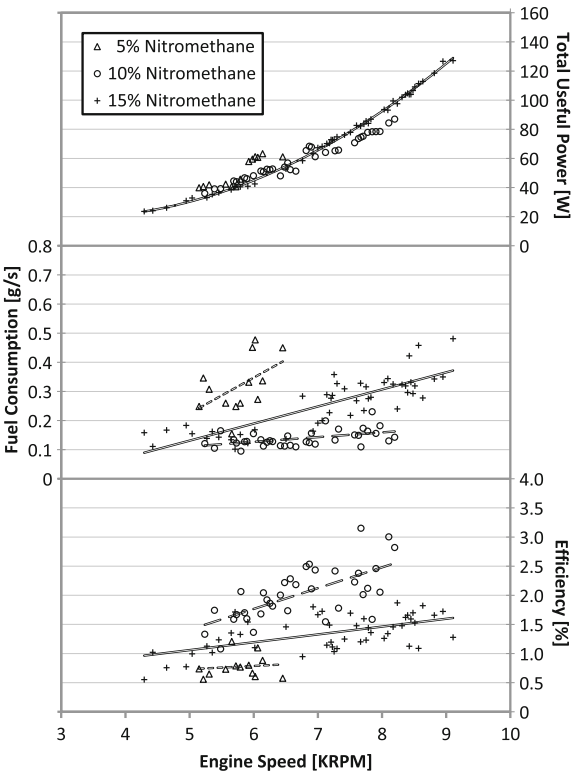

Fig. 14 Engine operating envelope for various nitromethane content fuels

The current design can run the glow engine for 2.08 h on 3 kg of fuel at the maximum efficiency point. Given the 88.8 Wh battery capacity on-board plus 90 W regeneration and assuming an average of 50 W power draw from electric propulsion and electronics results in an overall flight endurance of 5.52 h. With 60 W mechanical propulsion during engine on time and assuming 30 W electric propulsion on average the maximum range of the airship (with zero net wind) is 123 km.

The power and energy density of the glow engine hybrid system at the optimal operating point can be calculated for a given amount of fuel. The power density, δ_P, is found by,

$$\delta_P = \frac{P_U}{\sum m_f + \sum m_v}$$

and energy density, δ_E, is found by,

$$\delta_E = \frac{P_U \times t_r}{\sum m_f + \sum m_v}$$

where t_r is the operating time in [h], $\sum m_f$ is the sum of fixed or dead masses such as the engine, motor and frame, and $\sum m_v$ is the sum of variable masses such as fuel in in [kg] of batteries or a combination of both. These two equations form the operational limits of each system which are represented by lines shown in Fig. 15. The horizontal asymptote is the maximum power density and is governed by the maximum output power of the power plant considered. If the variable mass is infinitesimally small, maximum power density is

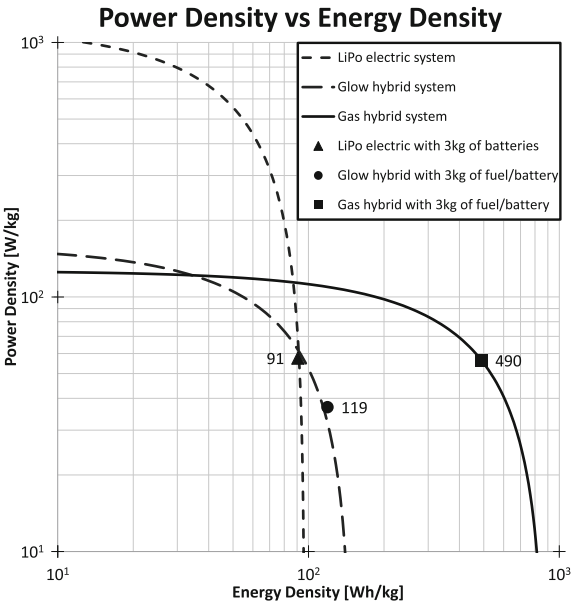

Fig. 15 Power density versus energy density for electric, glow hybrid and gas hybrid systems

achieved. The vertical asymptote is the maximum energy density and is governed by the energy density of the fuel source. If the power plant has an infinite supply of fuel or batteries, the maximum energy density is achieved, since the operating time depends on the about of fuel or the total capacity of batteries available.

A circular point is plotted on Fig. 15 for the current system supplied with 3 kg of fuel. Given the electric motor and propeller efficiency, and the same lithium polymer battery of the current system, similar points can be constructed for a fully electric system and a gasoline hybrid system. Figure 15 indicates a 30 % improvement in energy density can be achieved with the current system over that of a fully electric system with 3 kg of dedicated batteries. If the energy capacity of upcoming battery technologies were to increase, the vertical asymptote associated with fully electric systems would move to the right and rival that of hybrid systems.

Energy density is paramount over power density for long duration missions as the mass of the fuel becomes larger than the mass of the power plant. Considering this, further improvement is possible if a 4-stroke gasoline engine is used in the place of the 2-stroke glow engine. Gasoline has a 154 % increase in energy density over glow fuel with 15 % nitromethane and requires less oil in the mixture (which does not contribute towards useful work). A spark ignition would also provide practical benefits of reliable start up and ignition timing compared to a glow plug. Although 4-stroke engines generally weigh more than 2-stroke engines at the same power, they have significantly lower fuel consumption rates which becomes paramount when carrying over 1 kg of fuel. This can be seen in Fig. 15. For lower variable masses (i.e. fuel) glow fuel hybrid systems would exhibit a higher power density compared to gasoline hybrid engines.

The conservatively estimated overall cost for fabricating a single unit is $5,000 CAD. The low material and manufacturing cost was achieved from using or modifying commercially available, off-the-shelf components. The performance metric presented in Fig. 2 is given by,

$$C_P = \sqrt[3]{M_P \times D \times t_o}$$

where C_P [kg$^{\frac{1}{3}}$ km$^{\frac{1}{3}}$ h$^{\frac{1}{3}}$] is the performance metric, M_P is the payload mass in [kg] , D is the UAV's range in [km] and t_o is the maximum operating time or endurance in [h] . Given the estimated payload of 1 kg (does not include fuel) and the endurance and range previously calculated (5.52 h and 123 km respectively), the performance metric for this UAV design is 8.8. The average UAV cost metric at the same price point is 1.9. This represents a 363 % increase compared to existing designs.

5 Conclusion

The energy density of the purposed hybrid power plant design was proven to be higher than an equivalent purely electric system through experimental testing, despite sub-par engine performance. Further increases are expected if a 4-stroke gasoline engine is implemented in a similar configuration. Future plans involve testing the aforementioned air ballasting system, implementing a new power plant design focused around a 4-stroke gas engine, and performing full scale tests of the completed UAV system.

References

1. Rao, J., Gong, Z., Luo, J., Xie, S.: Unmanned airships for emergency management. In: Safety, Security and Rescue Robotics, Workshop, 2005 IEEE International, pp. 125–130. IEEE (2005)
2. Fukao, T., Yuzuriha, A., Suzuki, T., Kanzawa, T., Oshibuchi, T., Osuka, K., Kohno, T., Okuyama, M., Tomoi, Y., Nakadate, M.: Inverse optimal velocity field control of an outdoor blimp robot. In: Proc. of the 17th IFAC World Congress, pp. 4374–4379 (2008)
3. Saiki, H., Fukao, T., Urakubo, T., Kohno, T.: Hovering control of outdoor blimp robots based on path following. In: 2010 IEEE International Conference on Control Applications (CCA), pp. 2124–2129. IEEE (2010)
4. Jia, R., Frye, M., Qian, C.: Control of an airship using particle swarm optimization and neural network. In: IEEE International Conference on Systems, Man and Cybernetics, 2009. SMC 2009, pp. 1809–1814. IEEE (2009)
5. González, P., Burgard, W., Sanz Domínguez, R., López Fernández, J.: Developing a low-cost autonomous indoor blimp. J. Phys. Agents **3**(1), 43–52 (2009). ISSN 1888-0258
6. Valerdi, R., Merrill, J., Maloney, P.: Cost metrics for unmanned aerial vehicles. In: AIAA 16th Lighter-Than-Air Systems Technology Conference and Balloon Systems Conference (2005)
7. R. B. I. Limited: Uav directory (2010)
8. Defense, D.: Unmanned aircraft systems roadmap 2005–2030. Tech. Rep. (2005)
9. Defense, D.: 2009 worldwide uav roundup. Tech. Rep. (2009)
10. Khoury, G., Gillett, J.: Airship Technology. Cambridge University Press, London (1999)
11. Gawale, A., Pant, R.: Paper 2004-01-design studies of power plant system of non-rigid airships. Aerospace Engineering Department, Indian Institute of Technology Bombay, Mumbai-400076 (2004)
12. Pant, R.S.: A methodology for determination of the baseline specifications of a non-rigid airship. AIAA's 3rd Annual Aviation Technology, Integration, and Operations (ATIO) Tech 17–19 November 2003, Denver, Colorado, AIAA 2003–6830 (2003)
13. McCormick, B.: Aerodynamics, Aeronautics, and Flight Mechanics. Wiley, New York (1979)
14. Rizzoni, G., Hartley, T.: Principles and Applications of Electrical Engineering. McGraw-Hill Higher Education (2004)
15. Lee, H.: Advanced control for power density maximization of the brushless DC generator. Ph.D. thesis, Texas A&M University (2003)
16. W. C. Ltd: Battery and energy technologies (2010)
17. Yoshio, M., Brodd, R., Kozawa, A.: Lithium-Ion Batteries: Science and Technologies. Springer (2009)
18. Zimmer, G.: Battery management design for high power lithium battery stacks. Tech. Rep., Linear Technology (2009)
19. Lesley, E.P.: Propeller tests to determine the effect of number of blades at two typical solidities. Tech. Rep., Stanford University, Daniel Guggenheim Aeronautical Laboratory, NACA Technical Note 698 (1939)
20. Fox, R., McDonald, A., Pritchard, P.: Introduction to Fluid Mechanics, vol. 7. Wiley, New York (1985)

A.3. Hybrid Power Plant Design for a Long Range Dirigible UAV

Disclaimer: Reprinted from a previously published manuscript in the IEEE/ASME Transactions on Mechatronics, 19:606-614, 2014, entitled "Hybrid power plant design for a long range dirigible UAV".

Hybrid Power Plant Design for a Long-Range Dirigible UAV

Steven Recoskie, Atef Fahim, Wail Gueaieb, *Senior Member, IEEE*, and Eric Lanteigne

***Abstract*—Unmanned aerial vehicle (UAV) dirigibles are well suited for surveillance and surveyance missions since they can hover and maintain lift without consuming energy and can be easily deflated for packaging and transportation. The challenge is developing a long endurance system while maintaining a low unit cost. This paper presents a novel hybrid power plant design that addresses both of these requirements. The lightweight design consists of a 4-stroke 14cc gasoline engine in-line with a brushless dc motor/generator and variable pitch propeller capable of producing a maximum power output of 250 W. A method was also developed to compare its performance and endurance to other power plant configurations that could be used in dirigible UAVs. Overall, the proposed hybrid power plant has 674% increase in energy density over that of a purely electric system, thereby proportionally increasing UAV flight time for the same power and weight.**

***Index Terms*—Aircraft propulsion, benchmark testing, brushless machines, design methodology, hybrid power systems, internal combustion engines, power system management, unmanned aerial vehicles (UAVs).**

NOMENCLATURE

Abbreviation	*Description*
HTA	Heavier than air (aircraft)
LTA	Lighter than air (aircraft)
SOC	State of charge
UAV	Unmanned aerial vehicle

I. INTRODUCTION

DIRIGIBLES are well suited for use as reconnaissance platforms to aid rescue crews after disasters since they can maintain lift without consuming energy, can take off and land vertically, and can hover in place to monitor developments on the ground [1]–[5]. Fig. 1 shows how the current fixed wing, rotary wing, and airship UAVs are compared on the basis of endurance and payload. These data were collected and combined from multiple sources [6]–[9]. UAVs that do not travel, such as aerostats, and upper atmosphere UAVs were excluded. Data were also excluded if inconsistent between publications or when only a range was provided. A performance metric can also be used to compare the entire spectrum of UAVs [6]. Fig. 2 combines range, endurance, and payload versus unit cost for a baseline of existing technologies. The performance metric is defined as the cubed root of the product of range, endurance, and payload. The target areas shown in Figs. 1 and 2 represent favorable characteristics for UAVs for surveillance applications. Based on these findings, it is clear that a robust UAV system is needed to meet the operational requirements of both long endurance and long range while maintaining a low unit cost.

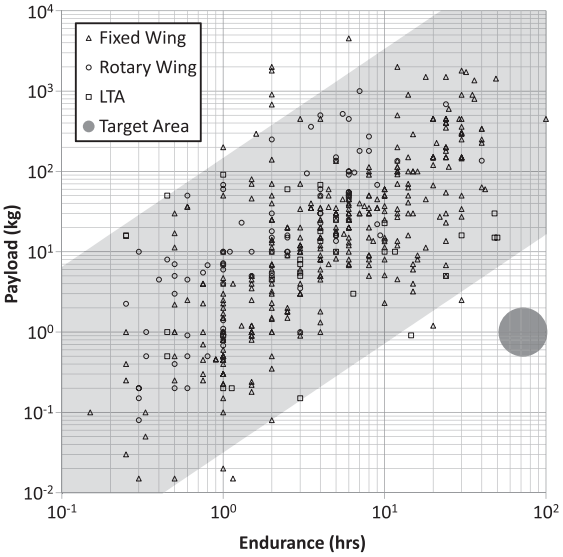

Fig. 1. UAV payload capacity versus endurance. Data were collected from both military and research agencies from several countries. These data were summarized from multiple sources [6]–[9].

This paper presents the design of a UAV hybrid power plant for UAV dirigibles and outlines the performance of the experimental system. Tests were performed to determine the power plant's power output, energy consumption, and overall efficiency with respect to changing the engine throttle, the fuel mixture richness, the propeller pitch, the electrical load resistance, and the freestream velocity. Using these results, a UAV dirigible design equipped with this power plant is then compared to existing UAVs on the basis of cost, payload, range, and endurance.

A. Dirigible UAV Power Requirements

The required range of propulsive power of LTA aircraft is far greater than that of HTA aircraft as LTA aircraft do not require propulsive power for lift. The range of power requirements for

Manuscript received February 14, 2012; revised August 31, 2012 and October 29, 2012; accepted February 21, 2013. Date of publication March 27, 2013; date of current version February 20, 2014. Recommended by Technical Editor Y. Li. This work was supported in part by the Natural Sciences and Engineering Research Council of Canada (NSERC) and in part by the Canada Foundation for Innovation (CFI).

S. Recoskie and E. Lanteigne are with the Department of Mechanical Engineering, University of Ottawa, Ottawa, ON K1N6N5, Canada (e-mail:).

A. Fahim, deceased, was with the Department of Mechanical Engineering, University of Ottawa, Ottawa, ON K1N6N5, Canada (e-mail:).

W. Gueaieb is with the Department of Electrical Engineering, University of Ottawa, Ottawa, ON K1N6N5, Canada (e-mail:).

Digital Object Identifier 10.1109/TMECH.2013.2252183

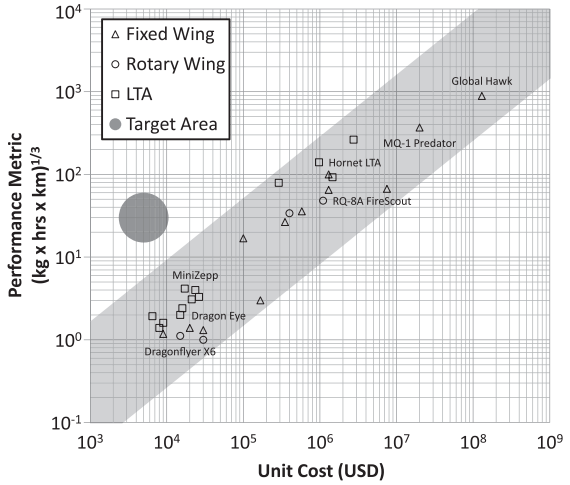

Fig. 2. UAV performance metric (payload × endurance × range) versus unit cost [6]–[9].

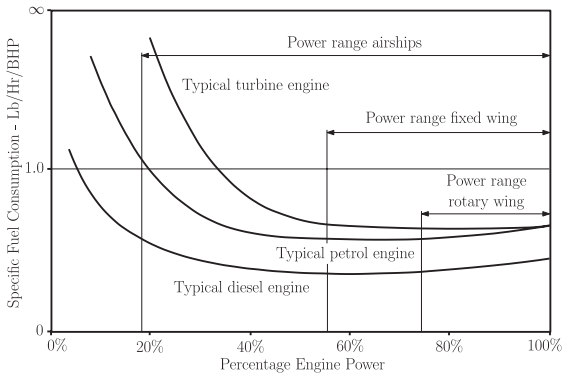

Fig. 3. Specific fuel consumption for different aircraft types [15]. Adapted from [10].

rotary wing, fixed wing, and LTA are presented in Fig. 3. This presents a problem when selecting a suitable prime mover. Electrical power requirements for LTA aircraft can be over 65% of the total power and average cruise speeds compared to 15% for HTA aircraft [10]. Purely electric propulsion designs have significantly shorter flight endurance due to the lower energy density of electric power storage coupled with high electrical power requirements. Purely piston-powered propulsion designs suffer from significant increases in specific fuel consumption at low engine power (during idling) and have a narrow peak efficiency range which makes varying the load on the engine undesirable. Furthermore, electrical energy storage is still required for avionics; therefore, neither fuel nor electric energy can be fully consumed during flight; the first depleted will limit flight endurance. The generally accepted ideal solution is to drive electric generators from piston-powered propulsion engines [10]–[14].

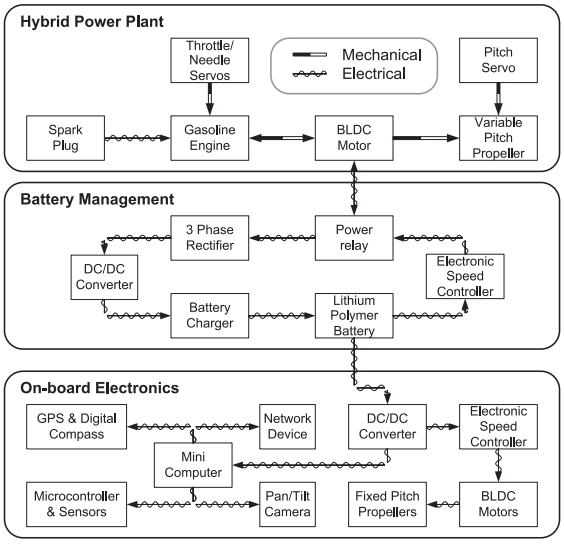

Fig. 4. Dirigible UAV component layout and power flow diagram.

B. Hybrid Power Plant Design

The hybrid power plant consists of an engine, brushless dc generator, and propeller connected in series. This configuration provides the most flexible operating conditions as both fuel and electrical energy can be depleted simultaneously, maximizing the flight endurance. The engine can then be shut down during periods when propulsion or electrical generation is not required and the generator can be run in reverse to start the engine when required, eliminating the need for a separate starter motor. Starting and stopping the engine as required keeps the engine under constant load and maximum efficiency, and maintains the batteries in their useful operating range. This is a common technique in the control of hybrid electric vehicles [16], [17]. Maximum propeller efficiency can be achieved by implementing a variable pitch propeller.

A block diagram of the power plant and UAV components is shown in Fig. 4. A rendering of the components mounted to the dirigible platform is shown in Fig. 5. Properly matching the engine and generator speed ranges can minimize specific fuel consumption of the engine. When the power plant is connected to the UAV, the engine is turned ON according to the current flight conditions. These flight conditions consist of distance remaining to target, UAV operating speed, opposing wind, and the SOC of the battery. This design can be adjusted for the following three scenarios that are specific to UAV dirigibles.

1) *Maximum engine efficiency:* Minimizing engine fuel consumption and maximizing flight duration are vital in this operating mode. The loading of the engine is held in its maximum efficiency zone by balancing the mechanical propulsion and electrical generation based on the current flight conditions, trip characteristics, and SOC of the battery.

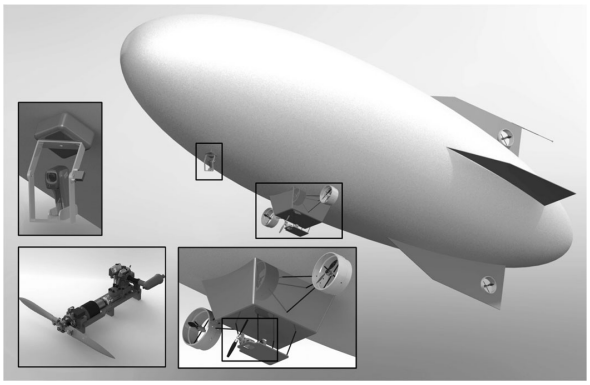

Fig. 5. (Middle) Dirigible design; (left) camera, GPS, and inertial navigation system; (lower left) hybrid power plant; and (below) auxiliary electric propulsion.

2) *Maximum propulsion:* This mode is used when propulsion, but not electrical generation, is required such as when the batteries are charged but the LTA needs to move to a position quickly. During this time, the battery cells can be electrically disconnected and the propeller pitch can be adjusted to maximum thrust based on current airspeed.
3) *Maximum electrical generation:* This mode is used when electrical generation, but not propulsion, is required such as when the batteries need to recharge and the LTA is hovering in place. During this time, the propeller pitch is adjusted to a feathered position and battery cells are electrically connected.

II. Hybrid Power Plant Design Overview

A. Hybrid Power Plant Configuration

Three configurations that are common among hybrid electric road vehicles are series, parallel, and power split (a combination of series and parallel). The ideal configuration for a dirigible UAV will minimize the number of components (i.e., weight) and will minimize energy conversions and transformations (i.e., losses). A series configuration requires two energy conversion processes that reduce efficiency and prevent the engine from contributing to the total available propulsion power. A parallel configuration would require a controllable clutch mechanism to decouple the electric motor from the engine to prevent it from back driving. The weight of two 40-g brushless dc motors and their mountings were found to be lighter than adding such a clutch, while the additional electric motors increase the total available propulsion power. The configuration chosen for this power plant presented in this paper is a power split configuration (full hybrid) with separately actuated propulsion.

The hybrid power plant is in a parallel configuration, while the additional electrically driven propellers also provide propulsion independently of the power plant as in a series configuration. Two other benefits are the reduced dependence on a single propulsion system and increased operational flexibility.

B. Engine

Based on previous research with a 2-stroke OS 25LA model engine [15], it was determined that energy density is more important than power density when selecting a prime mover for maximizing flight endurance. Gasoline engines generally have lower power densities than glow engines but also have lower fuel consumption rates which becomes necessary when carrying over 1 kg of fuel for the same power. Gasoline has a 154% increase in energy density over 15% glow fuel and requires less oil in the mixture (which does not contribute toward useful work). A spark ignition also provides reliable startup and ignition timing compared to a glow plugs. The experimental system presented in this paper uses a Saito 4-stroke gasoline engine that has a significantly higher fuel efficiency per horsepower, a larger range of peak engine performance, and a quieter and cleaner operation compared to the OS 25LA [15]. It also includes a closed-loop spark plug controller with Hall effect sensor feedback for optimal ignition timing.

C. Propulsion

The primary propulsion system consists of a variable pitch propeller connected to the model engine. The variable pitch propeller allows for the three different design scenarios proposed previously in this study.

Since the efficiency of the engine is lower at low engine speeds, four additional brushless dc motors are used for low speed cruising and directional control while the hybrid power plant is OFF. The UAV's electric propulsion is shown in Fig. 5. This configuration provides greater maneuverability and eliminates the need for operating the engine at low RPMs.

D. Starter/Generator

The most important consideration when using a motor as both a starter and generator is the selection of motor constant since the optimal values for these two operations are contradictory. As a generator, the motor constant needs to be sufficiently large such that voltage is generated at a higher potential than the batteries. As a starter, the motor constant needs to be sufficiently small such that the starting torque can overcome inertia and friction in the engine.

A common solution is to add a transmission stage or separate motors for each function; however, this adds weight, complexity, and nonnegligible frictional losses. The proposed solution was to use a large electrical motor (with a lower motor constant) and down convert the output voltage to a usable range when generating, using a high-efficiency switching dc/dc converter shown in the battery management module of Fig. 4.

Brushless dc motors need a specialized electronic speed controller. However, they benefit from higher efficiency and a high power to weight ratio over conventional brushed dc motors. They also have excellent heat dissipation, low noise, low maintenance, and great longevity and reliability because there are no brushes to replace [18]. An AXI 4120 brushless dc motor was selected since high-efficiency power electronic circuits for motor control, filtering, rectification, and dc/dc conversion have

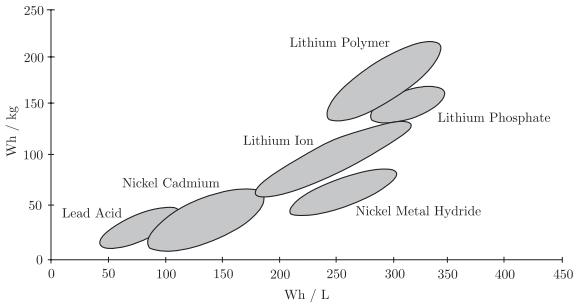

Fig. 6. Energy densities of various battery types [15]. Adapted from [20].

advanced to a point where they can be easily and inexpensively assembled in a small form factor using open source designs.

The main disadvantage of a brushless dc generator is that conventional rectification methods cannot achieve the maximum power possible because of a distorted or unsuitable current waveform [19]. A method is proposed by Lee [19] to maximize the power density of a brushless dc generator by actively switching rectifier diodes with pulse width modulation signals. Although this method of rectification provides higher efficiencies, its control is complex and requires a high-speed digital signal processor to detect the back EMF and current waveforms. Therefore, a full-bridge passive diode rectifier was implemented for its low cost, simple construction, and lack of complex control.

E. Power Management

A comparison of different battery chemistries on the basis of energy mass density and energy volume density (Watt-hours/Liter) is shown in Fig. 6. Lithium polymer batteries are the newest generation of lithium batteries offering the highest energy density compared to other types. They have no memory effect, a good life cycle, and high energy efficiency [21]. The most important attributes of this battery are its fast charge and discharge rates. This is vital to hybrid designs as one of the power limitations of hybrid power plants is the maximum charging current the battery bank can safely accept.

Lithium polymer batteries are not tolerant to over charging or over discharging which both lead to overheating and battery damage, so they require an added protection circuit to prevent these conditions [21]. Maximum heat generation in a properly ventilated battery occurs during the final stages of charging (trickle charging) and during discharging, especially as the SOC is low. Charging a lithium-ion battery to 100% SOC, or discharging to 0% SOC will degrade its long-term capacity [22]. The operational SOC range of a lithium-ion battery is usually limited to a smaller range, such as from 30% to 70%. This reduces the useful battery capacity to only 40% of the fully specified capacity [22]. Hybrid systems have the advantage of maintaining the battery in its useful range by charging more frequently.

Maintaining the battery within this useful battery capacity offers many advantages both for the battery and for the efficiency of the system. As with all batteries, their life is extended by avoiding the damaging and inefficient periods of overheating. In combination with a hybrid system, keeping the battery within its useful range increases the effective energy density of the system when combined with fuel. Avoiding low-power input trickle charge when the battery is near full SOC ensures that the loading on the engine is more stable and the engine is only used in its peak efficiency range. Avoiding near empty SOC prevents battery voltage fluctuations and voltage cutoff during discharging.

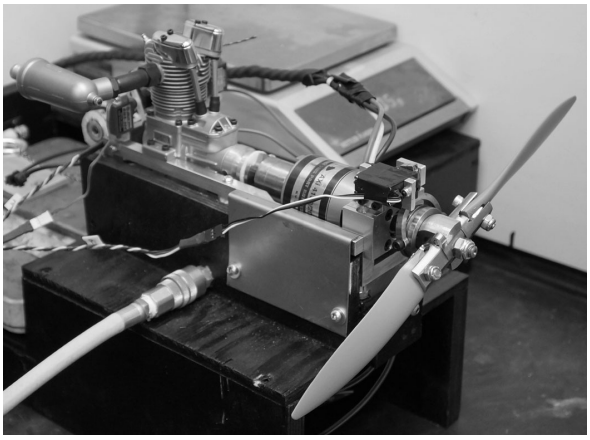

Fig. 7. Experimental hybrid power plant.

There are two branches to the battery management system: the first is the electronic speed controller controlling engine starting and the second is the rectification, filtering, power conversion, and charging circuitry controlling power generation. The engine start-up controller determines the optimal conditions to start the engine based on the flight conditions and the SOC of the battery. Once it is determined that usable electrical power can be collected from the generator, the series of rectifier, dc/dc converter, and battery charger are connected through the relay to accept the charge. The battery banks can be switched ON or OFF by means of a solid-state relay. Voltage, current, and temperature are monitored for cell protection and safety. The charge controller only uses the bulk or constant current charging mode to provide maximum power to the batteries while the engine is ON and generation is needed.

III. Methodology

The hybrid power plant shown in Fig. 7 consists of a gasoline engine, a brushless dc generator, and a controllable pitch propeller connected in series. The power plant frame is fixed to a pressurized air bed that provides a virtually frictionless contact to the test bench. The thrust of the propeller is measured by a cable operated lever arm connected to a digital scale as shown in Fig. 7.

Fuel flow is measured by taking mass readings every 10 s. The spark plug controller and electronic speed controller are connected to a double throw power relay that switches between the electronic speed controller (starter mode) and the 3-phase

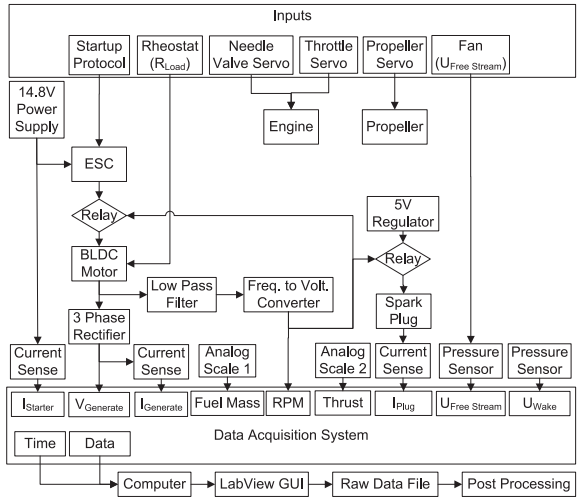

Fig. 8. Overview of testing apparatus configuration.

rectifier (generator mode). If the rotational speed of the brushless dc motor (measured by the frequency to voltage converter) is below 1000 r/min, the relay is switched to starter motor and the spark plug controller is powered. When generating, the electrical load of the battery and charger is simulated using a rheostat set to the appropriate resistance. A freestream air flow is induced by the use of variable speed axial blower to simulate the movement of the UAV.

The power plant was run for a minimum of 60 s at each setting to allow the system to reach steady state. The experimental data were collected using LabView 8.2 with an NI PCI 6229 DAQ. Each input channel was sampled at a rate of 25 kHz. The measurement error contribution of the data acquisition card for each channel was negligible ($\pm 57 \mu$V) for the full scale range of ± 100 mV. The measurement error in each scale was ± 0.5 and ± 0.1 g for the thrust and fuel scales, respectively. Two-pole digital low-pass filters were applied to the data recovered by both mass scale readings to eliminate noise caused by mechanical vibrations of the engine. The current drawn from the spark plug controller and electronic speed controller from their respective batteries was converted to a small proportional voltage using 4 Ω current sense resistor circuits which have measurement errors of $\pm 1\%$. Four pulse width modulated control signals were generated by the data acquisition board that control the brushless dc motor starting speed, throttle position, needle valve position, and propeller pitch position. The air speeds in both the wake of the propeller and the freestream air produced from a variable speed axial blower were measured by taking their respective air pressures with respect to a static pressure measurement which each have a measurement error of ± 0.25 m/s. The pressure sensors used to measure air speed have 1/10th the error of the ones used in previous work, which shown to be one of the largest source of error [15]. The data collected were output into a raw text file for manual postprocessing. A summary of the test apparatus can be seen in Fig. 8.

TABLE I
LIST OF CONTROLLED VARIABLES AND THEIR OPERATING RANGES

Parameter	Minimum	Maximum	Increment
Engine throttle	40%	100% (full)	10%
Needle value	530° (lean)	550° (rich)	5
Electrical resistance	2.8	8.8	Variable

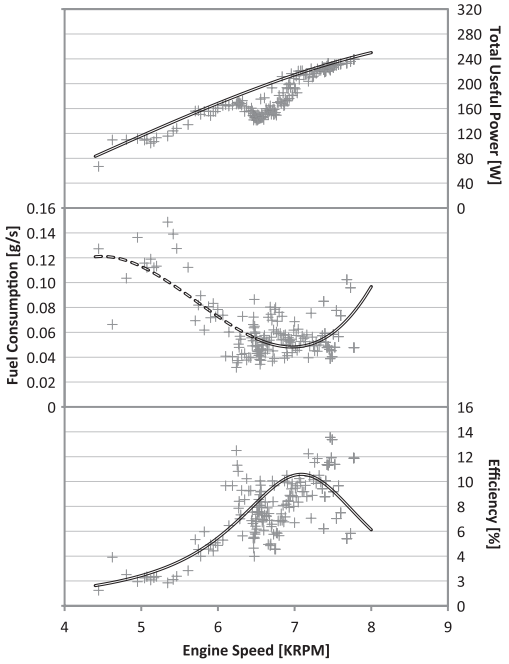

Fig. 9. Engine operating envelope for the hybrid power plant with an 11-in APC propeller.

Tests were performed to determine the power plant's useful power output, energy consumption, and overall efficiency with respect to changing engine throttle, fuel mixture richness, and the electrical load resistance for three propeller diameters. The pitch was set to a constant 15° and the freestream air velocity was set to 4.4 m/s. The angle of 15° was chosen based on previous findings of ideal efficiency [15]. Table I contains a list of controlled variables and their ranges, and the increment at which samples were collected.

IV. RESULTS

The recorded data points were segmented into groups according to engine speed, and averaged to produce the operating envelope shown in Fig. 9. Data points below the engine's start-up speed were omitted. Useful power was calculated based on the sum of propulsion and electrical power such that

$$P_U = P_P + P_G = F_T \times \nu_f + V_g \times I_g \tag{1}$$

where P_U (W) is the total useful power produced, P_P (W) is the propulsion power, P_G (W) is the electrical power, F_T (N) is the propeller thrust, ν_f (m/s) is the freestream velocity, V_g (V) is the generation voltage, and I_g (A) is the generation current.

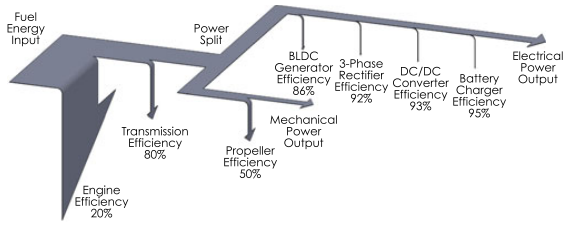

Fig. 10. Summary of hybrid power plant losses.

Data points in the 98th percentile were considered to represent the useful power operating envelope. Overall system efficiency η_O was calculated as the ratio of useful power over input power P_I [W]

$$\eta_O = \frac{P_U}{P_I} = \frac{F_T \times \nu_f + V_g \times I_g}{\dot{m_F} \times \rho_e} \tag{2}$$

where $\dot{m_F}$ (g/s) is the mass flow rate of fuel and ρ_e (W/g) is the fuels lower heating value.

As seen with the previous glow engine [15], the useful power begins to plateau while nearing the engines maximum speed (9000 r/min) and the maximum useful output power achieved was 250 W. In comparison, the engine's rated output given in the manual is 895.2 W at 9200 r/min with a fuel consumption of 0.096 g/s (22% engine efficiency). This difference can be attributed to the loses due to propeller and generator efficiencies (maximum of 50% and 86%, respectively) and the friction torque in the bearings (the transmission efficiency is variable with engine speed but is roughly estimated to be 80%). A summary of these losses can be seen in Fig. 10. The engine's fuel consumption was much higher than anticipated at engine speeds below 6000 r/min (idling speeds). For these speeds, it is suspected that the ideal needle setting were not found and more points are required to ensure the regression matches the engine's performance accurately. Therefore, the portion of the fuel consumption trend below 6000 r/min is represented with a dashed line.

APC propellers of 11-in, 12-in, and 14-in diameters were tested at 15° pitch. Each propeller machined using a computer-aided mill and then balanced in the prop shaft to an accuracy of within 1 gmm. The rated propeller for the selected engine is 14-in; however, due to the additional load of the generator, the engine would not start using the 14-in propeller. The propeller's power and efficiency versus advance ratio are illustrated in Fig. 11. The advance ratio is the ratio of the freestream fluid speed over the rate a propeller moves forward through the fluid and is defined as

$$J = \frac{\nu_f}{n_e \times d_p} \tag{3}$$

where n_e (r/s) is the engine speed and d_p (m) is the diameter of the propeller.

The maximum propeller power for 11-in and 12-in propellers is shown in Fig. 11 to be 60 and 65 W, respectively. Propeller efficiency values for the 11-in propeller correspond well with theoretical values presented by McCormick [23] and with the

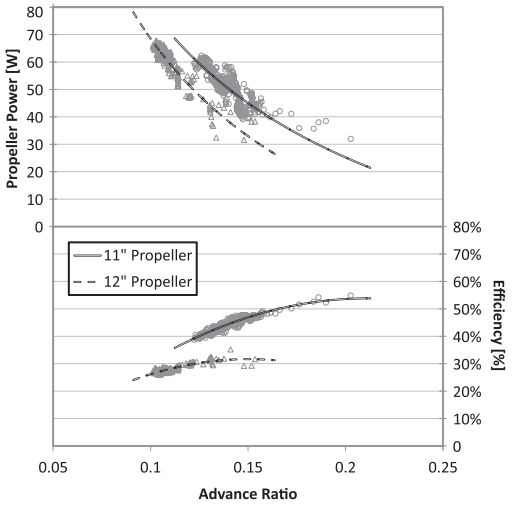

Fig. 11. Propeller efficiency for various propeller diameters at 3 Ω resistance and 15° pitch.

previously tested results [15]. The efficiency of the 12-in propeller was slightly lower than expected as both curves should have the same trend if their pitches are exactly the same. The drop is likely explained by either nonidentical pitch or a slight increase in unbalance compared to the 11-in propeller. Since there is an angle of twist to each propeller and due to limits in machining tolerances, the exact pitch of each propeller when placed in the holder may differ slightly. Also, the importance of propeller balance should not be understated. It was noticed that a static unbalance of as little as 40 gmm would violently shake the propeller blades from their holders.

The method used to calculate propeller efficiency is based on disk actuator theory [24]

$$\eta_{P2} = \frac{1}{1 + \frac{\nu_f - \nu_w}{\nu_f}} \tag{4}$$

where ν_w (m/s) is the velocity of the air in the wake of the propeller.

This method was chosen over the method previously used [15], since it does not require propeller torque estimation and it has lower error with the implementation of more accurate pressure sensors. Due to the size of the airship, flight speeds above 10 m/s are unfeasible based on the total available propulsion power on-board. Therefore, advance ratios above 0.3 are unfeasible. Based on Fig. 11, the results prove the previous claim [15] that slower rotating, smaller diameter propellers would result in higher advance ratios and therefore higher efficiency potential. Although propeller efficiency increases under these conditions, the propulsive power and therefore the productive work done decreases. A compromise between points of efficiency and performance must be chosen based on flight conditions and operational objectives.

The maximum generator power is shown in Fig. 12. The electrical resistance represents the electrical load applied from the

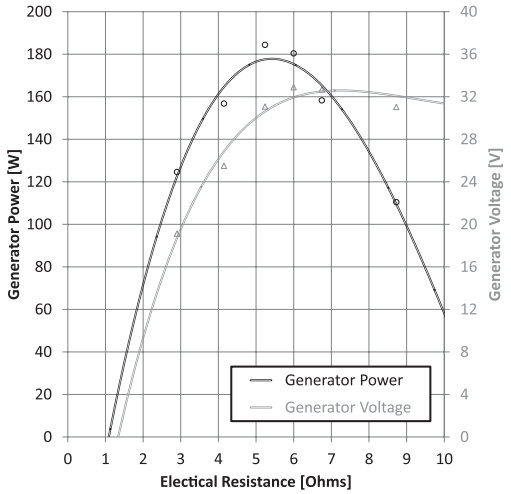

Fig. 12. Generator power with an 11-in APC propeller at 15° pitch.

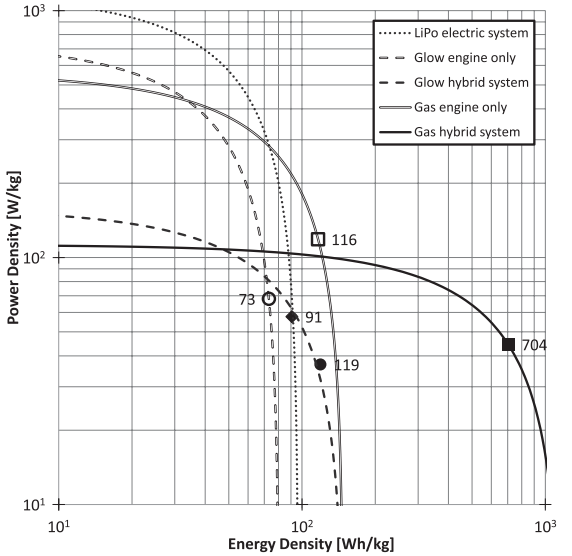

Fig. 13. Power density versus energy density for electric, glow hybrid, and gas hybrid systems.

electrical propulsion motors, servos, and other on-board electronics. Only electrical power produced with voltages above 14.8 V can be used due to the battery voltage; therefore, resistances below 2.5 Ω are not useful. A maximum electrical generation of 180 W is achieved between 5 and 6 Ω. Above 6 Ω, power begins to drop as the engine is no longer able to increase its speed to increase voltage further and the current reduces following Ohm's law.

The torque required to induce a single turn in the engine was experimentally determined to be approximately 1.25 Nm for the gasoline engine compared to 0.7 Nm for the previous glow engine. The average current draw required by the brushless dc motor to start the engine was measured to be 13.5 A at 14.8 V which translates into 199.8 W. However, the average time before the engine began driving the brushless dc was 0.67 s leading to an energy draw of the battery of 37.2 mWh. The servos used to vary the engine throttle and needle valve, and pitch angles drew 1.08, 1.08, and 2.00 W and were only powered between changes. The spark plug controller drew a constant 3 W continuously while the engine was running. The total energy required to start the engine once is 40.2 mWh or about 0.06% of the battery's capacity.

V. Discussion

The current design can run the gasoline engine for 17.7 h on 3 kg of fuel at the maximum efficiency point. Given the 75 Wh battery capacity on-board plus 170 W regeneration while the engine is running, and assuming an average of 50 W power draw from the electric propulsion and electronics combined, an additional 61.7 h of flight is expected on electric power. This totals a flight endurance of 79.4 h (over 3 days). With 55 W mechanical propulsion during engine "ON" time and assuming 30 W electric propulsion consumption on average, the maximum range potential of the airship (with zero net wind) is 1494 km. It should be noted that the term zero net wind does not refer to the absence wind, only that it is equal in magnitude and direction for both departure and return trips. Assuming a one-way flight with a constant head wind of 3 m/s (10.8 km/h), this reduces the range to 637 km.

The method used previously to compare different battery chemistries in Fig. 6 can also be extended to compare different power plant configurations. High power density indicates high-performance characteristics, while high energy density indicates long endurance. The power and energy density can be calculated for any power plant configuration (purely electric, purely fossil fuels, or hybrids) for a given amount of fuel source (batteries, fossil fuels, or a combination of both) and its optimal operating point.

The power density δ_P is found by

$$\delta_P = \frac{P_U}{\sum m_f + \sum m_v}$$

and energy density δ_E is found by

$$\delta_E = \frac{P_U \times t_r}{\sum m_f + \sum m_v}$$

where t_r is the operating time (in hours), $\sum m_f$ is the sum of fixed or dead masses such as the engine, motor, and frame, and $\sum m_v$ is the sum of variable masses such as fuel (in kilograms) of batteries or a combination of both. These two equations form the operational limits of each system which are represented by boundary lines shown in Fig. 13. The horizontal asymptote is the maximum power density (performance) and is governed by the maximum output power of the power plant considered divided by the power plant's fixed mass. If the variable mass is infinitesimally small, maximum power density is achieved. The vertical asymptote is the maximum energy density (endurance) and is governed by the energy density of the fuel source. Increasing

on-board fuel or battery mass will increase energy density to approach the fuel or battery energy density selected. However, this will also decrease power density as energy storage does not contribute to power output. Trend lines to this effect are included in Fig. 13.

As previously stated, the electrical power requirements for LTA aircraft can be up to 65% the total required power. To provide a fair comparison when introducing purely mechanical configurations, the percentage breakdown of mechanical and electrical useful power components must be specified as both electric and hybrid options can produce both types of power while pure piston engines cannot. The power split for Fig. 13 is shown for a 50% mechanical, 50% electrical power split; however, it could be easily modified for other percentages. Therefore, fossil-fuel-only-systems must carry batteries to support the power equal to that it generates which subtracts from the total weight of fuel. The power split only significantly affects the curves of the purely mechanical configurations as both the hybrid and electrical options can provide virtually any power split with little change in performance. If the power split is 90% mechanical or more of the total power, both the power density and energy density of glow and gas-only-systems surpass their hybrid counterparts. This indicates the crossover point when selecting between purely mechanical or hybrid configurations. In addition to the power split, the range of power required as illustrated in Fig. 3 is not captured in these two metrics as the efficiency of electrically driven motors is much more constant than the specific fuel consumption of piston engines [16]. Piston engines would need to include variable speed transmissions to have the same operational flexibility. However, to include the impact of this flexibility into the metrics would require selecting specific flight operating conditions which would diminish the applicability and significance of this comparison.

The solid square point is plotted in Fig. 13 for the current system with 3 kg of fuel and one battery. Given the same propeller efficiency, a similar points can be constructed for a fully electric system with 3 kg of the lithium-polymer batteries and for the fossil-fuel-only-systems with 3 kg of fuel. Each point is labeled with its energy density value. Fig. 13 indicates a 674% improvement in energy density with 3 kg worth of fuel plus battery over that of a fully electric system with 3 kg of batteries.

The conservatively estimated overall cost for fabricating a single unit is $6000. The low material and manufacturing cost was achieved from using or modifying commercially available off-the-shelf items and simple construction techniques. The performance metric presented in Fig. 2 is defined as

$$C_P = 3\sqrt{M_P \times D \times t_o} \tag{5}$$

where C_P ($\mathrm{kg}^{\frac{1}{3}}\mathrm{km}^{\frac{1}{3}}\mathrm{h}^{\frac{1}{3}}$) the performance metric, M_P (kg) is the payload mass, D (km) is the UAV's range, and t_o (h) is the maximum operating time or endurance. Given the estimated payload of 1 kg (does not include fuel) and the endurance and range previously calculated (79.4 h and 1495 km, respectively), the performance metric for this UAV design is 49.1. The average UAV performance metric is 1.9 at the same price point. This represents a 25-fold increase in operational performance compared to existing designs at the same unit cost. The performance, cost, and endurance goals set by the target areas of Figs. 1 and 2 have been achieved.

Now that the performance evaluation of the gas–electric hybrid power plant is complete, future work is required to apply power management algorithms for the different loading conditions. Many supervisory controllers previously developed for hybrid electric road vehicles could also be applied to a dirigible UAV power plant. One such option is the fuzzy logic controller for hybrid electric vehicles presented by Baumann *et al.* [16]. The major difference is that the load schedule (or "driving" schedule) is not standardized and is dependent on the planned flight path which is not bound by roads. The possibility of combining the power management algorithm into the path planning controller used for the UAV will be explored which will provide a manageable compromise between best performance and minimal energy consumption.

VI. Conclusion

An in-line gas–electric hybrid power plant was designed, developed, and evaluated as a low-cost solution for a long-range dirigible UAV. Tests were performed to study the effects of engine settings, propeller diameter, and electrical load on overall performance and to determine the optimal operating points. The power plant is then compared to other power plant configurations that could be used for a dirigible UAV. The energy density of the proposed hybrid power plant design was proven to be higher than equivalent purely electric, purely fossil fuel, or the previously developed glow hybrid systems through experimental testing. Future work will involve implementing advanced power management algorithms, and performing full-scale tests of the completed UAV system.

References

[1] J. Rao, Z. Gong, J. Luo, and S. Xie, "Unmanned airships for emergency management," in *Proc. IEEE Int. Safety Security Rescue Robot. Workshop*, Jun. 2005, pp. 125–130.

[2] T. Fukao, A. Yuzuriha, T. Suzuki, T. Kanzawa, T. Oshibuchi, K. Osuka, T. Kohno, M. Okuyama, Y. Tomoi, and M. Nakadate, "Inverse optimal velocity field control of an outdoor blimp robot," in *Proc. 17th IFAC World Congr.*, 2008, pp. 4374–4379.

[3] H. Saiki, T. Fukao, T. Urakubo, and T. Kohno, "Hovering control of outdoor blimp robots based on path following," in *Proc. IEEE Int. Conf. Contr. Appl.*, Sep. 2010, pp. 2124–2129.

[4] R. Jia, M. Frye, and C. Qian, "Control of an airship using particle swarm optimization and neural network," in *Proc. IEEE Int. Conf. Syst., Man, Cybern.*, Oct. 2009, pp. 1809–1814.

[5] P. González, W. Burgard, R. Sanz Domínguez, and J. López Fernández, "Developing a low-cost autonomous indoor blimp," *J. Phys. Agents*, vol. 3, no. 1., pp. 43–52, 2009.

[6] R. Valerdi, J. Merrill, and P. Maloney, "Cost metrics for unmanned aerial vehicles," presented at the AIAA 16th Lighter-Than-Air System Technology and Balloon System Conf., Arlington, VA, USA, 2005.

[7] Reed Business Information Limited, UAV directory. [Online]. Available: http://www.flightglobal.com/directory/search.aspx?navigationid=372&aircraftcategory=uav&manufacturertype=uav

[8] "Unmanned aircraft systems roadmap 2005-2030," U.S. Dept. Defense, Tech. Rep., 2005. [Online]. Available: https://www.fas.org/irp/program/collect/uav_roadmap2005.pdf

[9] "2009 worldwide UAV roundup," U.S. Dept. Defense, Tech. Rep., 2009. [Online]. Available: http://rmgsc.cr.usgs.gov/UAS/pdf/2009_UAV_Chart.pdf

[10] G. Khoury and J. Gillett, *Airship Technology*. Cambridge, U.K.: Cambridge Univ. Press, 1999.
[11] A. Gawale and R. Pant, "Paper 2004-01-design studies of power plant system of non-rigid airships," Aerosp. Eng. Dept., Indian Inst. Technol. Bombay, Mumbai, India, 2004.
[12] R. R. Glassock, J. Y. Hung, L. F. Gonzalez, and R. A. Walker, "Multimodal hybrid powerplant for unmanned aerial systems (UAS) robotics," presented at the 24th Bristol International Unmanned Air Vehicle Systems Conf., Bristol, U.K., 2009.
[13] P. Bogusz, M. Korkosz, and J. Prokop, "A study of design process of BLDC motor for aircraft hybrid drive," in *Proc. IEEE Int. Symp .Ind. Electron.*, Jun. 2011, pp. 508–513.
[14] D. Gaide, C. Humbargar, D. Larrabee, J. Marshman, E. Petersen, E. Serani, and E. Wormer, "Hybrid electric integrated optimized system (helios); design of a hybrid propulsion system for aircraft," Univ. Colorado, Boulder, CO, USA, Tech. Rep. AIAA 900675, 2011.
[15] S. Recoskie, A. Fahim, W. Gueaieb, and E. Lanteigne, "Experimental testing of a hybrid power plant for a dirigible UAV," *J. Intell. Robot. Syst.*, vol. 9764, pp. 69–81, 2012.
[16] B. Baumann, B. Washington, G. abd Glenn, and G. Rizzoni, "Mechatronic design and control of hybrid electric vehicles," *IEEE/ASME Trans. Mechatronics*, vol. 5, no. 1, pp. 58–72, Mar. 2000.
[17] G. Rizzoni, L. Guzzella, and B. M. Baumann, "Unified modeling of hybrid electric vehicle drivetrains," *IEEE/ASME Trans. Mechatron.*, vol. 4, no. 3, pp. 246–257, Sep. 1999.
[18] G. Rizzoni and T. Hartley, *Principles and Applications of Electrical Engineering*. New York, NY, USA: McGraw-Hill, 2004.
[19] H. Lee, "Advanced control for power density maximization of the brushless dc generator" Ph.D. dissertation, Texas A&M Univ., College Station, TX, USA, 2003.
[20] Woodbank Communications Ltd, (2005). Battery and energy technologies. [Online]. Available: http://www.mpoweruk.com/chemistries.htm
[21] M. Yoshio, R. Brodd, and A. Kozawa, *Lithium-ion Batteries: Science and Technologies*. New York, NY, USA: Springer-Verlag, 2009.
[22] G. Zimmer, "Battery management design for high power lithium battery stacks," Tech. Rep., Linear Technology Corp., Dec. 10, 2008.
[23] B. McCormick, *Aerodynamics, Aeronautics, and Flight Mechanics*. New York, NY, USA: Wiley, 1979.
[24] R. Fox, A. McDonald, and P. Pritchard, *Introduction to Fluid Mechanics*. New York, NY, USA: Wiley, vol. 7, 1985.

Steven Recoskie received the B.A.Sc. degree in mechanical engineering in 2007 from the University of Ottawa, Ottawa, ON, Canada, where he is currently working toward the Ph.D. degree in mechanical engineering.

He teaches part time at the University of Ottawa in free hand and computer-aided drafting. He has a background in machine design, robotics, and control systems. His current research interests include hybrid power generation, dirigible infrastructure design, and unmanned aerial vehicle control systems.

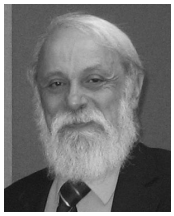

Atef Fahim received the B.Sc. degree from Cairo High Polytech Institute, Cairo, Egypt, in 1972, and the M.Sc. and Ph.D. degrees from Concordia University, Montreal, QC, Canada, in 1977 and 1983, respectively.

He was a Professor in the Department of Mechanical Engineering, Concordia University. He joined the Department of Mechanical Engineering, University of Ottawa, Ottawa, ON, Canada, in 1984. He taught primarily in the areas of CAD/CAM and controls. In addition to his regular administrative duties with the department and the faculty, he actively participated at all levels of university life: as the President of the Association of Professors at the University of Ottawa (1993/1995), a member of the Pension Plan Commitee (1989/2011), and a Faculty Advisor for numerous student competitions (RALOS, Shell Fuelathon, SAE). His research interests included computer control of mechanical systems, automation, and computer-aided design and manufacturing, advanced control for rigid and flexible manipulators and automatically guided vehicles, early warning systems for heavy vehicle instability and rollover, uniset for flexible manufacturing cells, CAD using object-oriented technologies, braiding automation, pultrusion, and winding processes for fiber composite materials.

Wail Gueaieb (M'04–SM'07) received the Bachelor's and Master's degrees in computer engineering and information science from Bilkent University, Ankara, Turkey, in 1995 and 1997, respectively, and the Ph.D. degree in systems design engineering from the University of Waterloo, Waterloo, ON, Canada, in 2001.

He is currently an Associate Professor with the School of Electrical Engineering and Computer Science (EECS), University of Ottawa, Ottawa, ON, Canada. He is also the Founder and Director of the Machine Intelligence, Robotics, and Mechatronics Laboratory in the EECS. He worked in industry from 2001 to 2004, where he contributed to the design and implementation of a new generation of smart automotive safety systems. He is the author/coauthor of more than 90 patents and articles in highly reputed journals and conferences. His research interests include intelligent mechatronics, robotics, and computational intelligence.

Dr. Gueaieb served as an Associate Editor, Guest Editor, and Program Co-Chair for several international journals and conferences, such as the IEEE/ASME TRANSACTIONS ON MECHATRONICS and the 2010 IEEE Conference on Decision and Control.

Eric Lanteigne received the Bachelor's degree in 2003, the Master's degree in 2006, both in mechanical engineering, from the University of Ottawa, Ottawa, ON, Canada and the Ph.D. degree in 2011 from the Royal Military College of Canada, Kingston, ON, Canada.

He was involved in a number of robotic projects including the development of a miniature manipulator module with shape memory alloy actuators, track-mounted mobile robots for the agricultural industry, and mechanisms for extracting pooled water and bitumen deposits from the pipes for the trench-less rehabilitation of municipal water mains. His general fields of interest are robot design and development, and path planning for highly articulated manipulators. His current research interests include the design and development of flexible robotic mechanisms, mobile robots, and unmanned aerial vehicles.

B. Nomenclature for Chapter 4

Variable		Subscript	
A	Reference area	a	Avoidance
$\mathbb{C}$	Cost	c	Constant
C	Constant	d	Drag
δ	Density	e	Energy
d	Distance	g	Goal
E	Energy	l	Terrain
F	Force	m	Pressure ceiling
η	Efficiency	o	Obstacle
n	Node ID	ot	Optimal for time
N	Number of nodes	oe	Optimal for energy
o	Orientation ratio	r	Remaining
ρ	Pressure	T	Thrust
P	Power	w	Wind
Q	Volume flow rate	v	Vehicle
t	Time	vg	Vehicle w.r.t. ground
v	Velocity	vw	Vehicle w.r.t. wind
V	Volume	$\parallel$	Parallel
W	Weight	$\perp$	Perpendicular
z	Elevation		

C. Nomenclature for Chapter 5

Variables		Subscripts	
α	Angle of attack	a	Air
a	Distance from CV to CM	b	Ballasts
A	Aerodynamics vector	b, f	Front ballast
β	Angle of side slip	b, r	Rear ballast
b	Distance from CV to ballasts	c	Forward thruster cluster
B	Input state matrix	CB	Centre of air ballasts
C	Drag coefficient	CM	Centre of mass
d	Distance	CV	Centre of volume
d	Distance matrix	d	Desired set point
D	Dynamic force vector	e	Euclidean
e	Errors	f	Fins
E	Energy	g	Ground or w.r.t. the earth frame
E	Uncertainty vector	L	Moment about OX
G	Gravity/buoyancy vector	m	Airship mass
I	Moment of inertia	M	Moment about OY
J	Polar moment of inertia	N	Moment about OZ
J	Jacobian	t	Tail thrusters
k	Lamb inertia ratios	t, t	Top tail thruster
K	Control/design constants	t, b	Bottom tail thruster
l	Length	o	Overpressure
σ	Set of random percentages	p	Pump

Variable		Subscript	
m	Mass	r	Reference trajectory
$\mathbf{M}$	Mass matrix	r, x	Relative air speed along OX
η	Efficiency	r, y	Relative air speed along OY
ρ	Density	v	vehicle or w.r.t. the vehicle frame
P	Power	x	along or w.r.t OX
$\hat{P}$	Pressure	X	Force along OX
$\mathbf{r}$	Radius vector	y	along or w.r.t OY
$\mathbf{R}$	Rotation matrix	Y	Force along OY
T	Thrust	z	along or w.r.t OZ
t	Time	Z	Force along OZ
$\mathbf{u}$	Input vector		
$\mathbf{U}$	Input force vector		
ν	Linear velocity vector		
υ	Scalar longitudinal speed		
V	Volume		
ω	Rotational velocity vector		
W	Control Lyapunov function		
$\mathbf{x}$	State vector		
x	Position along OX		
y	Position along OY		
z	Position along OZ		
ϕ	Roll about OX		
θ	Pitch about OY		
ψ	Yaw about OZ		

D. Testing Safety Procedure

Test Objectives

- Determine net lift
- Measure step responses of forward thrusters, tail thrusters and air ballasts (6 in total)
- Practice flying manually controlling the airship around the room while tethered
- Take assembly pictures and video

Test Plan 1. Ensure wind speed forecast is below 5kph for the testing period.

2. Clear A141 of debris, clutter, sharp objects, etc.

3. Determine if airship can get out of Lees through the doors

4. Place layered fabric on the construction table and tie ~10 foot tethers to each end. Tie the tethers to the table.

5. Initialize electronics: a. Connect power b. Ensure all actuators are functioning c. Sensor board is recovering data. d. Ensure battery(s) are fully charged 6. Inflate ballonets to roughly $\frac{1}{4}$ their volume.

7. Attach regulator and hosing to a helium tank, set pressure to absolute minimum and begin inflating.

8. While inflating, adjust/pull fabric where necessary to allow the material to expand without tearing

9. Measure internal air pressure off of a pressure sensor using multimeter or other means if available. Once internal air pressure supports a mild overpressure (~300 Pa), stop inflating.

10. Unreel tethers and incrementally attach weights (near gondola ideally) until airship remains neutrally buoyant.

11. Apply step inputs to each actuator incrementally. Be ready with tethers to avoid hitting obstacles, ceiling, etc.

12. Practice manual flight.

13. If weather permits, open double doors to A141 and garage door to A-wing and "walk" the airship outside using the tethers.

14. Test outdoors in open air stadium a. Always remain below 25m (85 feet) b. Have both tethers tied to human counterweights in case of emergency landing

15. Once finished, pilot airship to ground (onto a tarp or protective surface) or pull on tethers, if necessary.

16. Disconnect power.

17. Open helium valve and throw weighted fabric onto envelope to assist in deflation time.

18. Detach gondola and tail fins and roll fabric onto PVC tube. Contingency plan for outdoor testing

Risk to people The vehicle will be flow far from power lines. The dirigible will be powered by two 10" propellers that can cause minor cuts or contusion. The operators have to be aware that the propeller may start at any time. All parts on the dirigible will be securely attached so they do not fall during flight. The operator will not go under the vehicle during flight. Any incident causing injuries will be reporter to the Health and Safety office.

Fire hazard No fuel will be loaded on the vehicle for flight test on the University of Ottawa properties. The source of power will be lithium-ion battery. Lithium-ion batteries can create an open flame if misused or punctured. The vehicle batteries are secured inside the rigid nacelle to prevent puncture of their envelope. Manufactures specification on charge rate, minimum and maximum voltage as well as operating temperature will be followed. An extinguisher will be available during the test. The dirigible is filled with helium, an inert gas.

Risk to property If mishandled, the balloon could get tangled in a building. The dirigible will be flown with wind speed lower than 5kph under the supervision of an experienced radio-controlled helicopter pilot. The vehicle will be tether at all time with a rope attach to one of the operator. In the unlikely case that the vehicle touched a building, risk to the building are minimal because of the low speed involved and the construction material of the dirigible.